THE UNIVERSITY OF SHEFFIELD

Composition-Electrical Property Correlations of Doped $Na_{05}Bi_{0.5}TiO_3$ Ceramics

By

Patrick Wu

A thesis submitted for the degree of Doctor of Philosophy

Supervisor: Prof. D. C. Sinclair

Department of Material Science and Engineering

Faculty of Engineering

August 2018

Acknowledgments

I would like to first thank my supervisor Prof. Derek C. Sinclair for his patience, guidance, motivation and continuous support of my PhD study over past four years. His teaching in defect chemistry encourages me to continue my research in functional ceramics. His passion and excitement for my work are truly inspiring. I benefited from his experience and expertise.

I am also thankful to Prof. Anthony R. West for his insightful comments and advice thought out my PhD study.

I would like to thank Dr. Denis Cumming for giving me an opportunity to learn tape casting and colloidal deposition.

Special thanks to Dr. Ming Li and Linhao Li for their training, guidance and helpful discussions.

Especially thank you to Dr. Fan Yang for her assistance in sample making and Rietveld refinements.

Thanks to Mr. Andrew Mould, Mr. Emilio Pradal-Velázquez, Dr. Le Ma, Dr. Yang Liu and Dr. Zhilun Lu for their help and encouragement.

Finally, I would like to thank my family for their incredibly support. I would never have done this study without you.

Abstract

The influence of the Na/Bi ratio on the electrical properties of nonstoichiometric NBT has been investigated in the $Na_{0.5-x}Bi_{0.5+x}TiO_{3+x}$ series. The solid solution limit is very small $-0.02 < x < 0.02$, but the bulk conductivity has a dramatic change of ~ 4 orders of magnitude at 600 °C, where it switches from an insulator to an ionic conductor for Na/Bi ≥ 1. Within the solid solution limit, the maximum bulk conductivity is achieved by replacing 1 at% Bi with Na atoms on the A-site (acceptor doping), which generates oxygen vacancies. Furthermore, the limit of oxygen vacancies is identified to be ~ 0.33 at%, which is illustrated by the geometric-independent parameter f_{max}. In general, ceramics prepared by hand grinding have better control of the nominal starting composition.

The bulk conductivity of NBT can also be enhanced by Ga-acceptor doping on the B-site. By decreasing the Na/Bi ratio (donor doping) which compensates for oxygen vacancies, it switches from being an ionic conductor to an insulator. In contrast, by increasing the Na/Bi ratio (acceptor doping) which generates oxygen vacancies, the bulk conductivity remains the same, which is independent of the nominal oxygen content. In fact, the actual composition changes with increasing nominal oxygen vacancies, in order to maintain the actual oxygen content at a certain level. This self-recovery behaviour restricts the enhancement of ionic conductivity in NBT-based ceramics.

The influence of B-site acceptor dopants and highly polarised Bi ions on the electrical properties has been investigated in the solid solution of NBT with Bi-based perovskite end members, such as $BiGaO_3$ (BG), $BiFeO_3$ (BF) and $Bi(Ni_{0.5}Ti_{0.5})O_3$ (BNiT). In general, the ionic conductivity is suppressed with increasing doping level due to the mobile oxygen ions being trapped by the accepter dopants on the B-site. The electronic conductivity is enhanced by transition metal ions, such as Fe^{3+} and Ni^{2+}.

For the BG-NBT series, the solid solution limit is ~ 6%, where the ionic conductivity is eliminated. The actual composition may be influenced by the presence of secondary phases, leading to a slight mismatch of the charge configuration between the A and B-site results in a dramatic change in conductivity.

The rhombohedral phase is stabilised by BF-doping, where T_m associated with the permittivity increases from 320 to 445 ℃ when the BF content increases from 0 to 50%. The ionic conductivity is slowly supressed by the BF-doping, where p-type electronic conductivity becomes dominant for samples prepared in air when the BF content is 60%; however, ionic conduction may be dominant when annealed under N_2 at 600 ℃. Furthermore, 1 at% Nb-doping for Ti can efficiently suppress the ionic conductivity.

For the BNiT-NBT series, the solid solution limit is ~ 60%. Neutron diffraction studies confirm the high temperature tetragonal phase is stabilised at room temperature when the BNiT content is ≥ 40%. The coexistence of rhombohedral and tetragonal phases leads to permittivity peak broadening and a decrease of T_m to a lowest value of 186 ℃ during cooling when the BNiT content is 60%. p-type electronic conductivity becomes dominant when the BNiT content is ≥ 30% for samples processed and measured in air.

Contents

Chapter 1.

Introduction

1.1 Background

$Na_{0.5}Bi_{0.5}TiO_3$ (NBT) is commonly considered as a potential lead-free piezoelectric material to replace lead zirconate titanate (PZT) in applications of actuators, transducers and sensors, due to environmental concerns with the toxicity of lead. The major drawback of NBT for dielectric applications is its high leakage current. It was found that small deviations in Na or Bi content for A-site nonstoichiometric NBT can lead to a dramatic change in dc conductivity by ~ 3 orders of magnitude.[1] In previous studies reported by our group, Li *et al*.. indicated the electrical conductivity of A-site nonstoichiometric NBT can be determined by the Bi/Na ratio, where the nominal starting compositions with Bi/Na > 1 and Bi/Na ≤ 1 tend to be an insulator and an ionic conductor, respectively.[2] The electrical conduction mechanism has been studied by a combination of impedance spectroscopy (IS), electromotive force measurements (EMF) and ^{18}O tracer diffusion measurements.[2,3] It was shown that the leakage current is attributed to oxygen ion migration, where the Bi loss during processing and Bi-deficiency generate oxygen vacancies. Furthermore, the chemical stability under reducing atmospheres and ionic conductivity of Bi-deficient NBT ($Na_{0.5}Bi_{0.49}TiO_{2.985}$) can be enhanced by 2 at% Mg-acceptor doping on Ti, indicating NBT-based materials can also be used as an electrolyte for solid-oxide fuel cells (SOFC).

NBT has a complex crystal structure, which involves octahedral tilting, different displacement of Na and Bi ions and short range ordering.[4-6] Computational studies suggest the migration barrier for oxygen vacancies at Bi-Bi-Ti saddle points required the lowest activation energy.[7] Yang *et al*.. suggested the abnormal change in activation energy of the bulk ionic conductivity at ~ 300 ℃ is correlated to coexistence of rhombohedral and tetragonal phases.[8] Furthermore calculations performed by Mayer and Albe show the oxygen migration barriers are phase (polymorphic) dependent, decreasing from the rhombohedral to the tetragonal phase.[9] They also suggested the defect association energy introduced by acceptor dopants may further increase the oxygen migration barrier for the room temperature rhombohedral phase. The ionic conductivity of NBT may be promoted by small amounts of oxygen vacancies.

However, the oxygen migration in NBT may be strongly dependent on the (phase-related) local atomic configurations and the concentration of B-site acceptor dopants.

1.2 Aims and Objectives

1. Investigate the Bi-loss during processing via ball milling. The nominal stoichiometric NBT was prepared by ball milling and hand grinding. The electrical conductivity may behave differently according to the amount of Bi loss associated with the preparation method.

2. Investigate the influence of the Na/Bi ratio on the electrical properties of non-stoichiometric NBT, where the A-site is nominally fully occupied.

3. Establish the effect of adjusting the Na/Bi ratio in cooperation with Ga-acceptor doping on the Ti site to the electrical properties.

4. Explore potential NBT-based mixed electronic/ionic conductors by chemical doping with Bi-based perovskites, where variable valence transition metal ions can occupy the B-site, i.e. $BiFeO_3$ and $Bi(Ni_{0.5}Ti_{0.5})O_3$

5. Investigate the existence of oxygen vacancies in cooperation with the ionic conduction by Nb-donor doping on the Ti site, which normally eliminates ionic conductivity in NBT.

6. Examine the phase formation and microstructure of these NBT-based materials using X-ray diffraction (XRD), neutron diffraction (ND) and scanning electron microscopy (SEM).

7. Examine the electrical properties of these NBT-based materials using impedance spectroscopy (IS) and inductance-capacitance-resistance (LCR) measurements.

8. Determine the electrical conduction mechanism(s) in NBT-based materials using (pO_2 dependent) IS and oxygen ion transport number measurements (EMF).

1.3 References

1. Hiruma, Y., Nagata, H. and Takenaka T., Thermal depoling process and piezoelectric properties of bismuth sodium titanate ceramics, *Journal of Applied Physics* **105**, 084112 (2009)

2. Li., M., Zhang, H., Cook, S.N., Li, L, Kilner, J.A., Reaney, I.M. and Sinclair, D.C., Dramatic Influence of A-site Nonstoichiometry on the Electrical Conductivity and Conduction mechanisms in the Perovskite Oxide $Na_{0.5}Bi_{0.5}TiO_3$, *Chemistry of Materials* **27**, 629-634 (2015)

3. Li, M., Pietrowski, M.J., De Souza, R.A., Zhang, H., Reaney, I.M., Cook, S.N., Kilner, J.A. and Sinclair, D.C., A family of oxide ion conductors based on the ferroelectric perovskite $Na_{0.5}Bi_{0.5}TiO_3$, *Nature Materials* **13**, 31-35 (2014)

4. Jones, G.O. and Thomas, P.A., Investigation of the structure and phase transitions in the novel A-site substituted distorted perovskite compound $Na_{0.5}Bi_{0.5}TiO_3$, *Acta Crystallographica Section B* **58**, 168-178 (2002)

5. Levin, I. and Reaney, I.M., Nano- and Mesoscale Structure of $Na_{1/2}Bi_{1/2}TiO_3$: A TEM Perspective, *Advanced Functional Materials* **22**, 3445-3452 (2012)

6. Beanland, R. and Thomas P.A., Symmetry and defects in rhombohedral single-crystalline $Na_{0.5}Bi_{0.5}TiO_3$, *Physical Review B* **89**, 174102 (2014)

7. He, X. and Mo, Y., Accelerated materials design of $Na_{0.5}Bi_{0.5}TiO_3$ oxygen ionic conductors based on first principles calculations, *Physical Chemistry Chemical Physics* **17**, 18035-18044 (2015)

8. Yang, F., Zhang, H., Li, L., Reaney, I.M., and Sinclair, D.C., High Ionic Conductivity with low Degradation in A-site Strontium Doped Nonstoichiometric Sodium Bismuth Titanate Perovskite, *Chemistry of Materials* **28**, 5269-5273 (2016)

9. Mayer, K. and Albe, K., Influence of phase transitions and defect associates on the oxygen migration in the ion conductor $Na_{1/2}Bi_{1/2}TiO_3$, *Journal of Materials Chemistry A* **5**, 4368-4375 (2017)

Chapter 2.

Literature review

2.1 Perovskites

Perovskites, named after the Russian mineralogist Count Lev Aleksevich von Perovski, are a family of materials which have a general formula ABX_3. In general, A and B adopt metallic cations and X are non-metallic anions. The subject of this thesis is based on the inorganic oxides and therefore ABO_3. The ideal perovskite has a cubic structure ($Pm\bar{3}m$, No. 221) as shown in Fig. 2-1, where the larger A cations (equally or similar sized to oxygen ions) and smaller B cations occupied at the corners and the body centre are in cubo-octahedral and octahedral coordination, respectively. The oxygen ions sit at the face centre linked to six cations (4A+2B). However, in reality, only a limited amount of compounds can fulfil this criteria.

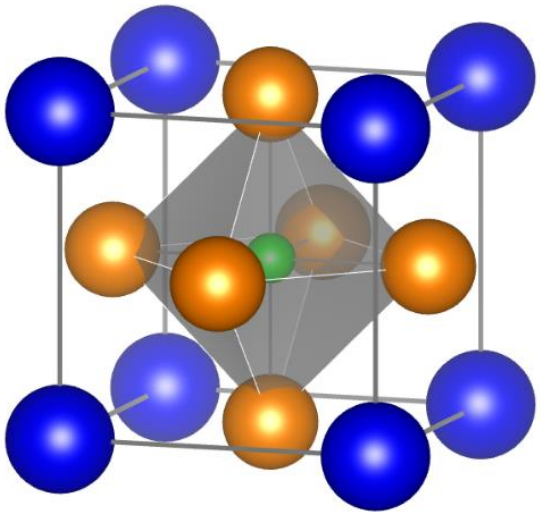

Fig. 2-1. Cubic perovskite unit cell where blue, green and orange spheres represent A, B and oxygen ions, respectively. Structure generated with VESTA software.[1]

Goldschmidt[2] introduced the tolerance factor (t)

$$t = \frac{r_A + r_O}{\sqrt{2}(r_B + r_O)} \quad \text{2-1.}$$

where r_A, r_B, and r_O are the ionic radii of A cation, B cation and the oxygen, respectively. The ideal cubic structure has t = 1, such as $SrTiO_3$. The Perovskite structure can be formed if it is close to 1, which is mostly stable when $0.8 < t < 1.05$.[3] As $t < 1$, distortions occur in order to maintain the stability of the perovskite structure due to the fact the relatively small A cations are unable to fully fill the A-site, leading to displacements of the A/B cations, chemical ordering and tilting of the BO_6 octahedra. These deformations often lower the crystal symmetry, such as orthorhombic, rhombohedral and monoclinic symmetry.[4] For $t > 1$, the B cations are relatively too small to fill the B-site, leading to ionic displacements. Two types of ionic displacements can occur: parallel and antiparallel displacement, where all ions are displaced in one direction and adjacent ions are displaced in opposite directions, respectively. $PbTiO_3$ is an example of parallel displacement for $t > 1$, where Ti^{4+} and O^{2-} are displaced along the c-axis and forms a tetragonal unit cell.[3]

Glazer defined a classification for tilting in BO_6 octahedra in perovskites, where all tilts are considered as combinations of component tilts about the three tetrad axes, which can be regarded to be about the pseudo-cubic axes prior to tilting for small tilt angles.[5] The magnitudes of the tilts about the $[001]_p$, $[010]_p$ and $[001]_p$ (the subscript ''p'' represents pseudo-cubic symmetry) are symbolically indicated by the letters *a*, *b*, and *c*, respectively. When an octahedron is titled along a particular axis, successive octahedra in the directions perpendicular to the tilt axis are constrained to tilt in opposite rotating direction to conserve octahedral connectivity, as shown in Fig. 2-2. However, successive octahedra along the tilt axis can tilt in the same or opposite rotating direction about that axis, which are described as being 'in-phase' and 'anti-phase' and denoted with superscript '+' and '-', as shown in Fig. 2-3 (a) and (b), respectively. A superscript '0' indicates there is no tilting along an axis.

Fig. 2-2. A titled perovskite structure along the [001] axis. The grey squares and black circle represent the oxygen octahedra containing B-site ions and A-site ions, respectively. The black arrows represent the direction of octahedral rotation. Figure is adopted from ref 6 (Figure 2).

Fig. 2-3. (a) An in-phase tilted perovskite, and (b) an anti-phase tilted perovskite along the [001] axis. Squares and open circles represent the oxygen octahedra containing B-site ions and A-site ions, respectively. Figures are adopted from ref 11 (Figure 7(a) and 2, respectively.)

Perovskites cover a wide range of applications from insulators to superconductors, i.e. ferroelectrics, piezoelectrics, semiconductors, ionic conductors and mixed conductors, due to their flexibility in their composition and structure. More than one type of cations, such as different valences and ionic sizes, can place into the A- and B-sites to form a stoichiometric or non-stoichiometric composition, leading to a large possible number of combinations to tune the physical and electrical properties via chemical doping.

2.2 Dielectric properties

Dielectrics are ideally considered as insulating materials, where no long range charge migration occurs with an applied electric field. Instead, only limited rearrangement takes place and introduces a dipole moment, which is called polarisation. The various polarisation processes are shown in Fig. 2-4.[7] When an electric field is applied, positive charges (+ve) and negative charges (-ve) tend to shift towards opposite directions. All materials can possess an atomic polarisation by a small displacement between the electron cloud (-ve) and nucleus (+ve) in an atom. For ionic compounds, a small displacement is introduced by cations (+ve) and anions (-ve). For dipolar materials, which are commonly seen in liquid and gases, the directions of the dipole in molecules are aligned towards the direction of an electric field and therefore produce a net polarisation. Space charge polarisation is attributed to the limited mobility of charge carriers, which is restricted by a potential barrier, such as a grain boundary, whereby +ve and –ve charges are trapped.

Fig. 2-4. Various polarisation process. Figure is adopted from ref 7 (Figure 2.25).

A good dielectric is also a good insulator, where the main parameters are relative permittivity (ε_r) and dielectric loss (tan δ). ε_r of a dielectric is the ratio of permittivity of dielectric (ε) to the permittivity of vacuum (ε_0), which is described as the following equation:

$$\varepsilon_r = \frac{\varepsilon}{\varepsilon_0} \qquad 2\text{-}1.$$

Permittivity (ε^*) of alternating voltage (ac) is complex which consists a real part (ε') and an imaginary part (ε'') component:

$$\varepsilon^* = \varepsilon' - i\varepsilon'' \qquad 2\text{-}2.$$

tan δ is defined as the ratio betweenε'' and ε':

$$\tan\delta = \frac{\varepsilon''}{\varepsilon'} \qquad 2\text{-}3.$$

The polarisation process is frequency dependent as shown in Fig. 2-5,[7] where dielectric dispersion (ε') and energy dissipation (ε'') associated with atomic, ionic, dipolar and space charge polarisations (ordered in decreasing frequency) occur at different time scales.

Fig. 2-5. Frequency dependence of the real part (ε_r') and imaginary part (ε_r'') of relative permittivity. Figure is adopted from ref 7 (Figure 2.38).

2.3 $Na_{0.5}Bi_{0.5}TiO_3$ (NBT)

Sodium bismuth titanate, $Na_{0.5}Bi_{0.5}TiO_3$ known as NBT or BNT, has a perovskite structure where an equal amount of Na and Bi ions randomly occupy on the A-site and Ti ions sit on the B-site. From an electrostatic point of view, the chemical ordering is expected due to the different valances between Na^+ and Bi^{3+} ions sharing the A-site occupancy.[8] However, over decades of study, there is still no strong evidence showing any preference of Na^+ and Bi^{3+} ions ordering in any structural form; however, NBT undergoes a series of complex phase transitions from cubic ($Pm\bar{3}m$) to a tetragonal (P4bm) and rhombohedral R3c/monoclinic Cc structure on cooling from above 520 ^oC to room temperature.

2.3.1 Room temperature structure

At an early stage, NBT was structurally refined with rhombohedral symmetry at room temperature based on the X-ray diffraction (XRD) patterns.[9] The first neutron diffraction study reported by Vakhrushev *et al*..[10] confirmed the rhombohedral R3c symmetry and observed an $a^-a^-a^-$ octahedral tilting system according to the oxygen positions, which was also confirmed by Jones and Thomas[11] from their neutron

diffraction studies on ground single crystals, where the cation displacement is parallel to $[111]_p$ axis.

The local environment of Bi atoms was approached by x-ray absorption fine structure (XAFS), where the shortest Bi – O bond distance (2.22 Å) is shorter than the one derived from the neutron diffraction data (2.5 Å), which suggested an additional displacement for Bi atoms leads to a lower crystal symmetry.[12] Gorfman and Thomas[13] observed Bragg peaks splitting in high resolution reciprocal-space maps obtained from a high-resolution diffractometer inspecting on flux-grown single crystals and showed that the monoclinic Cc symmetry (a monoclinic subgroup of R3c) had a better fitting than a combination of rhombohedral R3c and tetragonal P4bm phases. Aksel *et al.*[14] used this Cc model to refine high resolution powder diffraction patterns of calcined and sintered powders synthesised by conventional solid state synthesis, as shown in Fig. 2-6. They observed the 110_p diffraction peak splitting on the sintered powders which had a better fitting on the Cc model than the R3c model. The calcined powders can be refined by both Cc and R3c models due to the relatively similar 110_p diffraction peak. Their following studies improved the data refinements using cubic $Pm\bar{3}m$ phase + Cc model.[15] In general, laboratory based XRD can only determine the average structure of NBT. The rhombohedral R3c phase is often modelled as being pseudo-cubic in symmetry because the deviation of its angle ($\alpha = 89.86°$) to a cubic structure is very small.[11]

Fig. 2-6. Powder diffraction patterns (red crosses) of calcined (left) and sintered (right) NBT powders at room temperature refining as the space group R3c (bottom) and Cc (top) on the 110_p diffraction peak. Figures are adopted from ref 14 (Figure 1 and 2).

Further details of the local structure at room temperature were observed under transmission electron microscopy (TEM). It was found that some tetragonal platelets with $a^0a^0c^+$ tilting formed as residuals of the high temperature P4bm phase was in the rhombohedral R3c matrix with $a^-a^-a^-$ tilting, where the rhombohedral phase is consistent with the neutron diffraction study.[16-18] Levin and Reaney[19] proposed a 'continuous tilting' model to explain the 110_p peak distortion observed by XRD, as shown in Fig. 2-7. They indicated that the 110_p diffraction peak splitting (arrows) is strongly dependent on the thermal and mechanical history of the sample, such as the sintering temperature and residual stress introduced by grinding, and cannot be accounted for by rhombohedral distortion. The average structure (by XRD) depends on the completion of the coherence length of octahedral rotations and cation displacements, which is dominated by the long coherence length of the anti-phase tilting ($a^-a^-a^-$ (R3c) or $a^-a^-c^-$ (Cc)). Beanland and Thomas[18] unequivocally investigated the symmetry of the defect-free regions from single crystals and specified the average structure of bulk NBT is R3c. They also identified the defects in other regions, such as antiphase boundaries, tetragonal platelets and domain walls, which may locally interact with bulk NBT to form variable Cc symmetry with the $a^-a^-c^-$ tilting, where Ma *et al.*.[20] suggested the symmetry of NBT is Cc phase based on their TEM study.

Fig. 2-7. 110_p diffraction peak for NBT measured on ground powders at room temperature after sintering at (a) 950 ℃ for 96 h, (b) 1000 ℃ for 5 h, and (c) 1100 ℃ for 3 h, while (d) was obtained after additional annealing at 600 ℃ for all samples. Figure is adopted from ref 19 (Figure 1).

Rao et al. presented extensive studies regarding the electric-field-induced Cc to R3c phase transformation of NBT at room temperature.[21-23] XRD were performed on the ground powders of the sintered pellets before and after poling under an electric field. The XRD diffraction pattern obtained from sintered samples without poling was in good agreement with the Cc model reported by Aksel *et al*..[14]. However, the 110_p diffraction peak dramatically changed with poling, which can be perfectly fitted as the space group R3c, as shown in Fig. 2-8. They also confirmed that the 110_p diffraction peak profile is very sensitive to thermal, mechanical and electrical stimuli. Further annealing at 400 ~ 700 ℃ for unpoled or poled samples will return to the equilibrium state at room temperature, where the monoclinic-like global distortion occurs.

Fig. 2-8. Rietveld plot (red line) of $110_{p(pc)}$ diffraction peak (open circles) for NBT fitted with the space group Cc (bottom) and R3c (top). The diffraction patterns were obtained from the ground powders of the sintered (left) and poled sintered pellet (right). Figures are adopted from ref 21 (Figure. 1 and 3).

In general, cation ordering in perovskites is most likely to occur on the B-site. However, A-site cation ordering can still be driven by octahedral titling, anion vacancies, B-site cation ordering and A-site cation vacancies.[24] From an electrostatic point of view, B-site cations prefer rock salt (111) ordering in $A_2BB'X_6$ perovskites, whereas A-site cations prefer layered (001) ordering in $AA'B_2X_6$ or $AA'BB'X_6$ perovskites, as shown in Fig. 2-9.[24] In addition, it requires significant difference in size between A and A' cations to possess anion displacement in a cis coordination (Fig. 2-10) to release local stresses and balance local charge configurations in order to acquire A-site cation ordering. In NBT perovskite, the ionic radii of Na^+ and Bi^{3+} are similar,[25] suggesting A-site cation ordering is unlikely to occur. This is consistent with TEM studies.[17-19] However, based on computational studies, short-range chemical ordering may be potentially stabilised by Bi^{3+} lone pairs, especially in structures which consist of Bi-rich layers in {001} planes.[26] The local ordering is also suggested by Raman spectroscopic data.[27]

Fig. 2-9. Rock salt and layered cation ordering in $A_2BB'X_6$ (left) and $AA'B_2X_6$ (right) perovskites. Grey and orange spheres represent A-site cations. B-site cations sit in the middle of octahedrons. Figures are adopted from ref 24 (Figure.2)

Fig. 2-10. Oxygen environments for layered (001) ordering in cis coordination. Figure is adopted from ref 26 (Figure 5)

2.3.2 Phase transitions and dielectric properties

In general, NBT exhibits phase transitions from rhombohedral R3c to tetragonal P4bm to cubic $Pm\bar{3}m$ symmetry on heating, where the octahedral tilting changes respectively from $a^-a^-a^-$ to $a^0a^0c^+$ to $a^0a^0a^0$ according to neutron studies reported by Jones and Thomas.[11] Based on their studies as shown in Fig. 2-11, only the rhombohedral phase is observed below ~255 ℃. The coexistence of rhombohedral and tetragonal phases occurs between 255 ~ 400 ℃, which is consistent with the XRD results reported by Suchanicz and Kwapulinski.[28] Single tetragonal phase is observed between 400 ~ 500 ℃ and followed by coexisting with a cubic phase up to 540 ℃. The phase coexistence of rhombohedral/tetragonal and tetragonal/cubic is determined by the presence of the superlattice peaks associated with $a^-a^-a^-$ and $a^0a^0c^+$ tilting.

Fig. 2-11. Temperature dependence of phase volumes with different symmetry. Figure is adopted from ref 11 (Figure 12).

A typical plot for the fixed frequency temperature dependence of ε_r and tan δ for NBT are shown in Fig. 2-12.[29] The maximum in ε_r occurs at ~ 325 ℃, which is defined as T_m. Furthermore, a frequency dependent ε_r peak is observed at ~ 200 ℃, suggesting there are two phase transitions associated with the temperature dependence of ε_r and relaxor-like behaviour occurs below this temperature due to the frequency dependent relaxation. On the other hand, tan δ has a peak at ~ 200 ℃ obtained from the poled samples, which is correlated to the depolarisation temperature (T_d). Double P-E hysteresis loops were observed from the slightly Na-rich NBT ($Na_{0.51}Bi_{0.50}TiO_{3.005}$) as

temperature is approaching T_d on heating (Fig. 2-13), suggesting a ferroelectric (FE)-antiferroelectric (AFE) phase transition occurs at this temperature.[29] Similar results were also obtained from 15%$SrTiO_3$-85%NBT[30]. It should be noted that the undoped NBT often has high leakage, leading to unsaturated hysteresis loops. Some early studies suggested there is an AFE-paraelectric (PE) transition at 320 ℃ due to the disappearance of the domain structure observed in single crystals between 260 ~ 295 ℃.[31] Isupov[32] argued ferroelectricity should occur above 320 ℃ because domain structure reappear above 295 ℃ on heating, where the phase transition may be driven by oxygen octahedral tilting. Overall, the temperature dependence of the dielectric and ferroelectric properties does not coincide with the phase transitions observed by neutron studies,[11] as shown in Fig. 2-14.

Fig. 2-12. Temperature dependence of ε_r (ε_s) and tan δ for poled NBT. Figure is adopted from ref 29 (Figure 2(a)).

Fig. 2-13. Polarisation-Electric field hysteresis loops of $Na_{0.51}Bi_{0.5}TiO_{3.005}$ measured at 180 ~ 240 ℃. Figures are adopted from ref 29 (Figure 4).

By high temperature in-situ TEM studies, a platelet-shaped domains identified as orthorhombic phase Pnma with $a^-a^+a^-$ tilting were observed inside a rhombohedral R3c matrix at 200 ℃.[33] The volume fraction of the intermediate orthorhombic phase increases as temperature increases, where it completes transformation from rhombohedral phase at 280 ℃ and then turns into tetragonal phases ((disordered) P4/mbm and (ordered) $P4_2/mnm$) above 320 ℃.[34] Authors indicated the sequence of phase transitions and the associated temperatures correlate with the ferroelectric-antiferroelectric-paraelectric transitions, as shown in Fig. 2-14. However, no long-range Pnma or P4bm phase was observed by high-resolution XRD.[15] In the single-phase 'continuous tilting' model purposed by Levin and Reaney, it is suggested the orthorhombic Pnma structure originates from an increasing coherence length of the in-phase $a^-a^-c^+$ tilting at high temperature.[19] Recently, simulation results suggest the rhombohedral-orthorhombic-tetragonal transition pattern may potentially occur

because an orthorhombic tilt configuration is likely to appear in regions with (001) A-site ordering on a local scale.[35]

Fig. 2-14. Sequences of phase transition based on TEM, neutron diffraction studies and dielectric properties. Figures are modified from ref 36 (Figure 2).

In summary, the structure of NBT involves complexity of octahedral tilting associated with different displacement of Na and Bi ions, where short range A-site cation ordering may possibly occur especially with increasing thermal energy, leading to a complex phase transformation on heating. Therefore, the structure of NBT can be sensitive to the processing conditions, which provokes difficulties in phase analysis.

2.3.3 Phase formation

Aksel and Jones[37] studied the phase formation of NBT during the conventional solid state synthesis by in situ high-temperature diffraction, where NBT perovskite started to form at ~ 425 ℃ and completed reaction at ~ 600 ℃. Intermediate phases, such as $Bi_4Ti_3O_{12}$ (BTO) and $Bi_{12}TiO_{20}$ (BiT), are likely to form above 500 ℃, where BTO was also identified as an intermediate phase for NBT prepared by the hydrothermal synthesis and citrate method at the pre-sintering stage.[38,39] Furthermore, they proposed that Bi_2O_3 particles act as a structural host due to the continuation of the reactant peaks between 40 ~ 60 $2\theta^o$ as shown in Fig. 2-15.

Fig. 2-15. Temperature dependence of the Bragg peaks between 20 ~ 60 2θ°. Figure is adopted from ref 37 (Figure 4).

BTO and $Na_{0.5}Bi_{4.5}Ti_4O_{15}$ (NBiT) are common template seeds for texturing the microstructure of NBT-based ceramics, such as NBT, 85%NBT-15%$K_{0.5}Bi_{0.5}TiO_3$ and 94.5%NBT-5.5%$BaTiO_3$, via the templated grain growth method (TGG).[40-45] In general, plate like BTO and NBiT precursors were first prepared by molten slat synthesis (MSS), followed by further reacting with Na_2CO_3 and TiO_2 in a NaCl flux. The conversion of BTO/NBiT into NBT is according to the following chemical reactions:

$$Bi_4Ti_3O_{12} + 2Na_2CO_3 + 5TiO_2 \rightarrow 8Na_{0.5}Bi_{0.5}TiO_3 + 2CO_2 \qquad 2\text{-}4.$$

$$Na_{0.5}Bi_{4.5}Ti_4O_{15} + 2Na_2CO_3 + 5TiO_2 \rightarrow 9Na_{0.5}Bi_{0.5}TiO_3 + 2CO_2 \qquad 2\text{-}5.$$

The precursors prepared by MSS have preferred 001 orientation. Aurivillius phases BTO and NBiT have a layered structure which consist of pseudo-perovskite blocks and $(Bi_2O_2)^{2+}$ layers stacking along the c-axis, where the pseudo-perovskite blocks have a similar structure to NBT. During the topochemical reaction, it is suggested the $(Bi_2O_2)^{2+}$ layers are highly reactive with Na^+.[41] The conversion of NBiT into NBT perovskite is illustrated in Fig. 2-16.

Fig. 2-16. Schematic illustration of the conversion of layered NBiT into NBT perovskite. Figure is adopted from ref 41 (Figure 1).

Based on Setasuwon and Kijamnajsuk's studies, the 100 orientated NBT was fully converted from 001 orientated NBiT precursors after heating at 1100 ℃ for 4h by MSS, as shown in Fig. 2-14.[42] It is worth noting that some 001 orientated NBiT still remains after heating at 1000 ℃ for 4h, suggesting the conversion may require heating at a higher temperature. The standard (non-orientated) NBiT may possibly exist after heating at 1200 ℃ for 4h, which the authors did not mention in the article. This may suggest some NBiT (non-orientated) may form as a secondary phase if the heating temperature is above 1100 ℃. On the other hand, the template grain growth of NBT has preferred orientation along 100_p (Fig. 2-17), which is revealed by TEM studies where the NBT particles prefer to grow along the 100 direction, while the NBT particles prepared by conventional solid state synthesis grow along the 110 direction,[43,44] where the strongest intensity occurs in XRD.

Fig. 2-17. XRD patterns of conversion of NBiT into NBT via MSS at 800 ~ 1200 ℃ and TGG method. Figures are modified from ref 42 (Figure 2 and 5).

The concept of texturing microstructure of NBT-based ceramics is to enhance the piezoelectric properties. It has been shown that the maximum ε_r for 94.5%NBT-5.5%$BaTiO_3$ and 99.4%NBT-0.6%$BaZrO_3$ is slightly improved after texturing the microstructure of ceramics by TGG.[41,45]

2.4 Nonstoichiometric NBT

2.4.1 A-site nonstoichiometry

Both Na and Bi are volatile elements which may be potentially lost at high temperature, leading to form nonstoichiometric compositions. As a consequence, many researchers have focused on the influence of A-site nonstoichiometry of NBT, such as (a) $Na_{0.5}Bi_{0.5+x}TO_{3+1.5x}$ (x = -7% ~ 10%), (b) $Na_{0.5+y}Bi_{0.5}TiO_{3+0.5y}$ (y = -10% ~ 2%), (c) $(Na_{0.5}Bi_{0.5})_{1+z}TiO_{3+z}$ (z = -0.02 ~0.01).[46-54] In general, XRD results showed single-phase when the oxygen content is ≤ 3.03. However, small amounts of secondary phases were still observed for Na-excess (y = 1%), Na-deficiency (y ≤ -3%) and Bi-excess (z = 1%) by SEM and TEM studies.[46,52-54] For the Bi-deficient NBT (y ≤ -5%), the amount of Na-rich phases, such as $Na_2Ti_6O_{13}$ or $Na_2Ti_3O_7$, increased after thermally etching at high temperature, suggesting the chemical stability of Bi-deficient NBT is very sensitive to the sintering conditions, especially when ceramics are exposed in air at high temperature.[54] Only a small deviation in T_m and T_d was found which tends to increase and decrease with increasing leakage, respectively.[30, 46-53] Therefore, the actual compositions of A-site nonstoichiometric NBT may be different from the nominal starting compositions due to the presence of secondary phases. The dielectric properties are related to the chemical defects associated with the leakage.

As mention earlier, stoichiometric NBT often has a high leakage current, possibly due to Bi loss during the sintering process. Thermogravimetry (TG) results reported by Nagata showed weight loss of NBT ceramics starts at ~ 1130 ℃.[48] He further investigated the presence of oxygen vacancies by ^{18}O tracer diffusion measurements, as shown in Fig. 2-18, where the ^{18}O diffusion profile of NBT sintered at 1225 ℃ for 2h penetrated much further than the others, suggesting higher oxygen vacancy concentration. In contrast, sintering at a lower temperature (1050 ℃ for 100 h) or by adding Bi content (0.3 mass%) can reduce the oxygen vacancies. He therefore concluded the evaporation of Bi during sintering above 1130 ℃ may lead to the creation of oxygen vacancies. Following studies on A-site nonstoichiometry of NBT were reported by Hiruma *et al*..[29] It was found that the dc resistivity of Na-excess (y = 1%) is much lower than Na-deficiency (y = -1%) by ~3 orders of magnitude, whereas Bi-excess (x = 1%) has much higher resistivity than Bi-deficiency.

Fig. 2-18. ^{18}O diffusion profile for BNT-0 (stoichiometric NBT), BNT-0.3 (NBT+0.3 mass%) sintering at 1050 ℃ for 0.5 ~ 100h annealed in the ^{18}O atmosphere at 650 ℃ for 30 mins. (C_x: Concentration of ^{18}O in each depth, C_s: Concentration of ^{18}O in surface, C_o: background), Figure is adopted from ref. 48 (Figure 6).

Li *et al*. investigated the conduction mechanisms of A-site non-stoichiometric NBT by a combination of impedance spectroscopic (IS), electromotive force measurements (EMF) and ^{18}O tracer diffusion measurements.[51,52] Their studies showed a small change in the Na or Bi content (< 1 at%) in the nominal starting composition may lead to dramatic changes in conductivity, as shown in Fig. 2-19. Insulating phases, such as $Na_{0.49}Bi_{0.5}TiO_{2.995}$ ($Na_{0.49}BT$) and $Na_{0.5}Bi_{0.51}TiO_{3.015}$ ($NB_{0.51}T$) have bulk conduction activation energy values (E_a) of ~ 1.7 eV, whereas conducting phases, such as NBT, $Na_{0.51}Bi_{0.5}TiO_{3.005}$ ($Na_{0.51}BT$) and $Na_{0.5}Bi_{0.49}TiO_{2.985}$ ($NB_{0.49}T$) have E_a ~ 0.9 eV and 0.4 ~ 0.5 eV below and above T_m, respectively. The predominant conduction mechanism has been confirmed by EMF and ^{18}O diffusion profiles, where the ionic transport number t_{ion} was ~ 0.9 and ~ 0.1 for the conducting and insulating phases above 600 ℃ (Fig. 2-20), respectively. They concluded starting compositions with Bi/Na > 1 will lead to insulators which are dominated by n-type near-intrinsic electronic conduction, whereas starting compositions with Bi/Na ≤ 1 will lead to conductors which are dominated by ionic conduction.

Fig. 2-19. Arrhenius plots of bulk conductivity for A-site nonstoichiometric NBT. Figure is adopted from ref 52 (Figure 2 (c)).

Fig. 2-20. Oxygen ionic transport number (t_{ion}) for the nominally stoichiometric NBT, Bi-deficient $Na_{0.5}Bi_{0.49}TiO_{2.985}$ ($NB_{0.49}T$) and Bi-rich $Na_{0.5}Bi_{0.51}TiO_{3.015}$ ($NB_{0.51}T$). Figure is adopted from ref 51 (Figure 2(d)).

Li *et al*. reported the Bi-rich NBT series ($Na_{0.5}Bi_{0.5+x}TiO_{3+1.5x}$, x = 0 ~ 10%) and found Bi_2O_3 and $Na_{0.5}Bi_{4.5}Ti_4O_{15}$ (NBiT) as secondary phases for $x \geq 5\%$ by XRD and SEM.[53] In addition, Bi_2O_3-rich pockets were detected at triple point junctions between grains and along grain boundaries for $x \geq 1\%$ by TEM studies. For x = 0.5% and 1%, the electrical conductivity is dominated by n-type electronic conduction, where t_{ion} is < 0.1 at 600 ℃. A further increase in Bi content (x > 1%) leads to an increase in conductivity, where t_{ion} ~ 0.5 at 600 ℃, suggesting mixed ionic/electronic conduction.

They proposed two models to explain the increase in ionic conductivity for x > 1%: (1) the bulk composition is Bi-deficient due to the presence of Bi-rich secondary phases, leading to an increase in ionic conductivity; (2) the ionic conduction is attributed to the Bi_2O_3-type secondary phase, which normally exhibit high ionic conductivity.

In summary, the actual composition of A-site nonstoichiometric NBT may differ from the nominal starting composition due to the presence of secondary phases. The high leakage current of NBT is attributed to oxygen ion migration. The oxygen vacancies originated by Bi loss during processing, leading to generate oxygen vacancies, according to the following equation:

$$2Bi_{Bi}^{x} + 3O_{O}^{x} \rightarrow 2V_{Bi}^{'''} + 3V_{O}^{\cdot\cdot} + Bi_2O_3 \qquad 2\text{-}3.$$

2.4.2 Accepter-doping

Li *et al*. further investigated the influence of Mg-acceptor doping for Ti on conductive Bi-deficient NBT ($Na_{0.5}Bi_{0.49}Ti_{1-x}Mg_xO_{2.985-x}$).[51] It was found that the ionic conductivity and chemical stability are improved by 2 at% Mg-doping for Ti, where the former has ~ 0.01 Scm^{-1} at 600 °C. This enhancement makes NBT-based ceramics a potential electrolyte material for SOFC, which is comparable to other known oxide ion conductors, such as YSZ ($Zr_{0.92}Y_{0.08}O_{1.96}$), GDC ($Ce_{0.9}Gd_{0.1}O_{1.95}$ and LSGM ($La_{0.9}Sr_{0.1}Ga_{0.9}Mg_{0.1}O_{2.9}$), as shown in Fig. 2-21.

Koch *et al*. investigated the influence of acceptor doping for Ti on insulating Bi-rich NBT ($Na_{0.5}Bi_{0.51}Ti_{1-x}M_xO_{3-x}$, M = Mg^{2+} and Fe^{3+}).[55] It was shown that 0.5% Mg doping is enough to switch NBT from an insulator to an ionic conductor, while 2% Fe doped NBT still remains as an insulator. In addition, the conductivity of 1% Mg doped and 4%Fe doped NBT are similar, which increases ~ 4 orders of magnitude.

Fig. 2-21. Comparison of bulk conductivity for 2%Mg doped Bi-deficient NBT with other known oxide ion conductors. Figure is adopted from ref 51 (Figure 4).

Computational studies reported by He and Mo suggested that acceptor doping on Bi, such as Na and K as dopants, can further improve the ionic conductivity of NBT.[56] Acceptor dopants on the B-site may trap oxygen vacancies, leading to an increase in oxygen migration barriers.[56,57] Shih *et al*. reported Li-doped NBT showing 4 at% Li doping for Bi has the optimal improvement in ionic conductivity ~ one order of magnitude, where 6 at% Li doping shows no enhancement in conductivity.[58] They suggested acceptor dopants may form defect complex(es) with oxygen vacancies, leading to lower the mobility of oxygen ions. Carter *et al*. reported a Na : Bi 1 : 1 doping mechanism ($Na^{+}\leftrightarrow Bi^{3+}$, $Na_{0.5-x}Bi_{0.5+x}TiO_{3+x}$, x = ±1%), where they focus on the correlation between crystal structure and dielectric properties.[59] More details will be discussed in Chapter 4.

Yang *et al*. present series of Bi-deficient NBT ($Na_{0.5}Bi_{0.49}TiO_{2.985}$, $NB_{0.49}T$) with 2 at% A-site divalent doping for Bi ($Na_{0.5}Bi_{0.47}M_{0.02}TiO_{2.975}$, M = Ca^{2+}, Sr^{2+} and Ba^{2+}).[60] XRD results showed single-phase for all samples but $Na_2Ti_6O_{13}$ was identified as a secondary phase by SEM. The ionic conductivity can be improved ~ one order of magnitude. It was found that Sr-doped $NB_{0.49}T$ and Ba-doped $NB_{0.49}T$ have the highest and lowest conductivity at all temperature (Fig. 2-22), respectively. They suggested this is attributed to combination of size mismatch with Bi ions, polarisability and bonding strength with oxygen ions. In addition, Sr-doped $NB_{0.49}T$ was shown to be chemically stable under a reducing atmosphere (5%H_2/95%N_2) below 550 °C.[60]

Fig. 2-22. Dependence of bulk conductivity on the dopant to host ionic radius in $Na_{0.5}Bi_{0.47}M_{0.02}TiO_{2.975}$ at 150 and 500 ℃. Figures are adopted from ref 60 (Figure 9).

2.4.3 Donor doping

Li *et al*. investigated the influence of Nb-donor doping on the nominal stoichiometric NBT ($Na_{0.5}Bi_{0.5}Ti_{1-x}Nb_xO_{3+0.5x}$, x = 0 ~ 5%).[62] The solid solution limit is low < 2%, where $Bi_2Ti_2O_7$-related secondary phase was identified by XRD and SEM/EDS studies for x ≥ 2%. They showed that small amounts of Nb-doping (x ≤ 1%) can switch off ionic conductivity, where t_{ion} decreases from 0.93 for NBT to 0.06 for 0.5% Nb-doping, leading to a decrease bulk conductivity, as shown in Fig. 2-23. The 1%Nb-doped NBT shows n-type semiconducting behaviour, where it becomes more conductive under N_2 at 700 ℃. Li *et al*. further investigated a wider range of Nb-doping levels (x = 0.2 ~ 10%).[53] They showed that ionic conduction still remains for x ≤ 0.3%, where t_{ion} decreases to 0.47. A significant decrease in maximum ε_r for x = 0.5%, suggesting Nb-doping on the Ti-site may influence the lattice polarisation/ferroelectric domain wall motion.

Fig. 2-23. Arrhenius plots of bulk conductivity for Nb-doped NBT. Figure is adopted from ref 62 (Figure 2).

Two types of charge compensation may occur when Ti is replaced by Nb:

(a) Electronic compensation

$$Nb_5O_5 + 2Ti_{Ti}^{x} \rightarrow 2Nb_{Ti}^{\cdot}+2TiO_2+2e' + \frac{1}{2}O_{2(g)} \qquad 2\text{-}4.$$

(b) Ionic compensation

$$Nb_2O_5 + 2Ti_{Ti}^{x} + V_O^{\cdot\cdot} \rightarrow 2Nb_{Ti}^{\cdot} + 2TiO_2 + O_O^{x} \qquad 2\text{-}5.$$

NBT has high conduction band minimum and high valence band maximum, as shown in Fig. 2-24, suggesting electronic donor doping is relatively unfavourable.[63] On the other hand, the ionic conductivity is greatly suppressed by Nb-doping, indicating a decrease in oxygen vacancies.

Fig. 2-24. Energy band alignment of various oxides with respect to the Fermi level of RuO_2. Figure is adopted from ref 63 (Fig. 8)

2.5 $BiMO_3$ solid solutions

The potential Bi-based perovskite ($BiMO_3$) end members are list in Table 2-1. It should be noted that $BiGaO_3$ adopts a pyroxene-like KVO_3 structure, where Ga^{3+} ions prefer to occupy tetrahedral sites and Bi^{3+} has 6-fold coordination.[67] $BiNiO_3$ is not included in this table because Bi ions disproportionate into Bi^{3+} and Bi^{5+}, and therefore Ni tends to be +2.[81] In general, most $BiMO_3$ phases tend to decompose into mullite-type ($Bi_2M_4O_9$) and sillenite ($Bi_{25}MO_{39}$) phases. The solid solution of NBT with $BiMO_3$ tends to increase as the ionic size of M^{3+} increases. Only $BiFeO_3$ (BF) can form under ambient pressure, whereas others can only be synthesised under high pressure. Moreover, BF in which the ionic radius of Fe^{3+} (HS) ~ 0.645 Å is greater than Ti^{4+} (0.605 Å) in 6-fold coordination can have a near full solid solution with NBT with some secondary phases, such as $Bi_2Fe_4O_9$ and $Bi_{25}FeO_{39}$, occurring when the $BiFeO_3$ content is $\geq$ 80%.[79,80]

$BiMO_3$ **M[ref]**	**Decomposition temperature(K)**	**Decomposition components**	**Phase transition**	**Ionic radius(Å)**	**T_C or T_N /K**	**NBT SS [ref]**
Cr[64]	440	$Bi_2O_2CO_3$, CrO_3	Monoclinic(*C2*) $\xrightarrow{440K}$ orthorhombic(*Pnma*)	0.615	T_N ~ 114	0.15 [71,72]
Mn [65]	773-923	$Bi_2Mn_4O_{10}$, $Bi_{12}MnO_{20}$	Monoclinic(1) $\xrightarrow{483K}$ Monoclinic(2) $\xrightarrow{763K}$ Orthorhombic	0.58(LS) 0.645(HS)	T_C ~ 100	-
Co [66]	720	Co_3O_4, $Bi_{25}CoO_{39}$	Tetragonal (*P4mm*), varies with pressure.	0.545(LS) 0.61(HS)	T_N ~ 470	0.06 [73] Undefined
Al [67]	820	$Bi_2Al_4O_9$, $Bi_{25}AlO_{39}$	Rhombohedral (*R3c*), 140-820K	0.535	-	≤ 0.06 [74]
Ga [67]	820	$Bi_2Ga_4O_9$, $Bi_{25}GaO_{39}$	Orthorhombic (*Pcca*), 140-820K (pyroxene like)	0.62	-	-
Sc [68]	970	-	Monoclinic (C2/c) $\xrightarrow{3.5\ GPa,RT}$ Orthorhombic	0.745	-	≤ 0.3 [75,76]
In [69]	873	In_2O_3, $Bi_{25}InO_{39}$	Orthorhombic (*Pna2₁*), 140-873K	0.8	-	-
Fe [70]	1200	$Bi_2Fe_4O_9$, Bi_2O_3	Rhombohedral (*R3c*) $\xrightarrow{\sim 1100K}$ Orthorhombic	0.55(LS) 0.645(HS)	T_N ~ 643 T_C ~ 1103	0-1 [77-79]

Table 2-1. Decomposition temperature and composition, phase transition, ionic radius (VI) of M, T_C or T_N and solid solution (SS) with NBT of BiMO3. Note that the ionic radius of Ti^{4+}(VI) is 0.605 Å.

Yang *et al*. reported the solid solution limit of $(Na_{0.5}Bi_{0.5}TiO_3)_{1-x}(BiAlO_3)_x$ is ~ 6%, as confirmed by a combination of XRD and SEM/EDS studies.[74] Some Al-rich secondary phases were found on polished surfaces for x > 6% by SEM studies. T_m decreases from 325 ℃ for x = 0 to ~ 290 ℃ for x = 7%. The conductivity and activation energy decreases and increases with increasing $BiAlO_3$ (BA) content, respectively. t_{ion} decreases from > 0.9 for x = 0 to ~ 0.4 for x = 6% and to < 0.1 for x = 7%, indicating a suppression of ionic conductivity. The electrical conductivity is dominated by n-type electronic conduction for x = 7%. They suggest the mobility of oxygen ions decreases with increasing BA content due to the trapping of oxygen vacancies, where positively charged Al'_{Ti} trap negatively charged $V_O^{\cdot\cdot}$ to form the defect complex $(Al'_{Ti} - V_O^{\cdot\cdot})^{\cdot}$.

In the $(Na_{0.5}Bi_{0.5}TiO_3)_{1-x}(BiCrO_3)_x$ (x = 0 ~ 15%) solid solution reported by Selvamani *et al*.,[71] calcined powders prepared by solid state synthesis contain $Bi_4Ti_3O_{12}$ as a secondary phase. Single-phase can be achieved by sintering at an appropriate temperature.[72] The rhombohedral superlattice peaks at ~ 38 2θ° tends to decrease with increasing $BiCrO_3$ (BC) content.[71] They suggest this is due to a change in rhombohedral symmetry from R3c to R3m. The maximum ε_r decreases with increasing BC content in conjunction with peak broadening, especially for x = 10 and 15 %, as shown in Fig. 2-25. Similar behaviour is observed for the solid solution of NBT-$BiScO_3$.[75,76] They suggest acceptor dopants, such as Cr^{3+} and Sc^{3+}, introduce octahedral distortion, leading to an increase in T_m.[71,76] On the other hand, the leakage current increases with increasing BC content in cooperation with an increase in dc conductivity with an activation energy between 0.53 ~ 0.74 eV.[72] They proposed the leakage current may be attributed to oxygen ion migration.

Fig. 2-25. Temperature dependence of dielectric constant and tan δ for $(Na_{0.5}Bi_{0.5}TiO_3)_{1-x}(BiCrO_3)_x$. Figures are adopted from ref 71 (Figure 6).

In the xBF-(1-x)NBT system, the rhombohedral distortion is expected to increase with increasing BF content based on the tolerance factor. However, various studies showed the symmetry of NBT tends to be more pseudo-cubic when the BF content is low < 30% (Fig. 2-26).[77,79,82] Dorcet *et al*. suggest this fact is probably due to an increase in non-spherical Bi^{3+} ions with lone pairs which become predominant on the A-site.[77] T_m increases with increasing BF content from 350 ℃ for x = 0 to ~ 520 ℃ for x = 70%.[78] The leakage current also increases with increasing BF content, which limits the dielectric measurements. The dc conductivity for x = 70% has an activation energy of ~ 1.2 eV, which is close to the activation energy for oxygen ion hopping observed in other titanate ceramics.[83] Dorcet el al. suggested the oxygen vacancies originate from the reduction of Fe^{3+} to Fe^{2+}.[78] Their assumption is based on a decrease in conductivity after annealing under oxygen atmosphere.

Fig. 2-26. Lattice constant and rhombohedral angle α for xBF-(1-x)NBT. Figure is adopted from ref 82 (Figure 3).

2.6 References

1. Momma, K. and Izumi, F., VESTA 3 for three-dimensional visualization of crystal, volumetric and morphology data, *Journal of Applied Crystallography*, **44**, 1272-1276 (2011)

2. Beskow, G.V.M. Goldschmidt: Geochemische Verteilungsgesetze der elemente. *Geol. Feoreningani stock. Foerhandlingar* **46**, 738-743 (1924)

3. Jaffe, B., Cook, W.R.J. and Jaffe, H. Piezoelectric ceramics, London, *Academic Press* (1971)

4. Reaney, I.M., Colla, E.L. and Setter, N. Dielectric and Structure Characteristics of Ba- and Sr-based Complex Perovskites as a Function of Tolerance Factor, *Japanese Journal of Applied Physics* **33**, 3984 (1994)

5. Glazer, A.M., The Classification of Tilted Octahedra in Perovskites, *Acta Crystallographica Section B* **28**, 3384-3392 (1972)

6. Jones, G.A. and Thomas, P.A., The tetragonal phase of $Na_{0.5}Bi_{0.5}TiO_3$ – a new variant of the perovskite structure, *Acta Crystallographica Section B* **56**, 426-430 (2000)

7. Moulson, A.J. and Herbert, J.M., Electroceramics: materials, properties, applications, second edition, *John Wiley& Sons* (2003)

8. Davies, P.K., Wu, H., Borisevich, A.Y., Molodetsky, I.E. and Farber, L., Crystal Chemistry of Complex Perovskites: New Cation-Ordered Dielectric Oxides, *Annual Review of Materials Research* **38**, 369-401 (2008)

9. Zvirgzds, J.A., Kapostin, P.P., Zvirgzde, J.V. and Kruzina, T.V., X-ray study of phase transitions in ferroelectric $Na_{0.5}Bi_{0.5}TiO_3$ **40**, 75-77 (1982)

10. Vakhrushev, S.B., Isupov, V.A., Kvyatkovsky, B.E., Okuneva, N.M., Pronin, I.P., Smolensky, G.A. and Syrnikov, P.P., Phase transitions and soft modes in sodium bismuth titanate, *Ferroelectrics* **63**, 153-160 (1985)

11. Jones, G.O. and Thomas, P.A., Investigation of the structure and phase transitions in the novel A-site substituted distorted perovskite compound $Na_{0.5}Bi_{0.5}TiO_3$, *Acta Crystallographica Section B* **58**, 168-178 (2002)

12. Shuvaeva, V.A., Zekria, D., Glazer, A.M., Jiang, Q., Weber, S.M., Bhattacharya, P. and Thomas, P.A., Local structure of the lead-free relaxor ferroelectric $(K_xNa_{1-x})_{0.5}Bi_{0.5}TiO_3$, *Physical Review B **71***, 174114 (2005)

13. Gorfman, S. and Thomas P.A., Evidence for a non-rhombohedral average structure in the lead-free piezoelectric material $Na_{0.5}Bi_{0.5}TiO_3$, *Journal of Applied Crystallography* **43**, 1409-1414 (2010)

14. Aksel, E., Forrester, J.S., Jones, J.L., Thomas, P.A., Page, K. and Suchomel, M.R., Monoclinic crystal structure of polycrystalline $Na_{0.5}Bi_{0.5}TiO_3$, *Applied Physics Letters* **98**, 152901 (2011)

15. Aksel, E., Forrester, J.S., Kowalski, B. Jones, J.L. and Thomas, P.A., Phase transition sequence in sodium bismuth titanate observed using high-resolution x-ray diffraction, *Applied Physics Letters* **99**, 222901 (2011)

16. Dorcet, B. and Trolliard, G., A transmission electron microscopy study of the A-site disordered perovskite $Na_{0.5}Bi_{0.5}TiO_3$, *Acta Materialia* **56**, 1753-1761 (2008)

17. Beanland, R. and Thomas P.A., Imaging planar tetragonal sheets in rhombohedral $Na_{0.5}Bi_{0.5}TiO_3$ using transmission electron microscopy, *Scripta Materialia* **65**, 440-443 (2011)

18. Beanland, R. and Thomas P.A., Symmetry and defects in rhombohedral single-crystalline $Na_{0.5}Bi_{0.5}TiO_3$, *Physical Review B* **89**, 174102 (2014)

19. Levin, I. and Reaney, I.M., Nano- and Mesoscale Structure of $Na_{1/2}Bi_{1/2}TiO_3$: A TEM Perspective, *Advanced Functional Materials* **22**, 3445-3452 (2012)

20. Ma, C., Guo, H. and Tan, X., A New Phase Boundary in $(Bi_{1/2}Na_{1/2})TiO_3$-$BaTiO_3$ Revealed via a Novel Method of Electron Diffraction Analysis, *Advanced Functional Materials* **23**, 5261-5266 (2013)

21. Rao, B.N. and Ranjan, R., Electric-field-driven monoclinic-to-rhombohedral transformation in $Na_{1/2}Bi_{1/2}TiO_3$, *Physical review B* **86**, 134103 (2012)

22. Rao, B.N., Fitch, A.N. and Ranjan, R., Ferroelectric-ferroelectric phase coexistence in $Na_{1/2}Bi_{1/2}TiO_3$, *Physical review B* **87**, 060102(R) (2013)

23. Rao, B.N., Olivi, L., Sathe, V. and Ranjan, R., Electric field and temperature dependence of the local structural disorder in the lead-free ferroelectric $Na_{0.5}Bi_{0.5}TiO_3$: An EXAFS study, *Physical review B* **93**, 024106 (2016)

24. King, G. and Woodward, P.M., Cation ordering in perovskites, *Journal of Materials Chemistry* **20**, 5785-5796 (2010)

25. Shannon, R.D., Revised Effective Ionic Radii and Systematic Studies of Interatomic Distances in Halides and Chalcogenides, *Acta Crystallographica Section A* **32**, 751-767 (1976)

26. Groting, M., Hayn, S. and Albe, K., Chemical order and local structure of the lead-free relaxor ferroelectric $Na_{1/2}Bi_{1/2}TiO_3$, *Journal of Solid State Chemistry* **184**, 2041-2046 (2011)

27. Petzelt, J., Kamba, S., Fabry, J., Noujni, D., Porokhonskyy, V., Pashkin, A., Franke, I., Roleder, K., Suchanicz, J., Klein, R. and Kugel, G.E., Infrared, Raman and high-frequency dielectric spectroscopy and the phase transitions in $Na_{1/2}Bi_{1/2}TiO_3$, *Journal of Physics: Condensed Matter* **16**, 2719-2731 (2004)

28. Suchanicz, J. and Kwapulinski, J., X-ray diffraction study of the phase transitions in $Na_{0.5}TiO_3$, *Ferroelectrics* **165**, 249-253 (1995)

29. Hiruma, Y., Nagata, H. and Takenaka T., Thermal depoling process and piezoelectric properties of bismuth sodium titanate ceramics, *Journal of Applied Physics* **105**, 084112 (2009)

30. Sakata, K. and Masuda, Y., Ferroelectric and antiferroelectric properties of $(Na_{0.5}Bi_{0.5})TiO_3$-$SrTiO_3$ solid solution ceramics, *Ferroelectrics* **7**, 347-349 (1974)

31. Pronin, I.P., Syrnikov, P.P., Isupov, V.A., Egorov, V.M. and Zaitseva, V.N., Peculiarities of phase transitions in sodium bismuth titanate, *Ferroelectrics* **25**, 395-397 (1980)

32. Isupov, V., Ferroelectric $Na_{0.5}Bi_{0.5}TiO_3$ and $K_{0.5}Bi_{0.5}TiO_3$ Perovskites and Their Solid Solutions, *Ferroelectrics* **315**, 123-147 (2005)

33. Dorcet, V., Trolliard, G. and Boullay P., Reinvestigation of Phase Transitions in $Na_{0.5}Bi_{0.5}TiO_3$ by TEM. Part I: First order Rhombohedral to Orthorhombic Phase Transition, *Chemistry of Materials* **20**, 5061-5073 (2008)

34. Trolliard G. and Dorcet, V., Reinvestigation of Phase Transition in $Na_{0.5}Bi_{0.5}TiO_3$ by TEM. Part II: Second Order Orthorhombic to Tetragonal Phase Transition, *Chemistry of Materials* **20**, 5074-5082 (2008)

35. Meyer, K. Koch, L. and Albe K., Phase transformations in relaxor $Na_{0.5}Bi_{0.5}TiO_3$ studies by means of density functional theory calculations, *Journal of the American Ceramic Society* **101**, 472-482 (2018)

36. Reichmann K., Feteira, A. and Li, M., Bismuth Sodium Titanate Based Materials for Piezoelectric Actuators, *Materials* **8**, 8467-8495 (2015)

37. Aksel, E. and Johns, J., Phase formation of sodium bismuth titanate perovskite during solid-state processing, *Journal of the American Ceramics Society* **93**, 3012-3016 (2010)

38. Lu, R., Yuan, J., Shi, H.S., Li, B., Wang, W., Wang D. and Cao, M., Morphology-controlled synthesis and growth mechanism of lead-free bismuth sodium titanate nanostructures *via* the hydrothermal route, *CrystEngComm* **15**, 3984 (2013)

39. Xu, Q., Chen, S., Chen, W., Huang, D. Zhou, J., Sun, H. and Li, Y., Synthesis of $(Na_{0.5}Bi_{0.5})TiO_3$ and $(NA_{0.5}Bi_{0.5})_{0.92}Ba_{0.08}TiO_3$ powders by a citrate method, *Journal of Materials Science* **41**, 6146-6149 (2006)

40. Zeng, J.T., kowk, K.W., tam, W.K., Tian, H.Y., Jiang, X.P., and Chan, H.L.W., Plate-like $Na_{01.5}Bi_{0.5}TiO_3$ Template Synthesized by Topochemical Method, *Journal of the American Ceramics Society* **89**, 3850-3853 (2006)

41. Hussain, A., Rahman, J., Ahmed, F., Kim, J., Kim, M., Song, T. and Kim, W., Plate-like $Na_{0.5}Bi_{0.5}TiO_3$ particles synthesizes by Topochemical microcrystal conversion method, *Journal of the European Ceramic Society* **35**, 919-925 (2015)

42. Setasuwon, P. and Kijamnajsuk, S., Synthesis of $Na_{0.5}Bi_{0.5}TiO_3$ anisotropic particles with grain orientation by conversion of $Na_{0.5}Bi_{4.5}Ti_4O_{15}$ crystals, *Science and Technology of Advanced Materials* **7**, 780-784 (2006)

43. Jiang, C., Zhou, K., Zhou, X., Li, Z. and Zhang, D., Synthesis and characterization of $Na_{0.5}Bi_{0.5}TiO_3$ platelets with preferred orientation using Aurivillius precursors, *Ceramics International* **41**, 6858-6862 (2015)

44. Kimura, T., Takahashi, T., Tani, T. and Saito, Y., Crystallographic texture development in bismuth sodium titanate prepared by reactive-template grain growth method. *Journal of the American Ceramics Society* **87**, 1424-1429 (2004)

45. Wu, M., Wang, Y., Wang, D. and Li, Y., Enhanced Electrical Properties of Textured NBBT ceramics Derived From the Screen Printing Technique, *IEEE Transactions on Ultrasonics, Ferroelectrics, and Frequency Control* **58**, 2036-2041 (2011)

46. Spreitzer, M., Valant, M. and Suvorov D., Sodium Deficiency in $Na_{0.5}Bi_{0.5}TiO_3$, *Journal of the Materials Chemistry* **17**, 185-192 (2007)

47. Zuo, R., Su, S., Wu, Y., Fu, J., Wang, M. and Liu, L.m Influence of A-site nonstoichiometry on sintering, microstructure and electrical properties of $(Bi_{0.5}Na_{0.5})TiO_3$ ceramics, *Materials Chemistry and Physics* **110**, 311-315 (2008)

48. Nagata, H., Electrical properties and tracer diffusion of oxygen in some Bi-based lead-free piezoelectric ceramics, *Journal of the Ceramic Society of Japan* **116**, 271-277 (2008)

49. Sung, Y.S., Kim, J.M., Cho, J.H., Song, T.K., Kim, M.H., Cho, H.H., Park, T.G., Do, D. and Kim, S.S., Effects of Na nonstoichiometry in $(Bi_{0.5}Na_{0.5+x})TiO_3$ ceramics, *Applied Physics Letters* **96**, 022901 (2010)

50. Sung, Y.S., Kim, J.M., Cho, J.H., Song, T.K., Kim, H.M. and Park, T.G., Effects of Bi nonstoichiometry in $(Bi_{0.5+x}Na)TiO_3$ ceramics, *Applied physics Letters* **98**, 012902 (2011)

51. Li, M., Pietrowski, M.J., De Souza, R.A., Zhang, H., Reaney, I.M., Cook, S.N., Kilner, J.A. and Sinclair, D.C., A family of oxide ion conductors based on the ferroelectric perovskite $Na_{0.5}Bi_{0.5}TiO_3$, *Nature Materials* **13**, 31-35 (2014)

52. Li., M., Zhang, H., Cook, S.N., Li, L, Kilner, J.A., Reaney, I.M. and Sinclair, D.C., Dramatic Influence of A-site Nonstoichiometry on the Electrical Conductivity and Conduction mechanisms in the Perovskite Oxide $Na_{0.5}Bi_{0.5}TiO_3$, *Chemistry of Materials* **27**, 629-634 (2015)

53. Li, L., Li, M., Zhang, H., Reaney, I.M. and Sinclair, D.C., Controlling mixed conductivity in the $Na_{1/2}Bi_{1/2}TiO_3$ using A-site non-stoichiometry and Nb-donor doping, *Journal of Materials Chemistry C* **4**, 5779-5786 (2016)

54. Chen, X., Zeng, J., Yan, Z., Zhou, M., Tang, P., Liang, P. and Li, W., Effects of Bi deficiency on the microstructural and conductive properties of $Na_{0.5}Bi_{0.5}TiO_3$ (NBT) perovskites, *Solid State Ionics* **309**, 152-162 (2017)

55. Koch, L., Steiner, S., Meyer, K., Seo, I., Albe, K. and Frömling, T., Ionic conductivity of acceptor doped sodium bismuth titanate: influence of dopants,

phase transitions and defect associates, *Journal of Materials Chemistry C* **5**, 8958-8965 (2017)

56. He, X. and Mo, Y., Accelerated materials design of $Na_{0.5}Bi_{0.5}TiO_3$ oxygen ionic conductors based on first principles calculations, *Physical Chemistry Chemical Physics* **17**, 18035-18044 (2015)

57. Mayer, K. and Albe, K., Influence of phase transitions and defect associates on the oxygen migration in the ion conductor $Na_{1/2}Bi_{1/2}TiO_3$, *Journal of Materials Chemistry A* **5**, 4368-4375 (2017)

58. Shih, D.P.C., Aguadero, A. and Skinner, S.J., Imrpovement of ionic conductivity in A-site lithium doped sodium bismuth titanate, *Solid State Ionics* **317**, 32-38 (2018)

59. Carter, J., Aksel, E., Iamsasri, T., Forrester, J.S., Chen, J. and Jones, J.L., Structure and ferroelectricity of nonstoichiometric $(Na_{0.5}Bi_{0.5})TiO_3$, *Applied Physics Letters* **104**, 112904 (2014)

60. Yang, F., Wu, P. and Sinclair, D.C., Enhanced bulk conductivity of A-site divalent acceptor-doped non-stoichiometric sodium bismuth titanate, *Solid State Ionics* **299**, 38-45 (2017)

61. Yang, F., Zhang, H., Li, L., Reaney, I.M., and Sinclair, D.C., High Ionic Conductivity with low Degradation in A-site Strontium Doped Nonstoichiometric Sodium Bismuth Titanate Perovskite, *Chemistry of Materials* **28**, 5269-5273 (2016)

62. Li, M., Li, L., Zang, J. and Sinclair, D.C., Donor-doping and reduced leakage current in Nb-doped $Na_{0.5}Bi_{0.5}TiO_3$, *Applied Physical Letters* **106**, 102904 (2015)

63. Li. S., Morasch, J. Klein, A., Chirila, C., Pintilie, L., Jia, L., Ellmer, K., Naderer, M., Reichmann, K., Groting, M. and Albe, K., Influence of orbital contributions to the valence band alignment of Bi_2O_3, Fe_2O_3, $BiFeO_3$, and $Bi_{0.5}Na_{0.5}TiO_3$, *Physical Review B – Condensed Matter and Materials Physics* **88**, 045428 (2013)

64. Niitaka, S., Azuma, M., Takano, M., Nishibori, E., Takata, M. and Sakata, M., Crystal structure and dielectric and magnetic properties of $BiCrO_3$, *Solid State Ionics* **172**, 557-559 (2004)

65. Montanari, E., Calestani, G., Migliori, A., Dapiaggi, M., Bolzoni, F., Cabassi, R. and Gilioli, E., High-Temperature Polymorphism in Metastable $BiMnO_3$, *Chemistry of Materials* **17**, 6457-6467 (2005)

66. Belik, A.A., Iikubo, S., Kodama, K., Igawa, N., Shamoto, S., Niitaka, S., Azuma, M., Shimakawa, Y., Takano, M., Izumi F. and Takayama-Muromachi, E., Neutron Powder Diffraction Study on the Crystal and Magnetic Structures of $BiCoO_3$, *Chemistry of Materials* **18**, 798-803 (2006)

67. Belik, A.A., Wuernisha, T., Kamiyama, T., Mori, K., Maie, M., Nagai, T., Matsui Y. and Takayama-Muromachi, E., High-Pressure Synthesis, Crystal Structures, and Properties of Perovskite-like $BiAlO_3$ and Pyroxene-like $BiGaO_3$, *Chemistry of Materials* **18**, 133-139 (2006)

68. Belik, A.A., Polar and nonpokar phases of $BiMO_3$: A review, *Journal of Solid State Chemistry* **195**, 32-40 (2012)

69. Belik, A.A., Stefanovich, S.Y., Lazoryak B.I. and Takayama-Muromachi, E., $BiInO_3$: A Polar Oxide with $GdFeO_3$-Type Perovskite Structure, *Chemistry of Materials* **18**, 1964-1968 (2006)

70. Arnold, D.C., Knight, K.S. Morrison, F.D. and Lightfoot, P. Ferroelectric-Paraelectric Transition in $BiFeO_3$: Crystal Structure of the Orthorhombic β Phase, *Physical Review Letters*, **102**, 027602 (2009)

71. Selvamani, R., Singh, G., Sathe, V., Tiwari V.S. and Gupta, P.K. Dielectric, structure and Raman studies on $(Na_{0.5}Bi_{0.5}TiO_3)_{(1-x)}(BiCrO_3)_x$ ceramic, *Journal of Physics: Condensed Matter* **23**, 055901 (2011)

72. Selvamani, R., Singh, G., Sinha, A.K. and Tiwari, V.S., Oxidation state of Chromium in $(Na_{0.5}Bi_{0.5}TiO_3)_{(1-x)}(BiCrO_3)_x$ solid solution; investigated by XAS and impedance spectroscopy, *Journal of Materials* Science **47**, 2011-2015 (2012)

73. Guo, F., Yang, B., Zhang, S., Liu, X., Zheng, L., Wang, Z., Wu, F., Wang, D. and Cao, W., Morphotropic phase boundary and dielectric properties in (1-x)$Bi_{0.4}Na_{0.5}TiO_3$-x$BiCoO_3$ lead-free piezoelectric ceramics, *Journal of Applied Physics* **111**, 124113 (2012)

74. Yang, F., Wu, P. and Sinclair, D.C., Suppression of electrical conductivity and switching of conduction mechanisms in 'stoichiometric' $(Na_{0.5}Bi_{0.5}TiO_3)_{1-x}(BiAlO_3)_x$ ($0 \leq x \leq 0.08$) solid solutions, *Journal of Materials Chemistry C* **5**, 7243-7252 (2017)

75. Nagata, H. and Takenaka, T., Lead-Free Piezoelectric Ceramics of $(Bi_{1/2}Na_{1/2})TiO_3$-1/2($Bi_2O_3 \cdot Sc_2O_3$) System, *Japanese Journal of Applied Physics* **36** 6055-6057 (1997)

76. Marchet, P, Boucher E., Dorcet, V. and Mercurio J.P., Dielectric properties of some low-lead or lead-free perovskite-derived materials: $Na_{0.5}Bi_{0.5}TiO_3$-$PbZrO_3$, $Na_{0.5}Bi_{0.5}TiO_3$-$BiScO_3$ and $Na_{0.5}Bi_{0.5}TiO_3$-$BiFeO_3$ ceramics, *Journal of the European Ceramic Society* **26**, 3037-3041 (2006)

77. Dorcet, V., Marchet, P. and Trolliard, G. Structure and dielectric studies of the $Na_{0.5}Bi_{0.5}O_3$-$BiFeO_3$ system, *Journal of the European Ceramic Society*, **27**, 4371-4374 (2007)

78. Dorcet, V., Marchet, P., Pena, O. and Trolliard, G. Properties of the solid solution (1-x)$Na_{0.5}Bi_{0.5}TiO_3$-(1-x)$BiFeO_3$, *Journal of Magnetism and Magnetic Materials*, **321**, 1762-1766 (2009)

79. Venkata Ramana, E. Suryanarayana, S.V. and Bhima Sankaram, T., Synthesis and magnetoelectric studies on $Na_{0.5}Bi_{0.5}TiO_3$-$BiFeO_3$ solid solution ceramics, *Solid State Sciences*, **12**, 956-962 (2010)

80. Liu, H., Guo, Y., Guo, B. and Zhang, D. Synthesis and visible-light photocatalysis capability of $BiFeO_3$-$(Na_{0.5}Bi_{0.5})TiO_3$ nanopowders by sol-gel method, *Solid State Sciences*, **19**, 69-72 (2013)

81. Ishiwata, S., Azuma, M., Takano, M., Nishibori, E., Takata, M., Sakata, M. and Kato, K., High pressure synthesis, crystal structure and physical properties of a

new Ni(II) perovskite $BiNiO_3$, *Journal of Materials Chemistry* **12** 3733-3737 (2002)

82. Fujii, I., Ito, Y., Suzuki, T. and Wada, T., Ferroelectric and piezoelectric properties of $(Bi_{1/2}Na_{1/2})TiO_3$-$BiFeO_3$ ceramics, *Journal of Materials Research* **31**, 28-35 (2016)

83. Warren, W.L., Vanheusden, K., Dimos, D., Pike, G.E. and Tuttle, B.A., Oxygen Vacancy Motion in Perovskite Oxide, *Journal of the American Ceramic Society* **79**, 536-538 (1996)

Chapter 3

Experimental procedures

3.1. Ceramic processing

All samples were prepared using the conventional solid oxide route. The synthesised samples are listed in Table 3-1.

Series	Composition studied
$Na_{0.5-x}Bi_{0.5+x}TiO_{3+1.5x}$	x = -0.02~0.02
$Na_{0.5}Bi_{0.5+x}Ti_{1-y}Ga_yO_{3+1.5x-0.5y}$	x = -0.02~0.02, y = 0.005~0.16
$xBiGaO_3$-(1-x)NBT	x = 0.02~0.0.08
$xBiFeO_3$-(1-x)NBT	x = 0.10~0.70
$xBi(Ni,Ti)_{0.5}O_3$-(1-x)NBT	x = 0.10~0.80

Table 3-1. Series of studied compositions.

The raw reagents used in ceramic processing were: Na_2CO_3 (99.5%, Alfa Aesar, Ward Hill, MA), Bi_2O_3 (99.9%, Acros organics, Geel, Belgium), TiO_2 (99.9%, Sigma-Aldrich, Gillingham, UK), Ga_2O_3 (99.99%, Stanford Materials Corp., CA, USA), Fe_2O_3 (99%, Sigma-Aldrich, MO, USA), NiO (99%, Alfa Aesar, Heysham, UK), $SrCO_3$ (99%, Aldrich, MO, USA). Prior to use, all reagents were dried at appropriate temperatures as listed in Table 3-2. 0.04 and 0.08 moles of the batches were mixed in stoichiometric amounts for hand grinding and ball milling samples, respectively. The batches of hand ground samples were mixed using a mortar and pestle with acetone for ~45 mins. The batches of ball milled samples were placed in HDPE bottles with isopropanol and Y_2O_3 stabilized zirconia milling media, and ball milled for 6 hours. The milling media were removed and the remaining slurry dried at 80 ℃ in an oven overnight to remove the isopropanol. The dried powder was sieved with a mesh size of 250 μm. The mixed powders prepared by both methods were calcined twice in a lidded alumina crucible with a ramp rate of 5 ℃min^{-1} at 800 ~ 900 ℃. The same mixing procedure of both methods was applied after each calcination and the only exception was that the ball milling after first calcination had shorter time of 4 hours. The calcined powders were

consolidated into green bodies using an uniaxial press in a 10 mm diameter die and then cold isostatic pressed (CIP) applying ~15 and 200 MPa for 1 min, respectively. Some samples were only uniaxial pressed with the mixture of calcined powder and binder (5% polyvinyl alcohol (PVA), 95% distilled water) to improve densification when the CIP was not available. The green pellets were covered in sacrificial powder of the same composition to minimise volatilisation of Na or Bi, placing on an alumina boat, covered with a lid and sintered in air with a ramp rate of 5 °Cmin^{-1} at the appropriate temperature.

Drying temperature/°C	**Reagents**
180	$SrCO_3$
300	Na_2CO_3, Bi_2O_3
600	Fe_2O_3
800	NiO
900	TiO_2

Table 3-2. Drying temperature of raw reagents.

3.2. Density measurements

The relative density (ρ_r) is defined as the ratio of the bulk density (ρ_b) of the sintered sample to the theoretical density (ρ_t) of its composition.

$$\rho_r = \frac{\rho_b}{\rho_t} \qquad 3\text{-}1.$$

ρ_b was measured using Archimedes' method, which works on the principle of apparent loss in weight of an immersed object in a liquid is equivalent to the weight of the liquid displaced by the object.[1] Therefore, ρ_b was calculated using the following formula,

$$\rho_b = \frac{m_1}{m_1 - m_2} \cdot \rho_{H_2O} \qquad 3\text{-}2.$$

m_1: weight of sample in air (g)

m_2: weight of sample in water (g)

ρ_{H_2O}: density of water at experiment temperature (g/cm^3)

ρ_t was calculated from the atomic weight and the unit cell volume using the following formula,

$$\rho_t = \frac{MW \cdot n}{V_{cell} \cdot N_A} \qquad 3\text{-}3.$$

MW: molecular weight (g/mol)

n: number of atoms in the unit cell

V_{cell}: unite cell volume (cm^3)

N_A: Avogadro's number (mol^{-1})

3.3 X-Ray diffraction (XRD)

X-ray diffraction (XRD) is a technique to identify crystalline phases present in a sample as well as their lattice parameters.[2] All samples were examined before and after the sintering process. The phase analysis were performed by Bruker D2 Phaser (MA, USA) on calcined powders and on polished-sintered pellet surfaces. A STOE-STADI P diffractometer (Darmstadt, Germany) with Cu radiation was also used to examine samples where there was only a small amount of available powder. Data were collected in steps of 0.02° from 20 to 60° 2θ and analysed using 'ICDD PDF-4+' software (PA, USA). The lattice parameters were calculated from the diffraction pattern of crushed-sintered pellets using a STOE-STADI PSD diffractometer (Darmstadt, Germany) with Cu radiation. A small amount of Silicon powder as a calibrating standard was mixed with fine powder obtained from crushed pellets. Data were collected in steps of 0.02° from 20 to 80° 2θ and analysed with Win X^{pow} software (version 2.1, Darmstadt, Germany). The diffraction patterns were firstly calibrated using a linear calibration polynomial based on the Silicon peaks and then applied a least square fit to obtain lattice parameters.

3.4 Scanning electron microscopy (SEM)

Scanning electron microscopy (SEM) was performed on sintered ceramics to determine the porosity, phase purity and general microstructure.[3] The sintered pellets were firstly ground using 800, 1200 and 2500 grit silicon carbide paper and then polished using 6, 3 and 1 μm diamond paste on synthetic polishing clothes. In order to observe the microstructure, part of the polished pellets were thermally etched at 90% of the sintering temperature for 1 hour. Pellets were coated with a thin conducting layer and mounted on an aluminium stub using silver paste (Agar Scientific Ltd., Stansted, UK) to ground any charging of pellets under the electron beam. Carbon was chosen as the coating material to enable Energy Dispersive Spectroscopy (EDS) measurements. The microstructures were observed using a JOEL JSM 6400 (Tokyo, Japan) and a Philip XL30S FEG (Amsterdam, Netherland) and chemical composition was analysed using EDS (Link Analytical Ltd., Bucks, UK) both operating at 20 kV. For chemical compositional analysis by EDS, at least 5 different areas (~ 1 μm spot size) were randomly selected to collect data on the polished/etched pellet surfaces to determine the average chemical composition and standard deviation (used as the error bar).

3.5 Electrical measurements

The sintered pellets were polished and coated with thin conducting layers on both sides of the pellets using gold paste (T-10112, Metalor Technologies UK Ltd., Birmingham, UK) which was annealed at 800 ℃ for 2 hours. The electrical properties, i.e. the resistance and capacitance, can be determined by the Impedance Spectroscopy (IS).[4] A small ac voltage, typically 100 mV, and a wide frequency range (10^{-2} – 10^{6} Hz) were applied to the pellets in most experiments. The data analysis was performed using 'Zview' software (Scribner Associates Inc., USA).

3.5.1 Temperature dependence

The pellets were mounted on an alumina compression jig in a tube furnace. An Agilent E4980A Precision LCR Meter (Agilent Technology, CA, USA) was used for the frequency range 10 – 10^{6} Hz and for lower frequency measurements, a ModulabXM (Solartron Group Ltd., Hampshire, UK) was used to collect data down to 10^{-3} Hz. The

IS data were collected from room temperature up to 800 ℃ every 25 ℃ in air on heating or cooling.

3.5.2 Oxygen partial pressure (pO_2) dependence

The pellets were mounted in a spaghetti jig which consisted of two platinum wires that were isolated in thin alumina tubes (spaghetti) and then sealed in a silica glass tube in a tube furnace. The oxygen partial pressure of the pellets depends on the atmosphere in the glass tube and the gases were changed from high to low pO_2 (O_2 – air – N_2). A Solartron SI 1260 Impedance analyser (Solartron Group Ltd., Hampshire, UK) was used to collect IS data over the frequency range 10^{-2} - 10^6 Hz isothermally in the different atmospheres.

3.5.3 Fixed frequency measurements

The pellets were mounted in a compression jig in a tube furnace and connected to an Inductance-Capacitance-Resistance LCR meter (Hewlett-Packard GmbH, Böblingen, Germany). The capacitance and dielectric loss were recorded every minute at five different frequencies (1, 10, 100 and 250 kHz and at 1MHz) with heating or cooling rate of 1 ℃min^{-1} up to 850 ℃. The relative permittivity was calculated from the capacitance using the following formula:

$$\varepsilon_r = GF \cdot \frac{C}{\varepsilon_0} \qquad 3\text{-}4.$$

$$\mathrm{GF} = \frac{t}{A} \qquad 3\text{-}5.$$

ε_r: relative permittivity

ε_0: permittivity of free space (Fcm^{-1})

GF: geometric factor (cm^{-1})

C: capacitance (F)

t: thickness of pellet (cm)

A: area of face of the pellet (cm^2)

3.6 Oxygen ionic transport number measurements

EMF oxygen ionic transport number measurements were performed on a ProboStat system (NorECs Norwegian Electro Ceramics As, Oslo, Norway). In this system, samples were mounted on a tube which inner diameter is ~11.5 mm. Therefore, the diameter of sintered pellets had to be greater than the tube. In this measurement, the tube was a pure oxygen ion conductor made of high purity YSZ and Pt was the electrode material to optimise the diffusion of oxygen ions. Electrodes were applied on both faces of the pellets and on the inner and outer side of YSZ tube and connected to a Keithley 182 sensitive digital voltmeter (Keithley, OH, USA) using a Pt wire on each electrode to record voltage difference. The setup for EMF measurements is shown in Fig 3-1. Pellets were sealed using a glass frit on one end of the YSZ tube to isolate the inner and outer atmosphere of the tube at 550 ℃ and heated up to 800 ℃. The pO_2 gradient was created by flowing N_2 and O_2 as the inner and outer atmospheres, respectively and monitored by the voltage difference across the YSZ tube at 600 ~ 800 ℃ with a cooling rate of 3 ℃min^{-1}. The readings were taken after holding at the measuring temperature for 2 hours. Therefore, the oxygen ion transport number can be calculated by the ratio of the voltage difference of the pellets to the voltage difference of the YSZ tube.

Fig 3-1. Schematic diagram of the setup for EMF measurements. Figure is adopted from ref 6 (Figure S1).

3.7 Neutron diffraction (ND)

Neutron diffraction (ND) is a technique to analysis the crystalline phases and structure of a sample.[2] The crystalline structure can be determined by XRD, where the intensity of diffraction patterns is dominated by heavy atoms, such as bismuth. The advantage of ND is to locate the light atoms, such as oxygen. Therefore, ND is a useful technique for Rietveld refinement of a sample containing both extremely heavy and light atoms.

~6 g of fine powders for each sample was ground from the sintered pellets. The powder ND was performed by the general materials diffractometer (GEM) located at the ISIS Neutron and Muon Source facility (Rutherford Appleton Laboratory, Didcot, U.K.). The ND patterns were collected at room temperature. The structure refinement was analysed using Rietveld refinement program GSAS.[7]

3.8 References

1. Archimedes, On floating bodies, Book I. In: Heath, T. L. (Ed.) The work of Archimedes with The Method of Archimedes, New York, *Dover Publications Inc*. (1957)

2. West, A.R., Solid State Chemistry and its Applications-second edition, student edition, *Wiley* (2014)

3. Goldstein, J., Newbury, D.E., Joy, D.C., Lyman, C.E., Echlin, P. Lifshin, E., Sawyer, L. and Michael, J.R., Scanning Electron Microscopy and X-ray Microanalysis third edition, New York, *Springer* (2003)

4. Irvine, J. T. S., Sinclair, D. C. & West, A. R., Electroceramics: Characterization by Impedance Spectroscopy, *adv. Mater.* **2**, 132-8 (1990)

5. Scott, J. F., Ferroelectrics go bananas, *J. Phys.: Condens. Matter* **20**, 021001 (2008)

6. Li, M. *et al.* A family of oxide ion conductors based on the ferroelectric perovskite $Na_{0.5}Bi_{0.5}TiO_3$, *Nat. Mater.* **13**, 31-5 (2014).

7. Toby, B.H., EXPGUI, a graphical user interface for GSAS, *Journal of Applied Crystallography* **34**, 210-213 (2001)

Chapter 4

A-site Nonstoichiometric NBT

$Na_{0.5}Bi_{0.5}TiO_3$ (NBT) is a well-known ferroelectric and lead-free piezoelectric material. However, the electrical properties of stoichiometric NBT are very sensitive to the Na/Bi ratio, especially unintentional volatilization of Na and Bi above 1132 and 825 ºC during processing, respectively.[1] This results in undesirable leakage for stoichiometric NBT as a dielectric material. Hiruma *et al.*. have shown the A-site nonstoichiometry of NBT dramatically changes the dc conductivity at room temperature, where ceramics of slight Na-rich or Bi-deficient (Na/Bi > 1) starting compositions become more conductive whereas those from Na-deficient or Bi-rich (Na/Bi < 1) starting compositions become more resistive compared to stoichiometric NBT.[2] However, the conduction mechanism is still unclear. Further AC impedance studies reported by Li *et al*.. confirmed the dramatic influence of A-site nonstoichiometry ($Na_{0.49}Bi_{0.5}TiO_{2.995}$($N_{0.49}$BT), $Na_{0.51}Bi_{0.5}TiO_{3.005}$($N_{0.51}$BT), $Na_{0.5}Bi_{0.49}TiO_{2.985}$($NB_{0.49}$T), $Na_{0.5}Bi_{0.51}TiO_{3.015}$($NB_{0.51}$T)) on the electrical properties (Fig 4-1), where it becomes a conductor or an insulator when Na/Bi is greater and smaller than 1, respectively.[3] Li *et al*. also suggested the conduction mechanism of the leakage current of conducting NBT is oxygen ions hopping through the saddle-point between two A-site ions and a B-site ion based on ^{18}O tracer diffusion and electromotive force (EMF) measurements.[4]

Fig 4-1 Arrhenius-type plot of bulk conductivity for stoichiometry and A-site nonstoichiometry NBT. Figure is adopted from ref 3 (Figure 2(c)).

Their XRD results showed no evidence of any secondary phase after double calcination at 800 and 850 ºC for 2h. However, small amounts of secondary phases were observed under SEM and transmission electron microscopy (TEM) of sintered ceramics, as listed in Table 4-1. They also claimed the compositional analysis of the main phase using EDS revealed no significant compositional difference between all samples within instrument resolution and standard errors.[3,4] Therefore, it is possibly difficult to control the actual composition of synthesised samples using starting compositions with A-site Na or Bi-nonstoichiometry.

Composition	Microscopy	Secondary phase
$N_{0.49}BT$	TEM	TiO_2
$N_{0.51}BT$	SEM	Na-rich phases
$NB_{0.49}T$	SEM	$Na_2Ti_6O_{13}$
$NB_{0.51}T$	TEM	Bi-rich regions

Table 4-1. Secondary phases of selected A-site nonstoichiometry NBT under SEM or TEM.[3,4]

A series of $Na_{(0.5-x)}Bi_{(0.5+x)}TiO_{3+x}$, $-0.01 \leq x \leq 0.01$, were reported by Carter *et al.*. [5] where the A-site of NBT was fully occupied. Their high resolution synchrotron x-ray diffraction and Rietveld refinements showed decreased spontaneous strain when $x \neq 0$, where the lattice parameters trend towards those of a cubic lattice structure (a ~9.509Å, b & c ~ 5.49Å and $\beta \sim 125.2644°$) as shown in Fig. 4-2. They suggested the decrease in spontaneous ferroelastic strain and no significant change in ferroelectric properties for Bi-rich samples may be possibly driven by the point defects and clusters, and a small amount of excess Bi as secondary phase at the grain boundary, respectively. Samples become leaky and difficult to pole for $x < 0$ due to the existence of oxygen vacancies. The solid solution limit for $Na_{(0.5-x)}Bi_{(0.5+x)}TiO_{3+x}$ was not clearly identified.

Fig. 4-2. Refined lattice parameters of the *Cc* phase, weight percentage of the cubic phase and spontaneous strains (e_s) for $Na_{(0.5-x)}Bi_{(0.5+x)}TiO_{3+x}$. Figure is adopted from ref 5 (Figure 3).

This chapter is a further investigation on comparing A-site partially occupied nonstoichiometric NBT (deficient/excess Na or Bi, i.e. $NB_{0.49}T$) to A-site fully occupied nonstoichiometric NBT and the influence of processing methods (ball milling versus hand grinding) to synthesise NBT ceramics. A series of nominal A-site fully occupied but nonstoichiometric NBT based on the general formula $Na_{0.5-x}Bi_{0.5+x}TiO_{3+x}$ ($-0.02 \leq x \leq 0.02$) was prepared. This work follows on from Dr. Ming Li's work at the University of Sheffield. The aim is primarily to establish any differences in the electrical properties using impedance spectroscopy (IS) associated with adjusting the Na/Bi ratio with partially/fully occupied A-sites and different levels of Bi loss during processing via ball milling and hand grinding of powders. The geometrically independent term f_{max} extrapolated from the M'' Debye peak associated with the bulk response in the IS data is also discussed in this chapter.

4.1 Phase purity and microstructure

All samples prepared by hand grinding were calcined two times at 800 and 900 °C for 2 and 8 hours, respectively. The sintering temperature for the ceramics increased as x increased between 1100 to 1200 °C for 2 hours as shown in Table 4-2. XRD patterns at room temperature were obtained from powders after two calcinations and polished

sintered pellet surfaces as shown in Fig. 4-3 and 4-4, respectively. The calcined powders with Na/Bi ≥ 1 had no secondary phases and a clear secondary phase increased as x increased when Na/Bi < 1, which was identified as $Na_{0.5}Bi_{4.5}Ti_4O_{15}$ (NBiT, ICDD: 04-017-3364). The peak intensities of NBiT decreased after sintering at higher temperature and were barely detectable by XRD for x = 0.02. The main XRD peaks and a superlattice peak around 38.5 2θ° suggested all samples had a rhombohedral/monoclinic structure which is a slightly distorted cubic structure. The pseudo-cubic cell volumes are very similar and are essentially the same within errors because Na and Bi atoms have similar size in XII coordination, Fig. 4-5.

Composition	**Calcining process**	**Sintering Temperature/°C**	**Thermal etching temperature/°C**
By ball milling[3,4,7]			
$N_{0.49}BT$	1st @ 800°C 2h	1150	1035
$NB_{0.49}T$	2nd @ 850°C 2h	1150	1035
NBT		1150	1035
$N_{0.51}BT$		1125	1013
$NB_{0.51}T$		1150	1035
By hand grinding $Na_{0.5-x}Bi_{0.5+x}TiO_{3+x}$			
x = -0.02	1st @ 800°C 2h	1100	990
x = -0.01	2nd @ 900°C 8h	1100	990
x = 0		1150	1035
x = 0.01		1200	1080
x = 0.02		1200	1080

Table 4-2. Calcining, sintering and thermal etching temperature of A-site nonstoichiometric NBT prepared by ball milling and nonstoichiometric NBT prepared by hand grinding. Sintering and thermal etching periods were 2 and 1 hour, respectively.

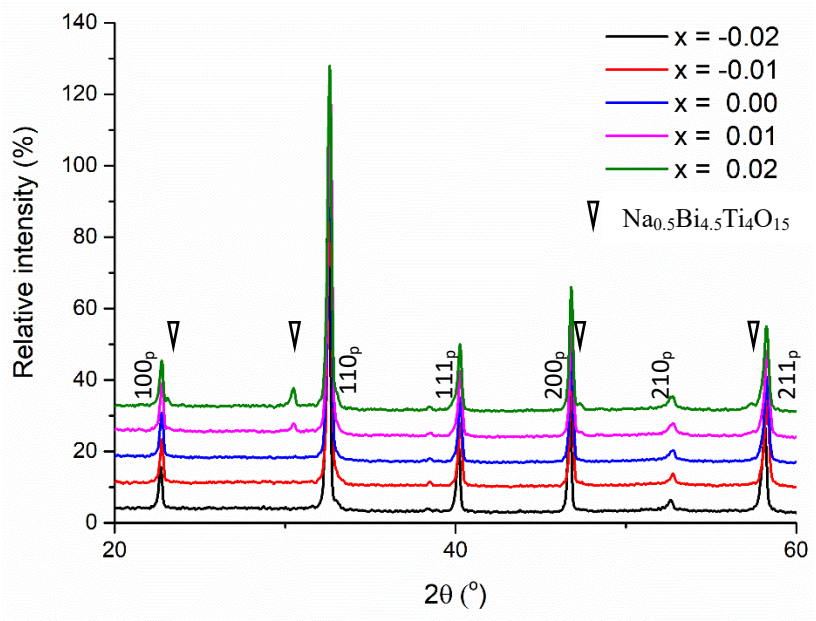

Fig. 4-3. Room temperature XRD patterns for the $Na_{0.5-x}Bi_{0.5+x}TiO_{3+x}$ series after calcination at 900 ℃ for 8h.

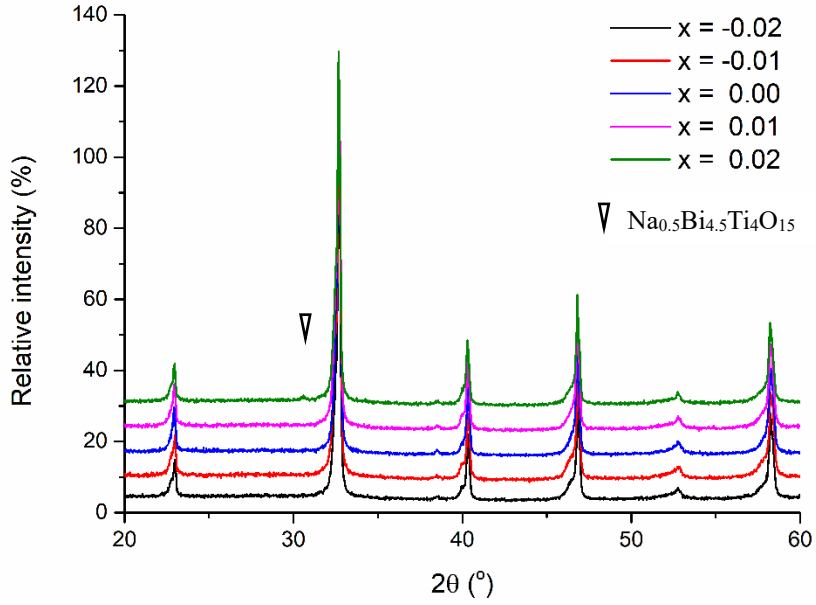

Fig. 4-4. Room temperature XRD patterns for the $Na_{0.5-x}Bi_{0.5+x}TiO_{3+x}$ series from polished sintered pellet surfaces.

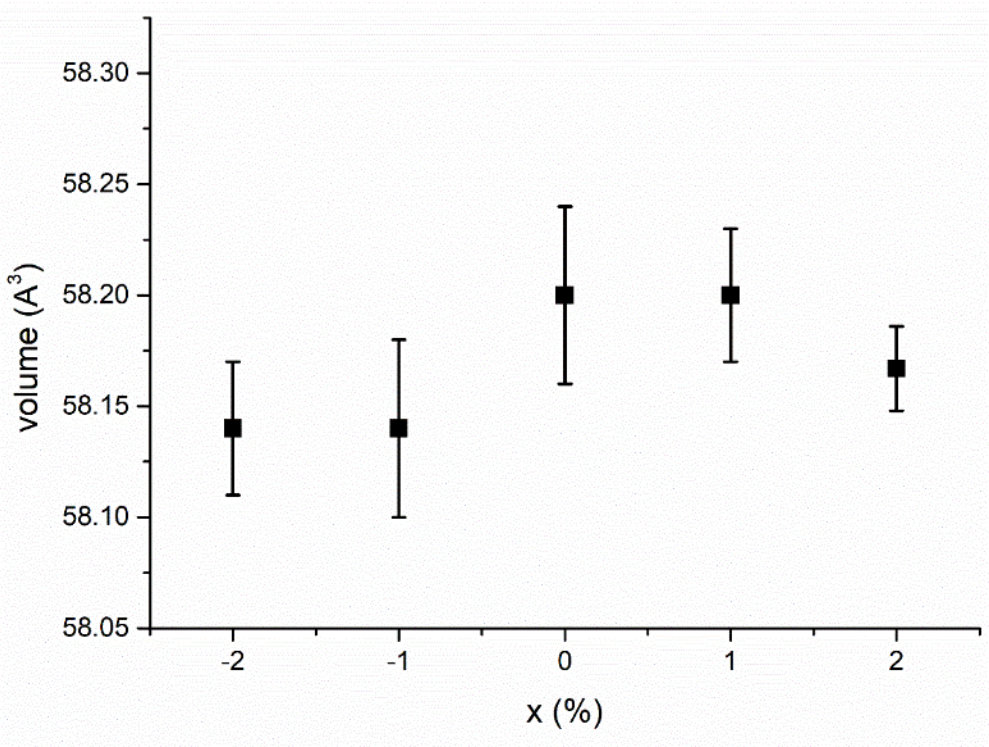

Fig. 4-5. Pseudo-cubic cell volume for the $Na_{0.5-x}Bi_{0.5+x}TiO_{3+x}$ series.

SEM backscattering images on polished pellet surfaces show some secondary phases for x = -0.02 and 0.02, Fig. 4-6 (a) and (e), respectively. Based on EDS results on these secondary phases, they were identified as $Na_2Ti_3O_7$ and $Na_{0.5}Bi_{4.5}Ti_4O_{15}$, respectively. The Na-rich phase was not detected by XRD for x = -0.02 and SEM/EDS results confirmed the existence of $Na_{0.5}Bi_{4.5}Ti_4O_{15}$ for x = 0.02.

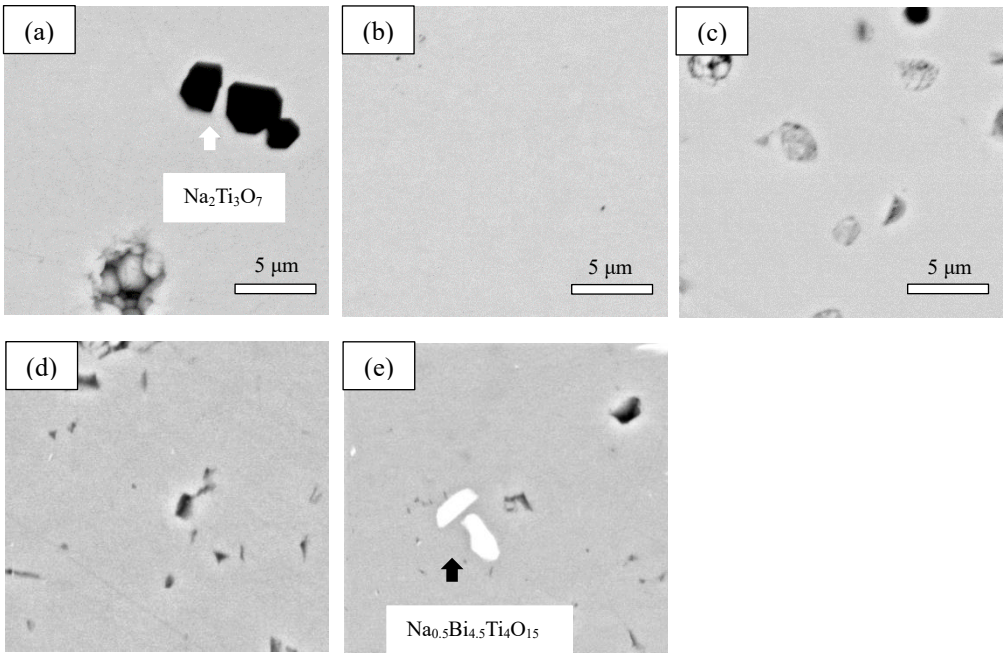

Fig. 4-6. SEM backscattering images of (a) x = -0.02 (b) x = -0.01 (c) x = 0 (d) x = 0.01 (e) x = 0.02 on polished pellet surfaces.

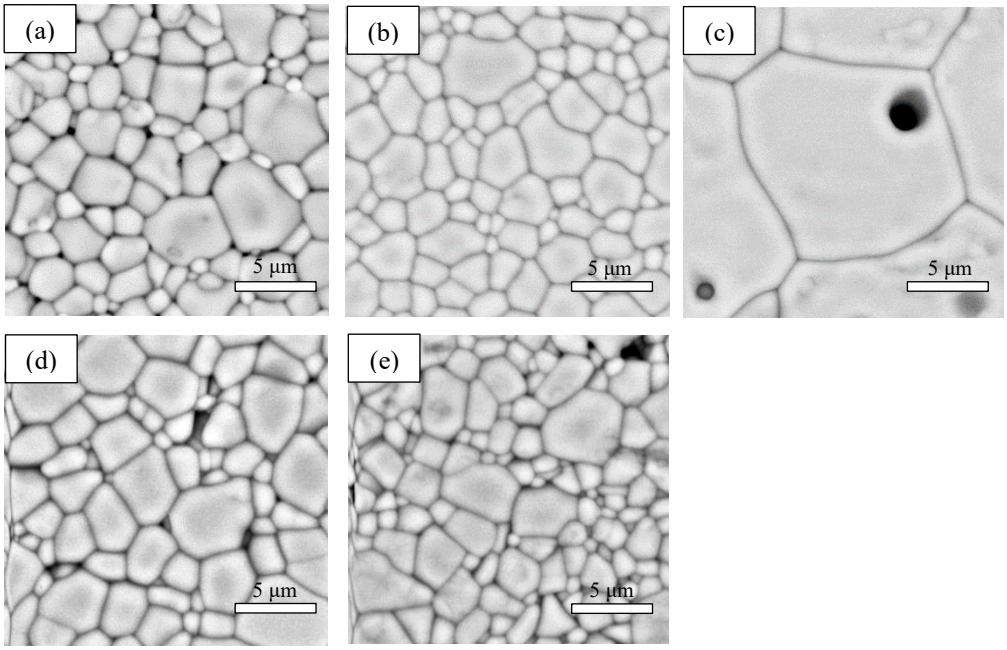

Fig. 4-7. SEM backscattering images of (a) x = -0.02 (b) x = -0.01 (c) x = 0 (d) x = 0.01 (e) x = 0.02 on thermally etched surface.

The bulk chemical compositions using EDS on polished and thermally etched surfaces are shown in Fig. 4-8 and 4-9, respectively. The average total at% of A-site ions (Na and Bi) is ~50.8 at% which is slightly higher than the expected value (50 at%) leading to a slight suppression of the Ti content on the B-site. The extra content of A-site ions comes from the Bi ions, i.e. the average Bi and Ti contents of stoichiometric NBT (x = 0) are 25.7 and 49.2 at%, which is slightly higher and lower than the expected values of 25 and 50 at%, respectively; however, the 1 at% difference in A and B-site is still within acceptable instrumental error. Apart from this, the Na and Bi contents change systematically with the starting composition and the Ti content remains similar on polished surfaces for all compositions, as shown in Fig. 4-8. It is hard to distinguish the chemical compositions on the thermally etched surfaces as the data have significantly larger standard errors which merges all compositions at the same level, as shown in Fig. 4-9. This is probably due to the volatilization of Na and Bi during thermally etching above 990 °C making inhomogeneous regions on pellet surfaces.

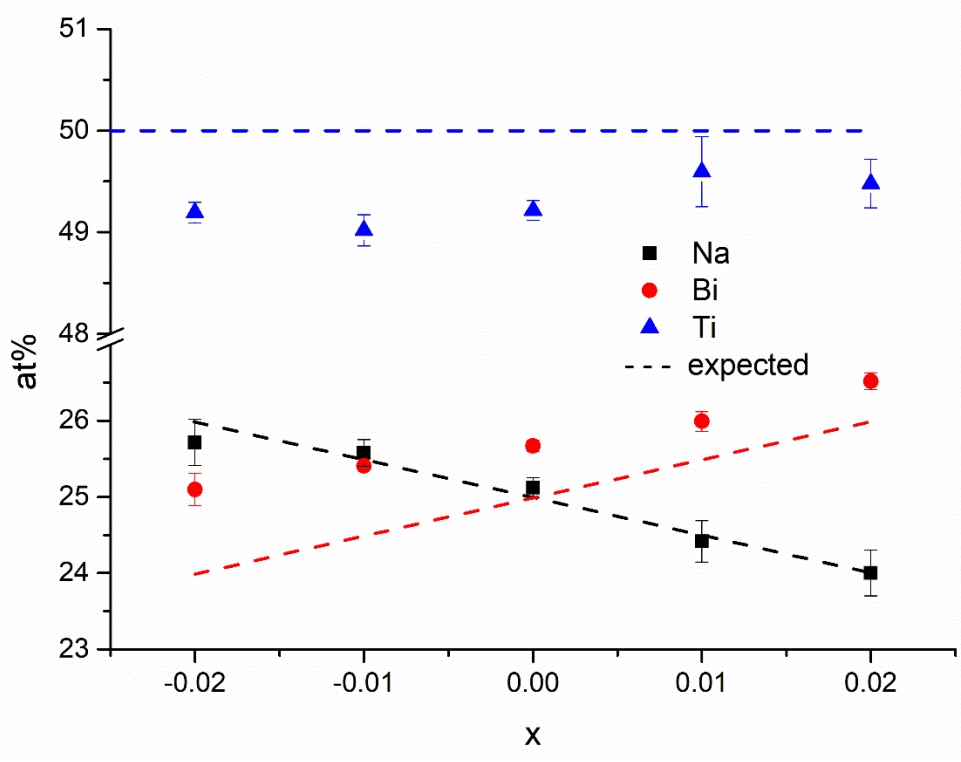

Fig. 4-8. EDS average chemical composition results for -0.02 ≤ x ≤ 0.02 on polished surfaces.

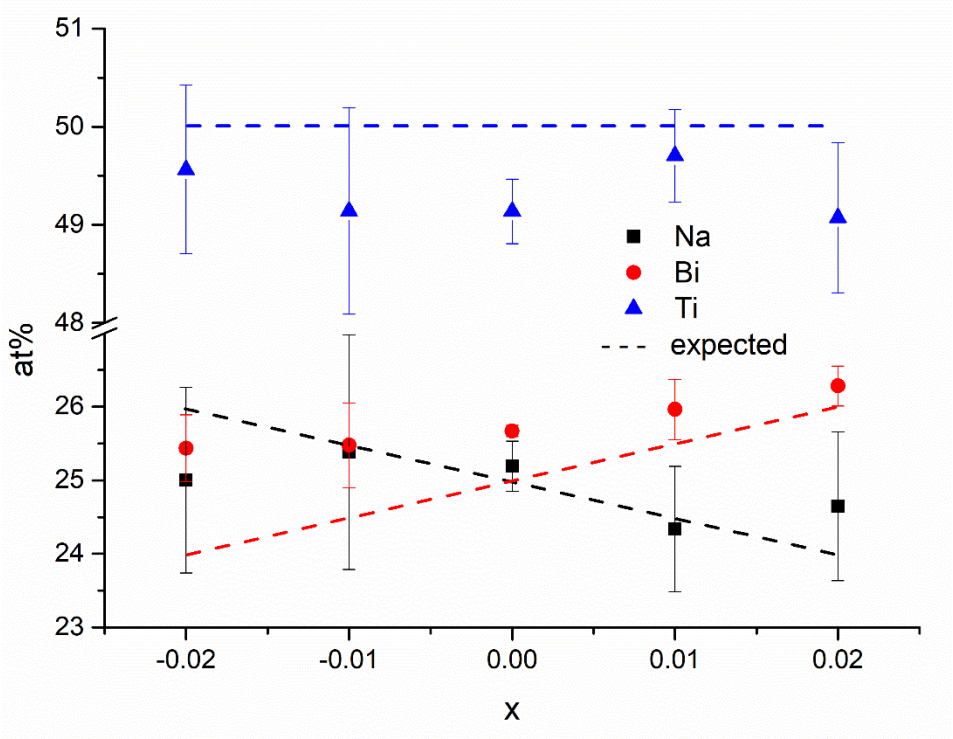

Fig. 4-9. EDS average chemical composition results for -0.02 ≤ x ≤ 0.02 on thermally etched surfaces.

Stoichiometric NBT should ideally have 25 at% Bi or less (volatile) and it is unlikely to have Bi content > 25% as the Na content is ~ 25 at%. Therefore, the standard difference is taken from the difference between experimental and theoretical Bi content as x = 0 on the polished surface ~ 0.67 at%. The EDS data on polished surfaces as shown in Fig. 4-8 is normalised using x = 0 as standard; Bi and Ti contents are subtracted and added the standard difference, respectively as shown in Fig. 4-10. The normalised data shows Ti contents become identical at ~ 50 at% and the Bi contents change systematically with x. However, the Bi-rich (x > 0) and Bi-deficient compositions (x < 0) are slightly lower and higher than the expected value, respectively.

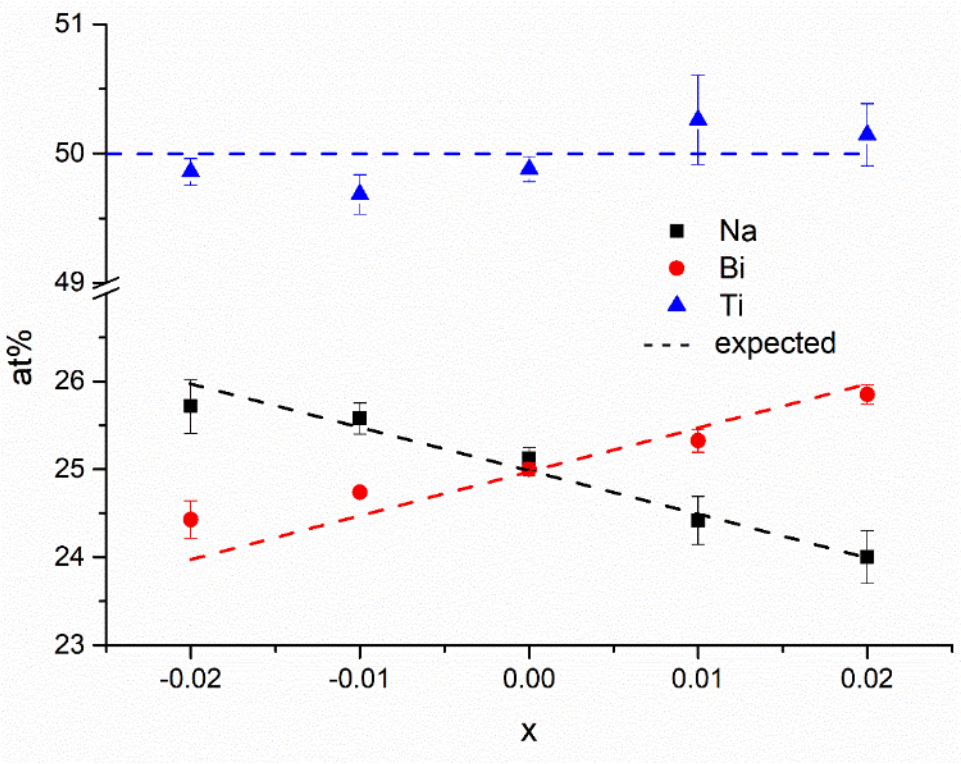

Fig. 4-10. Normalised EDS average chemical composition results for -0.02 ≤ x ≤ 0.02 on polished surfaces using x = 0 as a normalised standard.

4.2 Electrical Properties

The temperature dependence of the relative permittivity (ε_r) and dielectric loss (tan δ) for sintered ceramics are shown in Fig. 4-11. The nominally stoichiometric NBT (x = 0) prepared by hand grinding has the highest maximum relative permittivity (ε_{max} ~3000) which is slightly higher than the one prepared by ball milling and it decreases as the Na/Bi ratio increases or decreases for samples prepared by hand grinding as shown in Fig. 4-11(a). ε_r of x = -0.01 and -0.02 is much higher than other samples above ~400 °C which may be a contribution from a space charge effect or grain boundary component and more details will be discuss later. The temperature of ε_{max} (T_m) behaves linearly for -0.01 ≤ x ≤ 0.01 and has a significantly reduction in terms of temperature difference to reach limiting lower and upper values of 314 and 333 °C for x = -0.02 and 0.02, respectively, as shown in Fig. 4-12(b). It is possibly due to the presence of secondary phases which changes the bulk compositions and reaches solid solution limit.

The stoichiometric NBT prepared by hand grinding was more resistive than the one prepared by ball milling, with tan δ exceeding 10% at higher temperature (~425 °C) and with a lower depolarisation temperature (T_d) as indicated in Fi. 4.10 (b). For samples prepared by hand grinding, tan δ > 5% above ~180, 350 and 700 °C for x < 0, x = 0 and x > 0, respectively. T_d decreases as x increases between 96 and 260 °C.

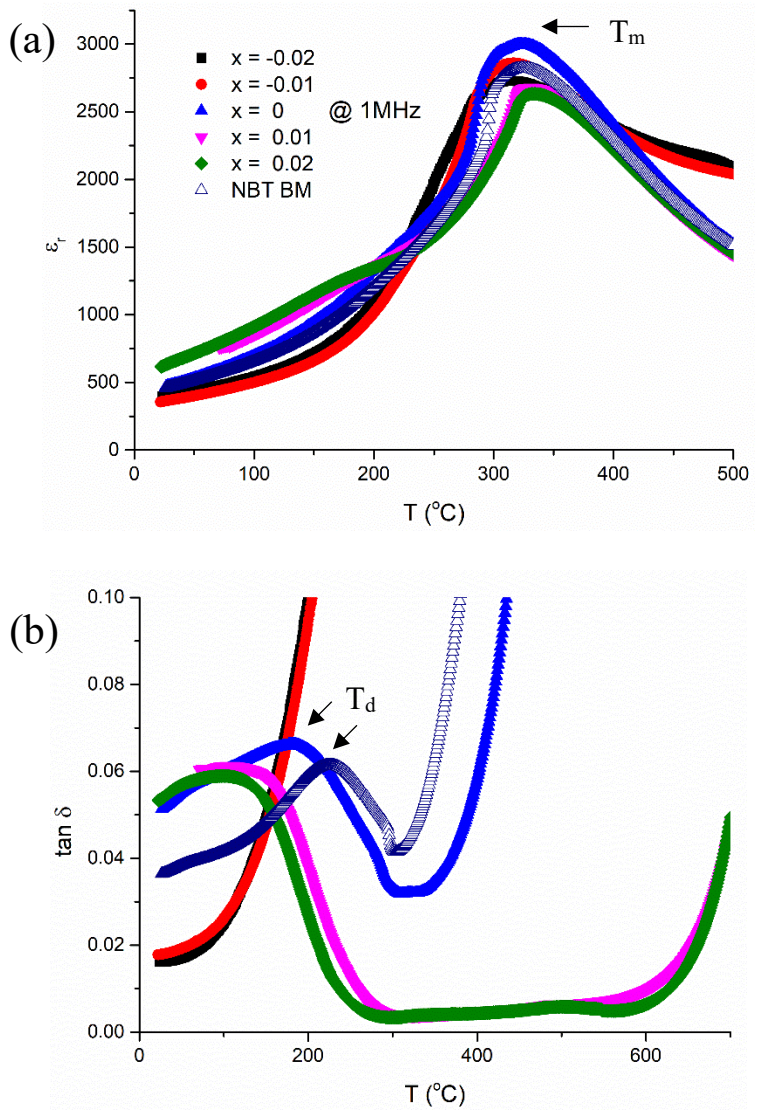

Fig. 4-11. Temperature dependence of (a) ε_r (b) tan δ at 1 MHz for $-0.02 \leq x \leq 0.02$ and comparison with stoichiometric NBT prepared by ball milling.

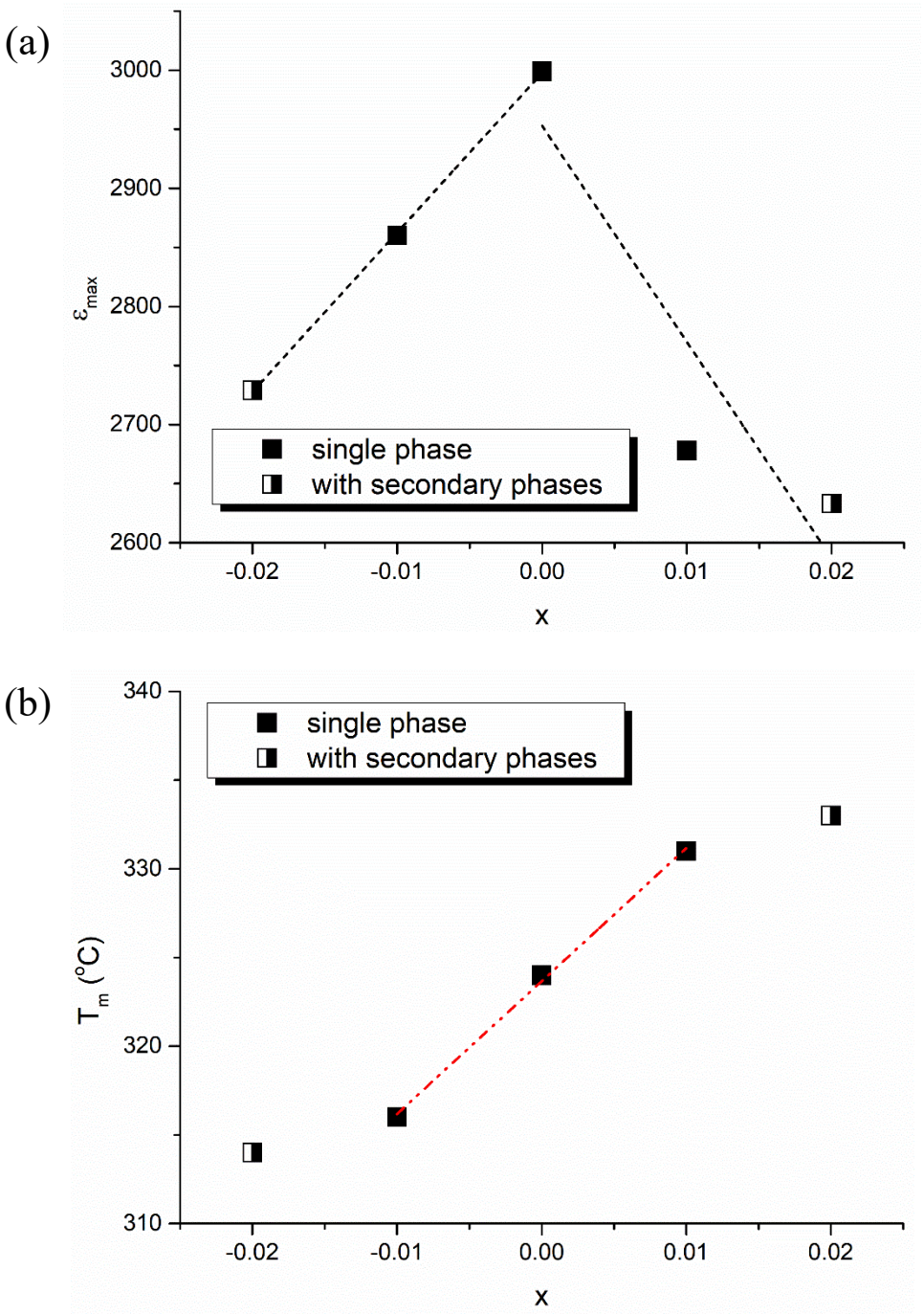

Fig. 4-12. The compositional dependence of (a) ε_{max} and (b) T_m for the $Na_{0.5-x}Bi_{0.5+x}TiO_3$ series.

The large Debye peak in the M" spectroscopic plots shown in Fig 4-13(a) were used to obtain bulk capacitance and resistance values of NBT. At the Debye peak maximum:

$$\omega RC = 1 \qquad 4\text{-}1.$$

$$\omega = 2\pi f_{max} \qquad 4\text{-}2.$$

where ω is angular frequency, R is resistance and C is capacitance. All data were corrected for sample geometry (G_f = Electrode Area/Sample thickness) so the units of C are Fcm^{-1} and R is the bulk resistivity in Ωcm. The M'' peaks have a minimum between 300 ~ 350 °C shown in Fig 4-13(a) and the capacitance derived from M'' peaks (Fig. 4-13(b)) shows a maximum ~325 °C, which matches the LCR results and confirms it is the bulk response.

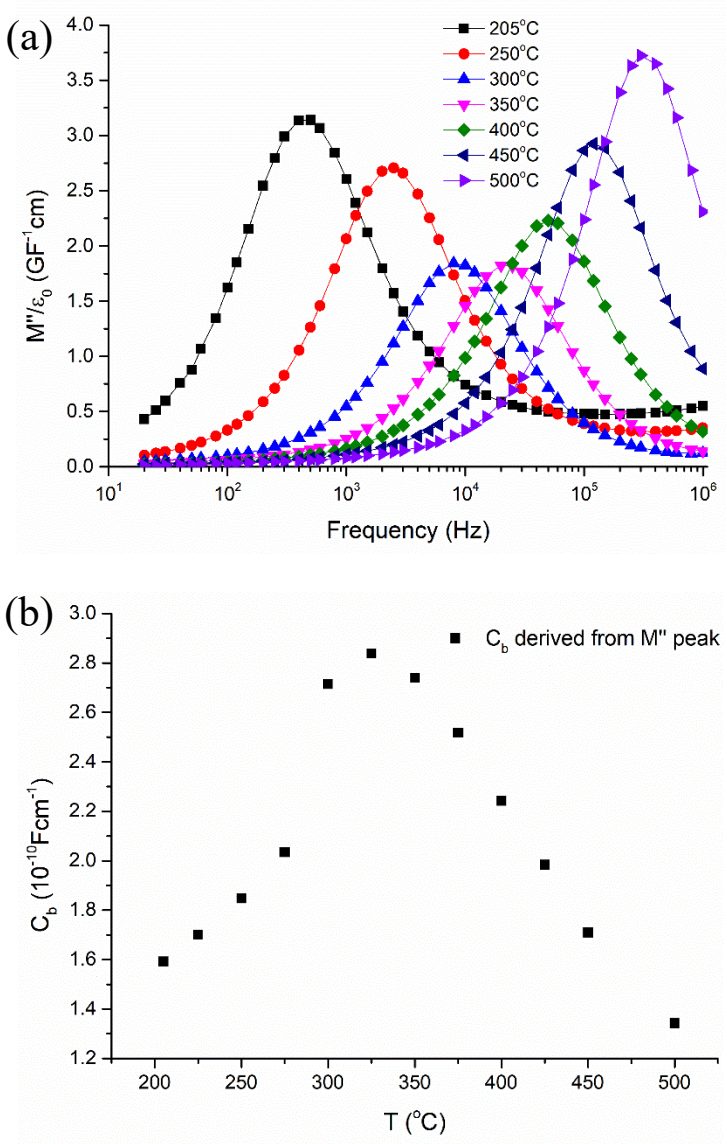

Fig. 4-13. (a) M'' spectroscopic plots and (b) variation of C_b versus T for a hand ground sample of x = 0 between 205 and 500 °C.

Complex plane Z* plots for $-0.01 \leq x \leq 0.01$ at 400 °C are shown in Fig. 4-14; those for x = -0.02 and 0.02 are similar to x = -0.01 and 0.01, respectively and are therefore not shown. For $x < 0$, Z* plots reveal the presence of at least three electro-active regions. The capacitance extrapolated at 1M, 10k and 20 Hz are ~ 2.15×10^{-10}, 2.85×10^{-9} and 1.55×10^{-7} Fcm^{-1} which are typical values of capacitance for bulk, grain boundary and electrode effects, respectively.[6] The capacitance for the high frequency incomplete arc is similar to the extracted capacitances for x = 0 and 0.01 (2.08×10^{-10} and 1.98×10^{-10} Fcm^{-1}) at 100 kHz, and are consistent with the LCR results. Therefore, the arc in the high frequency range is the bulk response and shows the bulk resistance to increase as x increases and for $x < 0$ is one order of magnitude smaller than x = 0 at 400 °C.

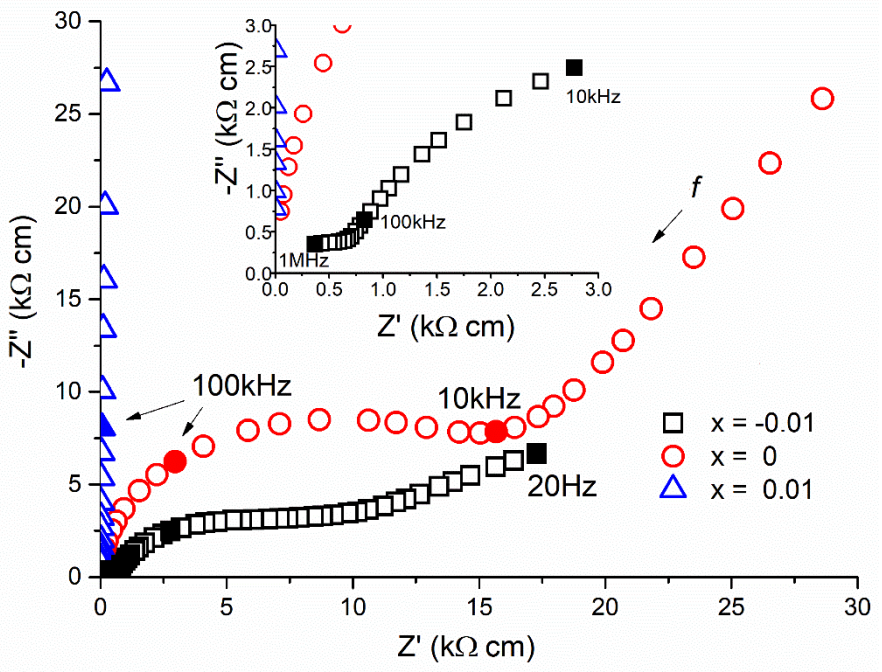

Fig. 4-14. Z* spectroscopic plots for $-0.01 < x < 0.01$ at 400 °C.

For conductive compositions, $x < 0$, the M'' Debye peaks associated with the bulk response is above the instrumental limit at 1 MHz and only the grain boundary response is visible above 400 °C. Therefore, the bulk conductivity of $x < 0$ is estimated by using the following equation:

Total resistance (R_{total}) = bulk resistance (R_b) + grain boundary resistance (R_{gb}) 4-3.

An example is shown in Fig. 4.15 for x = -0.01 at 600 °C. The grain boundary arc is fitted as the best approximated semi-circle (shown in red dashed line) using the limited data in the high frequency range in the Z* plots and the peak arc frequency at $2x10^5$ Hz is ~$1.19x10^{-9}$ Fcm^{-1} which confirmed it to be a grain boundary response (R_{gb}). Therefore, the total resistance can be extrapolated from the intercept of grain boundary arc at lower frequency and the bulk resistance can be calculated from $R_{total} - R_{gb}$.

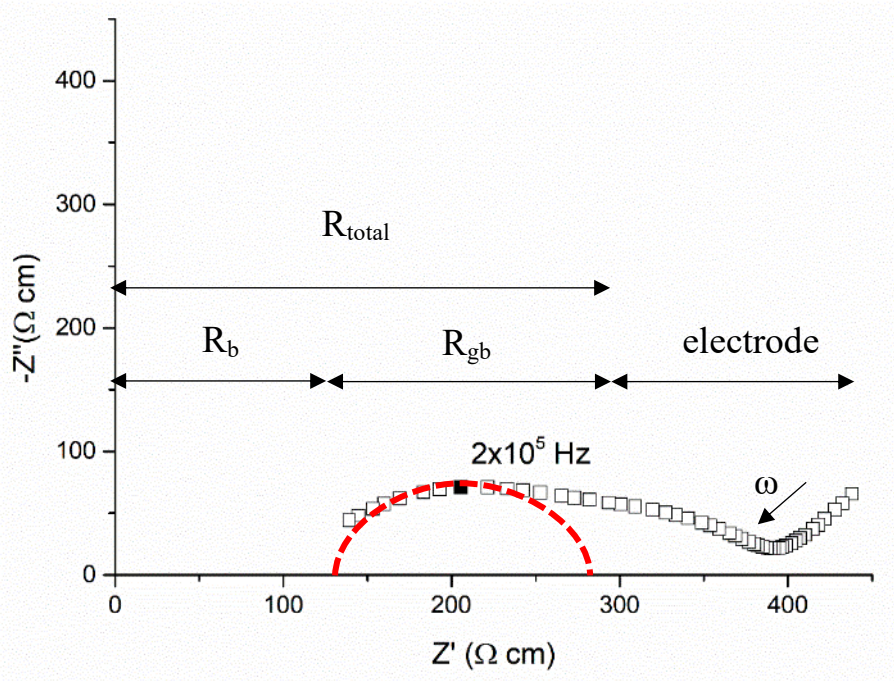

Fig. 4-15. Z* plot for x = -0.01 at 600°C. The red dashed line represents the semi-circle fitting for R_{gb} in the high frequency range.

Arrhenius plots of bulk conductivity ($\sigma_b = 1/R_b$) estimated from M'' peaks and the related activation energy (E_a) for -0.02< x < 0.02 are shown in Fig. 4-16. Based on the conductivity, they can be divided into two groups: (1) $x \leq 0$ and (2) $x > 0$. The difference in conductivity between groups (1) and (2) is more than 3 orders of magnitude. Therefore, group (1) and (2) can be categorised as conductors and insulators, respectively. In group (1), E_a changes from ~ 0.83 to ~ 0.5 to 0.54 eV below and above ~ 325 °C, respectively and the temperature for the change in E_a is similar to T_m observed from LCR results. E_a in group (2) is ~ 1.8 eV and is temperature independent.

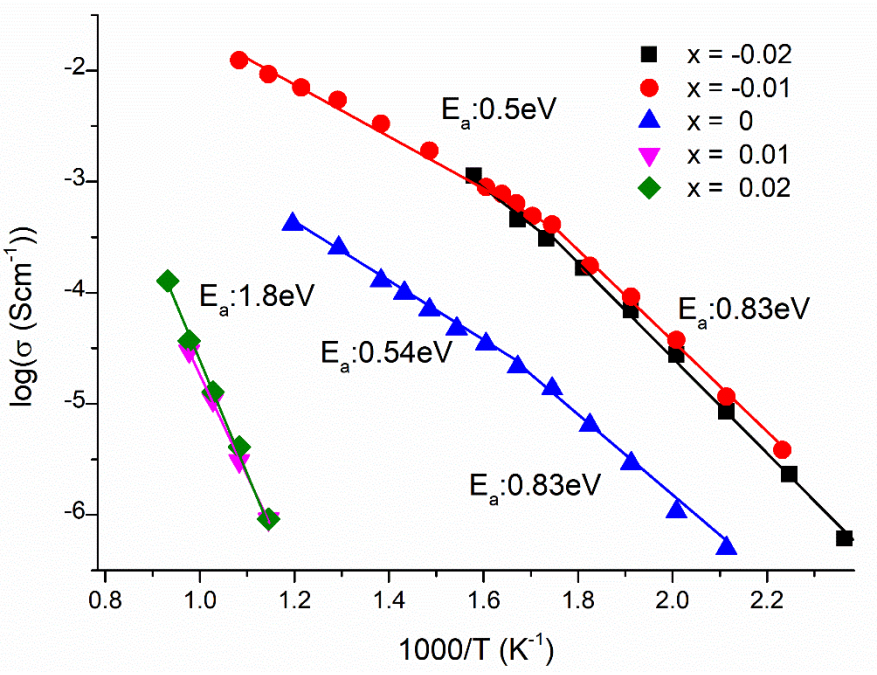

Fig. 4-16. Arrhenius plot of bulk conductivity for -0.02 < x < 0.02 (hand ground series).

4.3 Discussion

The list of compositions prepared by M. Li[3,4], L. Li[7] and myself prepared by ball milling and hand grinding is ranked in terms of oxygen content from low to high and is shown in Table 4-3. Based on XRD results, all samples in the table are single phase when pellets are sintered at the appropriate temperature with the exception of $Na_{0.48}Bi_{0.52}TiO_{3.02}$ (x = 0.02) prepared by hand grinding which has $Na_{0.5}Bi_{4.5}Ti_4O_{15}$ as a secondary phase. However, for A-site partially occupied nonstoichiometric NBT prepared by ball milling, Na-rich phases ($Na_2Ti_6O_{13}$) were observed under SEM for Na/Bi > 1 and secondary phases (Bi_2O_3 or TiO_2) were also observed at grain boundary regions under TEM except $Na_{0.5}Bi_{0.505}TiO_{3.0075}$ for Na/Bi < 1.[3,4]. Single phase can only be obtained with a small amount of Bi-excess which balances the Bi lost during processing. The conductivity depends on the Na/Bi starting ratio but does not correspond to oxygen content, i.e. samples are resistive if Na/Bi < 1, except for $Na_{0.5}Bi_{0.52}TiO_{3.03}$ which is an oxygen ion conductor due to the formation of Bi-rich secondary phases which may either deplete the NBT main phase of Bi or enhance the ionic conductivity.[7] The depletion of Bi and formation of secondary phases may show that NBT tends to maintain stoichiometry. Similar results are shown in the Ti-

nonstoichiometric NBT ($Na_{0.5}Bi_{0.5}Ti_{1-x}O_{3-2x}$) reported by M. Naderer *et al.*.[8], where the main phase shows a matrix consisting of NBT. Therefore, secondary phases are likely formed when the A-site is partially occupied which creates more challenges in controlling the oxygen content and therefore the conductivity and conduction mechanism(s).

For the $Na_{0.5-x}Bi_{0.5+x}TiO_{3+x}$ series prepared by hand grinding, the solid solution limit is $-0.02 < x < 0.02$ based on a combination of XRD and SEM, leading to a narrow range of Na/Bi (0.98~1.02). EDS results also confirm the bulk composition of the polished surface changes systematically and matches the starting compositions relatively well within these limits (Fig. 3-10). $Na_2Ti_3O_7$ was identified by EDS as a secondary phase in $Na_{0.52}Bi_{0.48}TiO_{2.98}$ which has higher Na/Ti than the $Na_2Ti_6O_{13}$ secondary phase observed in $Na_{0.5}Bi_{0.48}TiO_{2.97}$. This result indicates the mechanism of secondary phase formation is the same: the extra Na content in $Na_{0.52}Bi_{0.48}TiO_{2.98}$ (compared to $Na_{0.5}Bi_{0.48}TiO_{2.97}$) contributes in secondary phase formation. Since the A-site is fully occupied (based on the ideal perovskite formula of ABO_3) as a starting material, this mechanism is most likely driven by the limitation in oxygen vacancies in the NBT lattice. The conduction mechanism of leakage in NBT is driven by oxygen vacancies.[6] In this series, oxygen vacancies for $x < 0$ are generated according to the following equation:

$$Na_2O + 2Bi_{Bi}^{x} + 2O_O^{x} \rightarrow 2Na_{Bi}'' + 2V_O^{\cdot\cdot} + Bi_2O_3 \qquad 4\text{-}4.$$

Each Bi^{3+} replaced by a Na^+ ion creates one oxygen vacancy. The leakage of NBT ($x = 0$) is commonly attributed to Bi loss during sintering. The nominal oxygen content is directly linked to the conductivity, where it switches from conductive to insulating compositions when the nominal oxygen content > 3. By combing phase and electrical analysis, the defect mechanism is relatively clear but based on the assumption that the A-site is fully occupied.

Composition	Na/Bi ratio	Impurity (based on SEM)	Conductive(C)/ Insulating(I)
(M. Li and L. Li's results)[3,4,7]	*Ball milling*		
$Na_{0.5}Bi_{0.48}TiO_{2.7}$	1.04	$Na_2Ti_6O_{13}$	C
$Na_{0.5}Bi_{0.49}TiO_{2.85}$	1.02	$Na_2Ti_6O_{13}$	C
$Na_{0.5}Bi_{0.495}TiO_{2.925}$	1.01	$Na_2Ti_6O_{13}$	C
$Na_{0.49}Bi_{0.5}TiO_{2.995}$	0.98	-	I
$Na_{0.5}Bi_{0.5}TiO_3$	1.00	-	C
$Na_{0.51}Bi_{0.5}TiO_{3.005}$	1.02	Na-rich phases	C
$Na_{0.5}Bi_{0.505}TiO_{3.0075}$	0.99	-	I
$Na_{0.5}Bi_{0.51}TiO_{3.015}$	0.98	-	I
$Na_{0.5}Bi_{0.52}TiO_{3.03}$	0.96	-	C
(my results)	*Hand grinding*		
$Na_{0.52}Bi_{0.48}TiO_{2.98}$	1.08	$Na_2Ti_3O_7$	C
$Na_{0.51}Bi_{0.49}TiO_{2.99}$	1.04	-	C
$Na_{0.5}Bi_{0.5}TiO_3$	1.00	-	C
$Na_{0.49}Bi_{0.51}TiO_{3.01}$	0.96	-	I
$Na_{0.48}Bi_{0.52}TiO_{3.02}$	0.92	$Na_{0.5}Bi_{4.5}Ti_4O_{15}$	I

Table 4-3. A summary of Na/Bi ratio, phase purity and conductivity in stoichiometric and non-stoichiometric NBT sintered pellets.

Based on the LCR measurements, the temperature dependence of ε_r is very sensitive to the sintering conditions.[9] However, ε_{max} has maximum value when x = 0 and decreases as Na/Bi changes. ε_r of x < 0 show slight increase at 1M Hz above 400°C which is possibly contributed from grain boundary capacitance. For example, Fig. 4-17 shows the temperature dependence of ε_r at 1k, 10k, 100k and 1M Hz for x = -0.01. The temperature of f_{max} extracted from the bulk M'' Debye peaks are 150, 200, 275 and

375°C at 1k, 10k, 100k and 1M Hz, respectively. In the other words, the capacitances collected above these temperatures at each (fixed) frequency are not only bulk responses but are also influenced by the grain boundaries which have much higher capacitances.

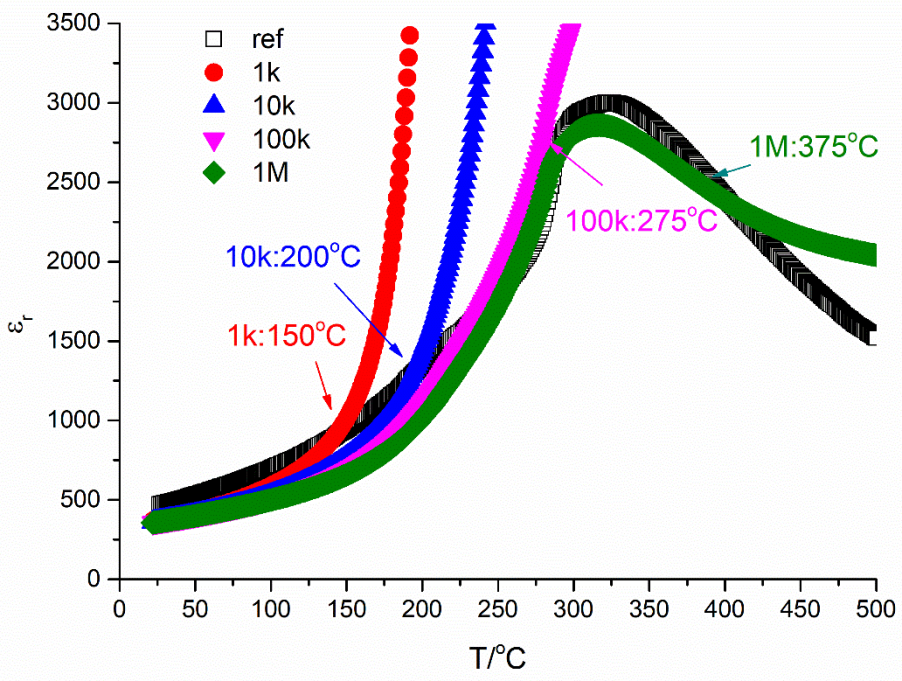

Fig. 4-17. Temperature dependence of ε_r at 1k, 10k, 100k and 1M Hz for x = -0.01. The reference is data for x = 0 at 1M Hz. The temperature dependence of f_{max} extracted from bulk M" peaks at 1k, 10k, 100 and 1M Hz are also included.

The difference between A-site partially and fully occupied nonstoichiometry NBT with oxygen vacancies in terms of conductivity is summarised in the Arrhenius plot of bulk conductivity shown in Fig. 4-18 (a). The conductivity of x = -0.02 and $N_{0.51}BT$ are similar to x = -0.01 and $NB_{0.49}T$, respectively. Stoichiometric NBT (x = 0) prepared by hand grinding is more resistive than the one prepared by ball milling. Since the conductivity of NBT is very sensitive to the Na/Bi ratio, samples prepared by hand grinding may have better control of the starting composition. For x = -0.01, Bi is replaced by Na and generates oxygen vacancies. The conductivity increases more than one order of magnitude compared to nominally stoichiometric NBT. The temperature where E_a changes from 0.83 to 0.44~0.5 eV is shifted from ~325 to 316 °C, similar to the behaviour of T_m from the LCR results. For A-site fully occupied nonstoichiometric

NBT, the ionic conductivity increases as the level of oxygen vacancies increases. The oxygen vacancies are generated by the following equation:

$$2Bi_{Bi}^{x} + 3O_{O}^{x} \rightarrow 2V_{Bi}^{'''} + 3V_{O}^{\cdot\cdot} + Bi_2O_3 \qquad 4\text{-}5.$$

For every Bi in Bi-deficient samples, 1.5 oxygen vacancies should be generated. However, Na-rich phases were found as secondary phases indicating the bulk composition contains more Bi than expected, leading to less oxygen vacancies actually being generated. This mechanism also applies for x = -0.02 which has Na-rich phases as secondary phases. The f_{max} extrapolated from bulk M'' Debye peaks for x = -0.01, -0.02 and $NB_{0.48}T$ overlap, as shown in Fig. 4-18 (b), indicating the similarity of these actual compositions, especially their oxygen content. This plot demonstrates the power of using this electrical data analysis of f_{max} which is a geometry independent parameter to assess any intrinsic changes of the bulk component associated with a small change in composition. Therefore, the limit of oxygen vacancies that can be generated by controlling Na/Bi to within $-0.01 \leq x < 0.00$ (~ 1 at%) of the solid solution is ~ 0.33 at% and where $Na_{0.51}Bi_{0.49}TiO_{2.99}$ has highest bulk conductivity.

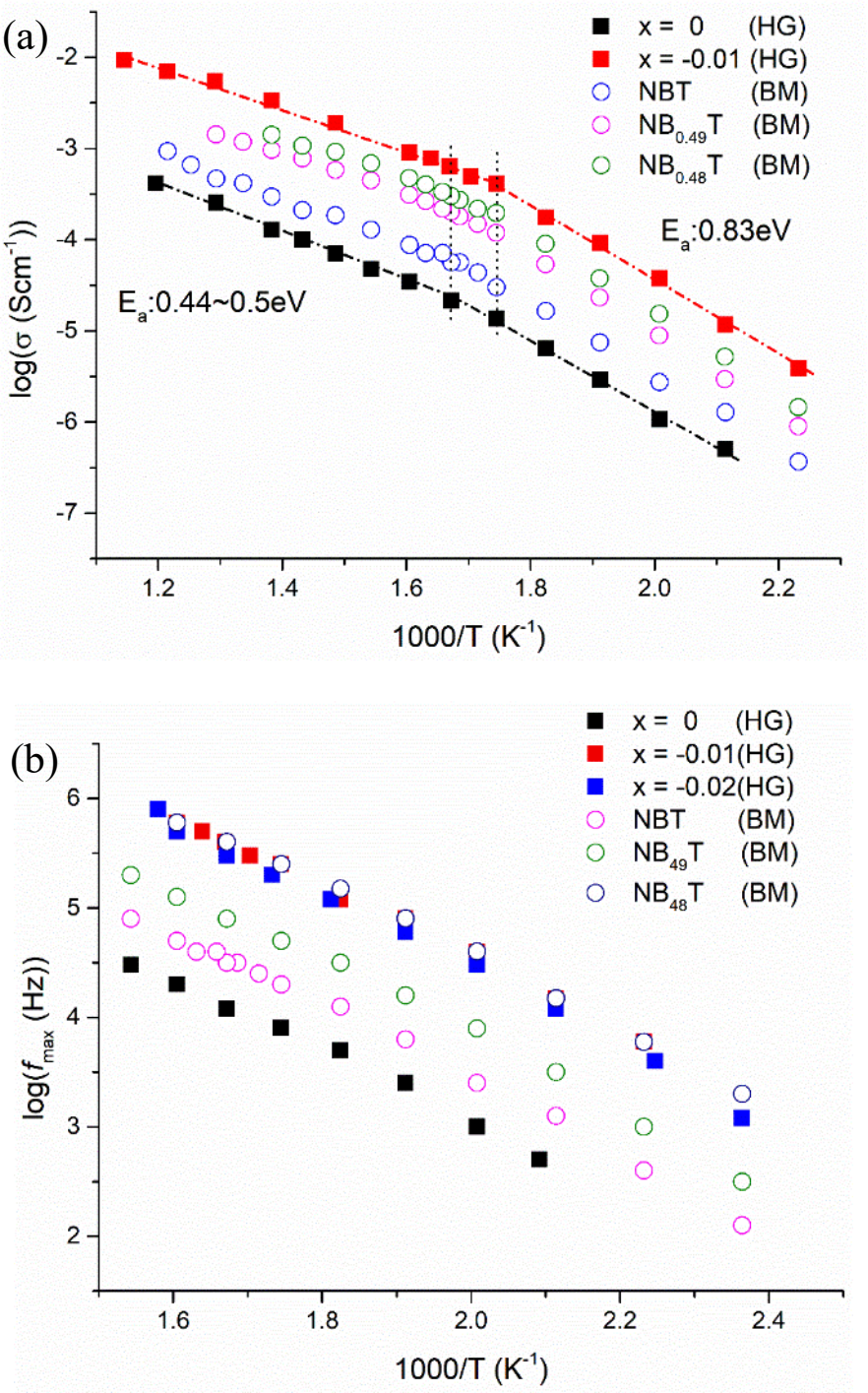

Fig. 4-18. Arrhenius plot of (a) bulk conductivity (b) f_{max} for conducting compositions; A-site stoichiometry $Na_{0.5-x}Bi_{0.5+x}TiO_{3+x}$ prepared by hand grind (HG) and A-site nonstoichiometry prepared by ball mill (BM).

4.4 Conclusions

1. Samples prepared by hand grinding at the mixing stage of raw reagents have better control of the nominal starting composition based on their lower conductivity for stoichiometric NBT.

2. For the $Na_{0.5-x}Bi_{0.5+x}TiO_{3+x}$ series, the solid solution limit is $-0.02 < x < 0.02$ as confirmed by XRD, SEM and LCR results (Fig. 3-12 (b)).

3. Within the solid solution limit, the conductivity of NBT is directly influenced by the Na/Bi ratio and oxygen content, where it switches from an insulator to an ionic conductor for Na/Bi ≥ 1.

4. By increasing the Na/Bi ratio, it is possible to create more oxygen vacancies and therefore enhance the ionic conductivity. However, the limit of oxygen vacancies is very low ~ 0.33 at%. For this simple doping mechanism (equation 3-4), f_{max} can help to indicate the solid solution limit.

5. For dielectric applications, x = 0.01 (1 at% Bi^{3+} doping for Na^{+} ions, leading to a decrease in the Na/Bi ratio) is enough to eliminate oxygen ion conduction.

4.5 Reference

1. Barin, I., *Thermochemical Data of Pure Substances*, 3rd ed., Wiley, Weinheim, Germany, Chap. 12 (2008)

2. Hiruma, Y., Nagata, H. & Takenaka, T., Thermal depoling process and piezoelectric properties of bismuth sodium Titanate ceramics, *J. Appl. Phys.* **105**, 84112 (2009)

3. Li, M., Zhang, H., Cook, S.N., Li, L, Kilner, J.A., Reaney, I.M. & Sinclair, D.C., Dramatic influence of A-site nonstoichiometry on the electrical conductivity and conduction mechanisms in the perovskite oxide $Na_{0.5}Bi_{0.5}TiO_3$, *Chem. Mater.* **27**, 629-634 (2015)

4. Li, M., Pietrowski, M.J., De Souza, R.A., Zhang, H., Reaney, I.M., Cook, S.N., Kilner, J.A. & Sinclair, D.C., A family of oxide ion conductors based on the ferroelectric perovskite $Na_{0.5}Bi_{0.5}TiO_3$, *Nat. Mater.* **13**, 31-35 (2014)

5. Carter, J., Aksel, E, Iamsasri, T., Forrester, J.S. & Jones, J.L. Structure and ferroelectricity if nonstoichiometric $(Na_{0.5}Bi_{0.5})TiO_3$, *Appl. Phys. Lett.* **104**, 112904 (2014)

6. Irvine, J.T.S., Sinclair, D.C., & West, A.R. Electroceramics: characterization by impedance spectroscopy. *Adv. Mater.* **2**, 132-138 (1990)

7. Li, L., Li, M., Zhang, H., Reaney, I.M. & Sinclair, D.C. Controlling Mixed conductivity in $Na_{1/2}Bi_{1/2}TiO_3$ using A-site non-stoichiometry and Nb-donor doping, *J. Mater. Chem. C*, **4**, 5779 (2016)

8. Naderer, M., Kainz, T., Schütz, D. and Reichmann, K. The influence of Ti-nonstoichiometry in $Bi_{0.5}Na_{0.5}TiO_3$, *J Eur Ceram Soc*, **34**, 663-667 (2014)

9. Suchanicz, J., Kluczewska, K., Czaja, P., Handke, B., Sokolowski, M., Wegrzyn, A. and Stachowski, G. Influence of sintering conditions on structural, thermal, electric and ferroelectric properties of $Na_{0.5}Bi_{0.5}TiO_3$ ceramics, *Phase Transitions*, DOI: 10.1080/01411594.2017.1341982 (2017)

Chapter 5

Ga-doped stoichiometric and nonstoichiometric NBT

The previous chapter reported on the solid solution limits and electrical properties of nonstoichiometric NBT with different Na/Bi ratios, where the A-site cations are similar in size. The electrical properties are strongly dependent on the level of oxygen vacancies compensated by chemical doping. For dielectric applications, small amounts of Bi^{3+} doping for Na^{+} can suppress leakage via ionic conduction; however, due to the small solid solution limit, only low levels of oxygen vacancies can be introduced by Na^{+} doping for Bi^{3+}. Yang *et al.*[1] in our group reported a series of A-site divalent dopants for Bi^{3+} using ions from the group IIA family, such as Ca^{2+}, Sr^{2+} and Ba^{2+} on Bi-deficient NBT ($NB_{0.49}T$). The results showed the ionic conductivity of 2at% Sr-doped $NB_{0.49}T$ is competitive with other oxide-ion conductors at low and intermediate temperatures, such as Yttria-Stabilised Zirconia (YSZ) and Gadolinium-Doped Ceria (GDC). The results also indicated that Sr^{2+} is the most effective A-site dopant to enhance ionic conductivity out of the three dopants considered and this was attributed to its optimum ionic size mismatch with Bi^{3+}, its relatively high polarizability and reasonable bonding strength with oxygen ions. A smaller size ion from the same IIA family, Mg^{2+}, was chosen as a B-site divalent dopant for Ti^{4+} on $NB_{0.49}T$ and reported by Li *et al.* to enhance the ionic conductivity for low and intermediate temperature applications.[2] In these two case, the enhanced ionic conductivity was mainly attributed to the oxygen vacancies created from acceptor doping; however, similar to the results presented in chapter 4, the enhancement of ionic conductivity is restricted by the low solid solution of the dopants.

X. He and Y. Mo recently reported a first principle computational study of oxide-ion conductivity in NBT which focused on investigating the oxygen diffusion mechanisms and the influence of local atomic configurations and dopants on oxygen diffusion.[3] They suggested the migration barrier for oxygen vacancies at Bi-Bi-Ti saddle points required the lowest activation energy (0.22 eV) compared to other diffusion pathways, such as Na-Bi-Ti (0.6~0.85 eV) and Na-Na-Ti (1~1.3 eV) saddle points due to the high polarisability of Bi ions, as shown in Fig. 5-1. Therefore, based on their modelling studies, it should also be possible to increase oxygen ionic

conductivity by increasing the Bi content on the A-sites to promote fast oxygen ion diffusion.

Fig. 5-1. Migration barriers for oxygen vacancies along different diffusion pathways, such as (a) Bi-Bi-Ti, (b) Na-Bi-Ti and (c) Na-Na-Ti saddle-points. Figures are adopted from ref 3 (Figure 4).

In this chapter, Na^+/Bi^{3+} and Ga^{3+} are chosen as dopants on the A and B-sites of NBT, respectively, to minimise the ionic size difference between dopants and hosts. Bi^{3+} is considered to have a similar ionic size to Na^+ in XII coordination and the ionic radius of Ga^{3+} (0.62Å) is slightly bigger than Ti^{4+} (0.605Å) in VI coordination. Several series of Ga-doped or Bi and Ga co-doped NBT were prepared:

1. Ga-doped NBT and Ga-doped $NB_{51}T$ ($Na_{0.5}Bi_{0.5}Ti_{1-x}Ga_xO_{3-0.5x}$ and $Na_{0.5}Bi_{0.51}Ti_{1-x}Ga_xO_{3.015-0.5x}$, x = 0.5~10%, denoted as Ga(x)%-NBT and Ga(x)%-$NB_{51}T$, respectively).

The nominally stoichiometric NBT prepared in our laboratory is normally an ionic conductor and it is believed that small amounts of Bi_2O_3 loss during sintering generates oxygen vacancies according to the following equation

$$2Bi_{Bi}^{x} + 3O_O^x \rightarrow 2V_{Bi}^{'''} + 3V_O^{\cdot\cdot} + Bi_2O_3 \qquad 5\text{-}1.$$

In our laboratory, nonstoichiometric $NB_{0.51}T$ is an insulator whereby the starting extra Bi content compensates the Bi_2O_3-loss during sintering. Oxygen vacancies can be

generated in both NBT and $NB_{0.51}T$ by acceptor doping according to the following equation:

$$Ga_2O_3 + 2Ti_{Ti}^{x} + O_O^{x} \rightarrow 2Ga'_{Ti} + V_O^{\cdot\cdot} + 2TiO_2 \qquad 5\text{-}2.$$

2. BG-NBT ($(BiGaO_3)_y(NBT)_{1-y}$, y = 2~8%, denoted as (y)%BG-NBT).

With $BiGaO_3$ (BG) doping on NBT, no additional oxygen vacancies generated according to the following equation

$$Bi_2O_3 + 2Ga_2O_3 + 2Na_{Na}^{x} + 4Ti_{Ti}^{x} \rightarrow 2Bi_{Na}^{\cdot\cdot} + 4Ga'_{Ti} + 4TiO_2 + Na_2O \qquad 4\text{-}3.$$

However, the local atomic configuration is changed with BG doping. Based on the modelling by He and Mo[3], an increase in concentration of Bi (A-site) and Ga (B-site) ions in the lattice may promote oxygen migration and trap oxygen vacancies, respectively.

3. Na/Bi and Ga co-doped NBT ($Na_{0.5-z}Bi_{0.5+z}Ti_{1-x}Ga_xO_{3+z-0.5x}$, x = 1~5%, z = -3 to 3%, denoted as Ga(x)%-$(NB)_{(z)}$T).

This series is followed on from the successful results in chapter 4 and further investigates the influence of the Na/Bi ratio on Ga-doped NBT. The oxygen vacancies generated from Ga acceptor doping may be compensated by partial (donor) replacement of Na^+ by Bi^{3+} (+ z) or be further enhanced by Na^+ acceptor doping for Bi^{3+} ions (-z).

The aim of this chapter is to explore the solid solution limits of Ga-doped NBT with different Na/Bi ratios. Within the solid solution limits, the influence of local atomic configurations, such as an increase in the concentration of high polarisable Bi^{3+} ions on the A-site and acceptor trapping dopants such as Ga^{3+} on the B-site are investigated.

5.1 Ga-NBT and Ga-$NB_{51}T$

Series	Nominal composition	x (%)	Calcining temperature (℃)	Sintering temperature (℃)
Ga-NBT	$Na_{0.5}Bi_{0.5}Ti_{1-x}Ga_xO_{3-0.5x}$	1,3,5,7	1st :800℃ 2h 2nd:900℃8h	1100℃ 2h
Ga-$NB_{51}T$	$Na_{0.5}Bi_{0.51}Ti_{1-x}Ga_xO_{3.015-0.5x}$	0.5,1,3,5,7,10	1st :800℃ 2h 2nd:800℃ 2h	
		3, 5, 7	Anneal at 900℃ 8h	

Table 5-1. Calcining and sintering temperatures of Ga-NBT and Ga-$NB_{51}T$ series.

Ga-NBT series (x = 1, 3, 5 and 7%) were prepared by hand grinding. Samples were calcined twice at 800 ℃ for 2h followed by 900 ℃ for 8h. The sintering temperature was at 1100℃ for 2h. The Ga-$NB_{51}T$ series (x = 0.5, 1, 3, 5, 7 and 10%) was prepared by ball milling. Samples were calcined twice at 800 ℃ for 2h. Additional samples for x = 3, 5 and 7% were annealed at 900 ℃ for 8h using the calcined powder before sintering. All samples were pressed into pellets and sintered at 1100 ℃ for 2h.

5.1.1 Phase purity and microstructure

For the Ga-NBT series, all samples were single-phase by XRD after calcination at 900℃ for 8h and no extra peaks were detected on XRD patterns for polished ceramic surfaces after sintering at 1100 ℃ for 2h within instrument error limit(s), as shown in Fig. 5-2 (a) and (b), respectively. For the Ga-$NB_{51}T$ series, extra peaks were observed ~31 and 34.5 2θº for x = 7% after a second calcination at 800 ℃ for 2h, which is possibly $Na_2Ga_{3.4}O_{6.1}$ (ICDD: 00-052-0398) as shown in Fig.5-3 (a). Additional peaks were also observed between 26~28 2θº for x = 7% after sintering ceramics at 1100 ℃ for 2h, which is possibly a Bi-rich phase (e.g. $Bi_{25}GaO_{40}$, ICDD: 00-046-0414) as shown in Fig. 5-3 (b). Based on these XRD results, the Ga-NBT series which were calcined at higher temperature for longer periods (i.e. 900℃ for 8h) can form single-phase samples up to x = 7%. The Ga-$NB_{51}T$ series samples which were calcined at lower temperature for shorter periods were only single-phase up to 5%. Therefore, the

calcined powder of x = 3, 5 and 7% were further annealed at 900 ℃ for 8h followed by sintering at 1100 ℃ for 2h. The phase purity of x = 7% significant improved after annealing at higher temperature, as shown in Fig. 5-4.

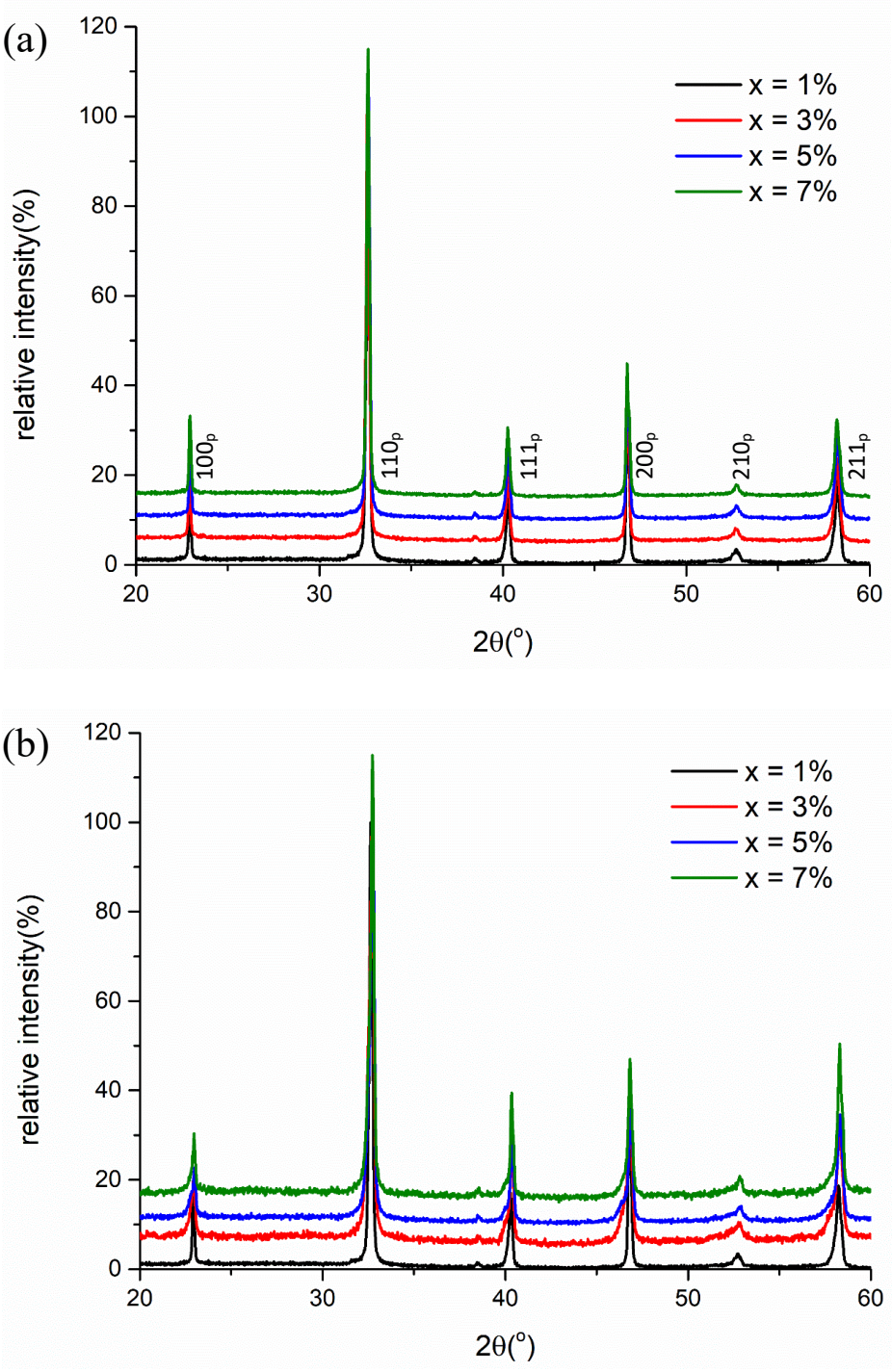

Fig. 5-2. Room temperature XRD patterns for the Ga-NBT series, (a) after 2nd calcination of powder at 900 ℃ for 8h, (b) polished ceramic surfaces after sintering at 1100 ℃ for 2h.

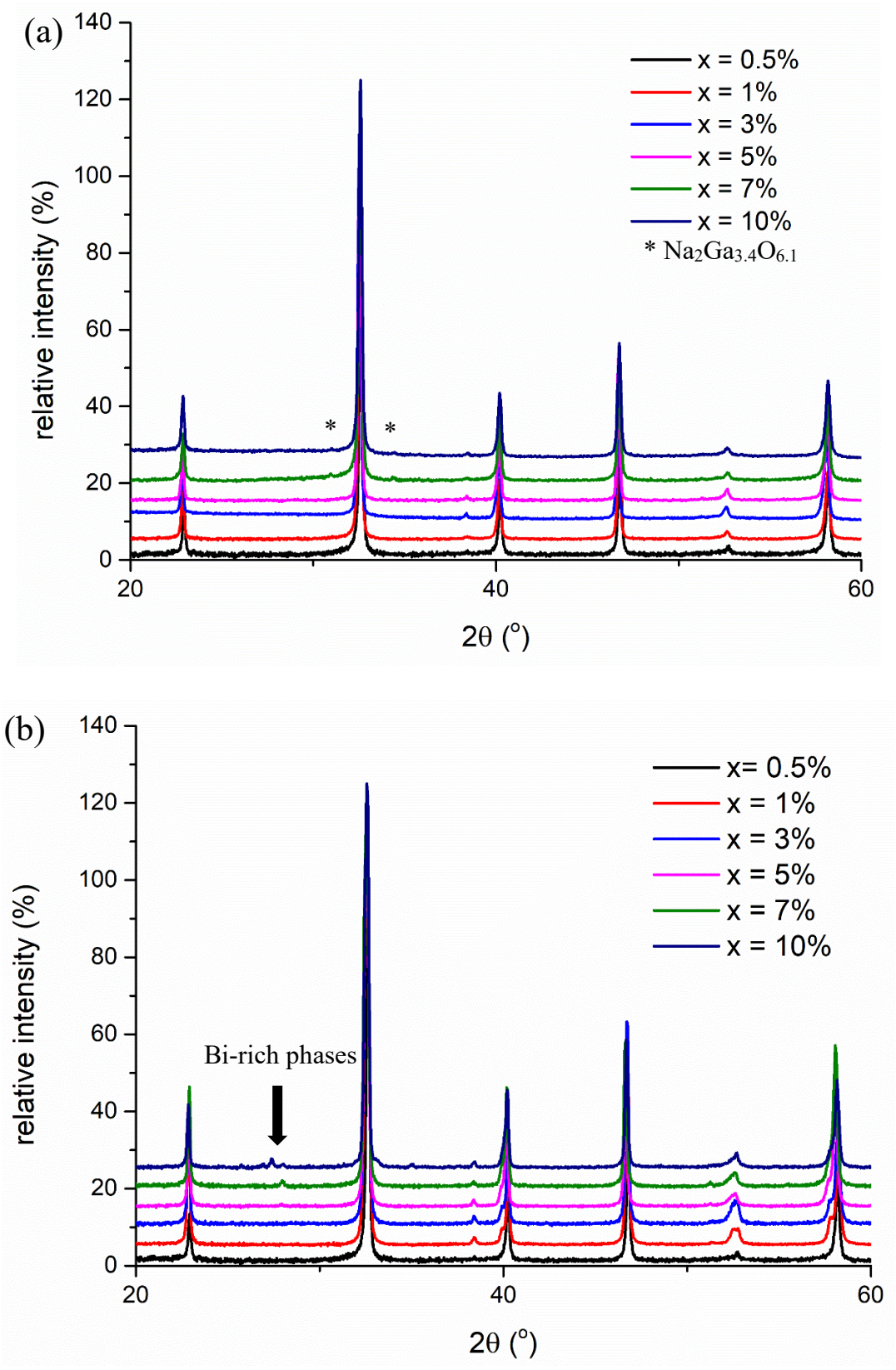

Fig. 5-3. Room temperature XRD patterns for the Ga-$NB_{51}T$ series, (a) after 2nd calcination of powder at 800 ℃ for 2h, (b) crushed pellets after sintering at 1100 ℃ for 2h.

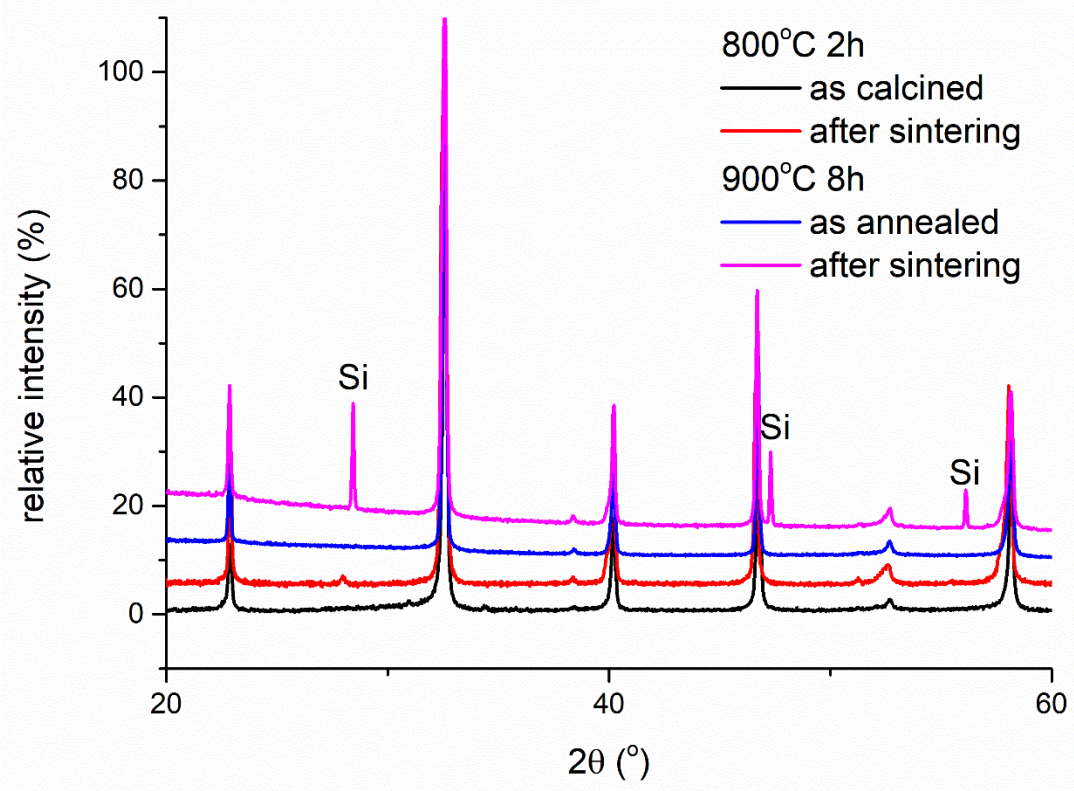

Fig. 5-4. XRD patterns of Ga7%-$NB_{51}T$ calcined powders and crushed pellets with different calcining profiles. Extra peaks observed from the sample annealed at 900 ℃ for 8h followed by sintering at 1100 ℃ for 2h are associated with the Si internal standard.

The pseudo-cubic cell volumes for Ga-NBT and Ga-$NB_{51}T$ series (including samples annealed at 900 ℃ for 8h) are shown in Fig. 5-5. The cell volume expands as x increases, indicating slightly bigger Ga^{3+} atoms are replacing smaller Ti^{4+} atoms, and becomes constant at ~ 58.44 and 58.41 $Å^3$ when x = 3 and 5% for Ga-NBT and Ga-$NB_{51}T$ series, respectively. With additional annealing, the cell volume increases but still saturates at x ~ 5%. Based on XRD results, therefore, the solid solution limits are ~ 3 and 5 % for the Ga-NBT and Ga-$NB_{51}T$ series, respectively. An addition of a small amount of Bi_2O_3 results in a modest expansion of the solid solution limit.

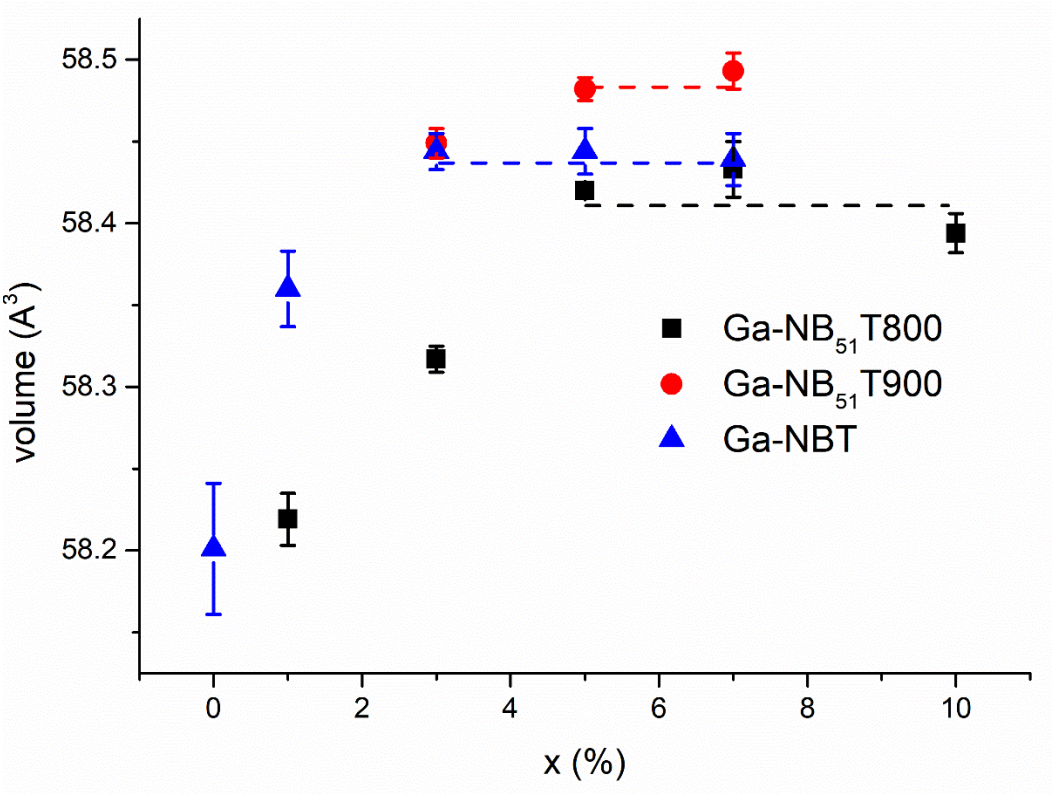

Fig. 5-5. Pseudo-cubic cell volumes for the Ga-NBT and Ga-NB_{51}T series (Ga-NB_{51}T800 and Ga-NB_{51}T900 represent samples calcined at 800 ℃ for 2h twice and 900 ℃ for 8h, respectively).

Further phase analysis was performed on polished sintered ceramics for selected samples using SEM/EDS in order to confirm the phase purity, such as (a) x = 5% without annealing, (b) x = 5% and (c) x = 7% annealed at 900 ℃ for 8h, respectively, as shown in Fig. 5-6. Small amounts of secondary phases were observed on all surfaces, indicating these compositions are beyond the solid solution limit. The chemical compositions of bulk and secondary phases were analysed by EDS and the bulk compositions are summarised in Table 5-2. All samples have consistent Bi content ~26.3 at% and slightly lower Na and Ga content than expected. The experimental composition of (a) is relatively close to the theoretical composition when considering the standard deviation of the errors. The average Ga content and Na/Bi ratio, however, tend to slightly decrease with further annealing at 900 ℃ for 8h. Some Bi-rich phases (> 80 at%) were found near the grain boundaries as shown in Fig. 5-6 (a), and other secondary phases with small particle size were poorly characterised due to their smaller surface area compared to the spot size of the EDS electron beam, as shown in Fig. 5-6

(b) and (c). Although XRD results for x = 7% show an improvement of phase purity with additional annealing, the experimental composition of (c) is close to x = 4% and small amounts of secondary phases were identified, indicating that it has passed the solid solution limit. In summary, the solid solution limit of Ga-$NB_{51}T$ series is likely < 5% based on a combination of XRD and EDS results.

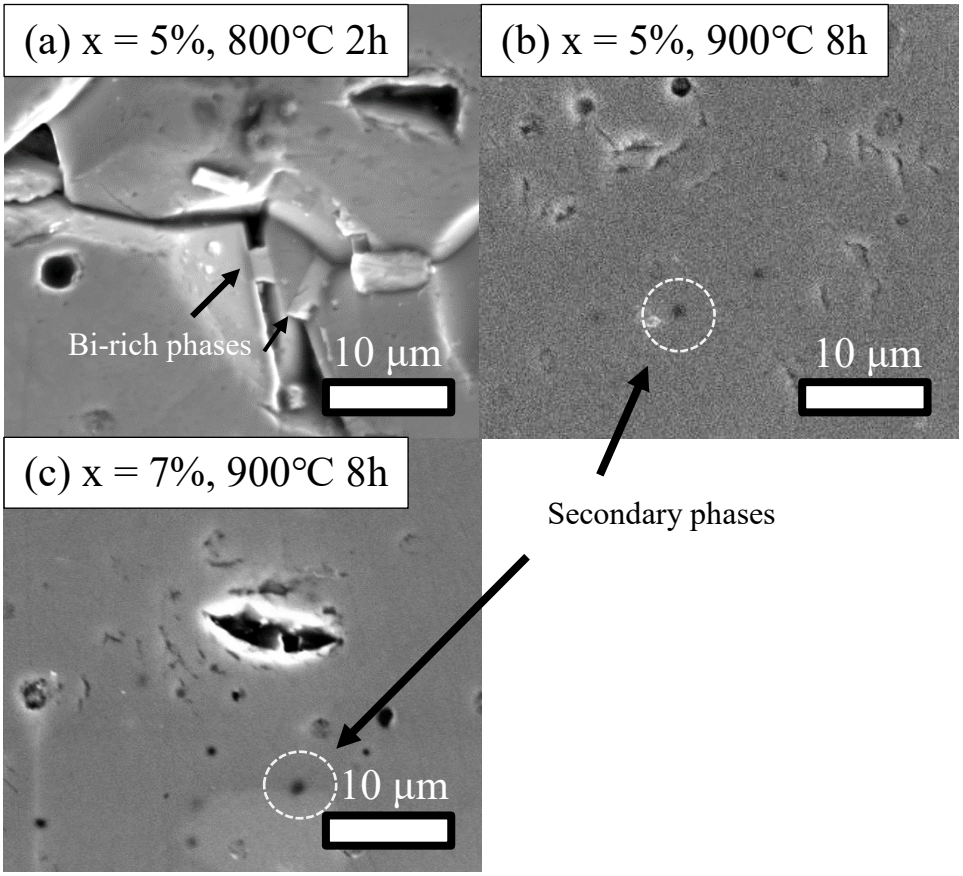

Fig. 5-6. SEM images of polished pellet surfaces for the Ga-$NB_{51}T$ series (a) x = 5% calcined twice at 800 ℃ for 2h, (b) x = 5% and (c) x = 7% further annealed at 900 ℃ for 8h prior to sintering.

Sample	Na (at%)	Bi (at%)	Ti (at%)	Ga (at%)
(a)	24.6 (±1.6)	26.3 (±0.4)	47.3 (±0.9)	1.8 (±0.6)
(b)	23.7 (±0.9)	26.1 (±0.4)	48.9 (±0.7)	1.3 (±0.5)
Theoretical	24.9	25.4	47.3	2.5
(c)	23.7 (±0.6)	26.3 (±0.3)	48.1 (±0.4)	1.9 (±0.5)
Theoretical	24.9	25.4	46.3	3.5

Table 5-2. EDS average chemical composition results (standard deviation) for the Ga-$NB_{51}T$ series for the main phases of (a) x = 5% without annealing (b) x= 5% and (c) x = 7% annealed at 900 ℃ for 8h prior to sintering.

5.1.2 Electrical properties

The Z* plots for the Ga-NBT (compared with $NB_{49}T$) and Ga-$NB_{51}T$ series measured at 400 and 500 ℃, respectively, are shown in Fig. 5-7. The bulk resistances of $1\% \leq x \leq 5\%$ are almost the same for the Ga-NBT series and therefore the bulk conductivity (the inverse of bulk resistance) is independent of the oxygen vacancies introduced by Ga^{3+} replacing Ti^{4+}. However, there is a significant change in grain boundary resistance. Compared to $NB_{49}T$, the bulk resistance of x = 1% is reduced by half but its grain boundary resistance has more significant reduction. Further reduction in grain boundary resistance is observed for x = 3% and stabilised up to 5%. Both bulk and grain boundary resistances increase when x increases to 7%.

For the Ga-$NB_{51}T$ series, the bulk resistance changes dramatically with x, especially between x = 0.5 and 1%. It decreases almost three orders of magnitude for x = 1% at 500 ℃. Both bulk and grain boundary resistances decreases as x increases up to x = 3% and then it begins to drop as x increases, i.e. $x \geq 5\%$. The isothermal plots of bulk conductivity and f_{max} for the Ga-NBT and Ga-$NB_{51}T$ series are shown in Fig. 5-8. The bulk conductivity of the Ga-$NB_{51}T$ series is more resistive than the Ga-NBT series, even though the Ga-$NB_{51}T$ series has a higher solid solution limit based on XRD. Overall, Ga-doping on the Ti-site can significantly reduce not only the bulk but also the grain boundary resistance, leading to a reduction in total resistance ($R_b + R_{gb}$). In the case of Ga5%-NBT, the total resistance is almost the same as the bulk resistance of $NB_{49}T$ at 400 ℃. The starting Na/Bi ratio has a strong influence on the bulk

conductivity and the reduction in bulk conductivity for the Ga-$NB_{51}T$ series is possibly due to an addition of Bi, leading to a reduced amount of oxygen vacancies.

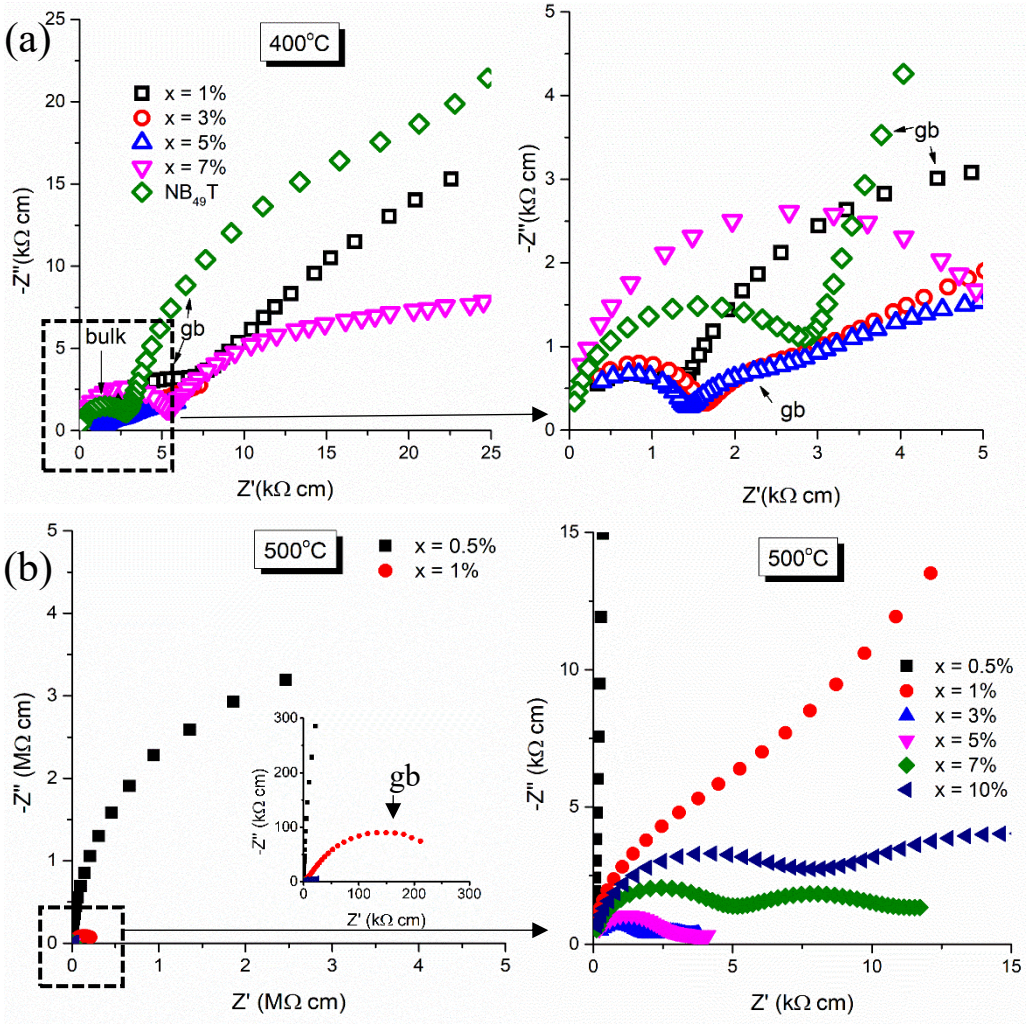

Fig. 5-7. Z* plots for the (a) Ga-NBT and (b) Ga-$NB_{51}T$ series measured at 400 and 500 °C, respectively. Figures on the right hand side are expanded views of the dashed squared area in (a).

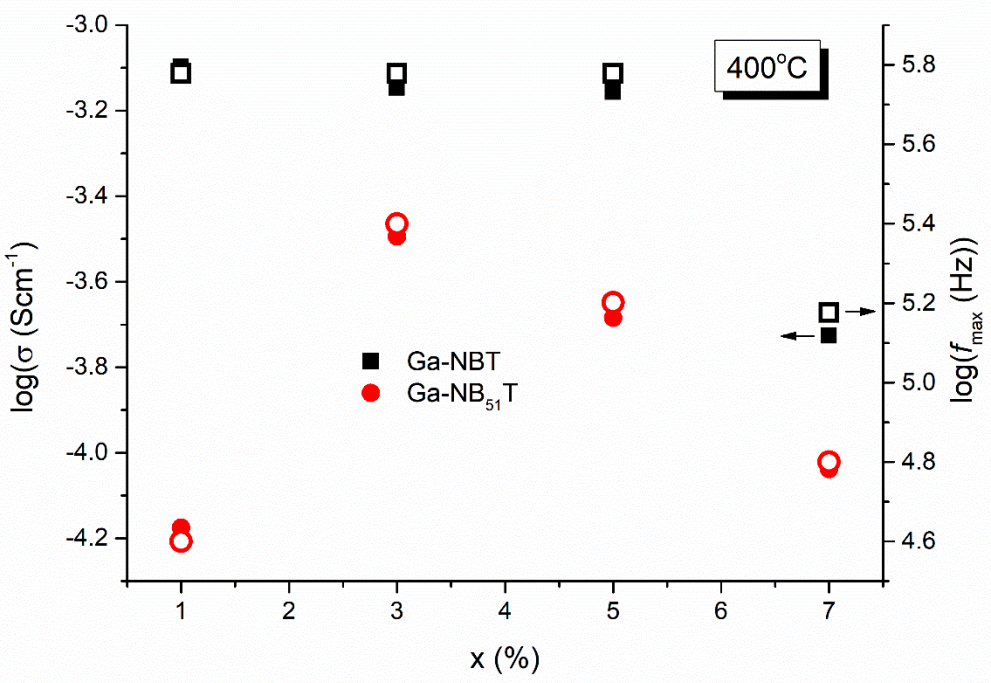

Fig. 5-8. The isothermal plots of bulk conductivity and f_{max} vs. Ga content (x) for the Ga-NBT and Ga-NB_{51}T series at 400 °C. The solid and open symbols represent bulk conductivity and f_{max}, respectively.

Arrhenius plots of bulk conductivity for Ga-NBT and Ga-NB_{51}T are shown in Fig. 5-9 (a) and (b), respectively. The bulk conductivity is significantly improved by Ga-doping up to x = 1 and 3% for the Ga-NBT and Ga-NB_{51}T series, respectively. The activation energy (E_a) changes from 0.71 ~ 0.91 to 0.36 ~ 0.63 eV at 300 ~ 325 °C where the maximum permittivity occurs. The more conductive samples tend to have lower E_a below 300 °C and E_a increases as the nominal Ga content increases above 325 °C, especially when the bulk conductivity begins to drop, suggesting trapping may occur in the more heavily doped samples. The trend of bulk f_{max} for the Ga-NBT and Ga-NB_{51}T series observed in Arrhenius-type plots behaves similar to its conductivity, except no change in E_a at 300 ~ 325 °C, as shown in Fig. 5-10 (a) and (b), respectively.

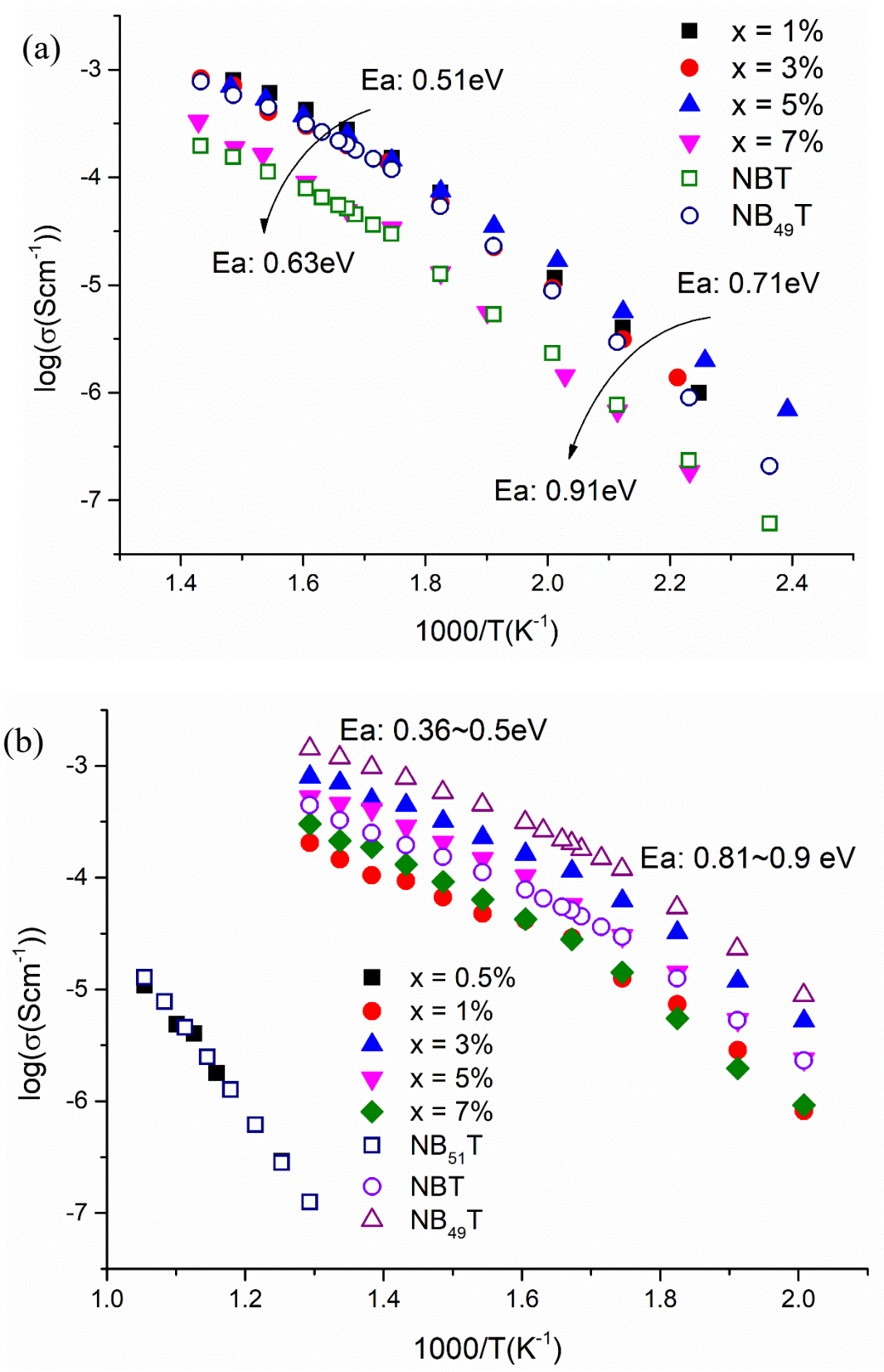

Fig. 5-9. Arrhenius plot of bulk conductivity for the (a) Ga-NBT series, x = 1~7%, and (b) Ga-$NB_{51}T$ series, x = 0.5~7%. Data are compared (as reference) with the conductivity of NBT and $NB_{49}T$ prepared by BM.

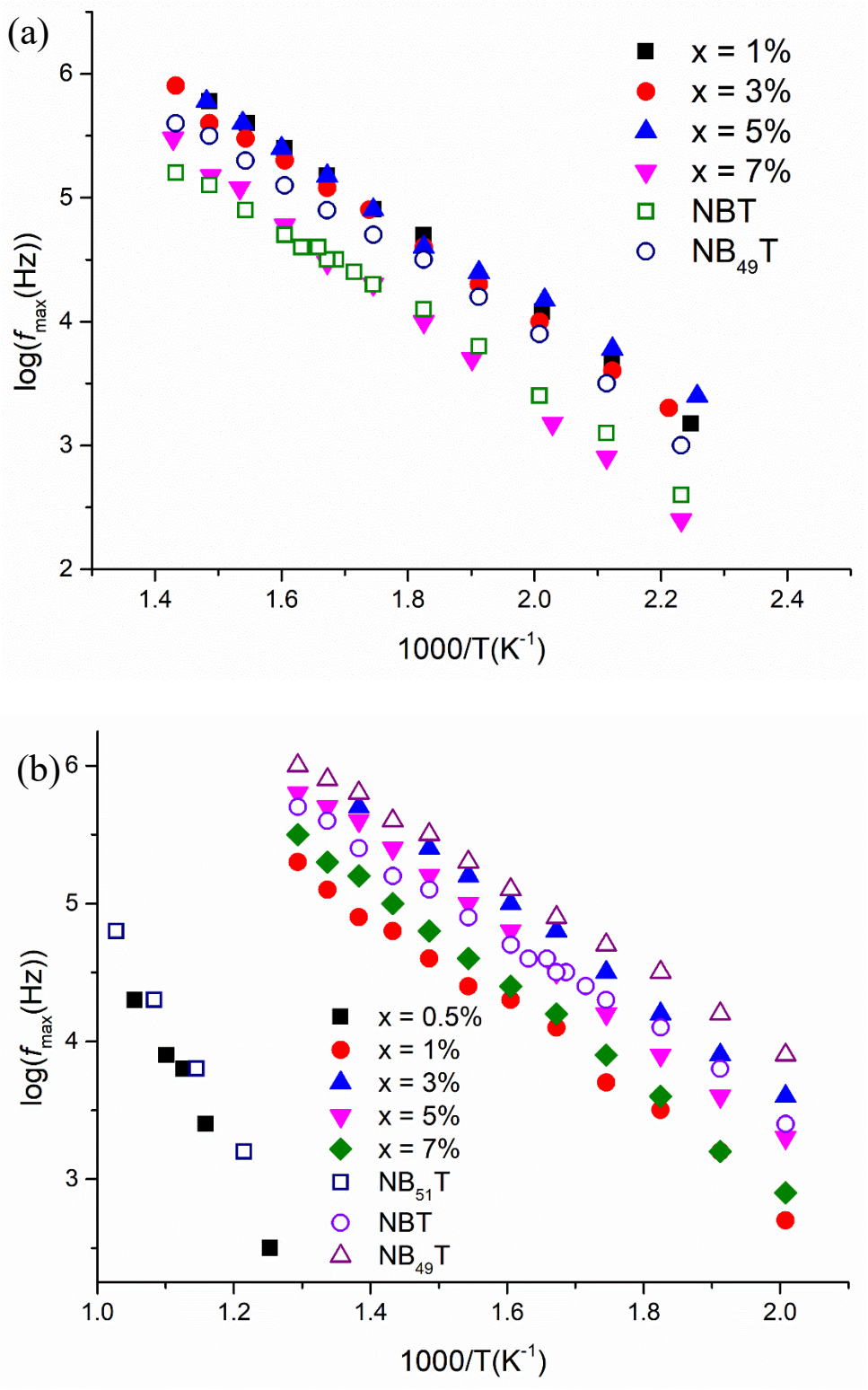

Fig. 5-10. Arrhenius plots of bulk f_{max} for the (a) Ga-NBT and (b) Ga-$NB_{51}T$ series. The bulk f_{max} of $NB_{51}T$, NBT and $NB_{49}T$ prepared by BM are represented for reference.

5.2 BG-NBT

BG-NBT series ($(BiGaO_3)_y(NBT)_{1-y}$, y = 2, 4, 6 and 8%) were prepared by hand grinding. Additional samples for y = 6 and 8% were prepared by ball milling. All samples were calcined at 800 ℃ for 2h followed by 900 ℃ for 8h and the sintering temperature was at 1150 ℃ for 2h.

5.2.1 Phase purity and microstructure

XRD patterns for the BG-NBT series obtained from calcined powders and crushed pellets are shown in Fig. 5-11. $Bi_2Ga_4O_9$ (ICDD: 04-009-0920) was identified as the major secondary phase for x ≥ 6% as shown in Fig. 5-11 (a). All patterns were single-phase after sintering based on XRD. The pseudo-cubic cell volume increases as y increases up to y = 6% and remains the same for x = 8%, indicating that the slightly bigger Ga^{3+} atoms replace smaller Ti^{4+} atoms and the solid solution limit is ~ 6%, as shown in Fig. 5-12. However, the bulk conductivity of y = 6 and 8% had abnormal behaviour at ~650℃ which will be discussed later. These samples were therefore also prepared by ball milling using the same calcining and sintering conditions. XRD results of these ball milled samples obtained from sintered pellets suggested they were also single-phase, as shown in Fig. 5-13.

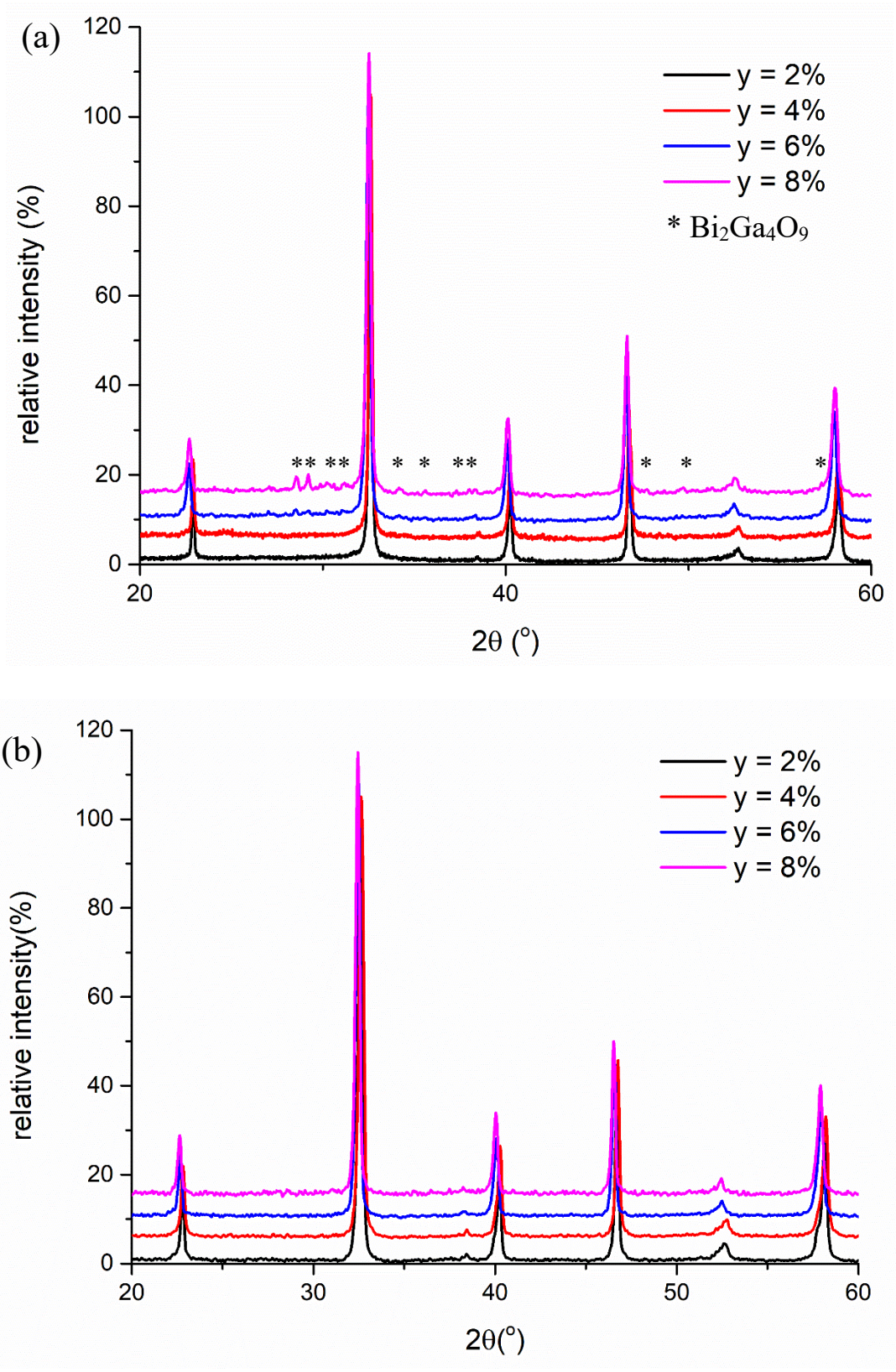

Fig. 5-11. XRD patterns for the BG-NBT series prepared by hand grinding obtained from (a) calcined powders and (b) crushed pellets.

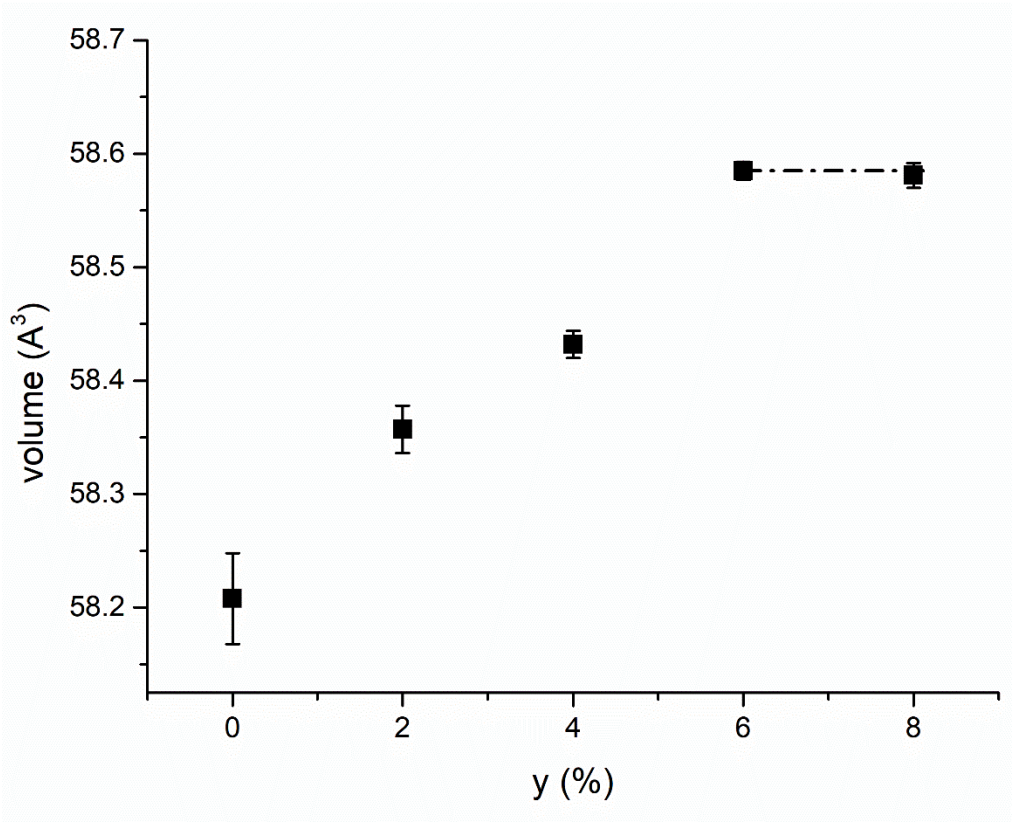

Fig. 5-12. The pseudo-cubic cell volumes of the BG-NBT series prepared by hand grinding.

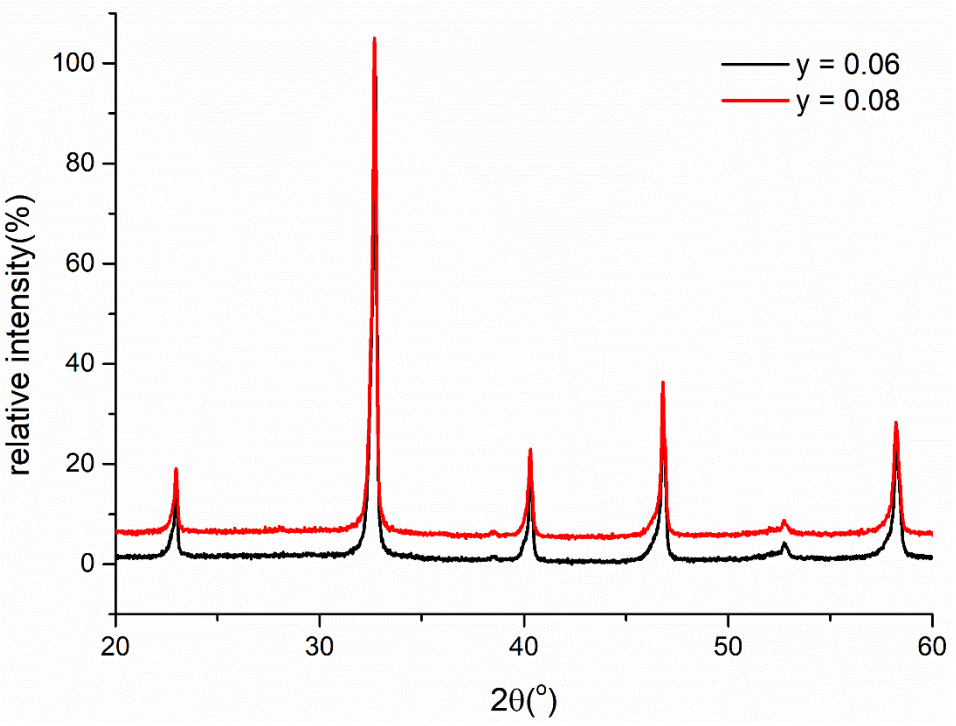

Fig. 5-13. XRD patterns for the BG-NBT series prepared by ball milling obtained from sintered pellets.

Further phase purity and microstructure was analysed by SEM/EDS for y = 2/4 % and 6/8% prepared by hand grinding and ball milling, respectively, as shown in Fig. 5-14. The average grain size tends to decrease from ~ 5 to 3 μm as y increases from 2 to 6%, as shown in Fig. 5-14 (a) to (c). Samples were phase-pure to y = 4% which is consistent with the XRD results. Small amounts of secondary phases were observed from the surface of a polished pellet for y = 6% and this substantially increased for y = 8%, as shown in Fig. 5-14 (e) and (f). The bulk compositions analysed by EDS are summarised in Fig. 5-15. For y ≤ 6%, the average Na, Bi and Ga contents changed consistently with the starting composition. It is noteworthy that the Na and Ti contents are much higher and lower than expected for y = 2%, respectively, which is possibly because the analysed Na (K_α = 1.041 keV) and Ga (L_α = 1.098 keV) peaks in the spectrum are overlapping, results in higher Na content and therefore an unbalanced A-site/Bi-site ratio. The bulk composition of y = 8% is similar to y = 6% which suggests the solid solution limit is ~ 6% in the BG-NBT series. The composition(s) of the secondary phases were not easily or accurately identified due to their smaller surface area compared to the spot size of the EDS electron beam. However, the brightness of secondary phases under backscattering imaging suggests the composition may contain a significantly higher ratio of heavy atoms such as Bi. Based on XRD/SEM/EDS results, the solid solution limit of BG-NBT series is close to y = 6%.

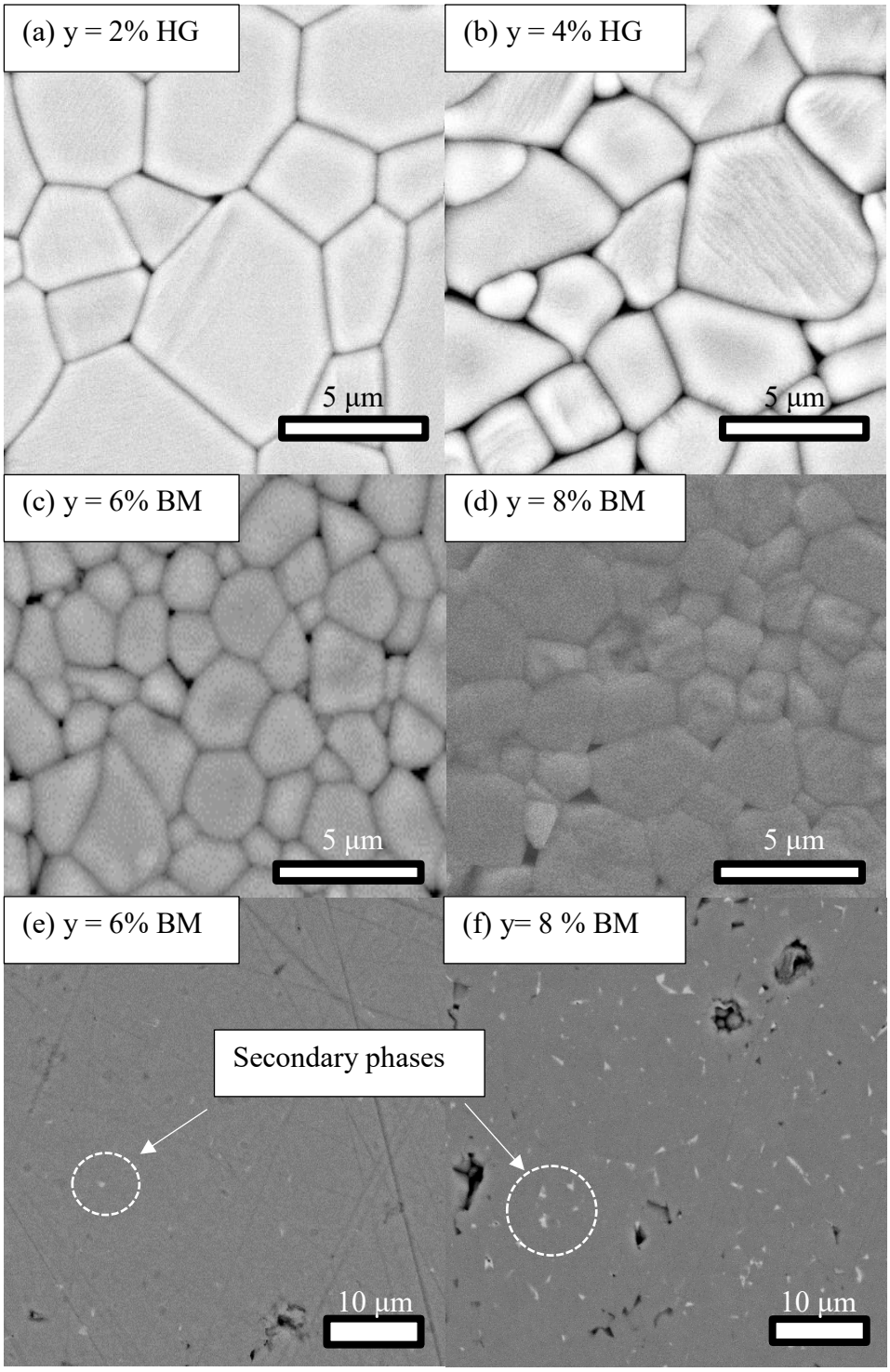

Fig. 5-14. SEM backscattering images of (a) y = 2% and (b) y = 4% prepared by hand grinding (HG) on thermally etched surfaces; (c) y = 6% and (d) y = 8% prepared by ball milling (BM) on thermally etched surface; (c) y = 6% and (d) y = 8% prepared by BM on polished pellet surfaces.

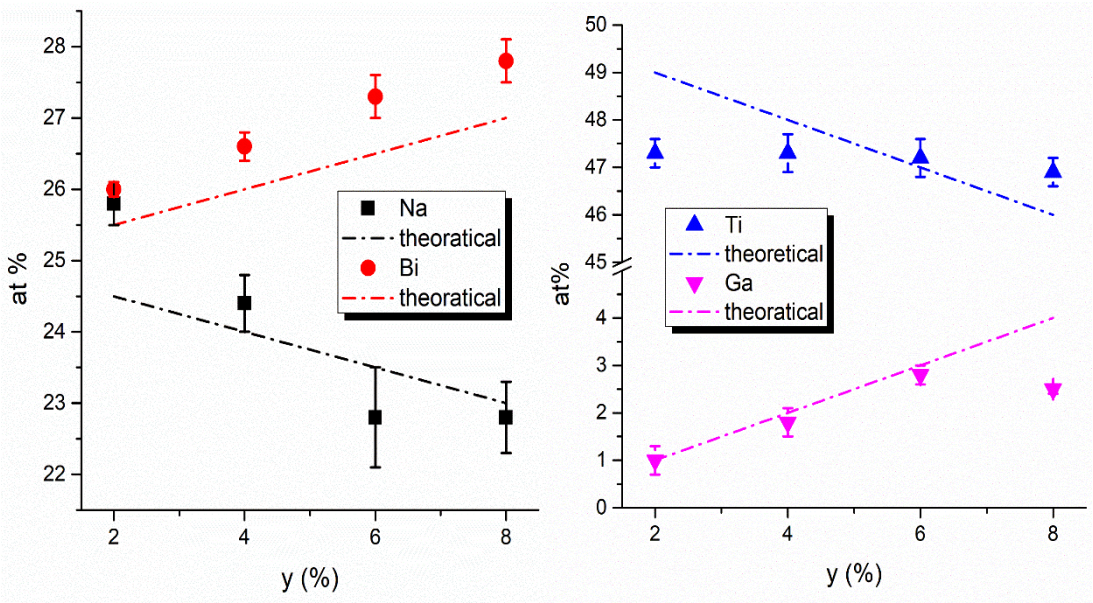

Fig. 5-15. EDS average chemical composition results of the main phases for y = 2% and y = 4% prepared by hand grinding; y = 6 and 8% prepared by ball milling. Data have been normalised using the standard error as discussed in chapter 4.

5.2.2 Electrical properties

Z* plots for the BG-NBT series prepared by hand grinding measured at 550 ℃ are shown in Fig. 5-16. The bulk resistance increases more than two orders of magnitude as y increases up to 6%, and then decreases when y = 8%. Arrhenius plots of bulk conductivity and f_{max} are shown in Fig. 5-17. Samples switch from (NBT-like) conducting phases into ($NB_{51}T$-like) insulating phases when y = 6%. For conducting phases, e.g. y = 2 and 4%, E_a above 325 ℃ is between 0.58~0.61 eV and behaves similar to NBT. For insulating phases, e.g. y = 6 and 8%, E_a increases from 1.68 to 2.46 eV compared to $NB_{51}T$ and has an abnormal change at ~650 ℃. Additional samples were prepared by ball milling for these two compositions and the comparison of bulk conductivity in Arrhenius plots is shown in Fig. 5-18. The bulk conductivity becomes very similar and systematically changing with temperature up to 750 ℃, with increasing E_a from ~ 1.5 to 1.7 eV as y increases.

Fig. 5-19 (a) shows Debye peaks of Z'' and M'' for y = 8% prepared by hand grinding and ball milling at 650℃. The insert shows the respective Z* plots and indicates the sample prepared by hand grinding has a distorted semi-circle with possibly

a second element and f_{max} for the Z'' and M'' Debye peaks do not overlap for this sample. Therefore, there is at least an extrinsic component which has higher resistance dominating the bulk response. Instead, the Z'' and M'' Debye peaks of the sample prepared by ball milling overlap (equal peak frequency) indicating the bulk component is more homogeneous than the one prepared by hand grinding.

The Arrhenius plots of bulk f_{max} extracted from M'' and Z'' peaks for y = 8% prepared by hand grinding and ball milling are shown in Fig. 5-19 (b). Three regions are divided according to the trends of f_{max}; (i) Region 1: all trends are aligned, indicating a similar composition and conducting mechanism which is insulating NBT. (ii)Region 2: an abnormal trend for f_{max} extracted from M'' peaks prepared by hand grinding but similar trends for f_{max} extracted from Z'' and M'' peaks prepared by hand grinding and ball milling, respectively, indicating an extrinsic conducting mechanism involved possibly due to secondary phases in the sample prepared by hand grinding. (iii) Region 3: The f_{max} extracted from M'' and Z'' prepared by hand grinding become similar, indicating an extrinsic conduction mechanism dominating possibly due to secondary phases. Although XRD shows only a single-phase for y = 8% prepared by hand grinding and ball milling, electrical measurements by IS are able to observe an extrinsic component possibly due to Bi-rich secondary phases which can only be detected by SEM.

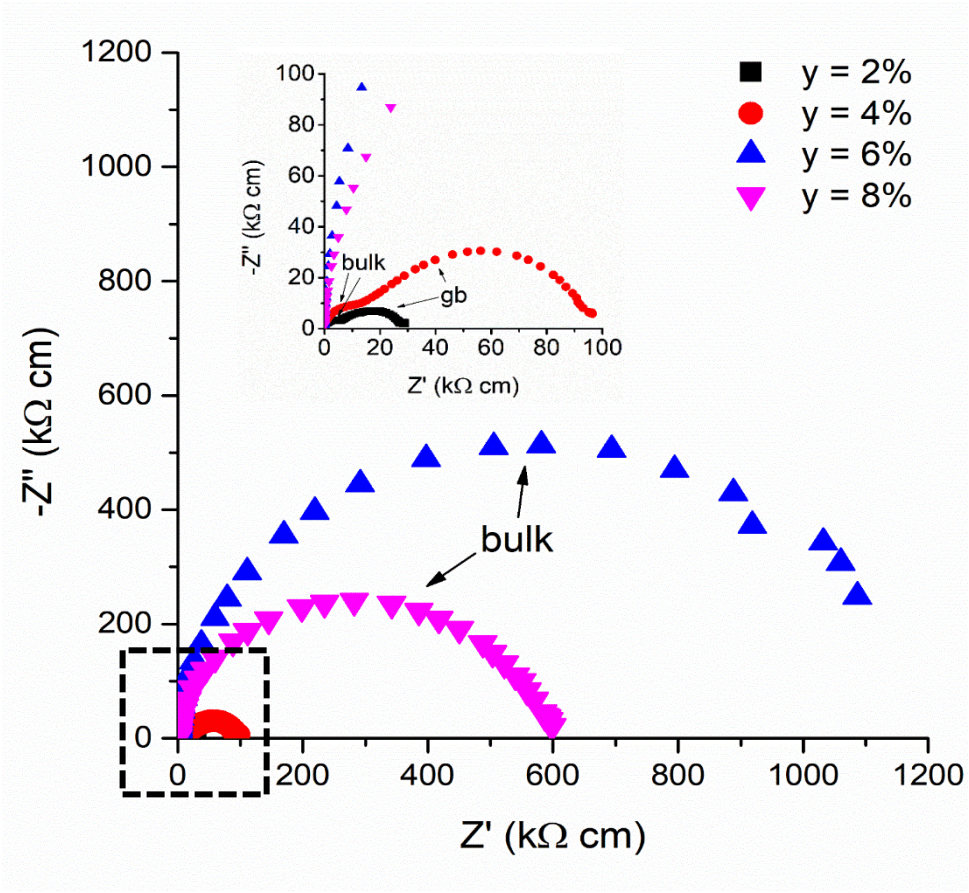

Fig. 5-16. Z* plots for the BG-NBT series measured at 550 °C. Inset shows expanded view of dashed squared area.

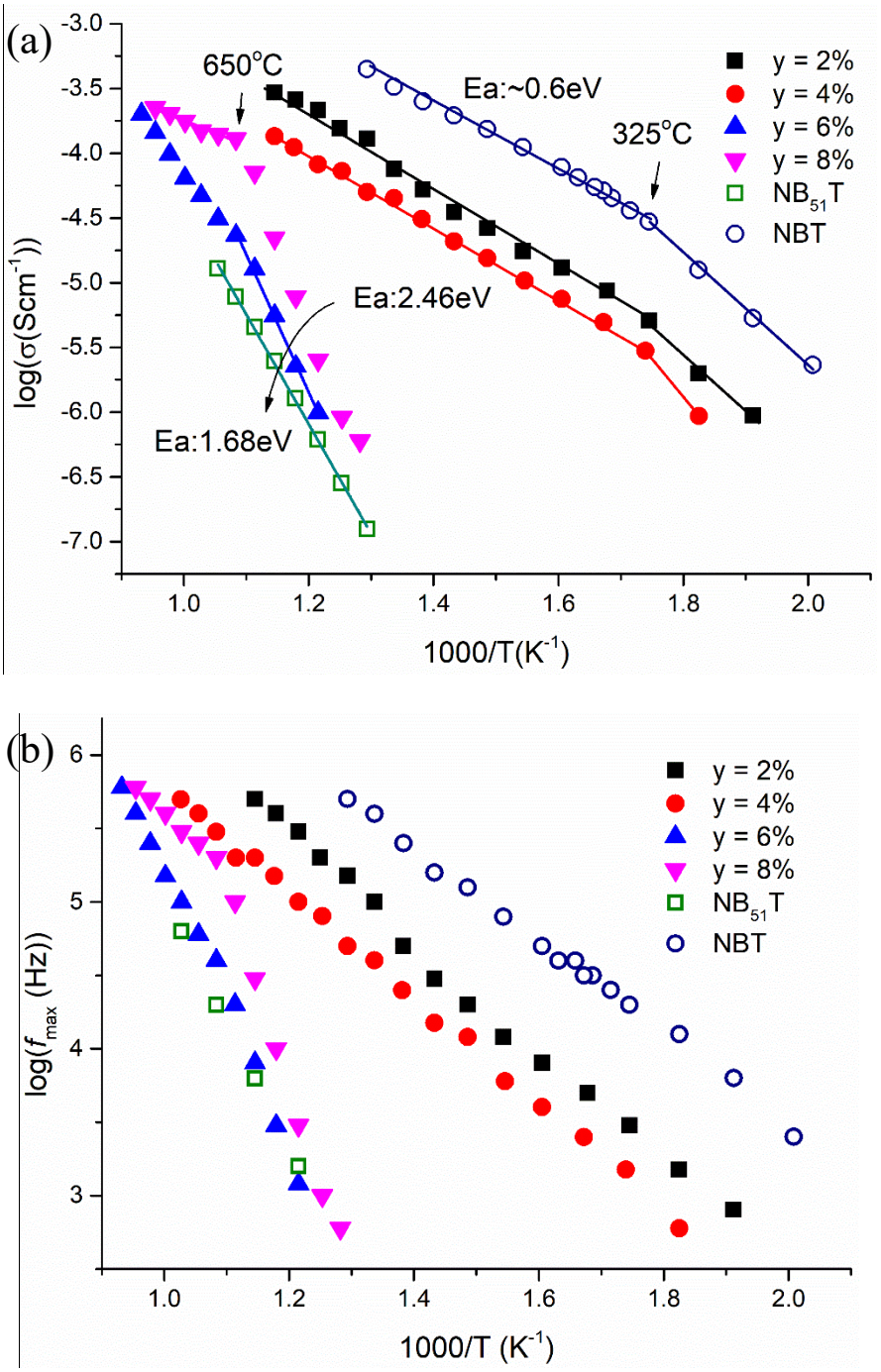

Fig. 5-17. Arrhenius plots of (a) bulk conductivity and (b) f_{max} for the BG-NBT series prepared by hand grinding.

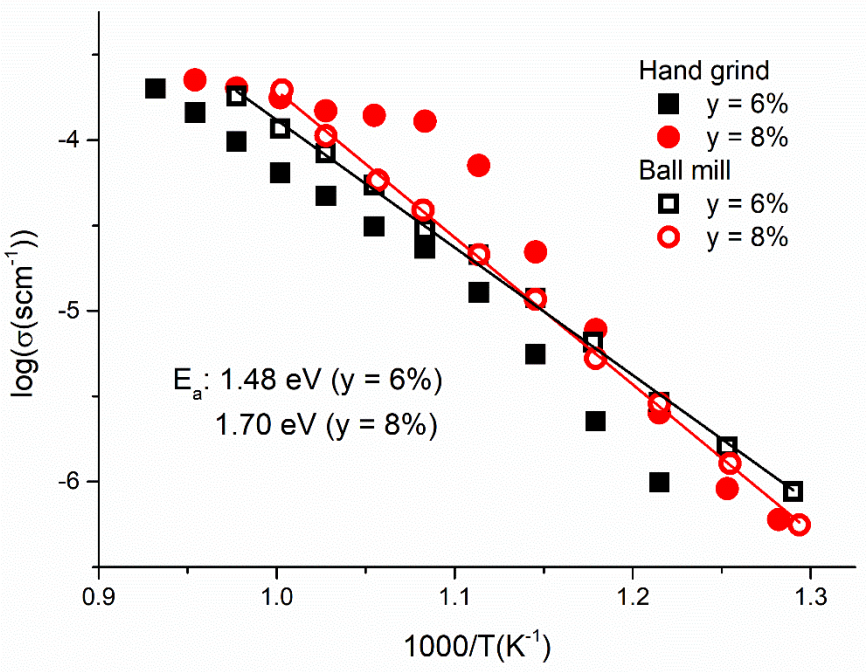

Fig. 5-18. Comparison of samples prepared by hand grinding and ball milling for x = 6 and 8% in Arrhenius plots of bulk conductivity.

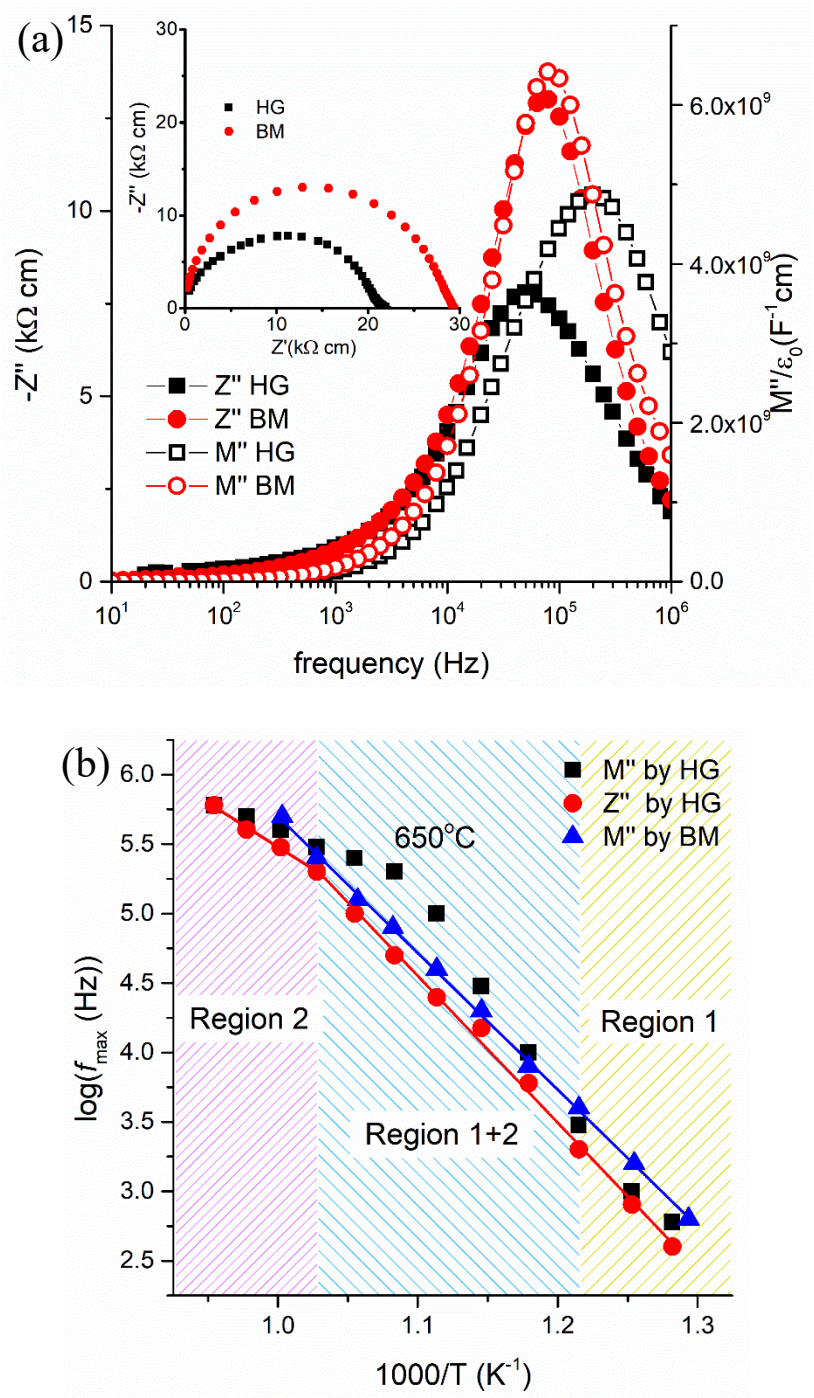

Fig. 5-19. (a) Combined Z'' and M'' spectroscopic plots at 650 °C (inset shows Z* plots) and (b) Arrhenius plots of bulk f_{max} extracted from M'' and Z'' for y = 8% prepared by hand grinding (HG) and ball milling (BM).

5.3 Na/Bi and Ga co-doped NBT

In this series ($Na_{0.5-z}Bi_{0.5+z}Ti_{1-x}Ga_xO_{3+z-0.5x}$), the Ga concentration (x) was fixed at 3 and 5% and the Na/Bi ratio (and therefore oxygen content) was controlled by z (-3% ≤ z ≤ 3%). All samples were calcined at 800 ℃ for 2h followed by 850~900 ℃ for 8h. The sintering temperature was fixed at 1100 ℃ for 2h, except for the insulating phases, such as $Na_{0.48}Bi_{0.52}Ti_{0.97}Ga_{0.03}O_{3.005}$ and $Na_{0.47}Bi_{0.53}Ti_{0.95}Ga_{0.05}O_{3.005}$, which were sintered at 1150 ℃ for 2h. The Ga1%-$(NB)_{\pm 0.02}$T series prepared by Fan Yang (PDRA in our group) using the same procedure is also discussed in this section.

5.3.1 Phase purity and microstructure

XRD patterns obtained from calcined powders for the Ga (x) = 3 and 5% series are shown in Fig. 5-20. Secondary phases were only observed when Na/Bi < 1 and identified as $Na_{0.5}Bi_{4.5}Ti_4O_{15}$ (NBiT, ICDD: 04-017-3364) for the peak at ~ 30.4 2θ°. Additional peaks observed between 28.5 ~ 29.5 2θ° for Ga = 5%/z = 3% (Fig. 5-20(b)) were identified as $Bi_2Ga_4O_9$ (ICDD: 04-009-0920). All samples were single-phase after sintering above 1100 ℃ for 2h based on XRD, as shown in Fig. 5-21. The adjustable Na/Bi ratio is expanded by Ga^{3+} doping of Ti^{4+}.

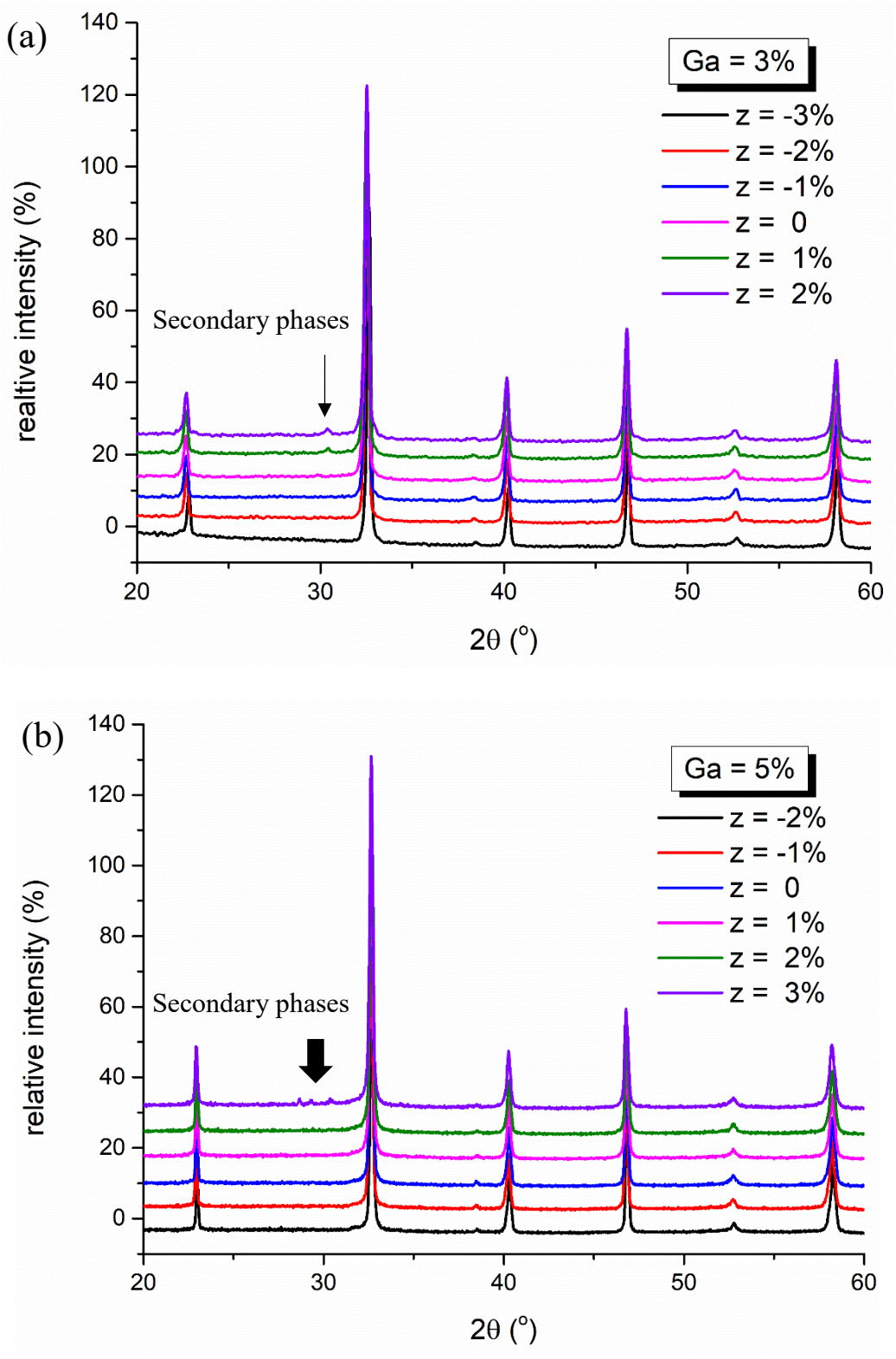

Fig. 5-20. XRD patterns of $Na_{0.5-z}Bi_{0.5+z}Ti_{1-x}Ga_xO_{3+z-0.5x}$ series for (a) x = 3% and (b) x = 5% after calcining at 900°C for 8h.

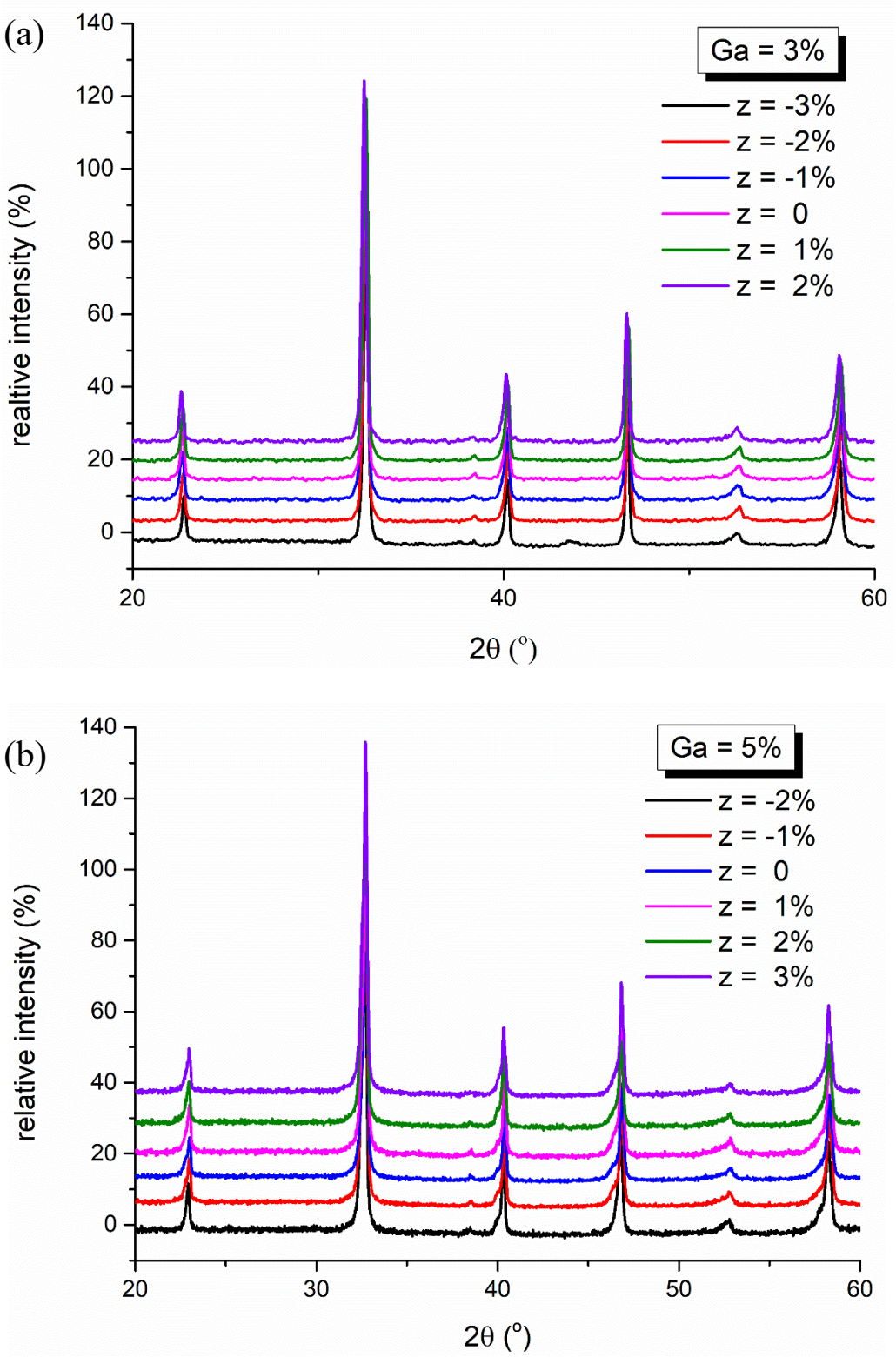

Fig. 5-21. XRD patterns of $Na_{0.5-z}Bi_{0.5+z}Ti_{1-x}Ga_xO_{3+z-0.5x}$ series for (a) x = 3% and (b) x = 5% on crushed pellets and polished pellet surfaces, respectively.

Selected pellets for fixed Ga content (x = 3%) with (a) z = -2% (b) z = 0 (c) z = 2% were polished and thermally etched for analysis using SEM/EDS, as shown in Fig. 5-22. The bright particle found in sample (a) is residual gold from the gold electrode used for electrical measurements before polishing. No obvious secondary phases were identified, except some tubular Ga-rich secondary phases were observed around triple junctions of grain boundaries in sample (b) but only on thermally etched surfaces. Sample (b) with Na/Bi =1 (z = 0) has the largest grain size and a similar behaviour was observed in A-site fully occupied nonstoichiometric NBT discussed in chapter 4, except the grain size is larger with Ga doping. The chemical composition of the main phases for all samples are summarised in Fig. 5-23. The Na and Bi contents change systematically with starting composition according to z, and the Ti content is constant at ~48.8 at% which is consistent with the nominally fixed compositional value of 48.5 at%. The experimental composition of z = 2% closely matches the theoretical (expected) composition. However, the Ga content tends to decreases as z decreases. The tubular shaped secondary phases observed on z = 0 possibly correspond to a sodium gallium titanate of general formula $Na_xGa_{4+x}Ti_{n-4-x}O_{2n-2}$ which starts to grow at the thermal etching temperature,[4] indicating relatively high Ga content around grain boundaries. This also suggests an inhomogeneous Ga distribution across grains and grain boundaries for O-deficient compositions, leading to Ga-deficient (average) bulk compositions.

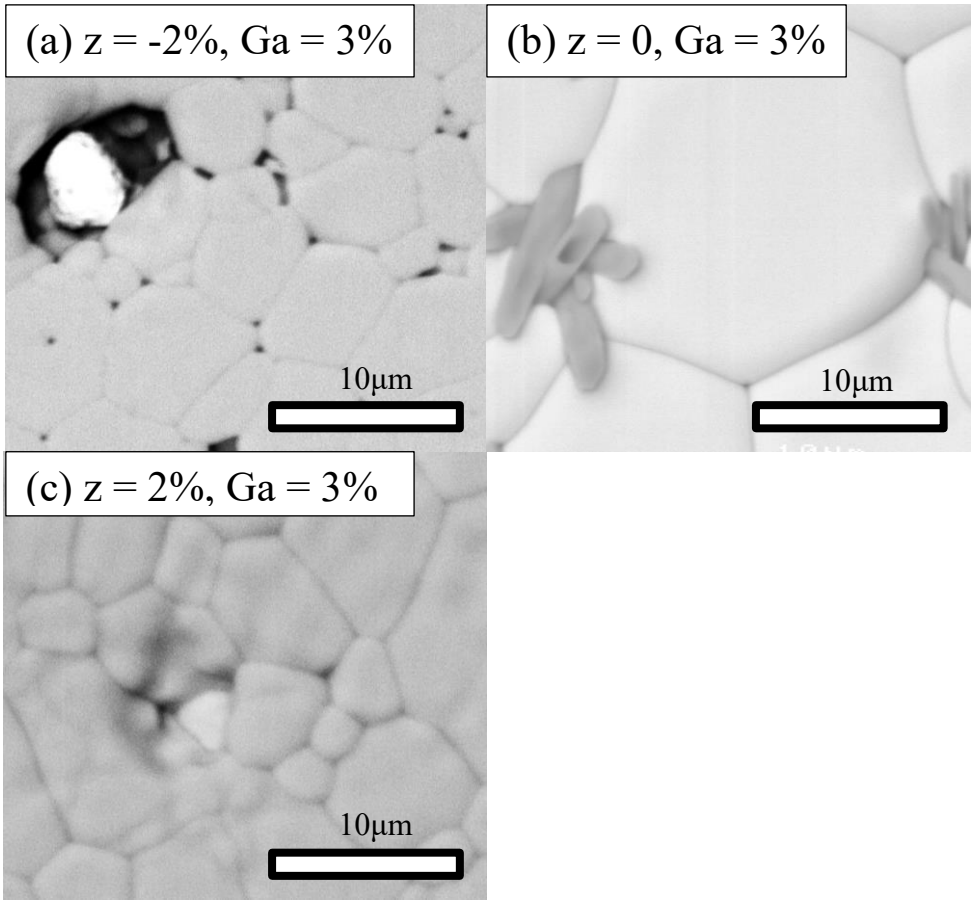

Fig. 5-22. Backscattered images of thermally etched surfaces for fixed Ga content (x = 3%) with (a) z = -2%, (b) z = 0 and (c) z = 2%. The bright particle observed in (a) is residual gold from a gold electrode used for electrical property measurements.

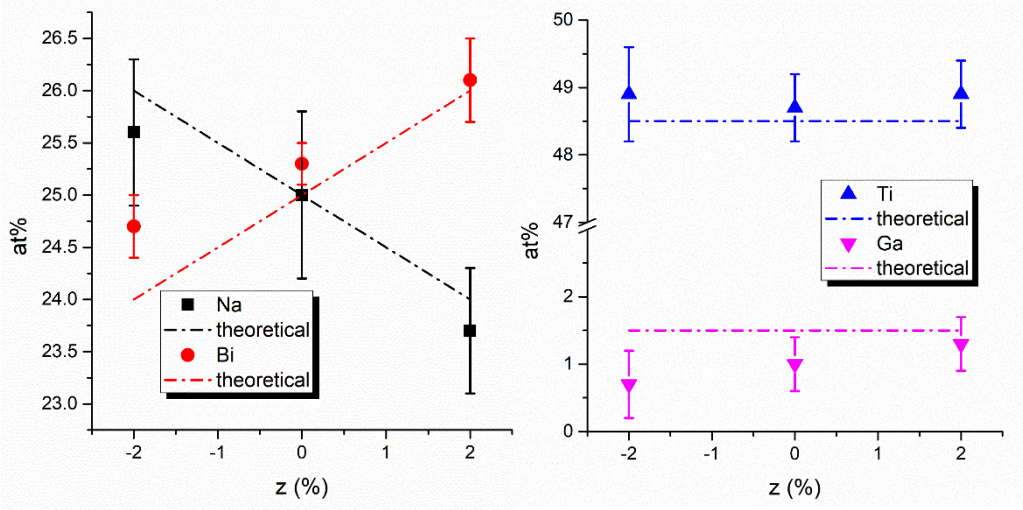

Fig. 5-23. EDS average chemical composition results of the bulk and for fixed Ga content (x = 3%) with z = -2, 0 and 2%.

5.3.2 Electrical properties

Z* plots for the $Na_{0.5-z}Bi_{0.5+z}Ti_{1-x}Ga_xO_{3+z-0.5x}$ series measured at 400 and 650 °C for conducting and insulating/semi-conducting phases, respectively, are shown in Fig. 5-24. Samples with O content ≥ 3.005 become insulating where the bulk response shows behaviour similar to $NB_{51}T$, except $Na_{0.48}Bi_{0.52}Ti_{0.99}Ga_{0.01}O_{3.015}$ (x = 1%, z = 2%, as shown in Fig. 5-24 (a)) which shows a low frequency tail and a decrease in bulk resistance as z increases from 1 to 2 % (and therefore becomes more Bi-rich). A similar result is also observed for 8%BG-NBT (Fig. 5-19(a)) and therefore this abnormal behaviour is possibly influenced by Bi-rich secondary phases as discussed in the BG-NBT series.

Isothermal plots of bulk conductivity and f_{max} vs z for conducting samples are shown in Fig. 5-25 to help illustrate the changes in the bulk resistance with z, where the bulk conductivity is the inverse of the bulk resistance. The bulk conductivity decreases as z increases (and therefore increase in bulk resistance) when z > 0 where oxygen vacancies are compensated by Bi^{3+} replacing Na^+. It becomes relatively similar (±50%) when -2% ≤ z ≤ 0 (8 samples with different nominal compositions as shown in the shaded area), except x= 3% has a significant increase for z = -2%. Therefore, the bulk conductivity is independent to the oxygen vacancies introduced by Na^+ replacing Bi^{3+} which should increase as z decreases. However, the grain boundary responses are more sensitive to the nominal composition for x = 1%. For example, the bulk resistance is similar when z ≤ 0 for x = 1% (Fig. 5-24(a)), but the grain boundary resistance significantly decreases when z < 0. Similar behaviour is also observed in the Ga-NBT series when x increases from 1 to 5%, as shown in Fig. 5-7 (a). Since grain size has significantly increased by Ga-acceptor doping as mentioned before, the change in grain boundary resistance is possibly due to a change in geometric factor, where the volume ratio of grain boundary to bulk decreases with increasing grain size.

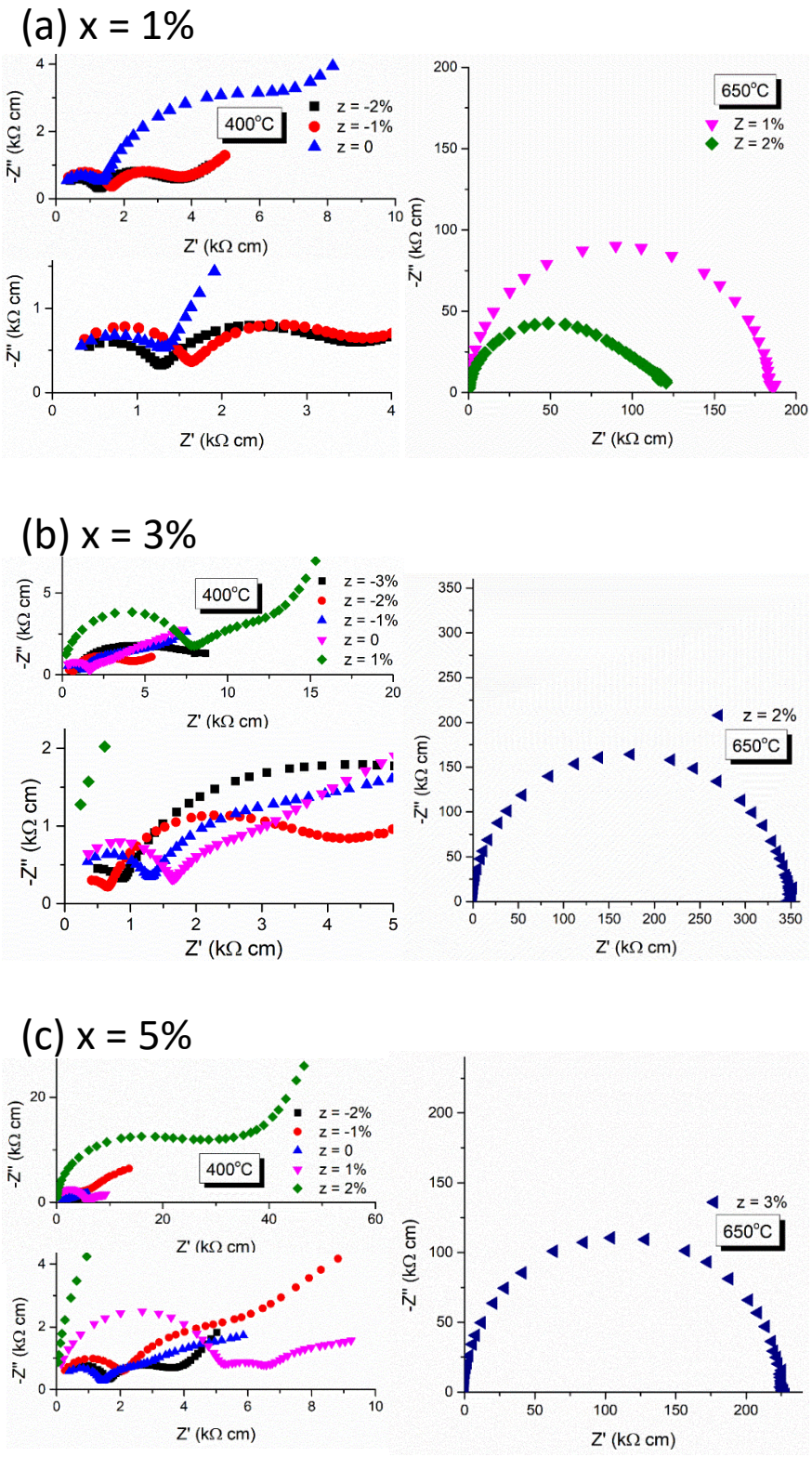

Fig. 5-24. Z* plots for the $Na_{0.5-z}Bi_{0.5+z}Ti_{1-x}Ga_xO_{3+z-0.5x}$ series which Ga (x) content was fixed at (a) 1% (b) 3% (c) 5% measured at 400 and 650 °C for conducting and insulating phases, respectively.

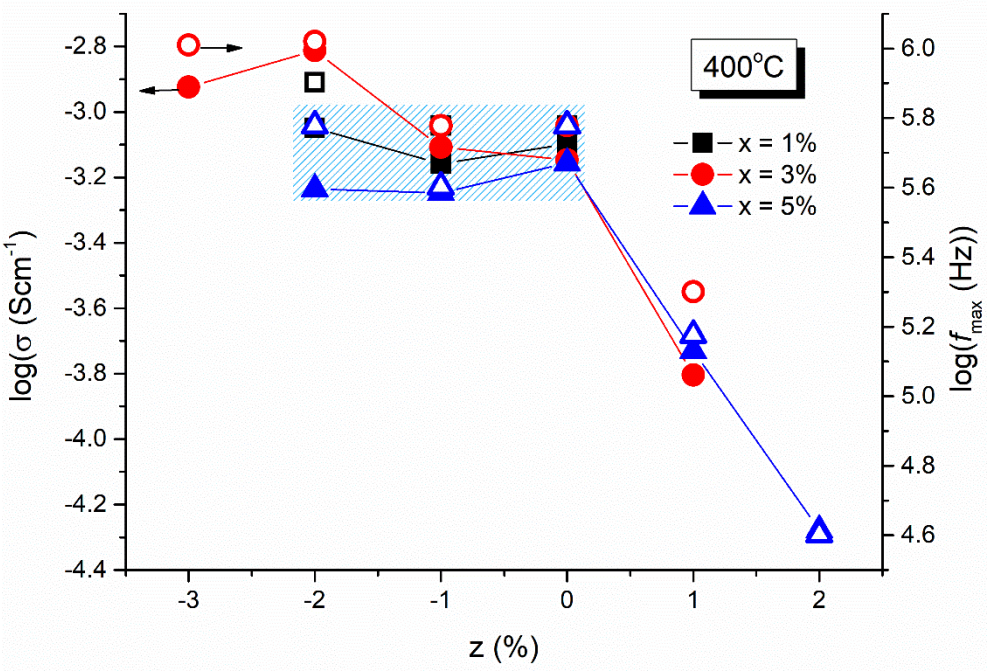

Fig. 5-25. Isothermal plots of bulk conductivity and f_{max} vs z for the $Na_{0.5-z}Bi_{0.5+z}Ti_{1-x}Ga_xO_{3+z-0.5x}$ series at 400 °C represented by solid and open symbols, respectively.

Since the bulk conductivity is independent to the oxygen vacancies introduced by Ga^{3+} and Na^{+} replacing Ti^{4+} and Bi^{3+}, respectively, samples with the same nominal oxygen contents (O_n) are compared in Z* plots as shown in Fig. 5-26. The bulk resistance significantly increase for $z > 0$ and remains the same for $z \leq 0$, indicating that the Na/Bi ratio (z) has a stronger influence on the conducting behaviour than Ga-acceptor doping (x), especially when $z > 0$, as shown in Fig. 5-26 (a) and (b). Similar bulk responses are observed for $O_n = 2.985$ and 2.975, although the latter shows minor dependence of x and z, as shown in Fig. 5-26 (c). For $O_n = 2.965$, the bulk resistance increases as x and z increase and a similar bulk response is observed for x = 5%/ z = 1% and x = 7%/ z = 0, as shown in Fig. 5-26 (b) and (d), respectively. This indicates that the Ga-acceptor doping on the B-site (x = 7%, z = 0) is less favourable than Na-acceptor doping on A-site (x = 3%, z = -2%) to maximise the oxygen vacancy concentration ($O_n = 2.965$).

The Arrhenius plots of bulk conductivity for the $Na_{0.5-z}Bi_{0.5+z}Ti_{1-x}Ga_xO_{3+z-0.5x}$ series are shown in Fig. 5-27. E_a changes at 300 ~ 325 °C where the maximum permittivity occurs. The most conductive samples for each Ga content (1 ~ 5%) tend to

have the lowest E_a, which is similar regardless of the Ga content. The trend of bulk f_{max} is similar to the conductivity in Arrhenius type plots, except no change in activation energy occurs at 300 ~ 325 °C.

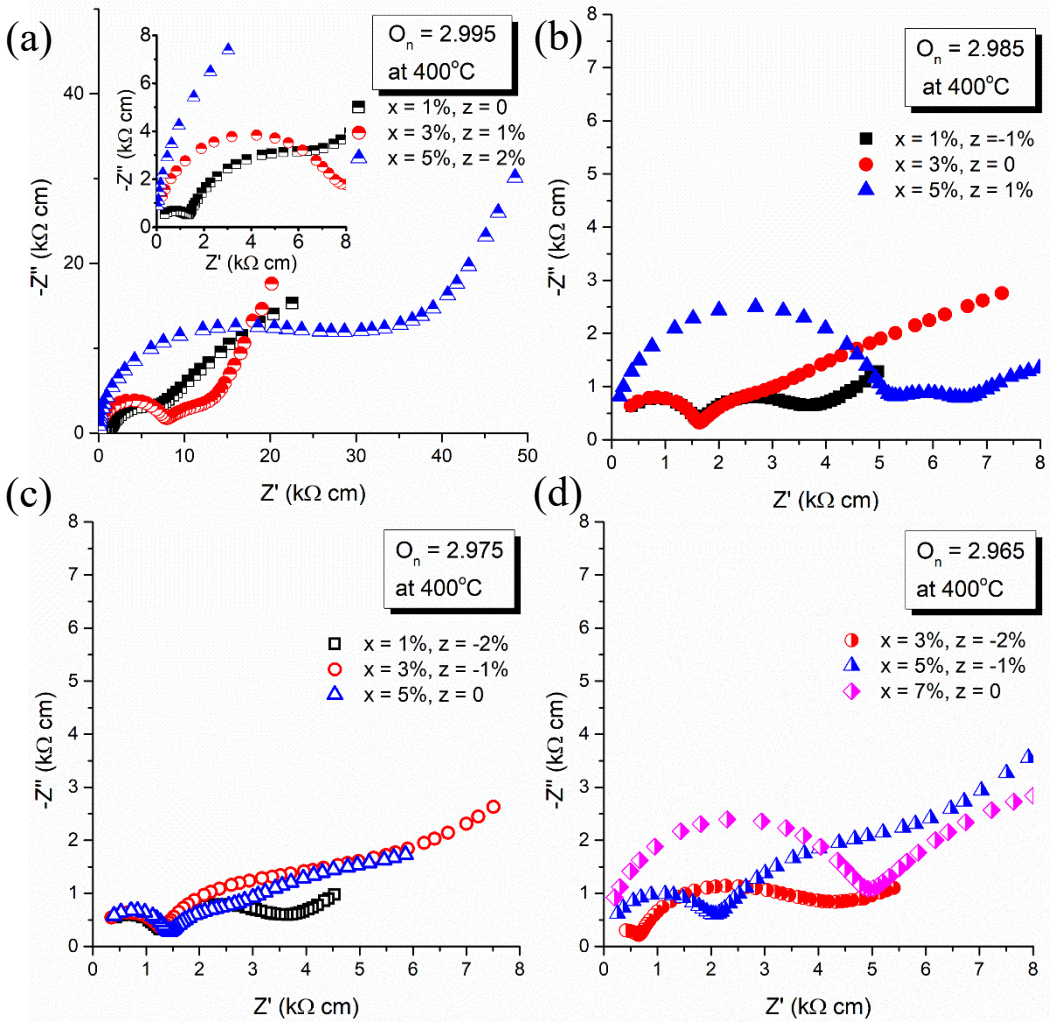

Fig. 5-26. Z* plots of fixed nominal oxygen content (O_n) (a) 2.995 (b) 2.985 (c) 2.975 (d) 2.965 for $Na_{0.5-z}Bi_{0.5+z}Ti_{1-x}Ga_xO_{3+z-0.5x}$ series measured at 400 °C.

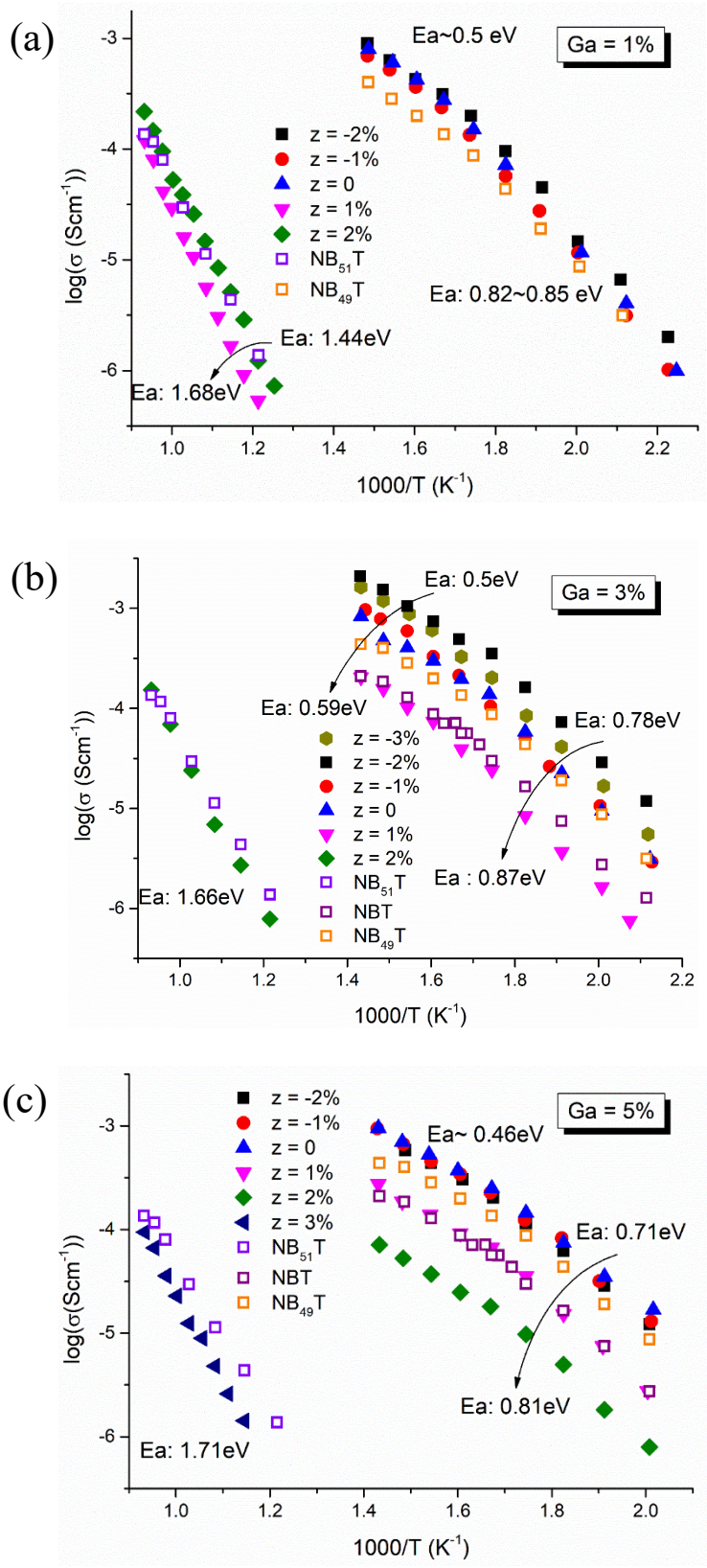

Fig. 5-27. Arrhenius plots of bulk conductivity for $Na_{0.5-z}Bi_{0.5+z}Ti_{1-x}Ga_xO_{3+z-0.5x}$ series which Ga content was fixed at (a) 1% (b) 3% (c) 5%.

5.4 Discussion

The compositions that contained secondary phases based on XRD for all series are summarised in Table 5-3. All these samples were nominally Bi-rich in their starting composition (Bi > 0.5) and Bi-rich and Bi-containing phases, such as $Bi_{25}GaO_{40}$ and $Bi_2Ga_4O_9$, were identified as secondary phases. The contents of these secondary phases can be reduced or even eliminated by increasing temperature. For example, $Na_{0.48}Bi_{0.52}Ti_{0.97}Ga_{0.03}O_{3.005}$ (x = 3%, z = 2%) had $Bi_2Ga_4O_9$ as a secondary phase after calcination at 900℃ for 8h. After sintering at 1100 ℃ for 2h, no secondary phases were detected by XRD/SEM and the chemical compositions based on EDS results matched the nominal starting composition. This shows the temperature dependence of the solubility for Ga.

An *in situ* high-temperature diffraction study for phase formation of NBT during solid-state processing by Aksel and Jones[5] showed that NBT starts to form at ~ 500 ℃ with other intermediate phases, such as $Bi_4Ti_3O_{12}$ and $Bi_{12}TiO_{20}$ and suggest that conversion into NBT occurs within Bi_2O_3 particles as Na and Ti constituent elements diffuse into the Bi_2O_3 grains. Therefore, the excess Bi_2O_3 may be stabilised with Ti or Ga at lower temperatures and decompose at higher temperatures where the sillenite phases ($Bi_{12}(Ti/Ga)O_{20}$) and $Bi_2Ga_4O_9$ melt below 875 ℃[6] and incongruently at ~1080 ℃[7], respectively. Small amounts of liquid phases may be involved during calcination and sintering. On the other hand, all secondary phases contain only trace levels of Na, thus the single-phase obtained at higher temperature was likely approached by the exchange of Na and Bi atoms or mainly diffusion of Na. Therefore, the phase formation is probably based on charge balance between the A and B-sites and controlled by Na/Bi ratio.

The BG-NBT series for y = 6 and 8 % are examples which had significant amounts of $Bi_2Ga_4O_9$ as secondary phases in calcined powders and became single-phase after sintering at 1150℃ 2h based on XRD. The abnormal behaviour in IS data for samples prepared by hand grinding suggests multiple components coexisted. This is possibly due to an interlayer being formed when $Bi_2Ga_4O_9$ was converting into perovskite NBT. The situation can be simply removed by preparing samples using ball milling, which reduces the particle size and improves homogeneity, leading to accelerated phase transformation. This temperature dependence of phase formation is

possibly due to relatively low oxygen vacancy or Na concentration compared to the conductive phases.

Series	Multi-phase samples based on starting composition*	Mixing method	Heat treat condition
Ga-NBT	None	HG	
Ga-NB$_{51}$T	$Na_{0.5}Bi_{0.51}Ti_{0.93}Ga_{0.07}O_{2.98}$	BM	800°C for 2h twice
			1100°C for 2h
BG-NBT	$Na_{0.47}Bi_{0.53}Ti_{0.94}Ga_{0.06}O_3$	HG and BM	900°C for 8h
	$Na_{0.46}Bi_{0.54}Ti_{0.92}Ga_{0.08}O_3$		
Ga-(NB)$_z$T	$Na_{0.49}Bi_{0.51}Ti_{0.97}Ga_{0.03}O_{2.995}$	HG	900°C for 8h
	$Na_{0.48}Bi_{0.52}Ti_{0.97}Ga_{0.03}O_{3.005}$		
	$Na_{0.47}Bi_{0.53}Ti_{0.95}Ga_{0.05}O_{3.005}$		

Table 5-3. Summary of multi-phase samples for all series based on various processing conditions. HG = hand grinding, BM = ball milling. *Phase analysis based on XRD results.

In the Ga-NB$_{51}$T series, the EDS results suggest the maximum Ga-acceptor doping is less than 5% and a noticeable reduction in Na/Bi ratio to ~0.93 which is expected to be 0.98 for x = 5% (Ga5%-NB$_{51}$T). This acceptor doping generates oxygen vacancies based on equation 5-2 and the maximum conductivity occurred when x = 3%. The average Ga content for x = 5% is ~ 0.04 which should generate more oxygen vacancies by acceptor doping than x = 3%. However, having lower Na/Bi ratio actually compensates those oxygen vacancies, leading to decrease in the oxygen vacancy concentration as well as the conductivity. This provides evidence that the oxygen vacancy concentration depends not only on the Ga content but also on the Na/Bi ratio.

To further investigate the influence between the Na/Bi ratio and the B-site Ga-acceptor doping level, two main approaches were pursued: (1) fixed the nominal oxygen content at 3 by making stoichiometric NBT solid solutions with the high pressure phase $BiGaO_3$, (2) adjust the oxygen content by changing the Na/Bi ratio beginning with Ga-NBT, for x =1, 3 and 5%. The EDS results and bulk conductivity of selected samples for the BG-NBT and Ga3%-(NB)$_z$T series are summarised in Table 5-

4. All samples are single-phase by XRD. For the BG-NBT series, EDS results change systematically with the starting composition, except the average calculated oxygen content according to EDS results is relative to the bulk conductivity, which decreases as the oxygen content increases and becomes an insulator when the oxygen content > 3. Similar to Ga5%-$NB_{51}T$, Ga6%BG-NBT (y = 6%) has a much lower Na/Bi ratio than expected to adopt the Ga content which is closed to the solid solution limit, leading to reduction in bulk conductivity. As approaching the solid solution limit, some undissolved Ga may result in B-site deficiency, leading to A-site surplus. Therefore, the bulk composition of Ga6%BA-NBT may contain slightly higher Bi but lower Ga content which allows oxygen vacancies introduced by Ga-acceptor doping to be compensated by Bi-donor doping, leading to similar electrical behaviour as $NB_{51}T$. For the Ga3%-$(NB)_zT$ series as shown in Table. 5-4, the Na/Bi ratio and average calculated O content change systematically with starting composition but the Ga content which should be fixed at 3% also decreases systematically from ~ 3% to ~ 1% as the Na/Bi ratio increases from 0.91 to 1.04, leading to the majority of oxygen vacancies which promote the conductivity of $Na_{0.52}Bi_{0.48}Ti_{0.97}Ga_{0.03}O_{2.965}$ (x = -3%, z =-2%) originating from Na-acceptor doping. This result indicates that the solubility of Ga depends on the starting Na/Bi ratio.

Starting composition	**Na/Bi**	**Na/Bi**	**Ga by EDS**	**O**	**σ (Scm^{-1}) at 400°C**
BG-NBT					
$Na_{0.49}Bi_{0.51}Ti_{0.98}Ga_{0.02}O_3$	0.96	0.99	0.02 (±0.6%)	2.96	$1.9x10^{-5}$
$Na_{0.48}Bi_{0.52}Ti_{0.96}Ga_{0.04}O_3$	0.92	0.92	0.04 (±0.6%)	2.99	$1.1x10^{-5}$
$Na_{0.47}Bi_{0.53}Ti_{0.94}Ga_{0.06}O_3$	0.89	0.84	0.05 (±0.4%)	3.02	$< 10^{-7}$
Ga3%-$(NB)_zT$					
$Na_{0.52}Bi_{0.48}Ti_{0.97}Ga_{0.03}O_{2.965}$	1.08	1.04	0.01 (±1%)	2.97	$1.4x10^{-3}$
$Na_{0.50}Bi_{0.50}Ti_{0.97}Ga_{0.03}O_{2.985}$	1	0.99	0.02 (±0.8%)	2.99	$6.1x10^{-4}$
$Na_{0.48}Bi_{0.52}Ti_{0.97}Ga_{0.03}O_{3.005}$	0.92	0.91	0.03 (±0.8%)	3.02	$< 10^{-8}$

Table 5-4. The Na/Bi ratio, EDS results, calculated O content and bulk conductivity for BG-NBT and Ga-$(NB)_zT$ series.

A summary of the bulk f_{max} for the samples which were single-phase based on XRD measured at 350 °C is shown in Fig. 5-28 and the data for $NB_{49}T$ and

$Na_{0.5}Bi_{0.505}TiO_{3.0075}$ ($NB_{50.5}T$) prepared by ball milling is also included using the equivalent z = -0.5 and 0.25% in terms of Na/Bi ratio, respectively. The z and x not only represent the nominal Na/Bi ratio and Ga concentration but also correspond to the addition and subtraction from the theoretical oxygen concentration, respectively. Each tick on both axes is equivalent to 1 at% oxygen content and samples aligned at 45° have the same nominal oxygen content (O_n). The f_{max} decreases from left to right where the colour turns from blue to red and the black circles represent insulating samples where the M'' bulk response was out of the frequency limits of the instrumentation at 350 °C. The Ga concentration tends to increase as z increases based on EDS results for Ga3%-$(NB)_zT$. The insulating boundary is predicted based on the line between $NB_{50.5}T$ and 6%BG-NBT. On approaching the insulating boundary, f_{max} significantly decreases as z increases when O_n is fixed. This result indicates the composition changes strongly with the nominal Na/Bi ratio. The nonstoichiometric NBT (x = 0) shows the electrical properties are very sensitive to the Na/Bi ratio (z ± 1%), where it switches from an insulator to an ionic conductor The Na/Bi ratio range is expanded by Ga-acceptor doping and increases as the Ga concentration increases. However, f_{max} tends to decrease with increasing z when O_n is fixed, e.g. grey (O_n = 3) and pink (O_n = 2.995) lines. Consequently, the conductivity decreases with increasing Bi content, respectively. This observation indicates the conductivity cannot be simply enhanced by increasing Bi content, which presumably can introduce more oxygen diffusion pathway through Bi-Bi-Ti saddle points. The conducing boundary is where the majority of oxygen vacancies is introduced by Na-acceptor doping (z < 1) and possibly close to the dashed line through where the highest f_{max} was observed for x = 0 and 3%.

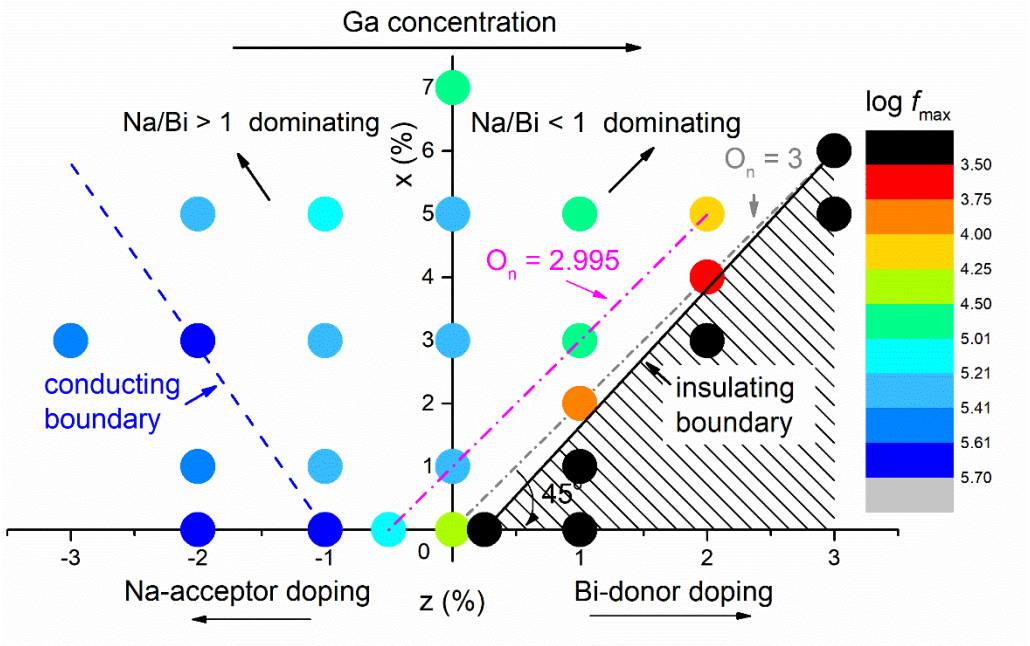

Fig. 5-28 A summary of bulk log f_{max} measured at 350 °C for various Ga content (x) and Na/Bi ratio (z) which are single-phase based on XRD. The black circles represent insulating samples where bulk responses were out of the instrumental limits. Note that Na/Bi > 1 when z < 0 and vice versa. Samples aligned at 45° have the same nominal oxygen content (O_n).

5.5 Conclusions

1. The solubility of Ga doping depends on the charge configuration between the A and B-sites of perovskite NBT which is dominated by Na/Bi ratio. This is possibly due to the phase formation of NBT starting from Bi_2O_3 particles where Na and Ti diffuse into in Bi_2O_3 particles.[5]

2. High Na concentration (z > 1) or the presence of oxygen vacancies accelerates the phase formation during calcination. Lower Na/Bi ratio (z > 1) can have higher Ga concentration due to the charge compensation between Bi-donor doping on Na and Ga-acceptor doping on Ti, respectively.

3. As approaching to a fully occupied perovskite lattice (O =3), a slight mismatch of the charge configuration between the A and B-sites results in a dramatic change in conductivity, especially close to the solid solution limit (i.e. 6%BG-NBT).

4. The enhancement of bulk conductivity with Ga-acceptor doping is limited by the self-recovery of NBT where the oxygen content tends to be fully occupied by reducing the Na/Bi ratio (z >1) or Ga concentration and forming a Na and Ga-rich grain boundary. Instead, the tuneable range of Na/Bi ratio between conducting and insulating boundary is expanded by Ga-acceptor doping.

5.6 Reference

1. Yang, F., Wu, P. and Sinclair, D.C., Enhanced bulk conductivity of A-site divalent acceptor-doped non-stoichiometric sodium bismuth titanate, *Solid State Ionics* **299**, 38-45 (2017)

2. Li, M., Pietrowski, M.J., De Souza, R.A., Zhang, H., Reaney, I.M., Cook, S.N., Kilner, J.A. & Sinclair, D.C., A family of oxide ion conductors based on the ferroelectric perovskite $Na_{0.5}Bi_{0.5}TiO_3$, *Nature Materials* **13**, 31-35 (2014)

3. He, X. and Mo, Y., Accelerated materials design of $Na_{0.5}Bi_{0.5}TiO_3$ oxygen ionic conductors based on first principles calculations, *Physical Chemistry Chemical Physics* **17**, 18035-18044 (2015)

4. Amoroso, J.W. and Edwards, D.D., Phase formation and stability of polycrystalline $Na_xGa_{4+x}Ti_{1-x}O_8$, (x~0.7), *Solid State Ionics* **179**, 878-880 (2008)

5. Aksel, E. and Jones, J.L. Phase Formation of Sodium Bismuth Titanate Perovskite During Solid-State Processing, *Journal of American Ceramic Society* **93**, 3012-3016 (2010)

6. Lobato, A.R., Lanfredi, S.L., Carvalho, J.F. and Hernandes, A.C. Synthesis, Crystal growth and Characterization of γ-Phase Bismuth Titanium Oxide with Gallium, *Materials Research*, **3**, 92-96 (2000)

7. Schreuer, J., Burianek, M., Mühlberg, M., Winkler, B., Wilson, D.J. and Schneider, H. Crystal growth and elastic properties of orthorhombic $Bi_2Ga_4O_9$, *Journal of Physics: Condensed Matter* **18**, 10977-10988 (2006)

Chapter 6

$BiFeO_3$-NBT

In previous chapters it was shown that stoichiometric NBT can be tuned from an ionic conductor to a semiconductor/insulator by controlling the Na/Bi ratio and doping with the high-pressure phase $BiGaO_3$. The conducting behaviour of NBT is sensitive to the oxygen content. An alternative way to suppress the ionic conduction of NBT is via Nb donor-doping on the Ti site as reported by Li *et al*. [1] whereby oxygen vacancies can be fully compensated between 0.5-1 at% according to the following equation

$$Nb_2O_5 + 2Ti_{Ti}^{x} + V_O^{\cdot\cdot} \rightarrow 2Nb_{Ti}^{\cdot} + O_O^{x} + 2TiO_2 \qquad 6\text{-}1.$$

Further studies in the Nb-donor doping reported by Li. *et al*. [2] showed that NBT can also be tuned into a mixed conductor when the Nb doping level is low, eg ~ 0.3 at% due to partial filling of oxygen vacancies which supresses the oxide-ion transport number from > 0.9 to 0.5 ~ 0.6. Based on those studies, only a small amount of oxygen vacancies is required to promote oxygen ion conduction.

NBT is commonly doped with other perovskite end members to improve the dielectric properties. $BiFeO_3$ (BF) is one of the end members which is reported to form a full solid solution with NBT.[3-5] However, leakage increases as the BF content increases which is unfavourable for dielectric applications. The conduction mechanism(s) has not been fully investigated. It is known that the conductivity of undoped BF is correlated to the oxidation state of Fe ions associated with the presence of oxygen vacancies and therefore very sensitive to the oxygen partial pressure (pO_2).[6,7]

Similar behaviour was also observed in the $yBiFeO_3$-$(1-y)K_{0.5}Bi_{0.5}TiO_3$ series, where p-type electrical conductivity becomes dominant with increasing BF content ($y \geq 25\%$).[8] Moreover, an additional annealing at 550 °C for 5 h in N_2 can reduce the ac conductivity for y = 70% at room temperature. It is suggested that the conduction mechanism is attributed to electron hole hoping between Fe^{4+} and Fe^{3+}.[8-10] In addition, the dc conductivity for high BF content, such as y = 80% and 90%, shifts from p to n-type conduction behaviour in a reducing condition by switching the atmosphere from

O_2 to N_2 above 700 °C.[10] Therefore, the oxidation state of Fe ions may potentially change under different atmospheres.

The aim of this chapter is to discover a potential NBT-based mixed conductor by chemical doping with Bi-based perovskites to promote the oxygen migration from the highly polarised Bi ions on the A-site. Mixed-valence transition metal ions on the B-site may enhance the electronic conductivity. Two series of samples were prepared:

1. BF-doped NBT (BF-NBT, denoted as (x)BF-(1-x)NBT), $Na_{0.5(1-x)}Bi_{0.5(1+x)}Ti_{1-x}Fe_xO_3$.

2. BF-NBT with 1 at% Nb doping on Ti (1%Nb-BF-NBT, denoted as 1%Nb-(x)BF-(1-x)NBT), $Na_{0.5(1-x)}Bi_{0.5(1+x)}Ti_{0.99-x}Fe_xNb_{0.01}O_{3.005}$.

The Bi concentration increases as the Fe acceptor-doping level increases based on the charge compensation on the A and B-sites to maintain the O content (O = 3). The starting materials for Fe is Fe_2O_3, where the oxidation state is assumed to be +3. Therefore, the charge compensation for BF-NBT series is based on the nominal equation

$$Bi_2O_3 + 2Fe_2O_3 + 2Na_{Na}^{x} + 4Ti_{Ti}^{x} \rightarrow 2Bi_{Na}^{\cdot\cdot} + 4Fe_{Ti}^{\prime} + Na_2O + 4TiO_2 \qquad 6\text{-}2.$$

For each Bi donor dopant for Na on the A-site, it requires two Fe acceptor dopants for Ti to obtain charge compensation. For room temperature XRD, the BF-NBT series (x = 0-100%) retains a rhombohedral structure[3-5,11]. Small amount of $Bi_2Fe_4O_9$ and $Bi_{25}FeO_{40}$ were identified as secondary phases for $x \geq 80\%$.[5,12] For the 1%Nb-BF-NBT series, the existence of oxygen vacancies in cooperation with the ionic conduction in the BF-NBT series according to equation 6.1 is also investigated.

6.1 Phase purity and microstructure

The BF-NBT series ((x)BF-(1-x)NBT, x = 10-70%) was prepared by hand grinding using conventional solid state synthesis. Samples were calcined twice at 800 °C for 2h followed by 850-875 °C for 8h. The sintering temperature was in the range 1000-1100 °C for 2h with the temperature decreasing as the BF content increased. For the1%Nb-BF-NBT series (x = 10-40%), samples were calcined at 800 °C for 2h followed by 880-900 °C for 8h and sintered at 1090-1150 °C for 2h.

All samples were single-phase by XRD after sintering and characterised as the rhombohedral phase at room temperature due to the super-lattice peak around 38 $2\theta^{o}$, as shown in Fig. 6-1. For the BF-NBT series (Fig. 6-1 (a)), the pseudo-cubic 111_p peak splits into two peaks for $x \geq 40\%$, such as the hexagonal 006_h and 202_h peaks, which are common indices for rhombohedral symmetry with R3c space group in undoped BF.[3] On the other hand, there is no obvious peak splitting for x = 40% in the 1%Nb-BF-NBT series as shown in Fig. 6-1 (b). The pseudo-cubic cell volume of the BF-NBT and 1%Nb-BF-NBT series increases systematically with x, indicating larger Fe^{3+} ions are replacing smaller Ti^{4+} ions (where the relevant ionic radii are 0.645 and 0.605 Å, respectively) as shown in Fig. 6-2 (a).

The Goldsmith tolerance factor decreases with increasing x because Na^{+} and Bi^{3+} ions are similar in size. Therefore, the rhombohedral distortion (90^{o} - rhombohedral angle (α) is expected to increase with BF content. However, the rhombohedral angle for the BF-NBT series slightly increases from 89.74^{o} to ~89.93^{o} for $x \leq 30\%$ and suddenly drop to 89.79^{o} when x = 40% and then decreases with increasing x, as shown in Fig. 6-2(b). In contrast, only a small deviation is observed between x = 10 to 40% for the 1% Nb-BF-NBT series, where the rhombohedral angle remains greater than 89.90^{o}. Based on the literature, the rhombohedral angle either remained greater than 89.90^{o} (from ref 11) or only had small deviation (from ref 3). In this study, the rhombohedral distortion by BF-doping is observed for $x \geq 40\%$ in the BF-NBT series, where the 111_p peak starts to split into 006_h and 202_h. The crystal structure retains pseudo-cubic symmetry ($\alpha \geq 89.90^{o}$) for 1 at% Nb-doping of $x \leq 40\%$.

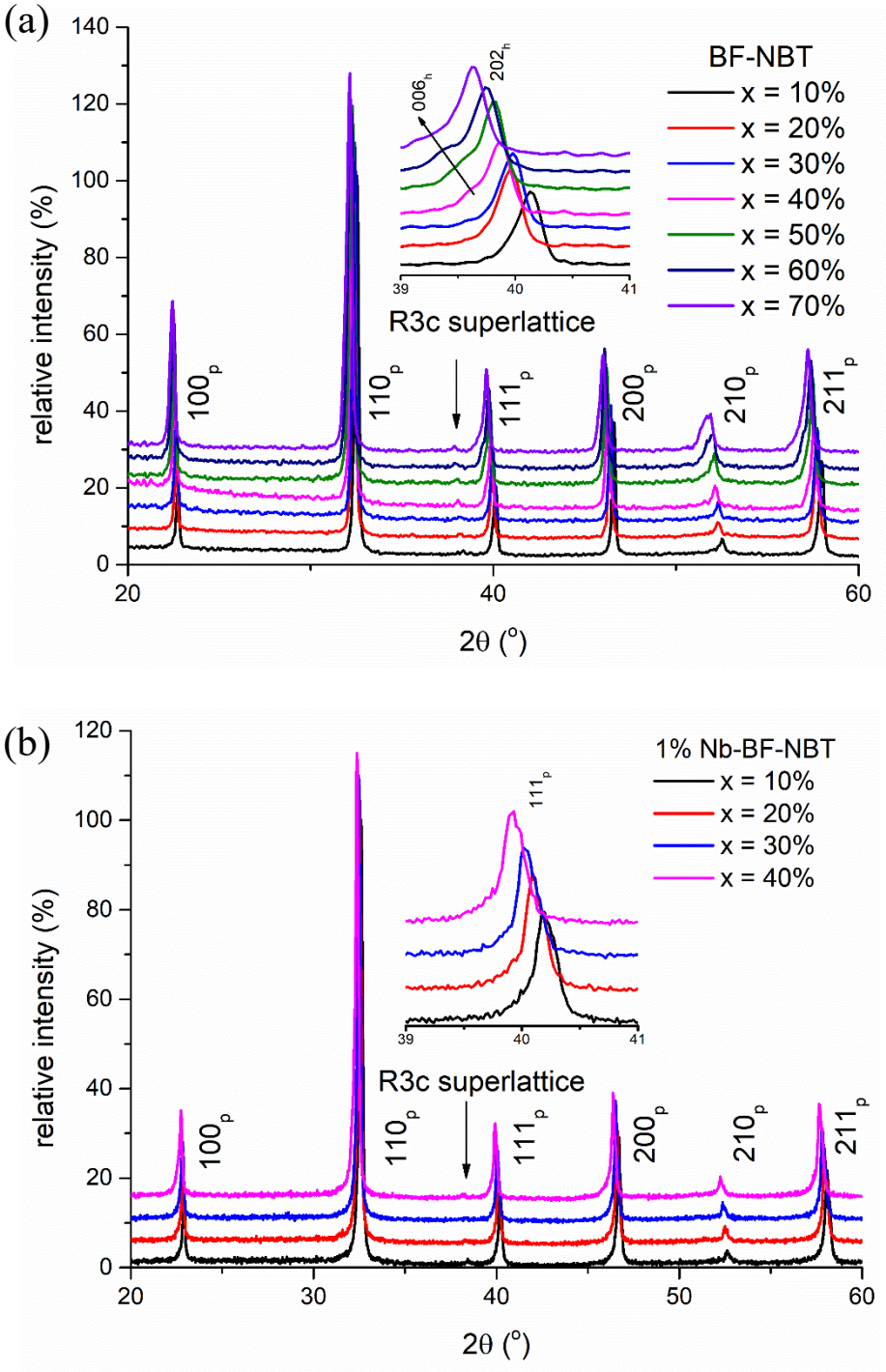

Fig. 6-1. Room temperature XRD patterns of (a) BF-NBT and (b) 1%Nb-BF-NBT series as crushed pellets. Insets show the diffraction patterns between 39~41 2θ°.

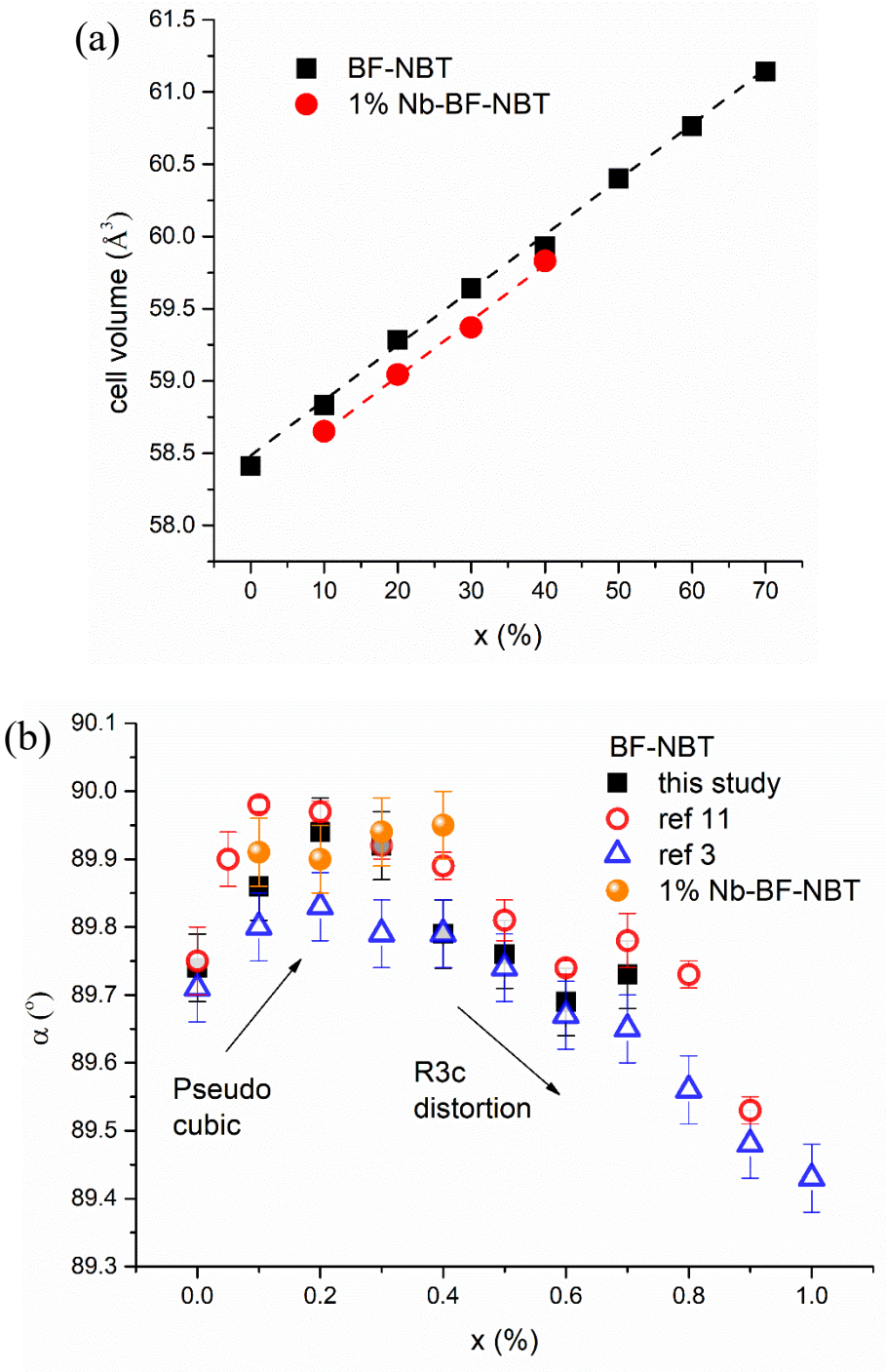

Fig. 6-2. (a) Pseudo-cubic cell volumes (b) rhombohedral angle (α) of the BF-NBT and 1%Nb-BF-NBT series. The error bars in (a) are within the symbols.

Further phase purity and microstructural analysis was performed by SEM/EDS for selected samples (x = 20 and 60%) on polished and thermally etched surfaces, where the latter were annealed at 90% of the sintering temperature for 1h. High density surfaces were observed on all samples. A homogeneous and some heterogeneous phases

were obtained for x = 20% and 60% as shown in Fig. 6-3 (a) and (c), respectively. The grain size of x = 60% was slightly smaller than x = 20% possibly due to the lower sintering temperature.

The average EDS chemical composition results suggest the bulk compositions were close to the expected values; however, the total atomic ratio of the A-site atoms (Na and Bi), especially Bi, was greater than one compared to the B-site atoms (Ti and Fe), as shown in Table 6-1. The experimental atomic ratio of Fe was about 90% of the expected value. The standard deviation of results from the thermally etched surfaces was higher than those for the polished surface samples, especially for Na.

The chemical EDS analysis of the light region of x = 60% on the polished surface (Fig. 6-3 (c)) showed slightly higher BF content than the bulk composition (additional ~7 at% of BF). The dark region surrounded by the light region was too small to be analysed. However, it possibly contained lower BF content than the lighter region. The homogeneity of x = 60% could possibly be improved by reducing the particle size of the calcined powders by ball milling or increasing the sintering temperature and annealing time.

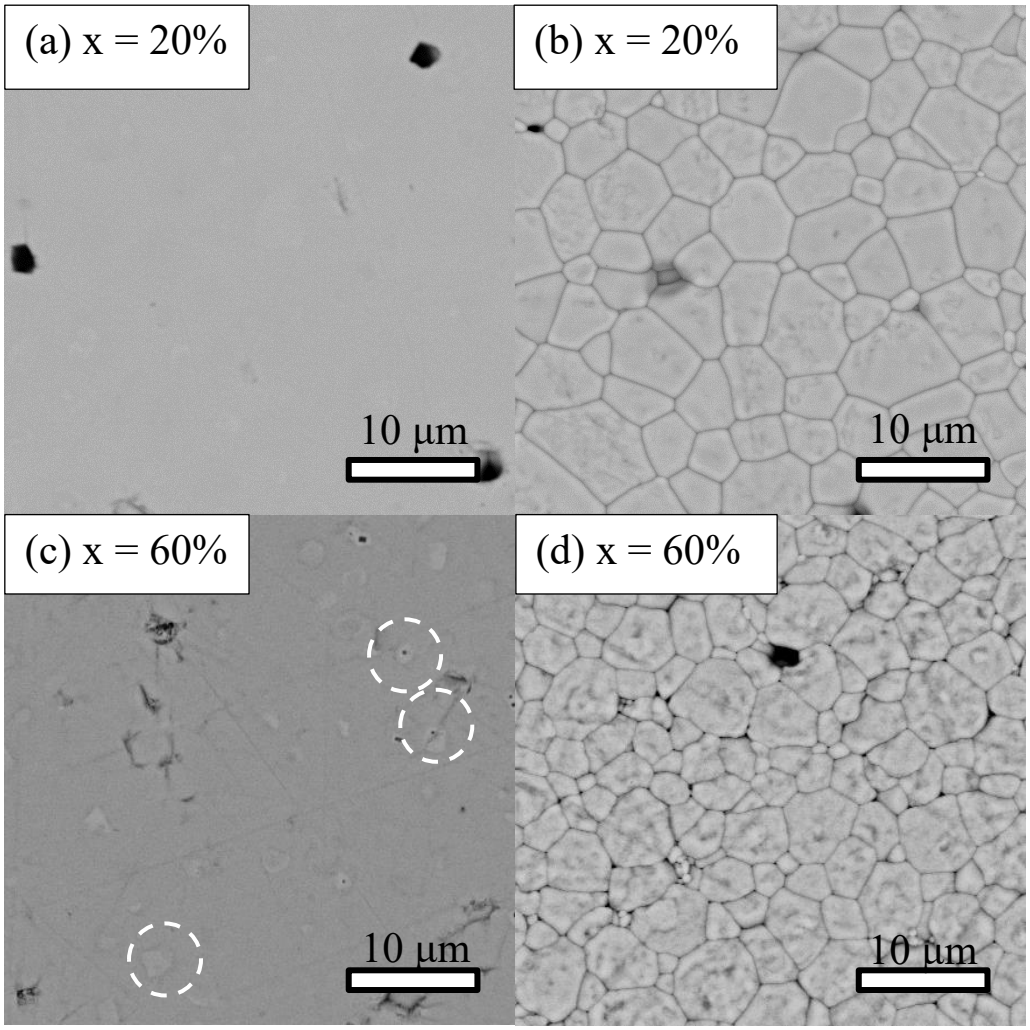

Fig. 6-3. SEM backscattering images of (x)BF-(1-x)NBT (a) and (b) x = 20%; (c) and (d) x = 60%. Figures on the left and right hand side are on polished pellets and thermally etched surfaces, respectively.

Sample	Na (at%)	Bi (at%)	Ti (at%)	Fe (at%)
x = 20%				
Polished surface	19.68 (0.4)	32.19 (0.52)	39.18 (0.59)	8.95 (0.45)
Thermally etched	19.98 (0.95)	32.26 (0.56)	38.85 (0.50)	8.91 (0.72)
expected	20	30	40	10
x = 60%				
Polished surface	10.47 (0.72)	42.41 (0.59)	19.73 (0.31)	27.40 (0.39)
Light region	8.58 (-)	44.26 (-)	16.13 (-)	31.04 (-)
Thermally etched	10.54 (1.65)	42.04 (0.8)	20.23 (0.68)	27.19 (1.39)
expected	10	40	20	30

Table 6-1. EDS average chemical composition results (standard deviation) of bulk areas for (x)BF-(1-x)NBT on polished and thermally etched surfaces.

6.2 Electrical properties

The temperature dependence of relative permittivity (ε_r) and dielectric loss (tan δ) for the BF-NBT and 1%Nb-BF-NBT series are shown in Fig 6-4 and 6-5, respectively. The maximum permittivity ($\varepsilon_{r,\,max}$) of NBT is supressed by BF doping from ~3000 to < 2000 and further suppression of $\varepsilon_{r,\,max}$ was obtained by 1 at% Nb doping on Ti, as shown in Fig. 6-4 (a) and 6-5 (a), respectively. For the BF-NBT series, the temperature dependence of the bulk response for x = 40, 50, 60 and 70% has exceeded the instrumental limit (1 MHz) above 575, 550, 500 and 425 °C according to the IS data, where the temperature dependence of ε_r at 1MHz begins to drop dramatically towards negative values, respectively, as shown in Fig. 6-4 (a). This is an indication of high conductivity and introduces an inductance effect, possibly due to a leaky grain boundary associated with high electronic conduction. The tan δ of NBT increases as x increases where tan δ is > 5% above room temperature for x = 40%, as shown in Fig 6-4 (b). The 1 at% Nb doping for Ti suppresses the leakage with tan δ < 5% below 500 °C, as shown in Fig 6-5 (b). Both $\varepsilon_{r,\,max}$ and leakage were reduced by 1% Nb donor-doping, suggesting ε_r for the BF-NBT series may be possibly influenced by a space charge effect.

For the BF-NBT series, the temperature of $\varepsilon_{r,\,max}$ (T_m) increases continuously from 320 to 445 °C as x increases from 0 to 50%, as shown in Fig 6-6, and moves towards the Curie temperature of BF (820-830 °C) where it transforms from a rhombohedral to an orthorhombic phase.[13] The T_m of NBT occurs between the rhombohedral to tetragonal phase transition and the presence of BF may stabilise the rhombohedral phase of NBT and therefore increases T_m. However, T_m of x = 60 and 70% was unattainable due to very high leakage (inductance effect). For the 1%Nb-BF-NBT series, the trend is similar to the BF-NBT series, except T_m for x = 40% significantly decreases from 423 to 393 °C by 1 at% Nb-doping.

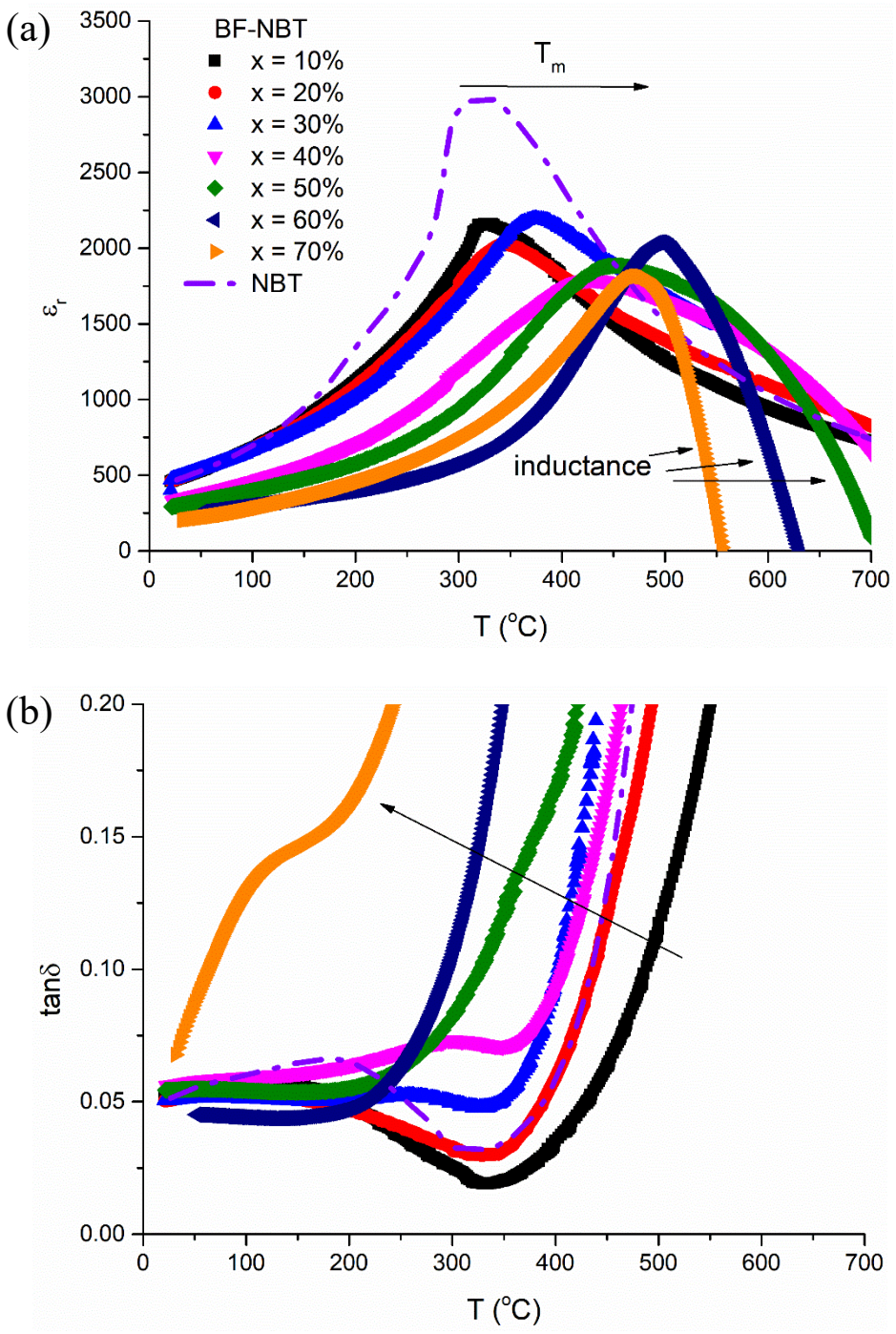

Fig. 6-4. Temperature dependence of (a) ε_r and (b) tan δ at 1 MHz for the BF-NBT series.

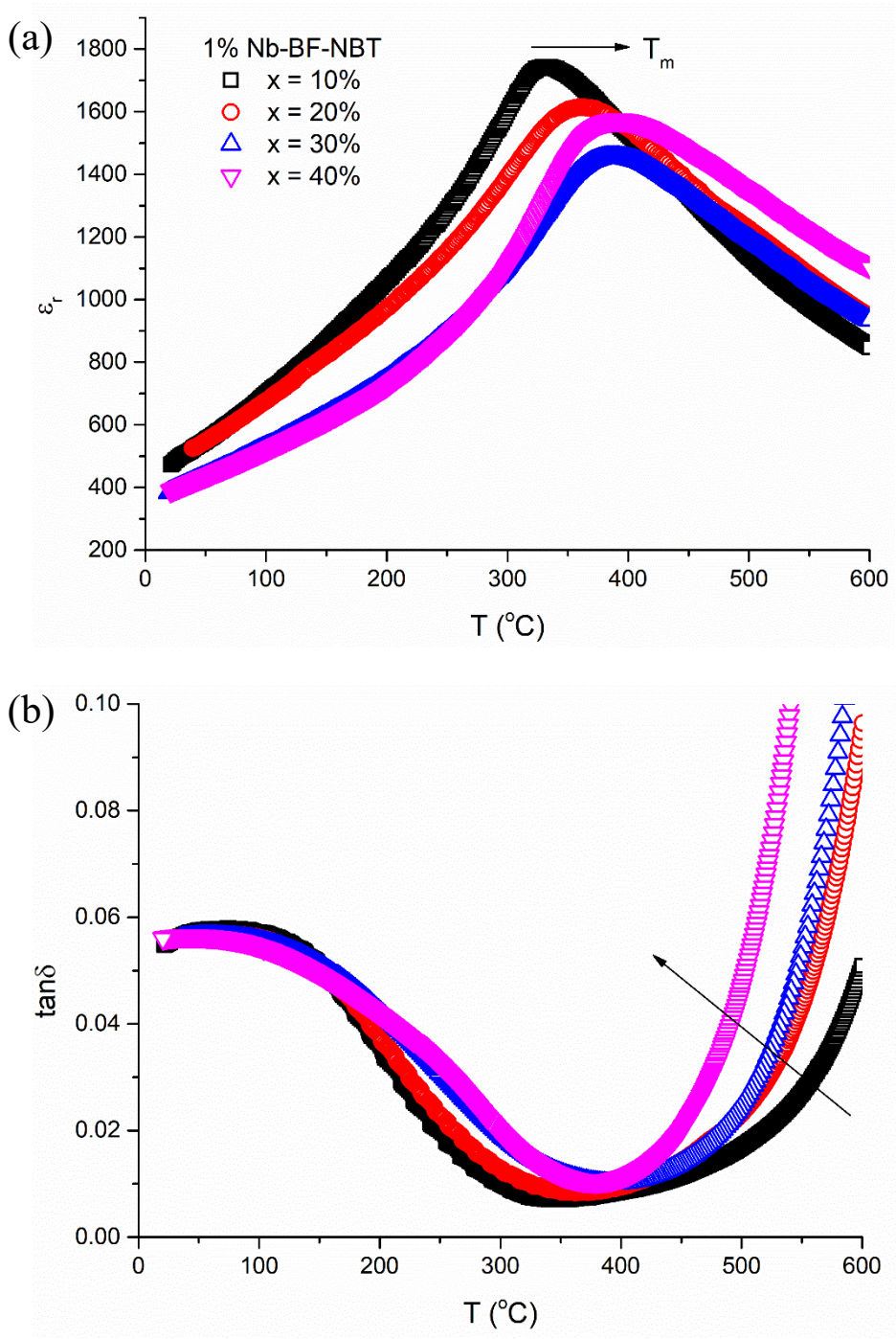

Fig. 6-5. Temperature dependence of (a) ε_r and (b) tan δ at 1 MHz for the 1%Nb-BF-NBT series.

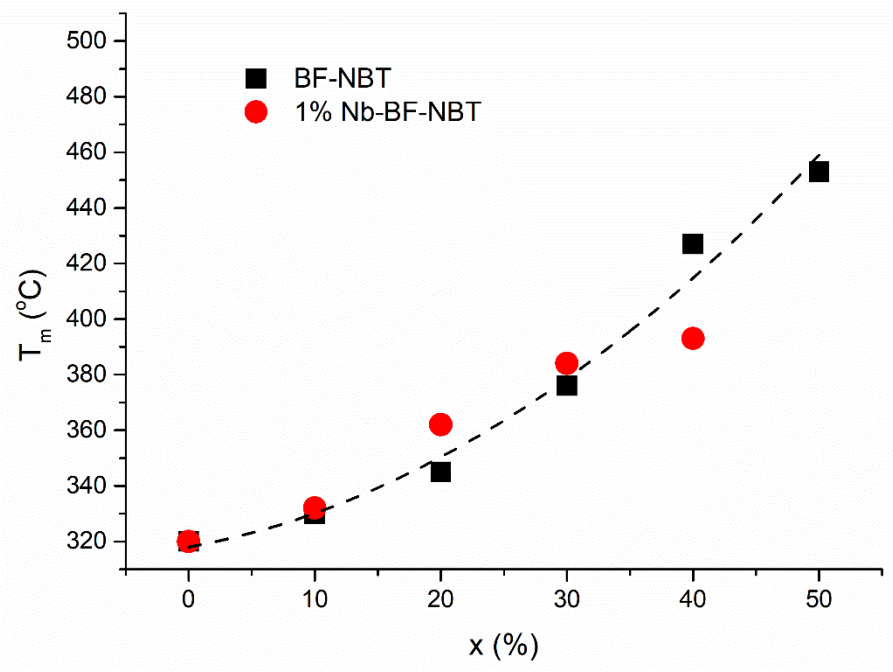

Fig. 6-6. The compositional dependence of T_m for the BF-NBT and 1%Nb-BF-NBT series.

Z* and M''/Z'' spectroscopic plots for the BF-NBT series where x = 10, 20 and 40% measured at 500 °C are shown in Fig. 6-7. Two semi-circles are observed for x = 10 and 20% as shown in Fig. 6-7 (a), where the high and low frequency arcs correspond to a bulk and grain boundary response, respectively. The capacitance difference between the bulk and grain boundary (gb) response is about one order of magnitude. For x ≥ 40%, only one arc is observed in Z* plots above 250 °C where the impedance data starts to have a clear response due to the instrumental limit(s). The corresponding M'' and Z'' peaks in the combined spectroscopic plots for x < 40 % are not overlapping, indicating there are at least two components, as shown in Fig 6-7 (b).

For the 1%Nb-BF-NBT series (Fig. 6-8 (a)), only a bulk arc is observed and the resistance increases by one order of magnitude compared with the BF-NBT series. From M'', Z'' spectroscopic plots as shown in Fig. 6-8 (b), the samples are electrically homogeneous, indicating that one of the electrical responses from the BF-NBT series is eliminated by 1 at% Nb doping. In this section, samples were measured at 10 Hz to 1M Hz due to the instrumental limit(s). The electrical behaviour for a lower frequency range, such as the Warburg diffusion response which may help to identify the predominant conducting mechanism, will be discussed in the next section. In the

presence of oxygen diffusion, oxygen ions may be blocked by Au electrodes, leading to a charge pile-up between the surfaces of the ceramic with the Au electrodes, which gives rise to a charge-transfer resistance and therefore a diffusive response (spike) in low frequency range.

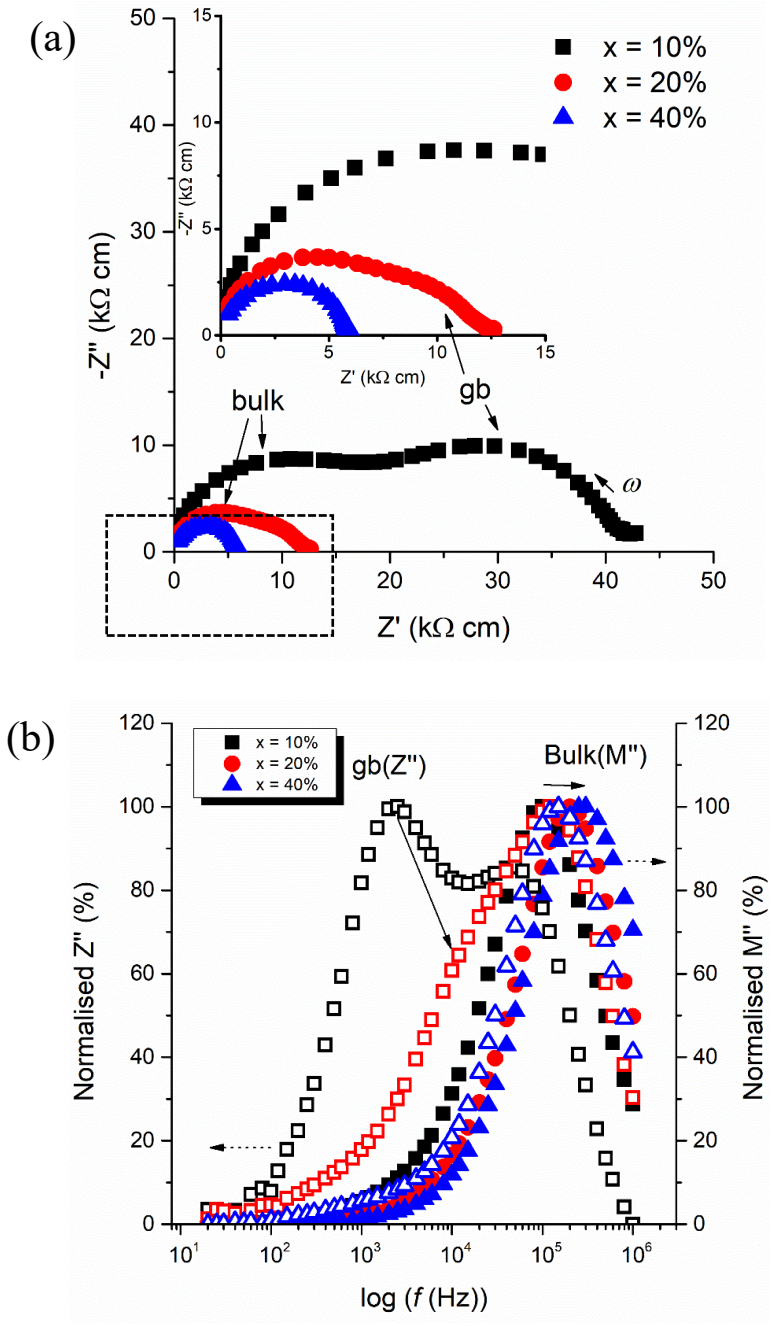

Fig. 6-7. (a) Z* and (b) M'' and Z'' spectroscopic plots for the BF-NBT series measured at 500 °C. Inset shows an expanded view of the dashed squared area. The M'' and Z'' peaks are represented as closed and open symbols, respectively.

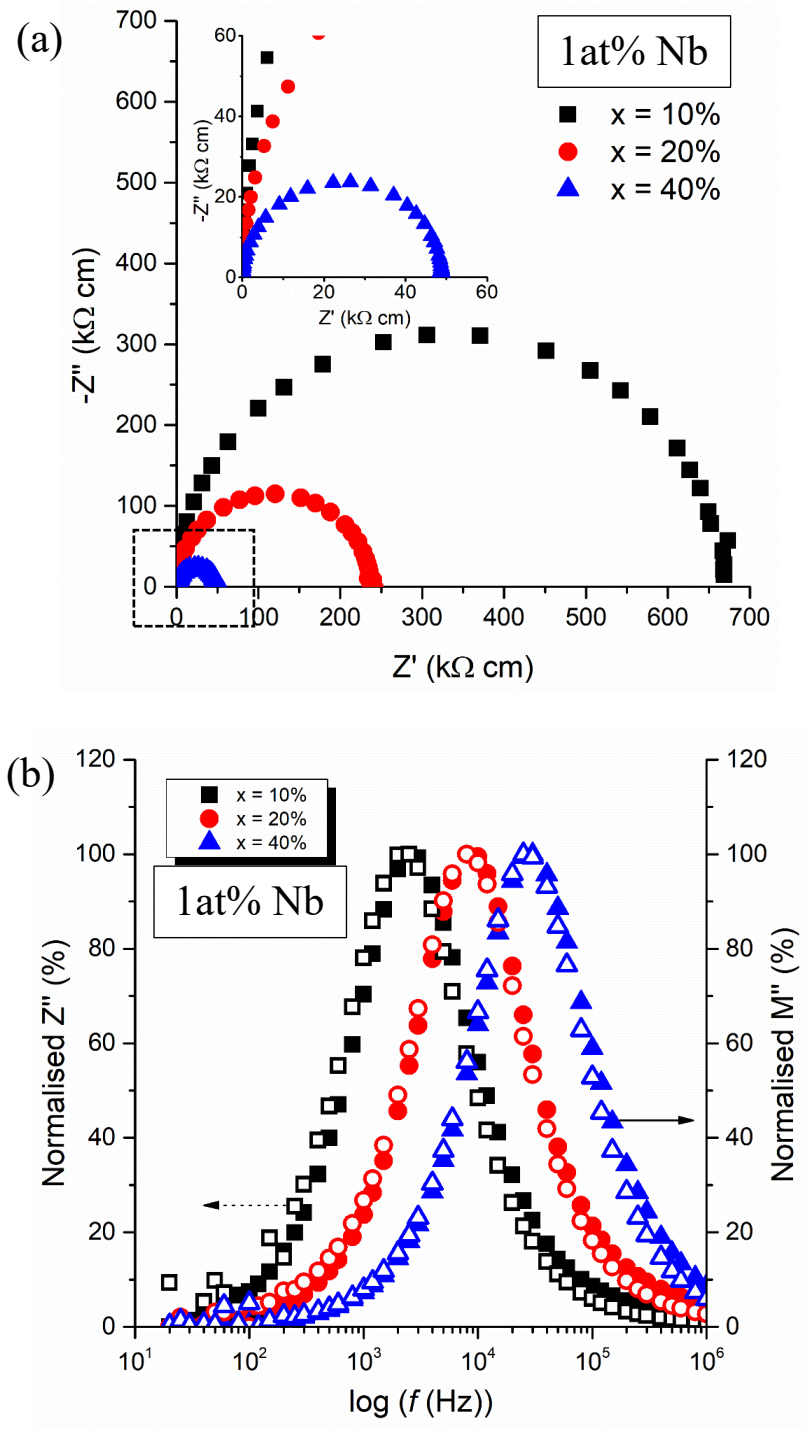

Fig. 6-8. (a) Z* and (b) M'' and Z'' spectroscopic plots for the 1%Nb-BF-NBT series measured at 500 °C. Inset in (a) shows expanded view of dashed squared area. The M'' and Z'' peaks in (b) are represented as closed and open symbols, respectively.

The pO_2 dependence of the impedance response for the BF-NBT series for x = 20, 40 and 60% are shown in Fig. 6-9 to 6-11, respectively. A low frequency spike (<

10Hz) is observed for x = 20 and 40%, which is a typical Warburg diffusion response and can be observed up to x = 50%, suggesting the presence of ionic conduction.

For x = 20% as shown in Fig. 6-9, the bulk M'' peak remains the same but the magnitude of the grain boundary Z'' peak increases and shifts towards lower frequency as pO_2 decreases. Therefore, the bulk and grain boundary are consistent with ionic and p-type electronic behaviour, respectively. For x = 40% (Fig. 6-10 (a)), the sample becomes relatively stable under different atmospheres and an electrode spike is still observed. The M'' and Z'' peaks are pO_2 independent (Fig. 6-10(b)), suggesting the bulk type response is dominated by ionic conduction. However, the total resistance tends to slightly increase with increasing pO_2, which is consistent with n-type electronic behaviour. This may be attributed to the secondary/grain boundary or electrode response. Similar behaviour is also observed for x = 50%. For x = 60% (Fig. 6-11), the data become noisy < 100 Hz and no Warburg diffusion is observed in the Z* plots. The resistance clearly decreases as pO_2 decreases which is consistent with p-type electronic behaviour. However, the electrical behaviour becomes relatively smooth/diffusive in the low frequency range under N_2, (see Fig 6.11) suggesting the electronic conduction can be suppressed under lower pO_2 such that ionic conduction is still present in the sample.

The pO_2 dependence of 1%Nb-BF-NBT for x = 20 and 40% are shown in Fig. 6-12. The Warburg diffusion response is eliminated by 1%Nb doping, suggesting that the ionic conduction associated with oxygen vacancies is suppressed according to equation 6-1. For x = 20%, the resistance decreases as pO_2 decreases which is consistent with n-type electronic behaviour. Similar results are also observed in Nb-doped NBT.[1] However, for x = 40 % the electrical response becomes relatively independent of pO_2 and the resistance increases as pO_2 decreases which is consistent with p-type electronic behaviour. By increasing the BF content, the electronic behaviour changes from n- to p-type at ~ x = 30%. No diffusive response in the lower frequency range under N_2 was observed for all samples, i.e. compares with Fig. 6-11.

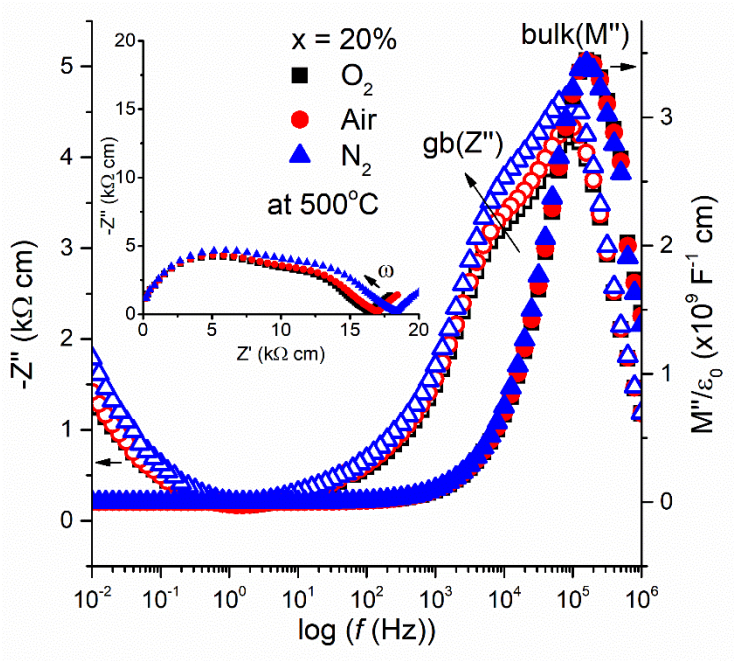

Fig. 6-9. M'' and Z'' spectroscopic plots for x = 20% under different flowing gas atmospheres measured at 500 °C. Inset shows Z* plots.

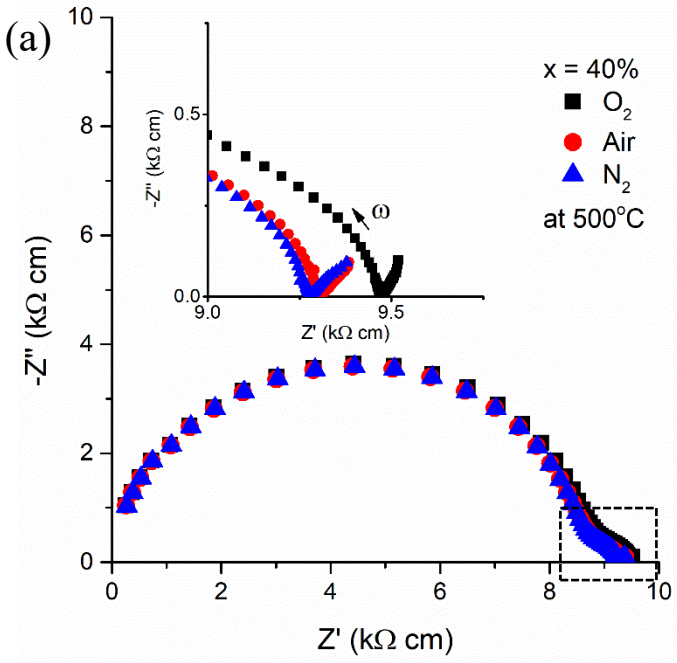

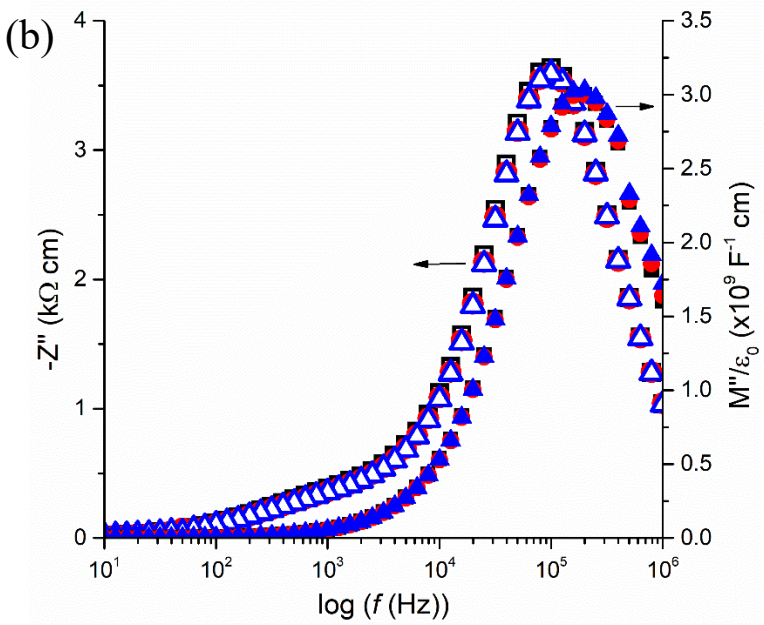

Fig. 6-10. (a)Z* and (b) M'' and Z'' spectroscopic plots for x = 40% under different flowing gas atmospheres measured at 500 °C. Inset in (a) shows expanded view of low frequency data (dashed squared area).

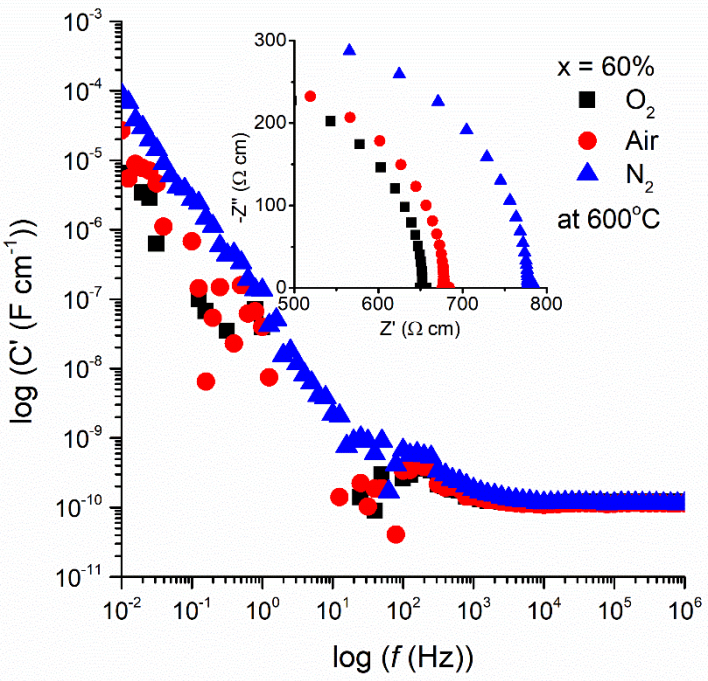

Fig. 6-11. Frequency dependence of log capacitance for x = 60% under different flowing gas atmospheres measured at 600 °C. Inset shows corresponding Z* plots.

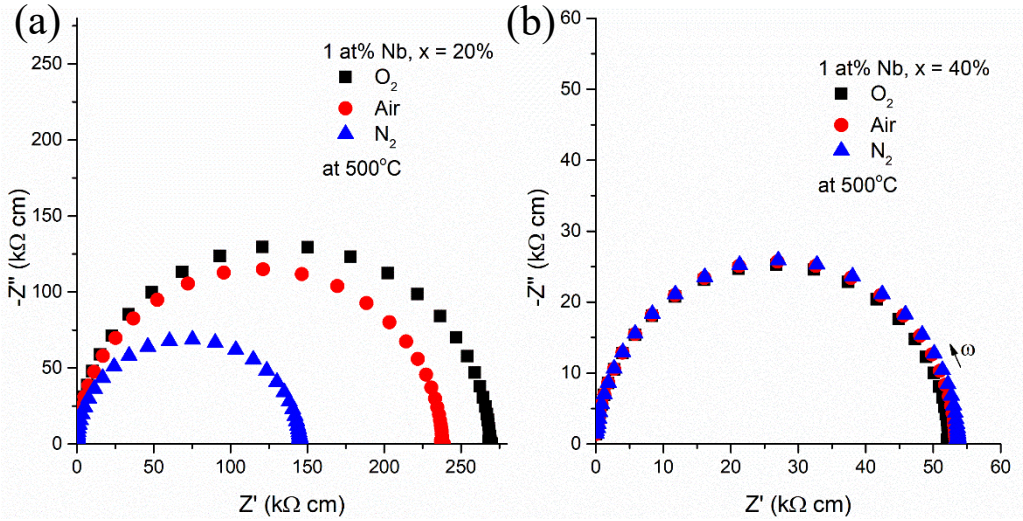

Fig. 6-12. Z* plots of the 1%Nb-BF-NBT series for (a) x = 20% and (b) x = 40% under different flowing gas atmosphere measured at 500 °C.

As mentioned in Fig. 6-7, the grain boundary response for the BF-NBT series decreases as the BF content increases and eventually a single electrical response is observed when x ≥ 40%, resulting in the Z'' peaks shifting slightly towards lower frequency. The 'bulk-like' Z'' peaks are almost equivalent to the overall response of the bulk and grain boundary and therefore they can be attributed to the total conductivity (σ_{total}). In general, the bulk (σ_b) and grain boundary (σ_{gb}) conductivity is extracted using the larger M'' and Z'' peaks, respectively.

Arrhenius plots of σ_b and bulk f_{max} for the BF-NBT are shown in Fig. 6-13. σ_b is relatively independent of the BF content up to x = 50% and increases again for x ≥ 60%. For x = 0 to 30 %, the activation energy (E_a) changes at around 350 °C which is consistent with the LCR results where T_m increases from 325 to 376 °C for x = 0 to 30% and indicates oxide-ion conduction dominated the bulk response in these samples. However, E_a becomes independent of T_m for x ≥ 40% which suggests a switch away from oxide-ion conduction towards mixed ionic/electronic conduction. Arrhenius plots of bulk f_{max} (Fig. 6-13 (b)) suggests the conduction behaviour for x ≤ 50% is similar to NBT which is dominated by ionic conduction, except for a significant difference at low temperature. It is noteworthy that there is a significant and systematic increase in f_{max} for x =60 and 70 %. The isothermal plots of σ_b for the BF-NBT series measured at 300 °C are shown in Fig. 6-14. σ_b continuously decreases with increasing BF content for x ≤ 50%, where the conduction behaviour is similar to NBT. This indicates that ionic

conduction may be suppressed by the BF-doping. A further increase in the BF content, such as x ≥ 60%, may enhance the electronic conductivity.

Arrhenius plots of σ_b and bulk f_{max} for the 1%Nb-BF-NBT series are shown in Fig. 6-15, which is compared to σ_{gb} and grain boundary f_{max} for the BF-NBT series. σ_b for the 1%Nb-BF-NBT series increases systematically with the BF content. σ_{gb} for the BF-NBT series (Fig. 6-15 (a)) also increases as x increases and its E_a is similar to σ_b of 1%Nb-BF-NBT ~ 1.13 eV. Arrhenius plots of bulk f_{max} for the 1%Nb-BF-NBT series compared with the grain boundary f_{max} of the BF-NBT series are shown in Fig. 6-15 (b). The grain boundary f_{max} of BF-NBT for x = 10-30% overlaps with the bulk f_{max} of the 1%Nb-BF-NBT for x = 10 and 40%, indicating that they may both have similar conducting mechanisms which is predominantly electronic conduction. Furthermore, the slope of the bulk f_{max} for x = 40% in Arrhenius plots significantly changes from 1.01 to 1.22 eV at T_m but E_a of σ_b is independent to T_m. However, no data is available around T_m for x ≤ 30%. In general, σ_b of BF-NBT for x ≤ 40% decreases more than 2 orders of magnitude by 1 at% Nb-doping.

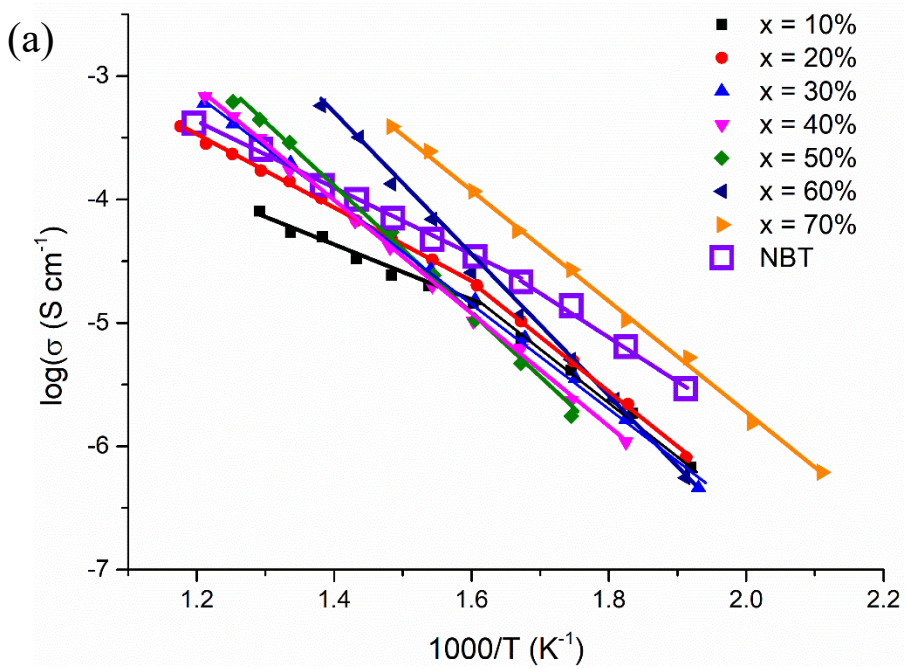

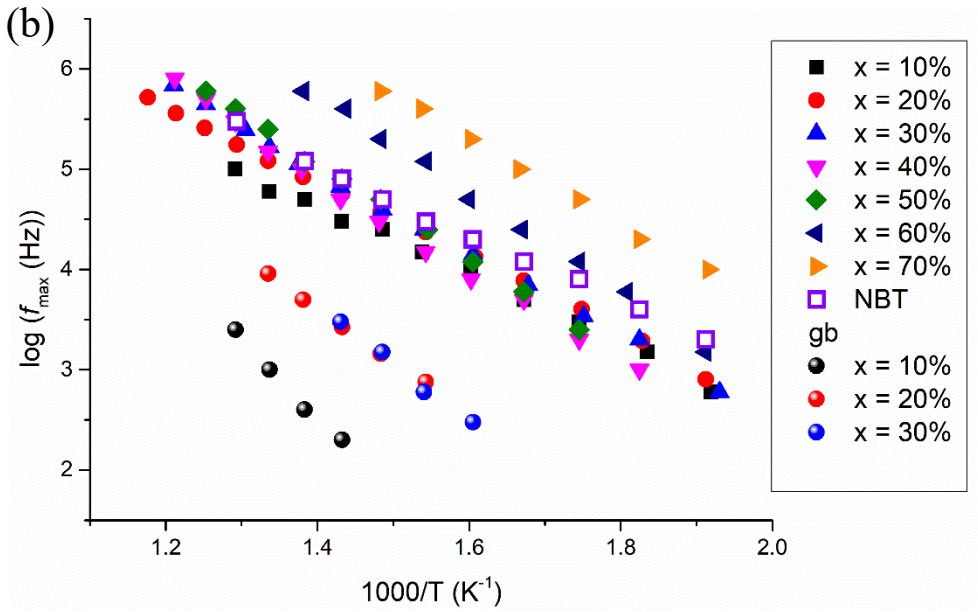

Fig. 6-13. Arrhenius plots of (a) σ_b and (b) bulk f_{max} extracted from M'' peaks for the NB-NBT series. Grain boundary f_{max} values extracted from Z'' peaks are also included in (b).

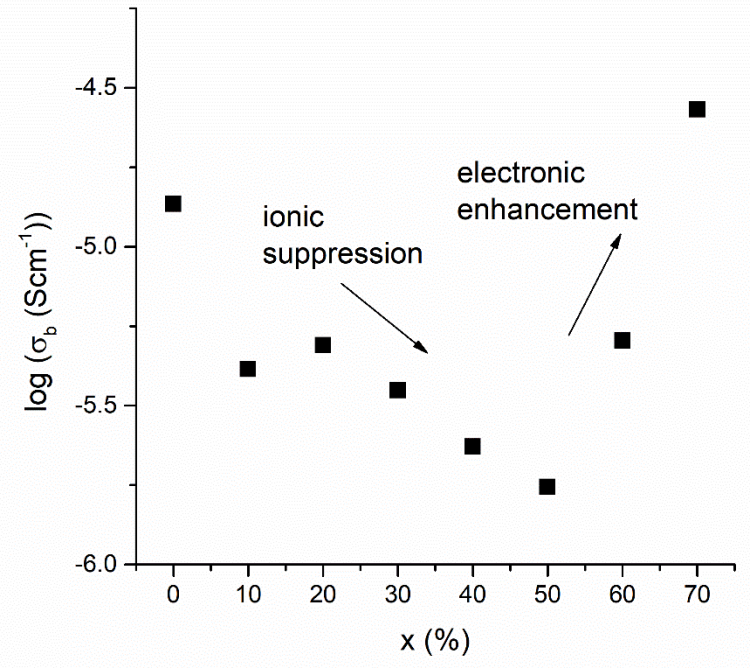

Fig. 6-14. Isothermal plots of σ_b measured at 300 °C for the BF-NBT series.

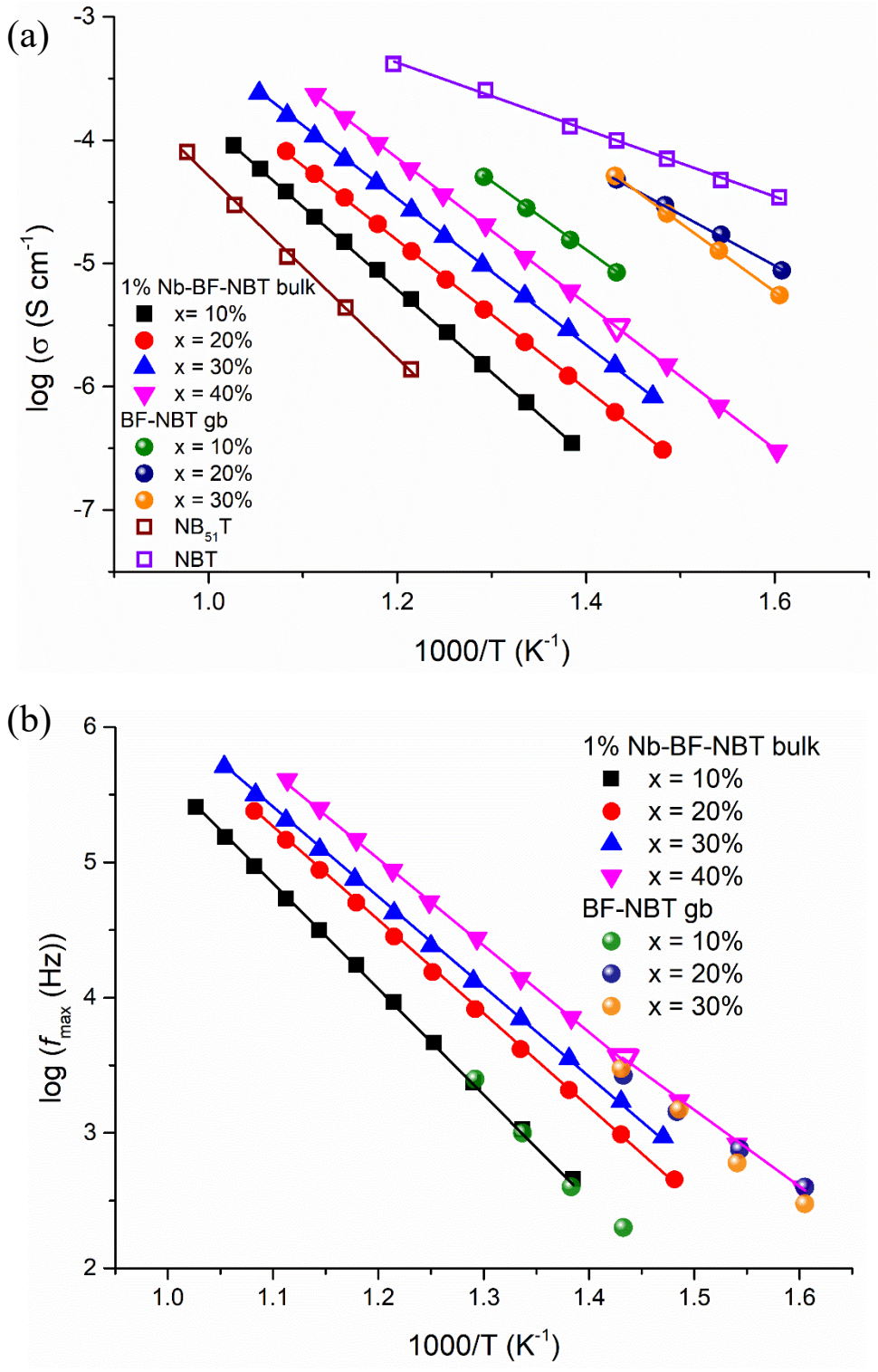

Fig. 6-15. Arrhenius plots of (a) σ_b and (b) bulk f_{max} for the 1%Nb-BF-NBT series. σ_{gb} for BF-NBT are also included. The open symbol indicates the data point at T_m for x = 40%.

The compositional dependence of E_a for σ_b of the BF-NBT and 1%Nb-BF-NBT series is summarised in Fig. 6-16. For the BF-NBT series, the change in E_a at T_m for $x \leq 30\%$ is possibly related to the coexistence of rhombohedral to tetragonal phases, where the migration barrier for oxygen ions in the rhombohedral phase (below T_m) is higher than in the tetragonal phase (above T_m).[14] For $x > 30\%$, E_a become independent of T_m, suggesting there is no difference in the migration barrier for oxygen vacancies in rhombohedral and tetragonal phases, presuming ionic conduction is dominant for $x = 40\%$ and 50%. For $x \leq 60\%$, E_a associated with tetragonal phase above T_m increases linearly from 0.46 to 1.12 eV with increasing BF content and eventually becomes close to E_a associated with rhombohedral phase below T_m 0.84~0.9 eV when $x = 40\%$. This suggests the increase in E_a may be attributed to the disassociation of oxygen vacancies trapped by B-site acceptor dopants, leading to overcome the deviation in the migration barrier for oxygen ions in the rhombohedral and tetragonal phases. For $x = 70\%$, E_a decreases to 0.89 eV, which is significantly lower than the 1.2 eV reported by Dorcet *et al.*.[4] However, E_a seems to decrease between $x = 60 \sim 100\%$ when electronic conduction is dominant.

For the 1%Nb-BF-NBT series, E_a decreases from 1.69[2] to 1.15 eV as the BF content increases from $x = 0$ to 40%, which is nearly half of the optical bandgap of NBT (3.0 ~ 3.5 eV)[15,16] and BF (2.3 ~ 2.8 eV)[17-19], respectively. The Nb-doped (1-3 mol%) BF reported by Jun *et al.*.[20] has similar E_a (1.01~1.11 eV), which is nearly half of the optical band gap of 80%BF-20%NBT (2.08 eV).[12]

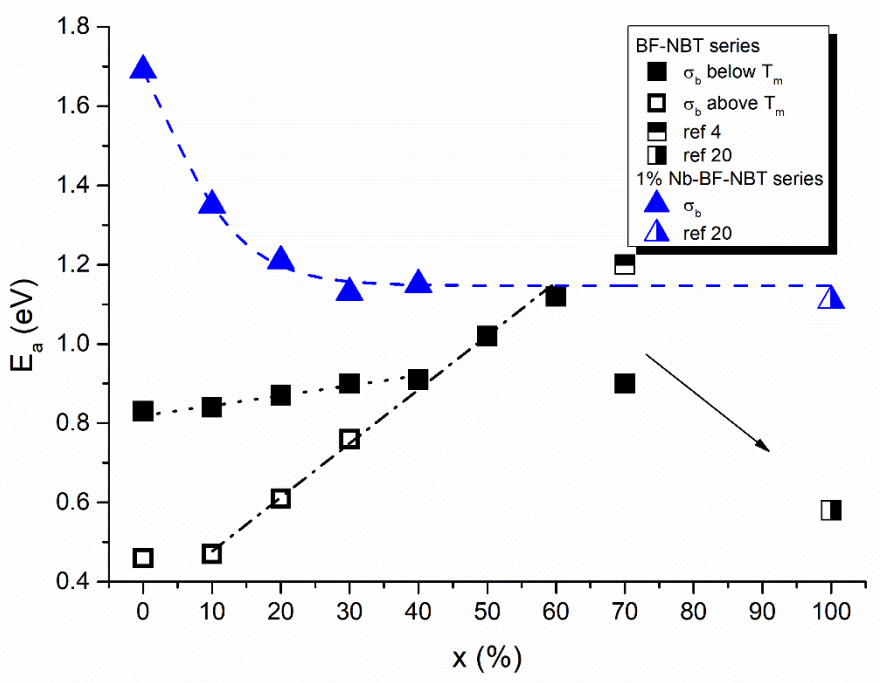

Fig. 6-16. Compositional dependence of E_a associated with σ_b for the BF-NBT and 1%Nb-BF-NBT series.

6.3 Discussion

For undoped NBT, the ionic conductivity is attributed to the formation of oxygen vacancies from Bi loss during ceramic processing according to the following equation[21]

$$2Bi_{Bi}^{x} + 3O_{O}^{x} \rightarrow 2V_{Bi}^{'''} + 3V_{O}^{\cdot\cdot} + Bi_2O_{3(g)} \qquad 6\text{-}3.$$

For undoped BF, it is known that the high leakage/conductivity is attributed to the formation of oxygen vacancies during sintering at high temperature, leading to the valence fluctuation of Fe ions, such as Fe^{2+} and Fe^{3+}.[22] The charge compensation can be described as the following equation:

$$2Fe_{Fe}^{x} + 2O_{O}^{x} \rightarrow 2Fe_{Fe}^{'} + V_{O}^{\cdot\cdot} + O_{2(g)} \qquad 6\text{-}4.$$

In the solid solution of BF-NBT, both defect mechanisms (equation 6-3 and 6-4) may possibly occur at high temperature and generate oxygen vacancies. This is consistent with the pO_2 dependence for $x \leq 50\%$, where the bulk response is dominated by ionic conduction. σ_b tends to decrease with increasing BF content and then increases for $x \geq 60\%$, where the predominant conduction mechanism switches from ionic to p-type

electronic behaviour, as shown in Fig. 6-14. This suggests that partial oxygen vacancies may be compensated by oxidising Fe^{3+} to Fe^{4+} during cooling and therefore reduce ionic conductivity according to the following equation:

$$V_O^{\cdot\cdot} + 2Fe_{Fe}^{x} + O_{2(g)} \rightarrow 2Fe_{Fe}^{\cdot} + 2O_O^{x} \qquad 6\text{-}5.$$

In addition, the decreasing σ_b with increasing E_a (Fig. 6-16) for x ≤ 50% may be attributed to trapping, where positively charged ($V_O^{\cdot\cdot}$) combines with negatively charged (Fe_{Ti}') to form the defect complex $(Fe_{Ti}' - V_O^{\cdot\cdot})^{\cdot}$. Therefore, the migration barrier and concentration of oxygen vacancies may increase and decrease with increasing BF content, respectively. Once the migration barrier energy increases to a value similar (or in excess) to half that of the bandgap for BF-NBT ~2.08 eV (i.e. 80%BF-20%NBT)[12], electronic conduction may become dominant, such as x ≥ 60%. It was found that ionic conduction may be still present in a sample measured at 600 °C under N_2 for x = 60%, as shown in Fig. 6-11. According to equation 6-5, Fe^{4+} ($Fe_{Fe}^{\cdot}$) ions may reduce to Fe^{3+} (Fe_{Fe}^{x}) ions under low pO_2, leading to a reduction in the electronic charge carrier concentration as a consequence the electronic conductivity. In addition, the concentration of oxygen vacancies ($V_O^{\cdot\cdot}$) may increase, leading to promote ionic conduction. Further analysis of oxygen ionic transport number by EMF measurements may help to confirm the conducting mechanism(s), where ionic conduction is expected to drop with increasing BF content.

The electrical behaviour of BF-NBT for x ≤ 40% is dramatically changed by 1 at% Nb-doping on Ti, such as an increase in resistance and E_a. The elimination of the Warburg diffusion response indicates the suppression of ionic conduction, where the ionic compensation is according to equation 6-1. In other words, the free charge carriers of the ionic conduction, such as oxygen vacancies, is extremely low and the suppression of ionic conduction leads to reduce the conductivity by more than 2 orders of magnitude. For the 1%Nb-BF-NBT series, E_a decreases continuously from 1.69 eV[2] for x = 0 and then stabilises ~ 1.15 eV for x ≥ 30%, whereas the electrical behaviour switches from relatively strong n- to weak p-type semi-conductivity at ~ x = 30%. For resistive/semi-conducting NBT, such as Nb-doped or Bi-rich NBT,[1,2] the electrical conduction is dominated by near intrinsic electronic conduction (E_g (bandgap) ~ $2E_a$) with a slight excess of n-type semi-conducting behaviour. Therefore, the intrinsic electron conduction of NBT may dominate for x ≤ 20%, where the predominant electrons are

hopping via the Ti-O-Ti bond between Ti^{3+} (Ti'_{Ti}) and Ti^{4+} (Ti^{x}_{Ti}) ions. The free electrons may be originated from partial Nb-doping on Ti according the following equation:

$$Nb_2O_5 + 4Ti^{x}_{Ti} \rightarrow 2Nb^{\cdot}_{Ti} + 2Ti'_{Ti} + 2TiO_2 + \frac{1}{2}O_{2(g)} \qquad 6\text{-}6.$$

where each Nb-donor dopant on Ti^{4+} ($Nb^{\cdot}_{Ti}$) may generate one electron, which is compensated by forming one Ti^{3+} (Ti'_{Ti}) ion.

The bond angle may be effectively changed with expansion of the lattice as the BF content increases, leading to suppress E_g and therefore a decrease of E_a. However, E_g of BF is significantly lower than NBT. Consequently, the electrons may be potentially hopping via the Fe-O-Fe bond between Fe^{4+} ($Fe^{\cdot}_{Fe}$) and Fe^{3+} (Fe^{x}_{Fe}) ions with increasing BF content, where the filling of the oxygen vacancies introduced by low pO_2 at high temperature causes the oxidation of Fe^{3+} to Fe^{4+} according the equation 6-5. The switch of n- to p- type semi-conduction for x = 30% may possibly be due to a change in conducting pathway from the Ti-O-Ti to Fe-O-Fe bond, where E_a becomes nearly half of E_g of BF or BF-NBT.

The compositional dependence of σ_b for the 1%Nb-BF-NBT series is shown in Fig. 6-17. The 70%BF-30%NBT and Nb-doped BF reported by Dorcet *et al.*[4] and Jun *et al.*[20], respectively, has E_a ~ half of E_g of BF and therefore the conductivity is also included for comparison. Surprisingly, the conductivity shown in Fig. 6-17 seems to increase almost linearly across the full solid solution of 1%Nb-BF-NBT. The BF-NBT series reported by Dorcet *et al.*[4] had lower leakage than my results, where the authors mentioned the conductivity of 70%BF-30%NBT can be further reduced by annealing treatment under O_2 atmosphere. However, no resulting data after annealing treatment was presented. In Nb-doped BF[20], the conductivity reduced by six orders of magnitude at 200 °C by 1 mol% Nb-doping and the associated E_a increased from 0.58 to 1.01 eV. 3 mol% Nb-doping only increased E_a to 1.11 eV without further reduction in conductivity. Therefore, as oxygen vacancies are compensated, the electrical conduction is increasingly dominated by electronic conduction. The conductivity directly depends on the BF content, where it increases with increasing BF content and the conducting mechanism switches from NBT-like to BF-like behaviour at ~ x = 30%.

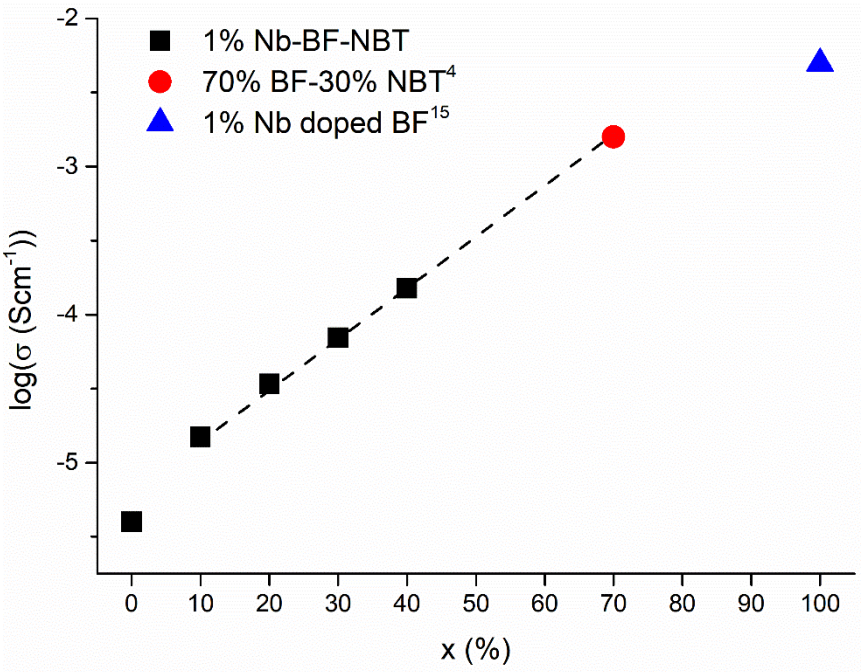

Fig. 6-17. Isothermal plots of σ_b for the 1%Nb-BF-NBT series measured at 600 ℃. The red circle and blue triangle are the conductivity of 70%BF-30%NBT and 1 mol% Nb-doped BF at 600 ℃ adopted from ref 4 and 20, respectively.

6.4 Conclusions

1. For the BF-NBT series, x = 0 ~ 70%, single-phase materials were obtained by conventional solid state synthesis using hand grinding as the mixing method. All samples can be characterised as the rhombohedral phase at room temperature, which is consistent with the literatures (ref 3 – 5). Similar results were obtained in the 1%Nb-BF-NBT series for x = 0 ~ 40%.

2. For the BF-NBT series, T_m increases continuously from 320 to 445 ℃ as x increases from 0 to 50% due to stabilisation of rhombohedral phase. However, leakage also increases with increasing BF content, leading to introduce an inductance for x > 50% at high temperature. On the other hand, 1 at% Nb doping for Ti can significantly suppress leakage to < 5% below 500 ℃ for x = 40%.

3. In the solid solution of BF-NBT, the ionic conductivity is slowly suppressed by the trapping of oxygen vacancies or oxidation of Fe, where the p-type electronic conductivity becomes predominant for x ≥ 60%.

4. The concentration of oxygen vacancies is small because 1 at% Nb-doping for Ti is enough to eliminate ionic conduction and (near) intrinsic conductivity becomes dominant.

5. To prepare a good NBT-based mixed conductor, oxygen vacancy trapping associated with B-site acceptor-dopants has to be avoided. For dielectric applications, Nb-doping on Ti looks promising to reduce the leakage current associated with oxygen vacancies.

6.5 References

1. Li, M., Li, L., Zhang, J. and Sinclair, D.C. Donor-doping and reduced leakage current in Nb-doped $Na_{0.5}Bi_{0.5}TiO_3$, *Applied Physics Letters*, **106**, 102904 (2015)

2. Li, L., Li, M., Zhang, H., Reaney, I.M. and Sinclair, D.C. Controlling mixed conductivity in $Na_{1/2}Bi_{1/2}TiO_3$ using A-site non-stoichiometry and Nb-donor doping, *Journal of Materials Chemistry C,* **4**, 5779 (2016)

3. Dorcet, V., Marchet, P. and Trolliard, G. Structure and dielectric studies of the $Na_{0.5}Bi_{0.5}O_3$-$BiFeO_3$ system, *Journal of the European Ceramic Society*, **27**, 4371-4374 (2007)

4. Dorcet, V., Marchet, P., Pena, O. and Trolliard, G. Properties of the solid solution (1-x)$Na_{0.5}Bi_{0.5}TiO_3$-(1-x)$BiFeO_3$, *Journal of Magnetism and Magnetic Materials*, **321**, 1762-1766 (2009)

5. Venkata Ramana, E. Suryanarayana, S.V. and Bhima Sankaram, T., Synthesis and magnetoelectric studies on $Na_{0.5}Bi_{0.5}TiO_3$-$BiFeO_3$ solid solution ceramics, *Solid State Sciences*, **12**, 956-962 (2010)

6. Dai, Z. and Akishige, Y., Electrical properties of multiferroic $BiFeO_3$ ceramics synthesized by spark plasma sintering, *Journal of Physics D: Applied Physics* **43**, 445403 (2010)

7. Paudel, T.R., Jaswal, S.S. and Tsymbal, E.Y., Intrinsic defects in multiferroic $BiFeO_3$ and their effect on magnetism, *Physical Review B – Condensed Matter and Materials Physics* **85**, 104409 (2012)

8. Morozov, M.I., Einarsrud M. and Grande, T., Control of conductivity and electric field induced strain in bulk $Bi_{0.5}K_{0.5}TiO_3$-$BiFeO_3$ ceramics, *Applied Physics Letters* **104**, 122905 (2014)

9. Morozov, M.I., Einarsrud M. and Grande, T., Atmosphere controlled conductivity and Maxwell-Wagner relaxation in $Bi_{0.5}K_{0.5}TiO_3$-$BiFeO_3$ ceramics, *Journal of Applied Physics* **115**, 044104 (2014)

10. Wefring, E., Einarsrud M. and Grande, T., Electrical conductivity and thermopower of (1-x)$BiFeO_3$-x$Bi_{0.5}K_{0.5}TiO_3$ (x = 0.1, 0.2) ceramics near the ferroelectric to paraelectric phase transition, *Physical Chemistry Chemical Physics* **17**, 9420-9428 (2015)

11. Fujii, I., Ito, Y., Suzuki, T. and Wada, T., Ferroelectric and piezoelectric properties of $(Bi_{1/2}Na_{1/2})TiO_3$-$BiFeO_3$ ceramics, *Journal of Materials Research*, **31**(1), 28-35 (2016)

12. Liu, H., Guo, Y., Guo, B. and Zhang, D. Synthesis and visible-light photocatalysis capability of $BiFeO_3$-$(Na_{0.5}Bi_{0.5})TiO_3$ nanopowders by sol-gel method, *Solid State Sciences*, **19**, 69-72 (2013)

13. Arnold, D.C., Knight, K.S. Morrison, F.D. and Lightfoot, P. Ferroelectric-Paraelectric Transition in $BiFeO_3$: Crystal Structure of the Orthorhombic β Phase, *Physical Review Letters*, **102**, 027602 (2009)

14. Meyer, K. and Albe, K., Influence of phase transitions and defect associates on the oxygen migration in the ion conductor $Na_{1/2}Bi_{1/2}TiO_3$, *Journal of Materials Chemistry A*, **5**, 4368-4375 (2017)

15. Li, J., Wang, G., Wang, H., Tang, C. Wang, Y., Liang, C., Cai, W., and Zhang, L. *In situ* self-assembly synthesis and photocatalytic performance of hierarchical $Bi_{0.5}Na_{0.5}TiO_3$ micro/nanostructures, *Journal of Materials Chemistry*, **19**, 2253-2258 (2009)

16. Bousquet, M., Duclere, J.R., Orhan, E., Boulle, A., Bachelet, C. and Champeaux, C., Optical properties of an epitaxial $Na_{0.5}Bi_{0.5}TiO_3$ thin film grown by laser ablation: Experimental approach and density functional theory calculations, *Journal of Applied Physics*, **107**, 104107 (2010)

17. Gujar, T.P., Shinde, V.R. and Lokhabde, C.D., Nanocrystalline and highly resistive bismuth ferric oxide thin films by a simple chemical method, *Material Chemistry and Physics*, **103**, 142-146 (2007)

18. Xu, Y., and Shen, M., Structure and optical properties of nanocrystalline $BiFeO_3$ films prepared by chemical solution deposition, *Materials Letters*, **62**, 3600-3602 (2008)

19. Palai, R., Katiyar, R.S., Schmid, H., Tissot, P., Clark, S.J., Robertson, J., Redfern, S.A.T., Catalan, G. and Scott, J.F., β phase and γ- β metal-insulator transition in multiferroic $BiFeO_3$, *Physical Review B*, **77**, 014110 (2008)

20. Jun, Y., Moon, W., Chang, C., Kim, H., Ryu, H.S., Kim, J.W., Kim, K.H. and Hong, S., Effects of Nb-doping on electric and magnetic properties in multi-ferroic $BiFeO_3$ ceramics, *Solid State Communications*, **135**, 133-137 (2005)

21. Li, M., Zhang, H., Cook, S.N., Li, L., Kilner, J.A., Reaney, I.M. and Sinclair, D.C., Dramatic Influence of A-Site Nonstoichiometry on the Electrical Conductivity and Conduction Mechanisms in the Perovskite Oxide $Na_{0.5}Bi_{0.5}TiO_3$, *Chemistry of Materials*, **27**, 629-634 (2015)

22. Palkar, V.R., John, J. and Pinto, R., Observation of saturated polarization and dielectric anomaly in magnetoelectric $BiFeO_3$, *Applied Physics Letters*, **80**, 1628 (2002)

Chapter 7

BNiT-NBT

$BiNi_{0.5}Ti_{0.5}O_3$ (BNiT) is a high pressure phase which has orthorhombic symmetry.[1,2] It can form a wide solid solution with $PbTiO_3$ and $BaTiO_3$ as end members under ambient pressure.[3,4] The objective of such solid solutions is to develop high T_c ceramics for dielectric applications; however, an increase in dielectric loss for a certain level of BNiT-doping (> 30 mol%) was observed in the low frequency range (100 Hz) at high temperature.[3,4] Bai *et al*..[5] investigated the solid solution of BNiT-NBT (xBNiT-(1-x)NBT, x = 2 ~ 18 %) using conventional solid state synthesis. Two morphotropic phase boundaries (MPB) associated with the optimized piezoelectric constant (d_{33}) and strain response (S_{max}/E_{max}) were observed for x = 6 and 14%, respectively. They suggested that the non-cubic (rhombohedral) distortion decreased with increasing BNiT content and therefore the coexistence of rhombohedral and tetragonal phases occurred for x ≥ 6 %, where the ferroelectric properties were dominated by the rhombohedral phase for x < 14%. However, the solid solution limit and the electrical properties of high BNiT content (> 18%) remain unknown.

In this chapter, a BNiT-NBT series (x = 10~80%, $Na_{0.5-x}Bi_{0.5+x}Ti_{1-x}Ni_xO_3$. denoted as (x)BNiT-(1-x)NBT) was prepared by conventional solid state synthesis using ball milling as the mixing method. The doping mechanism of the BNiT-NBT series is similar to the BF-NBT series, where the acceptor-dopant on the B-site is compensated by the donor-dopant on the A-site. The starting material for Ni is NiO and the oxidation state is assumed to be +2. Therefore, the charge compensation for BNiT-NBT series is based on the following nominal equation:

$$Bi_2O_3 + 2NiO + 2Na_{Na}^{x} + 2Ti_{Ti}^{x} \rightarrow 2Bi_{Na}^{\cdot\cdot} + 2Ni_{Ti}^{\prime\prime} + Na_2O + 2TiO_2 \qquad 7\text{-}1.$$

For each Bi donor dopant for Na on the A-site, it requires one Ni acceptor dopant for Ti on the B-site to obtain charge compensation. This mechanism does not involve any change in oxygen content.

This chapter follows the investigation of the BF-NBT series, regarding the influence on the electrical properties of NBT by B-site accepter doping using a transition metal ion with a different oxidation state (Fe^{3+}→Ni^{2+}). . The solid solution

limit was confirmed by XRD and SEM. The complexity of the phase coexistence at room temperature was revealed by neutron diffraction (ND) studies. The temperature dependence of the relative permittivity and conductivity were studied by LCR and IS. The conducting mechanism was investigated by EMF measurements.

7.1 Phase purity and microstructure

Samples were calcined twice at 800 ℃ for 2h followed by 825 ℃ for 2h. The sintering temperature was 1100 ℃ for 6h, except for x= 10% which was sintered at 1150 ℃ for 4h. Room temperature XRD patterns of calcined powders for selected samples are shown in Fig. 7-1. The XRD pattern for x = 20% consists of NBT and $Na_{0.5}Bi_{4.5}Ti_4O_{15}$ (NBiT, ICDD: 04-017-3364) as the main and secondary phase, respectively, where the latter has a single peak at ~ 30.4 2θ^o. Three main secondary phases were identified as $Bi_{12}TiO_{20}$ (BiT, ICDD: 04-006-1863), NBiT and NiO (ICDD: 01-089-3080) for x ≥ 30%, which increased with x. The calcined powders for x = 60% were annealed at higher temperature from 850-950 ℃ for 2h (placed on a gold foil in a covered crucible) in attempts to improve the phase purity. Powders were weighed before and after annealing. XRD patterns show the NBT peaks to increase significantly as the annealing temperature increases as shown in Fig. 7-2. However, large amounts of secondary phases still remained at 950 ℃ and a significant amount of weight loss was also observed (up to 12 wt%) possibly due to the volatile Bi-rich phases which melt at < 875 ℃. Therefore, the calcining temperature was kept at 825 ℃ for all samples.

XRD patterns obtained from polished pellet surfaces sintered above 1100 ℃ are shown in Fig. 7-3. Single-phase samples were obtained for x ≤ 60% and secondary phases (same as obtained in calcined powders) increased with x for x ≥ 70%. The rhombohedral superlattice peak at ~ 38.5 2θ^o becomes undetectable for x > 20%, indicating the rhombohedral distortion decreases with x. The pseudo-cubic cell volume increases continuously up to x = 60% and then becomes relatively similar for x > 60%, as shown in Fig. 7-4. This indicates that x = 60% is very close to the solid solution limit. However, the slope of the trend line changes at ~ x = 30%, suggesting the average structure may change with decreasing rhombohedral distortion.

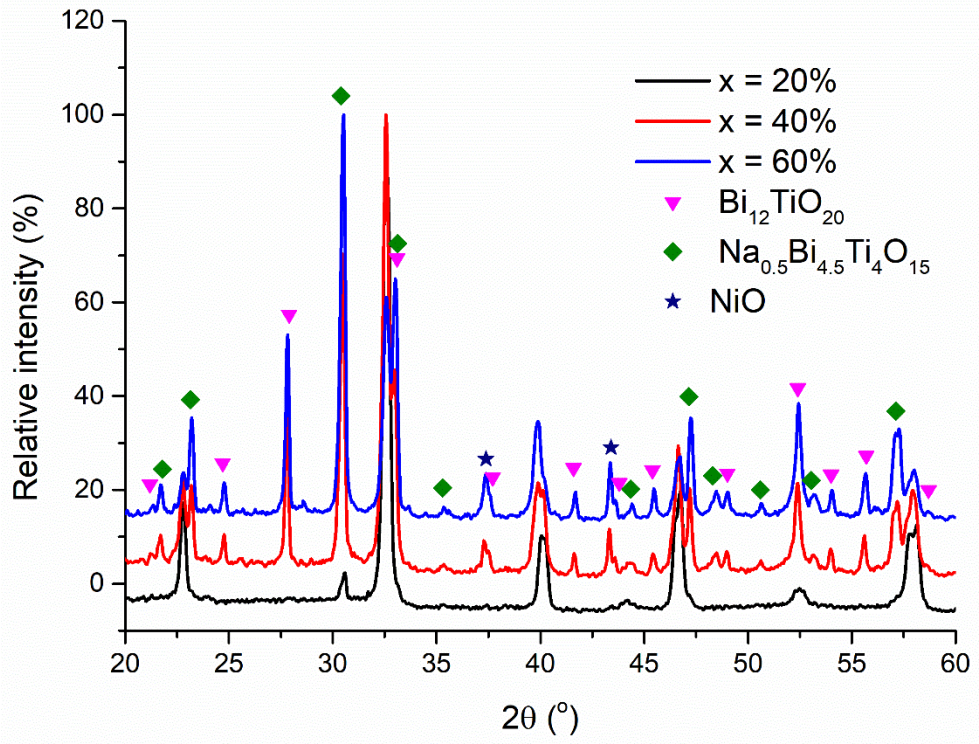

Fig. 7-1. Room temperature XRD patterns of calcined powders for selected samples.

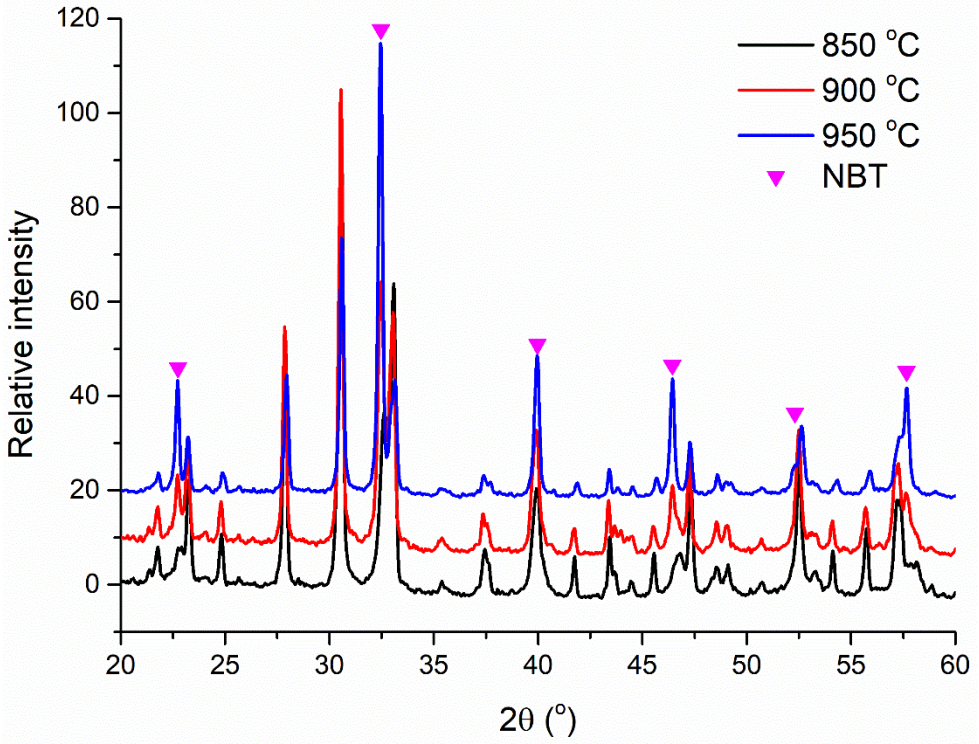

Fig. 7-2. Room temperature XRD patterns of x = 60% calcined at different temperatures for 2h.

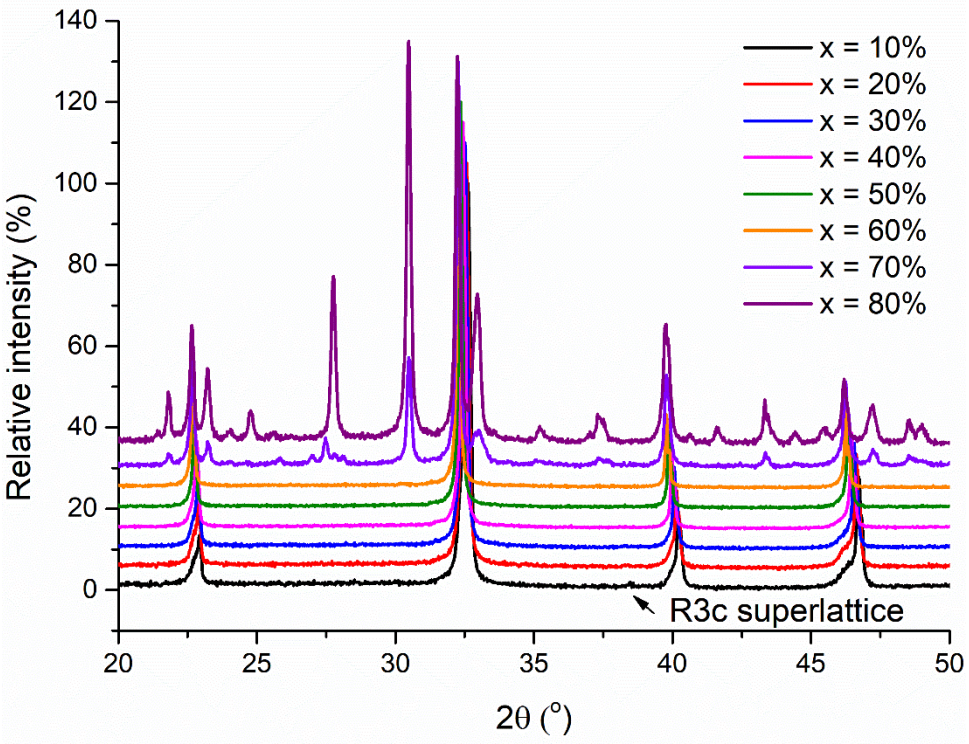

Fig. 7-3. Room temperature XRD patterns for the BNiT-NBT series obtained from polished pellet surfaces sintered above 1100 °C.

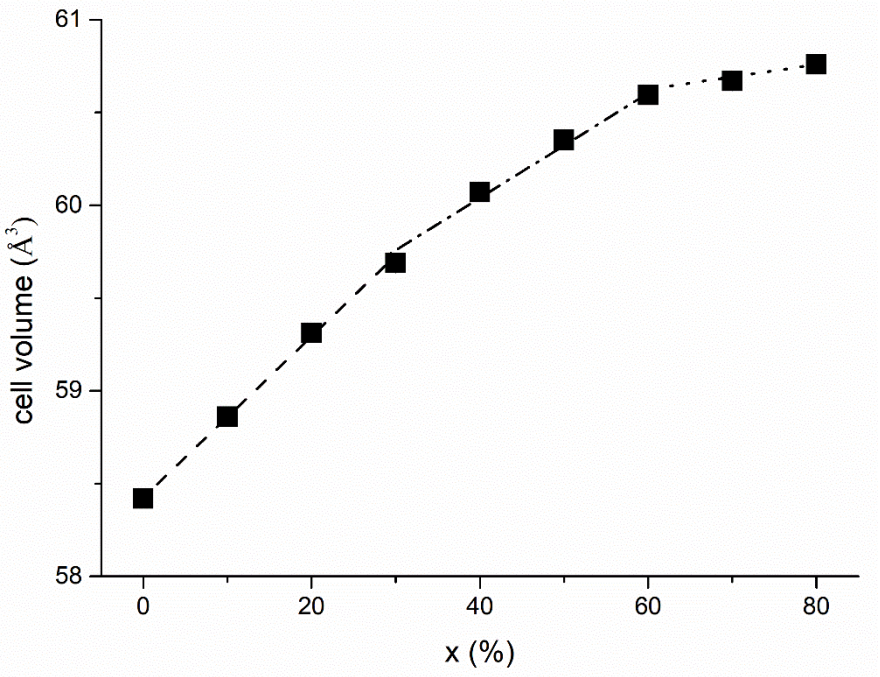

Fig. 7-4. The pseudo-cubic cell volume for the BNiT-NBT series. Error bars are within the symbols.

ND patterns for x = 20, 40 and 60% obtained from ground powders at room temperature are shown in Fig. 7-5. Samples were sintered at 1100 ℃ for 6h except for x = 60% which was sintered at a lower temperature of 1050 ℃. The reflections were refined according to the neutron PDF data reported by Jones and Thomas[6]. The fitting results for x = 20% (Fig. 7-5 (a)) were in good agreement with the rhombohedral (R) phase with space group R3c. However, extra peaks were observed for x = 40 and 60% as shown in Fig. 7-5 (c), which can be indexed as the tetragonal (T) phase with space group P4bm (Fig. 7-5 (b)). No secondary phases were detected for any of the samples. Therefore, the tetragonal and rhombohedral phases coexist at room temperature for x = 40 and 60%, where the tetragonal phase is ~ 74.3 and 63.2 wt%, respectively. The ratio of tetragonal phase at room temperature may be related to the sintering condition, where x = 60% which was sintered at a lower temperature tends to have a lower weight ratio of tetragonal phase compared to x = 40%. These results are consistent with XRD results, as shown in Fig. 7-5 (d), where the rhombohedral distortion can only be observed for x = 20%, which gives rise to the peak broadening/splitting of the 111_p reflection and the superlattice peak at ~38.5 $2\theta^o$ associated with oxygen octahedral tilting.[6] In contrast, the diffraction peaks for x = 40 and 60% become sharper and narrower, which have better fitting(s) with a pseudo-cubic phase than with a tetragonal phase, suggesting the tetragonal distortion (c/a) is very small, i.e. the lattice parameter for x = 60% indexed as a tetragonal phase with space group P4bm: a = 3.9280(4) Å and c = 3.9265(4) Å. The change in the tendency of lattice parameter at x = 30% (Fig. 7-4) may possibly be an indication of where the average structure starts to change from the rhombohedral to tetragonal phase due to the phase coexistence.

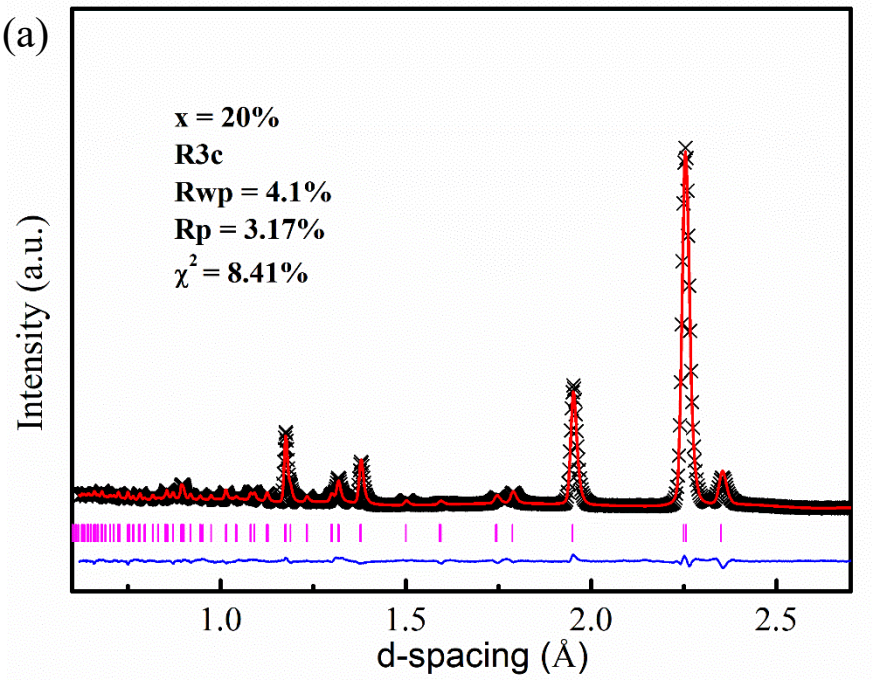
(a)
x = 20%
R3c
Rwp = 4.1%
Rp = 3.17%
χ² = 8.41%
Intensity (a.u.)
1.0
1.5
2.0
2.5
d-spacing (Å)

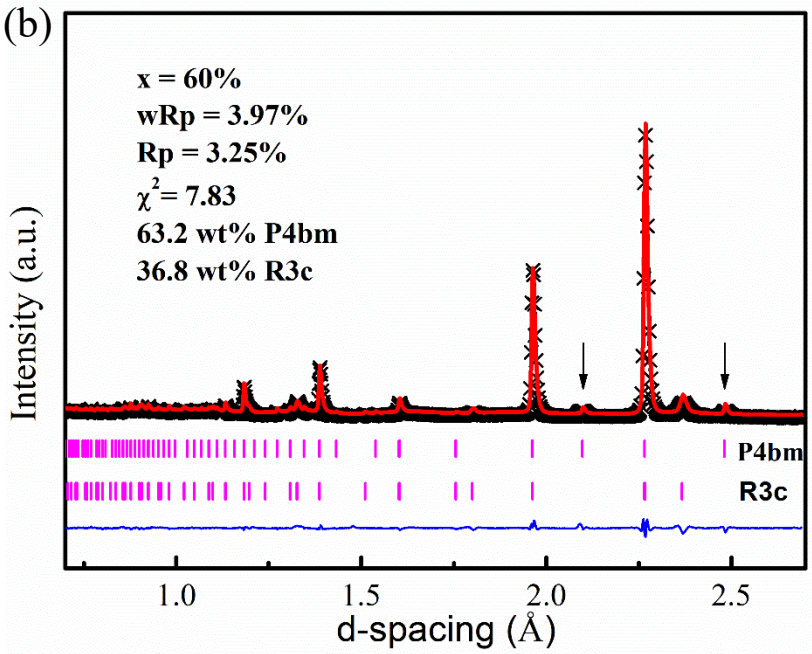
(b)
x = 60%
wRp = 3.97%
Rp = 3.25%
χ²= 7.83
63.2 wt% P4bm
36.8 wt% R3c
P4bm
R3c
Intensity (a.u.)
1.0
1.5
2.0
2.5
d-spacing (Å)

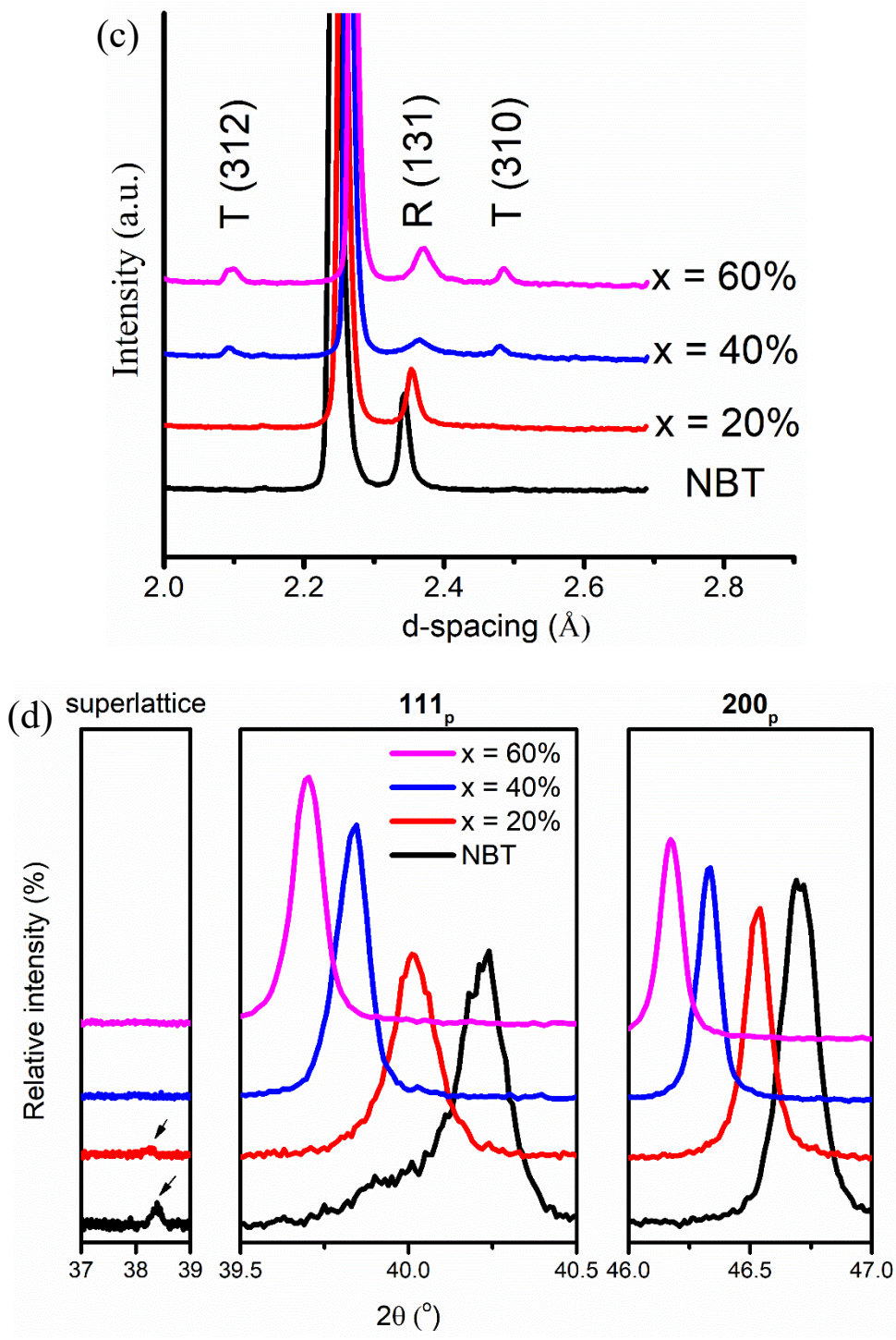

Fig. 7-5. Rietveld refinement of ND patterns for (a) x = 20% in R3c and (b) x = 60% in R3c and P4bm obtained at room temperature. The observed and calculated patterns are presented as the black crosses and red solid line, respectively. Bragg reflections of R3c and Pb4m are indicated by tick marks. The R-factors (Rwp and Rp) and goodness-of-fit (χ^2) of each fit are also indicated in the figure. (c) ND and (d) XRD patterns for x = 0~60%; R and T represents rhombohedral and tetragonal phase, respectively.

Further phase purity and microstructural analysis was performed by SEM and EDS. The SEM images for x = 20 and 40% are shown in Fig. 7-6, with similar results also observed for x ≤ 30% and x ≥ 40%, respectively. Small amounts of NiO are identified as a secondary phase for x ≥ 40% as shown in Fig. 7-6 (c) and (d). The grain size is similar ~ 6.5 μm. No plate-like grains related to the NBiT phase were observed. The EDS results for bulk compositions are summarised in Fig. 7-7. The bulk compositions are consistent with the expected values, except that the experimental compositions have slightly higher Bi content ~ 1.5 at% due to the instrumental setup as this happened for all samples. The Ni content is slightly lower than expected for x > 30%, where the NiO as a secondary phase tends to increase with x. This is possibly due to the Bi-loss accelerated by the liquid phase BiT at high temperature, leading to precipitate partial BNiT dopants out, such as NiO.

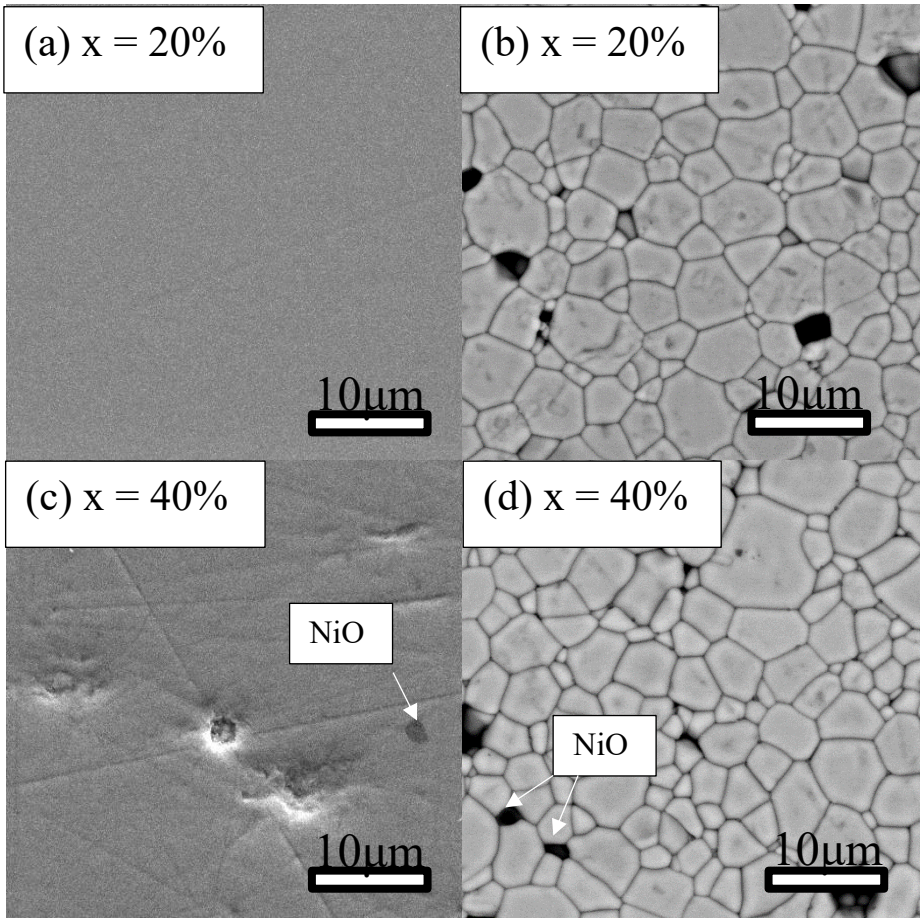

Fig. 7-6. SEM secondary electron images of (a) and (c) for x = 20 and 40%, respectively. Backscattering images (b) and (d) of thermally etched surfaces for x = 20 and 40%, respectively.

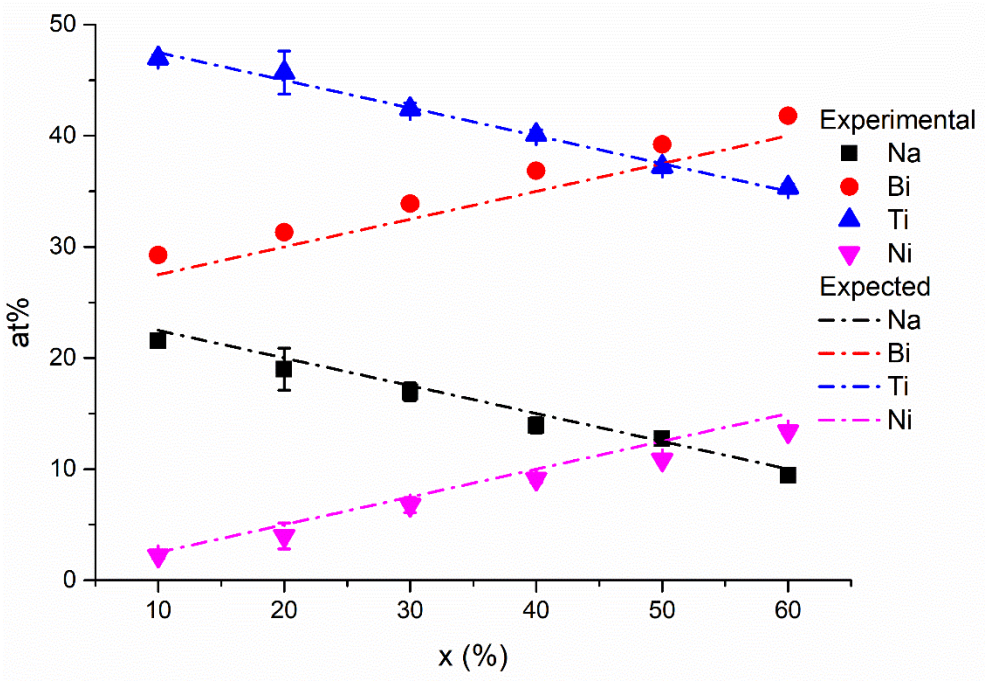

Fig. 7-7. EDS average chemical bulk composition results for the BNiT-NBT series.

7.2 Electrical properties

The temperature dependence of ε_r and tan δ at 1 MHz for single-phase compositions (x ≤ 60%) measured on heating are shown in Fig. 7-8. $\varepsilon_{r,\,max}$ and T_m measured on heating and cooling are summarised in Fig. 7-9. During heating, $\varepsilon_{r,\,max}$ decreases continuously with x. T_m slightly increases from 323 to 342 °C for x ≤ 20%, where the maximum occurs for x = 10%. Similar results have been reported by Bai *et al.*[5] where the maximum T_m ~ 340 °C occurred for x = 8%. T_m begins to drop dramatically for x > 20% in cooperation with the peak flattening, as shown in Fig. 7-8 (a). tan δ of NBT (x = 0) significantly decreases for x = 10% and then continuously increases with x. It is worth noting that the high permittivity of ~ 950 for x = 60% is relatively temperature independent between 100 ~ 500 °C. However, tan δ is above 5% from room temperature, which is unfavourable for dielectric applications. During cooling, the permittivity profile is similar to that of heating, except T_m is significantly lower for x > 20%, as shown in Fig. 7-9.

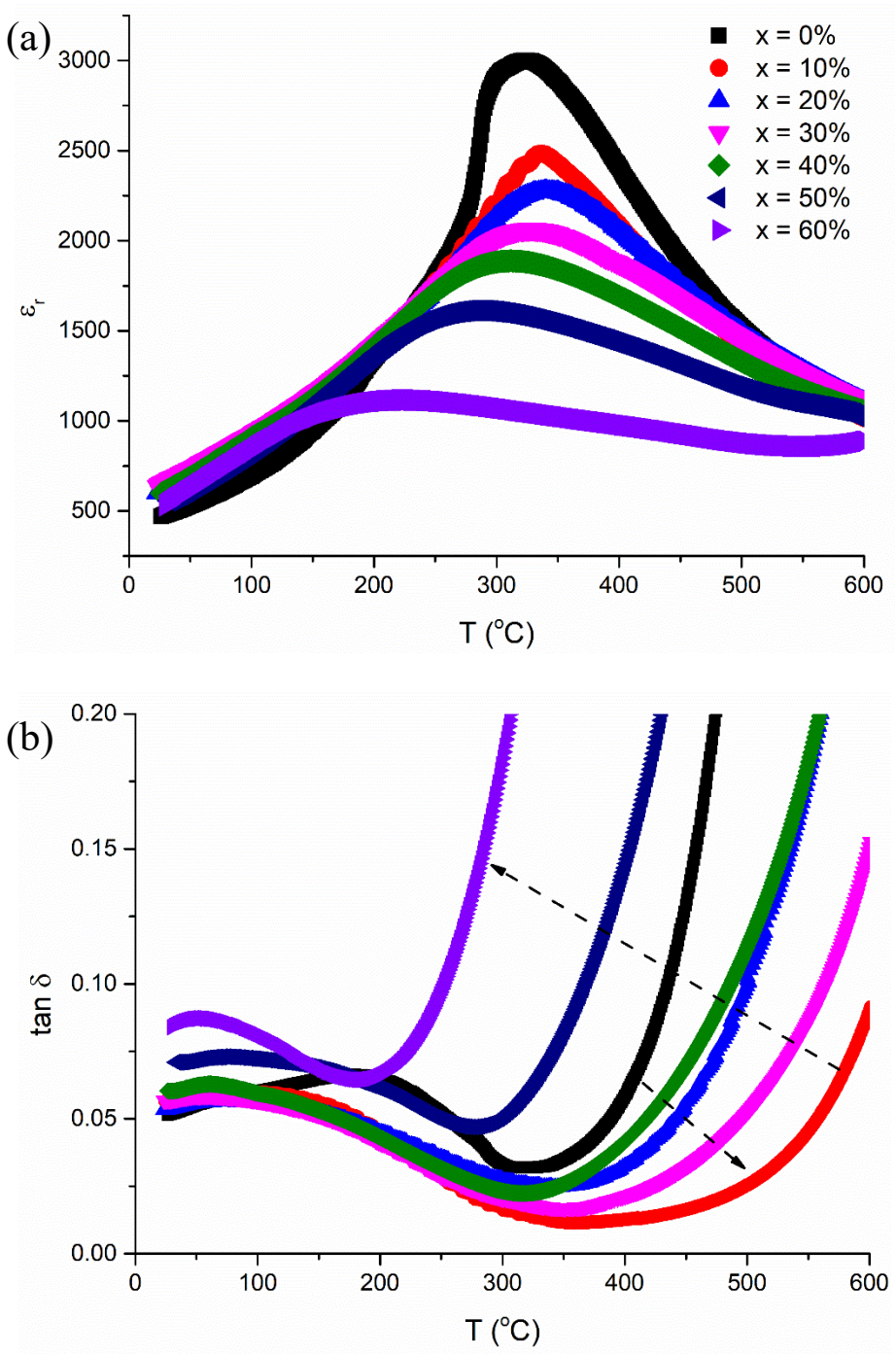

Fig. 7-8. Temperature dependence of (a) ε_r (b) tan δ at 1 MHz for x ≤ 60% at 1 MHz measured on heating.

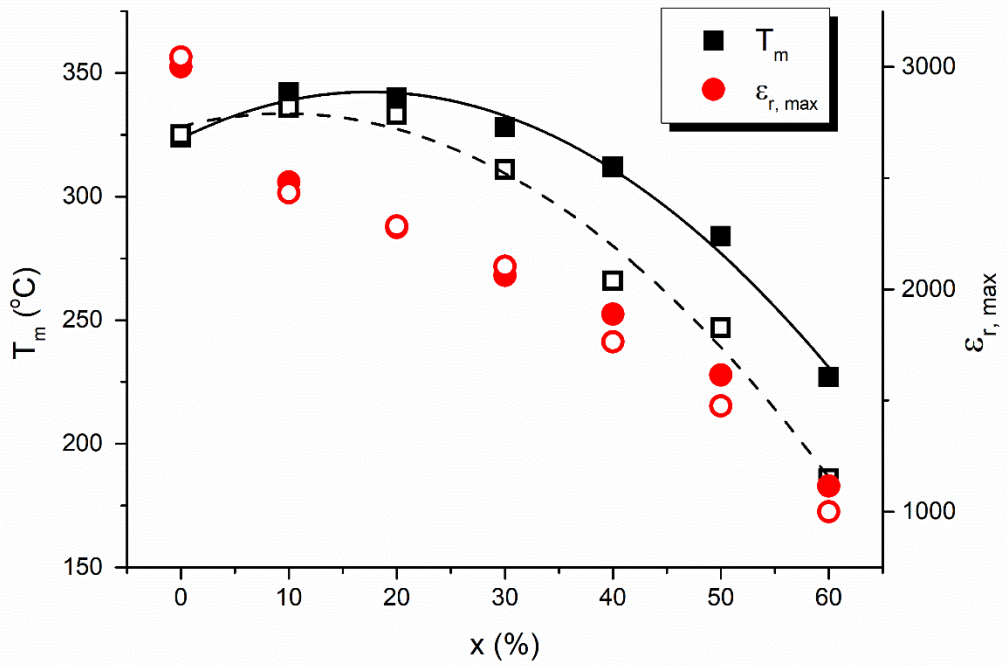

Fig. 7-9. Compositional dependence of $\varepsilon_{r,\,max}$ and T_m for $x \leq 60\%$. Closed and open symbols indicate data collected during heating and cooling, respectively.

Z* plots and equivalent circuit fittings for x = 20 and 40 % measured at 300 and 250 °C are shown in Fig. 7-10. There are three and two arcs for $x \leq 20\%$ and $x \geq 30\%$ at low temperature, respectively. The low frequency arcs tend to merge into the high frequency arc at higher temperatures. A resistor connected in parallel with a constant phase element (R-CPE) was used to fit the data for each arc, where the (R-CPE) units were connected in series for the equivalent circuit. The capacitance is calculated from the CPE parameters based on the following equation[7]

$$C = \left(R^{(1-n)} \times Q\right)^{\frac{1}{n}} \qquad 7\text{-}2.$$

where C (F cm^{-1}) and R (Ω) are capacitance and resistance, respectively. The Q (F cm^{-2} $S^{(n-1)}$) and n are CPE parameters, where the latter has a value $0 < n < 1$. The CPE behaves capacitive and resistive when n is close to 1 and 0, respectively and an ideal capacitor has n = 1.

The bulk arc fitting (R-CPE1) has $n > 0.98$, indicating the fitted data is sensible for extracting bulk capacitance and resistance. Fig. 7-11 shows the temperature dependence of bulk ε_r extracted from fitted IS data. A similar trend is observed

compared to the LCR results (obtained at 1 MHz) presented in dashed lines, where $\varepsilon_{r,\,max}$ and T_m decrease as x increases, indicating the LCR results are dominated by the bulk response. However, the LCR results show a relatively large $\varepsilon_{r,\,max}$ suppression for $x \leq 20\%$ compared to the bulk responses, where the samples consist of three arcs at low temperature. The second arc fitting (R-CPE2) for $x \leq 20\%$ has $n > 0.97$ which could reasonably be considered as a simple RC element, where the resistance (R_2) is almost the same as the bulk resistance (R_1) and the ratio of the calculated capacitance (C_2) to the bulk capacitance (C_1) is 3 ~ 7 between 250 to 550 °C, as shown in Fig. 7-12. C_1 and C_2 decrease above ~ T_m, indicating they both have bulk-type behaviour with similar compositions. The capacitance ratio (C_2/C_1) seems to be stable at ~ 3.8 and 5.2 above T_m for x = 10 and 20%, respectively, suggesting the bulk (R-CPE1) and secondary (R-CPE2) component may have a fixed volume fraction. Based on these observations, a core-shell type behaviour may occur for $x \leq 20\%$, where two bulk-type components (R-CPE1 and R-CPE2) with a small compositional deviation and a fixed volume fraction are connected in series. Furthermore, C_3 extracted from the R-CPE3 is between 10^{-8} and 10^{-9} F cm^{-1} and the difference between C_3 and C_1 is more than one order of magnitude, which is a typical grain boundary response. Similar results are also obtained from C_2 for $x \geq 30\%$. Therefore, C_3 and C_2 for respective $x \leq 20\%$ and $x \geq 30\%$ correspond to the grain boundary responses.

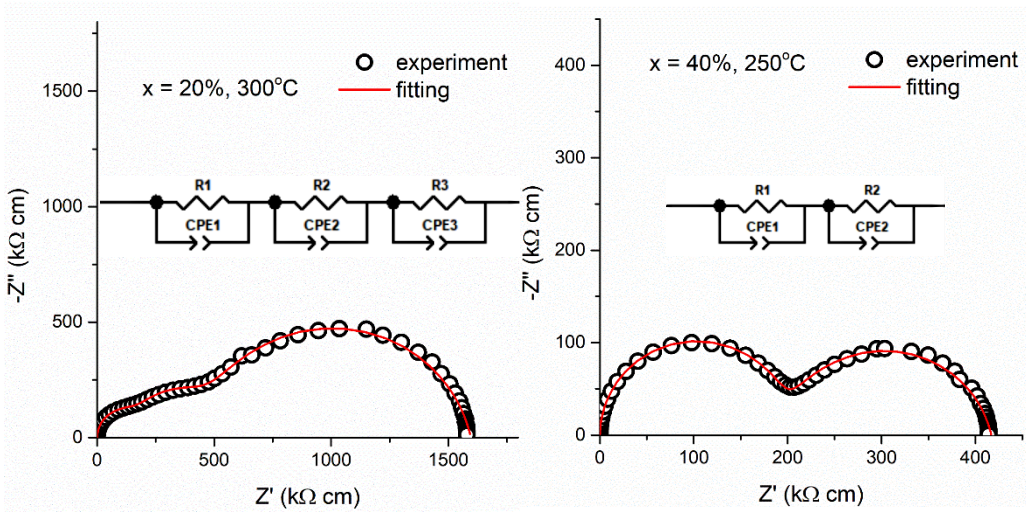

Fig. 7-10. Z* plots and equivalent circuit fittings (inset figures) for x = 20% and 40% measured at 300 and 250 °C, respectively.

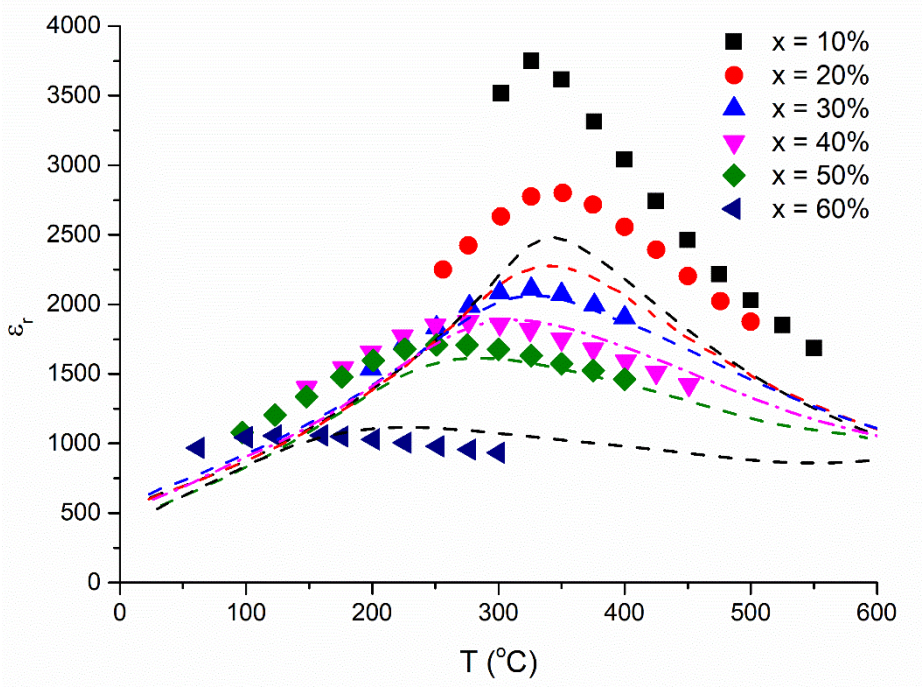

Fig. 7-11. Temperature dependence of bulk ε_r extracted from the fitted IS data. The LCR results (for 1 MHz) are presented as dashed lines.

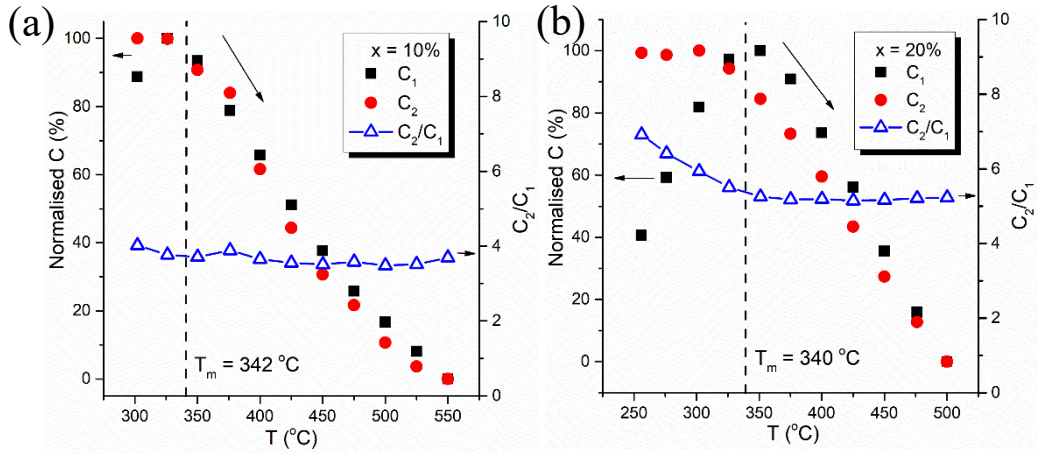

Fig. 7-12. Temperature dependence of normalised C_1 and C_2 (left y-axis), and capacitance ratio (C_2/C_1, right y-axis) for (a) x = 10 and (b) 20%.

EMF measurements show the oxygen ionic transport number (t_{ion}) for x = 20, 40 and 60%, as shown in Fig. 7-13. t_{ion} becomes < 10% at 600 °C, indicating oxygen ionic conduction of NBT (t_{ion} ~ 0.94 at 600 °C)[8] is dramatically suppressed by BNiT-doping. The electronic conduction becomes dominant below 600 °C for x = 40 and 60%,

where t_{ion} is < 2%. However, t_{ion} tends to increase as temperature increases, suggesting that significant ionic conduction may occur at high temperature (> 700 °C).

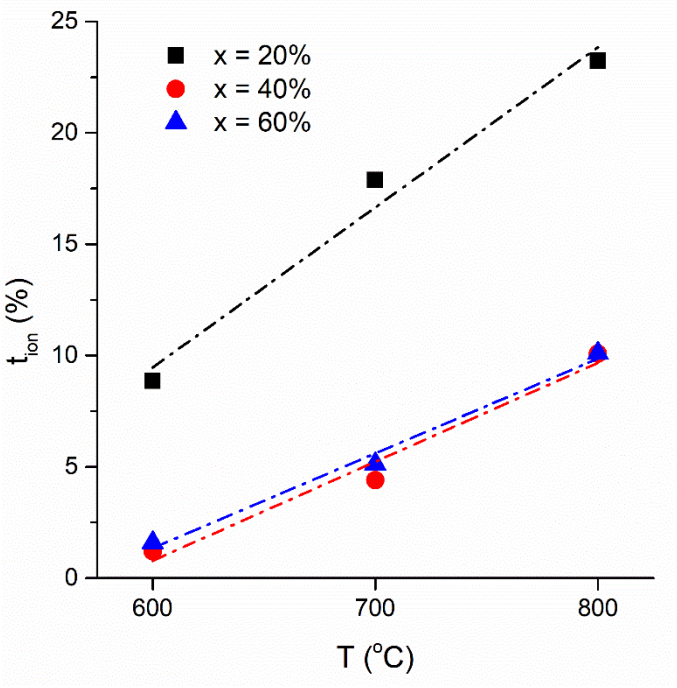

Fig. 7-13. Oxygen ionic transport number (t_{ion}) for selected BNiT-NBT samples from EMF measurements using air/N_2 gas.

The pO_2 dependence for x = 20 and 40% measured at 600 °C are shown in Fig. 7-14, where similar behaviour was also observed for x = 10% and x ≥ 30%, respectively. A distorted semi-circle originating from the combination of R_1 and R_2 was obtained for x = 20%. The low frequency spikes show a typical Warburg diffusion response, which is consistent with EMF results, where ionic conduction is present. However, the resistance increases as pO_2 decreases, indicating that it also shows p-type electronic conduction behaviour and is therefore a mixed conductor. For x > 30%, i.e. x = 40% as shown in Fig. 7-14, only one semi-circle was observed without a Warburg diffusion response and the resistance increases as pO_2 decreases, indicating the samples are dominated by p-type electronic conduction behaviour.

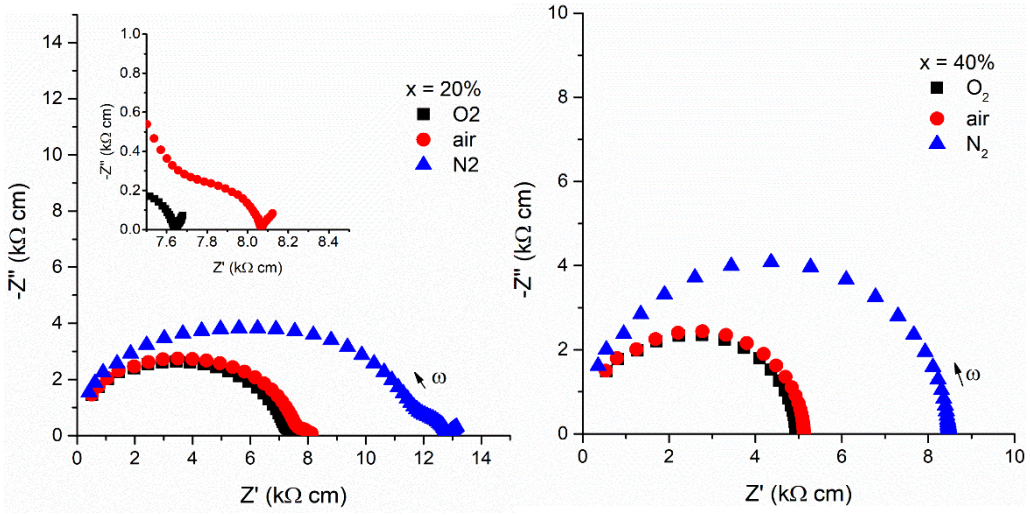

Fig. 7-14. Z* plots for x = 20 and 40% under different flowing gas atmospheres measured at 600 °C, respectively.

Arrhenius plots of σ_b and f_{max} extracted from the fitted IS data for x ≤ 60% are shown in Fig. 7-15. σ_b of NBT is suppressed for x = 10% and then increases for x = 20%. Further doping, such as x = 30%, suppresses σ_b and then it increases systematically with x for x > 20%, where electronic conduction becomes dominant, as shown in Fig. 7-16. Therefore, the enhancement of electronic conductivity for x > 20% may possibly be due to the increase in the Ni content from the BNiT-doping. Suppression of bulk conductivity for x = 10% may be possibly due to oxide ion trapping by the B-site acceptor dopants or by filling of oxygen vacancies with partial oxidation of Ni^{2+} to Ni^{3+} ions. The abnormal behaviour of x = 20% may be attributed to the mixed conduction. Further details will be discussed later. E_a of σ_b decreases systematically from 0.84 to 0.4 eV with x, as shown in Fig. 7-17. It changes at T_m for x ≤ 20% where ionic conduction is present and becomes independent of T_m for x > 20% (Fig. 7-15 (a)) where electronic conduction is dominant. In contrast, E_a of f_{max} obtained from Arrhenius plots (Fig. 7-15 (b)) significantly changes at ~ T_m for x = 20 and 30%. In summary, x = 20% is close to the boundary where the conductivity switches from a mixed conductor to an electronic conductor.

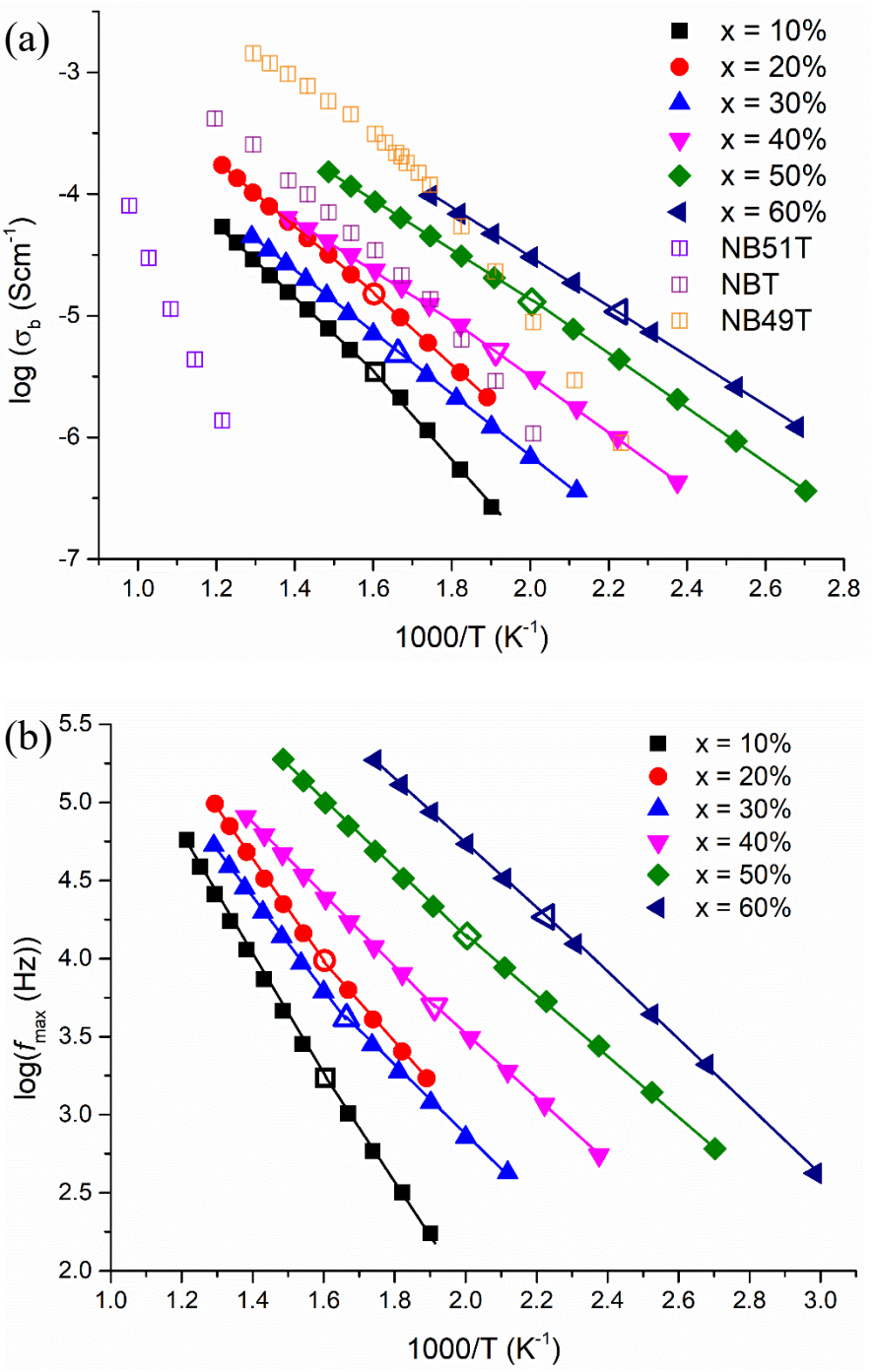

Fig. 7-15. Arrhenius plots of (a) σ_b and (b) bulk f_{max} extracted from the fitted IS data for x ≤ 70%. Open symbols indicate data points close to T_m for each composition.

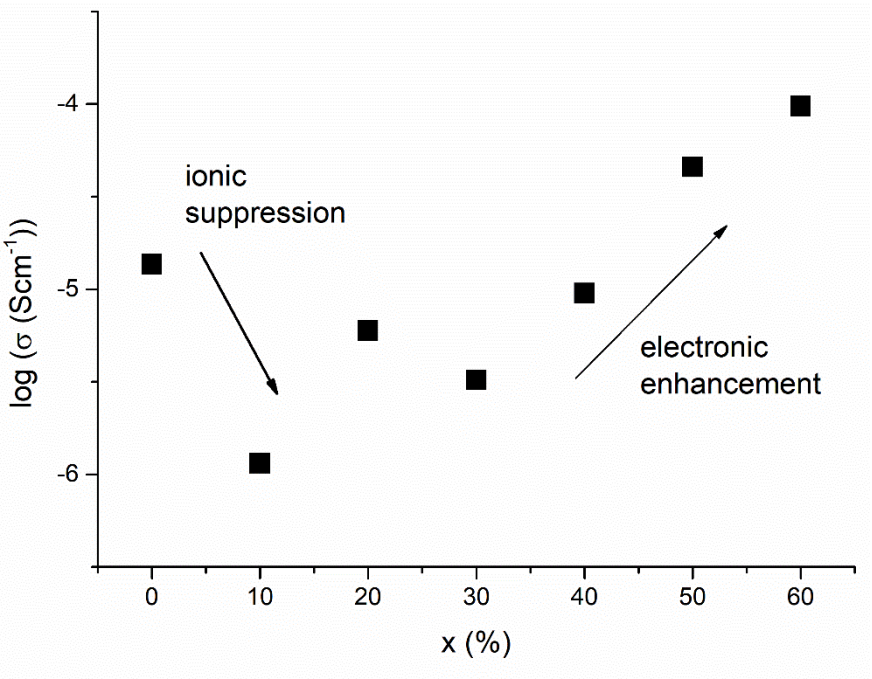

Fig. 7-16. Isothermal plots of σ_b for $x \leq 60\%$ measured at 300 °C.

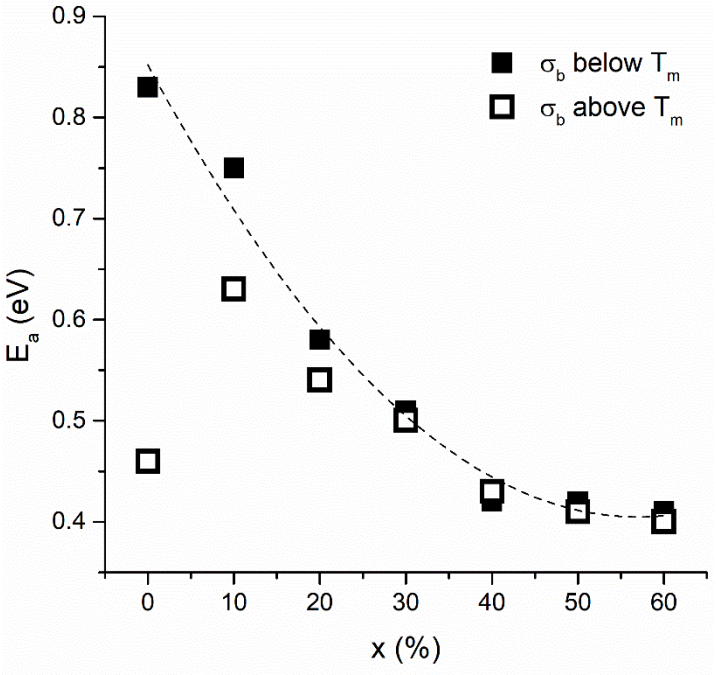

Fig. 7-17. Compositional dependence of bulk E_a for $x \leq 60\%$.

7.3 Discussion

Based on the tolerance factor (t), where Na^+ and Bi^{3+} atoms on the A-site are similar in size (1.39 Å, CN = 12) for the BNiT-NBT series, the larger Ni^{2+} atoms (0.69 Å, CN = 6) replacing smaller Ti^{4+} atoms (0.605Å, CN = 6) on the B-site may increase the lattice distortion(s), leading to form a low symmetry phase with a lower t such as a rhombohedral, orthorhombic or monoclinic phase. Instead, the high temperature tetragonal phase of NBT with the space group P4bm seems to be stabilised at room temperature as the BNiT content increases, i.e. $x \geq 40\%$ based on ND results (Fig. 7-5 (c)). In general, a high symmetry phase, such as a tetragonal or cubic, occurs when $t \sim 1$, where the A-site or B-site atoms of NBT are replaced by larger or smaller atoms, respectively.

For example, in the NBT-KBT ($K_{0.5}Bi_{0.5}TiO_3$) solid solution, the symmetry of NBT transforms from rhombohedral with the space group R3c to tetragonal with the space group P4mm as the larger K^+ atoms (1.69 Å, CN = 12) replaced smaller Na^+ atom on the A-site.[9] However, in the solid solution of NBT-BMT ($Bi(Mg_{0.5}Ti_{0.5})O_3$), the larger Mg^{2+} atoms (0.72 Å, CN = 6) was introduced into the B-site, leading to a decrease in t. The rhombohedral superlattice peak began to disappear when the mole fraction of BMT was 4 ~ 5 %, where the maximum d_{33} occurred ~ 110 pC/N.[10,11] In this case, the symmetry tended to become pseudo-cubic or cubic when the mole fraction of BMT was 6 ~ 50% based on the XRD results.[10-12] Similar behaviour was reported by Bai *et al*. in the solid solution of BNiT-NBT, where the rhombohedral distortion decreased as the BNiT-doping level increased.[5] It is possible that partial oxidation of larger Ni^{2+} ions to smaller Ni^{3+} ions for higher levels of doping may be a plausible explanation that is consistent with arguments based on the simple concept of tolerance factor.

The calcined powders for the BNiT-NBT series always contain NBiT as a secondary phase, indicating that a partial perovskite structure is converted from the Aurivillius structure of NBiT after sintering at 1100 °C for 6h. NBiT is also the precursor for synthesizing a textured NBT using the template grain growth (TGG) or topochemical microcrystal conversion (TMC) method,[13-16] where anisotropic NBiT platelets were obtained using molten salt synthesis sintered at 1050 ~ 1100 °C prior to the conversion of NBT obtained from the mixture of NBiT, Na_2CO_3 and TiO_2 using molten salt synthesis samples sintered at 950 ~ 1100 °C. The preferred orientation of

particle growth for the NBT prepared by the TMC method and conventional solid state synthesis were $[100]_p$ and $[110]_p$, respectively.[16] Fig. 7-18 shows the compositional dependence of the relative intensity for the 100_p peak. The relative intensity increases almost linearly with x, indicating a preference of orientation may possibly occur. Few points are in common for the conversion of perovskite NBT between the solid state synthesis of BNiT-NBT and the TGG/TMC method: (1) BNiT as the template, (2) similar reaction temperatures, (3) liquid phase involved, i.e. BiT secondary phase for x > 20% and (4) preferred orientation $[100]_p$. It is worth noting that the tetragonal phase with space group P4bm and a monoclinic phase with space group Cc coexisted for 7%Ba-doped NBT ($(Na_{0.5}Bi_{0.5})_{0.93}Ba_{0.07}TiO_3$) prepared by the TGG/TMC method, where strip-like domains (ordered regions) were found in a disordered matrix.[17]

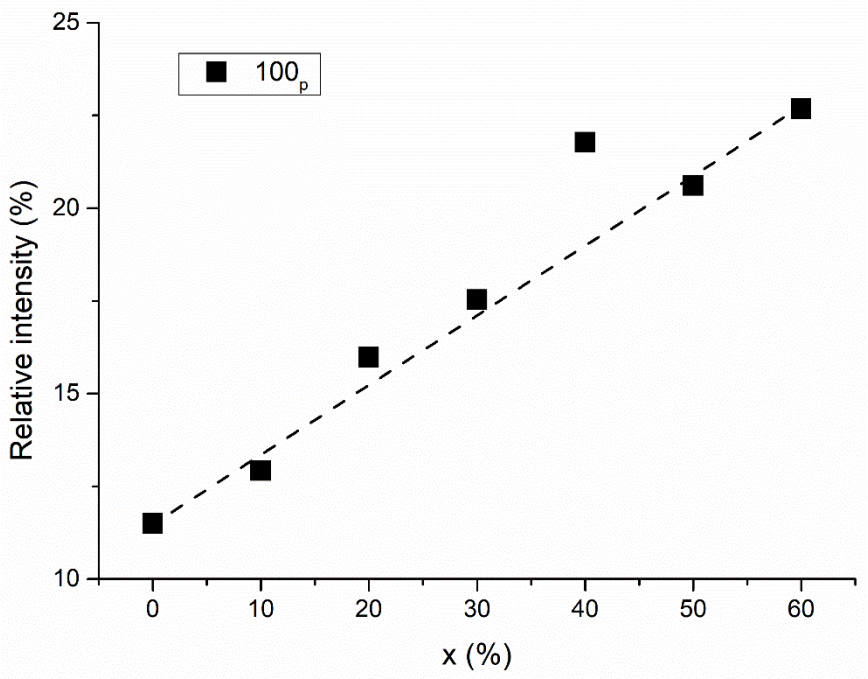

Fig. 7-18. Compositional dependence of the relative intensity for the 100_p peak in the BNiT-NBT series.

The rhombohedral phase based on space group R3c always exits at room temperature, which was confirmed by ND studies, where the rhombohedral superlattice peak (131_R) associated with the $a^-a^-a^-$ tilting was retained up to x = 60%, as shown in Fig. 7-5 (c). Moreover, the two extra peaks observed for x = 40 and 60% can be indexed as tetragonal superlattice peaks (312_T and 310_T) associated with the space group P4bm

with $a^0a^0a^+$ tilting. Therefore, two phases with different tilting systems coexist at room temperature as the BNiT content increases. Similar co-existence behaviour was also observed at 300 °C for NBT by ND studies.[6] It is worth noting that some nanometre-scale tetragonal platelets with preferred orientation along {100} were found at room temperature by TEM studies,[18-20] where Beanland and Thomas[19] showed that they were with the $a^0a^0a^+$ tilting embedded in the rhombohedral $a^-a^-a^-$ matrix. They also indicated that these tetragonal platelets acted strongly to impede domain wall motion. T_m occurred during the phase transition from the rhombohedral to tetragonal phase. Based on the LCR results shown in Fig. 7-8 and 7-9, T_m increases from 323 to 342 °C when the average structure is dominated by the rhombohedral phase at room temperature for $x \leq 20\%$. In contrast, the presence of a tetragonal phase at room temperature for $x \geq 40\%$ leads to a decrease in T_m in conjunction with peak flattening, where a significant decrease in T_m during cooling suggests the high temperature tetragonal phase is stabilised by the BNiT-doping. Similar behaviour is also observed at x = 30%, suggesting that the phase coexistence at room temperature may occur for $x \geq 30\%$. The tetragonal phase may be stabilised by the BNiT-doping because the perovskite NBT converted from the NBiT templates has a preferred orientation. Further TEM studies may be required to clarify this hypothesis.

From the EMF measurements, all compositions have significant t_{ion} (i.e. ~10 - 20 %) at 800 °C, indicating the presence of oxygen vacancies due to the Bi loss during ceramic processing according to the following equation:

$$2Bi_{Bi}^{x} + 3O_{O}^{x} \rightarrow 2V_{Bi}^{'''} + 3V_{O}^{\cdot\cdot} + Bi_2O_3(\mathrm{g}) \qquad 7\text{-}2.$$

Based on the pO_2 dependence, all compositions have p-type electronic conducting behaviour, which may be attributed to the presence of Ni^{3+} atoms, which are oxidised from Ni^{2+} during cooling according to the following equation:

$$2Ni_{Ni}^{x} + V_{O}^{\cdot\cdot} + \frac{1}{2}O_2(g) \rightarrow 2Ni_{Ni}^{\cdot} + O_{O}^{x} \qquad 7\text{-}3.$$

E_a of σ_b decreases from a high of 0.84 eV to a low of 0.4 eV as x increases from 0 to 60% as shown in Fig. 7-17, where the former and latter are consistent with the activation energy for oxygen ions and electron hole hopping, respectively. Therefore, the predominant charge carrier changes from oxygen ions to electron holes as the BNiT content increases, which is confirmed by the EMF measurements (Fig. 7-13). For $x \leq$

20%, the heterogeneous electrical response is attributed to mixed (ionic and electronic) conduction, leading to a decrease in E_a of σ_b below T_m (Fig. 7-17). However, E_a of σ_b above T_m significantly increases from 0.46 to 0.63 eV for x = 0 and 10%, respectively, in cooperation with a decrease in σ_b. This suggests the ionic conductivity may be suppressed by oxygen ion trapping, where positively charged ($V_O^{\cdot\cdot}$) combines with negatively charged (Ni_{Ti}'') to form the defect complex $(Ni_{Ti}'' - V_O^{\cdot\cdot})^x$. The mobility of oxygen ions is expected to decrease with increasing BNiT content as well as negatively charged B-site acceptor dopants (Ni_{Ti}''), leading to a decrease in ionic conductivity. In contrast, p-type electronic conduction may be certainly improved with increasing Ni^{2+} content (electron hole hopping between Ni^{3+} ($Ni_{Ni}^{\cdot}$) and Ni^{2+} (Ni_{Ni}^{x})). Somehow the bulk conductivity of x = 20% seems to benefit from both ionic and electronic conduction, leading to an increase in bulk conductivity compared to x = 10% and 30%. As the mobility of oxygen ions is restricted by trapping or the oxygen vacancies are decreased by oxygen-pick up on cooling according to equation 7-3, i.e. x > 20%, p-type electronic conductivity becomes dominant and increases with BNiT content, where the associated E_a tends to be ~ 0.4 eV.

7.4 Conclusions

1. The solid solution limit for the BNiT-NBT series is ~ 60%, which is confirmed by XRD and SEM/EDS.

2. Based on XRD and ND results, the high temperature tetragonal phase with the space group P4bm is stabilised at room temperature by BNiT-doping for x ≥ 40%.

3. Stabilisation of the tetragonal phase may possibly be related to the conversion of the perovskite NBT from the Aurivillius NBiT with liquid phase BiT assistance, which is similar to the TGG/TMC processing method.

4. Based on LCR results, coexistence of rhombohedral and tetragonal phases leads to permittivity peak broadening and a decrease of T_m to a lowest value of 186 °C during cooling for x = 60%.

5. The ionic conductivity is suppressed by BNiT-doping due to oxygen ion trapping, where p-type electronic conductivity becomes dominant for $x \geq 30\%$ which systematically increases with increasing BNiT content.

7.5 References

1. Inaguma, Y. and Katsumata, T. High Pressure Synthesis, Lattice Distortion and Dielectric Properties of a Perovskite $Bi(Ni_{1/2}Ti_{1/2})O_3$, *Ferroelectrics*, **286**, 111-117 (2003)

2. Zhu, J., Feng, S., Liu, Q., Zhang, J., Xu, H., Li, Y., Li, X., Liu, J., Huang, Q., Zhao, Y., and Jin, C., Temperature and pressure effects of multiferroic Bi_2NiTiO_6 compound, *Journal of Applied Physics*, **113**, 143514(2013)

3. Coi, S.M., Stringer, C.J., Shrout, T.R., and Randall, C.A., Structure and property investigation of a Bi-Based perovskite solid solution: $(1-x)Bi(Ni_{1/2}Ti_{1/2})O_3$-$xPbTiO_3$, *Journal of Applied Physics*, **98**, 034108 (2005)

4. Fujii, I, Nakashima, K. Kumada, N. and Wada, S., Structural, dielectric and piezoelectric properties of $BaTiO_3$-$Bi(Ni_{1/2}Ti_{1/2})O_3$ ceramics, *Journal of the Ceramic Society of Japan*, **120**(1), 30-34 (2012)

5. Bai, W., Liu, F., Li, P., Shen, B., Zhai, J. and Chen, H., Structure and electromechanical properties in $Bi_{0.5}Na_{0.5}TiO_3$-based lead-free piezoceramics with calculated end-member $Bi(Ni_{0.5}Ti_{0.5})O_3$, *Journal of the European Ceramic Society*, **35**, 3457-3466 (2015)

6. Jones, G.O. and Thomas, P.A., Investigation of the structure and phase transitions in the novel A-site substituted distorted perovskite compound $Na_{0.5}Bi_{0.5}TiO_3$, *Acta Crystallographica Section B*, **58**, 168-178 (2002)

7. Fleig, J. The grain boundary impedance of random microstructures: numerical simulations and implications for the analysis of experimental data, *Solid State Ionics*, **150**, 181-193 (2002)

8. Li, M., Pietrowski, M.J., De Souza, R.A., Zhang, H., Reaney, I.M., Cook, S.N., Kilner, J.A. and Sinclair, D.C., A family of oxide ion conductors based on the ferroelectric perovskite $Na_{0.5}Bi_{0.5}TiO_3$, *Nature Materials*, **13**, 31-35 (2014)

9. Jones, G.O., Kreisel, J. and Thomas, P.A., A structural study of the $(Na_{1-x}K)_{0.5}Bi_{0.5}TiO_3$ perovskite series as a function of substitution (x) and temperature, *Powder Diffraction* **17**(4), 301-319 (2002)

10. Wang, Q., Chen, J., Fan, L., Liu, L. Fang, L. and Xing, X., Preparation and Electric Properties of $Bi_{0.5}Na_{0.5}TiO_3$-$Bi(Mg_{0.5}Ti_{0.5})O_3$ Lead-free Piezoceramics, *Journal of the American Ceramic Society* **96**(4), 1171-1175 (2013)

11. Jain Ruth, D.E., Muneeswaran, M., Giridharan, N.V. and Sundarakannan, B., Structural and electrical properties of bismuth magnesium titanate substituted lead-free sodium bismuth titanate ceramics, *Journal of Materials Science: Materials in Electron* **27**, 7018-7023 (2016)

12. Wang, X. and Cao, W., Dielectric properties of new perovskite ceramics $(Na_{1/4}Bi_{3/4})(Mg_{1/4}Ti_{3/4})O_3$ and $(K_{1/4}Bi_{3/4})(Mg_{1/4}Ti_{3/4})O_3$, *Journal of the European Ceramic Society* **27**, 2481-2484 (2007)

13. Setasuwon, P. and Kijamnajsuk, S., Synthesis of $Na_{0.5}Bi_{0.5}TiO_3$ anisotropic particles with grain orientation by conversion of $Na_{0.5}Bi_{4.5}Ti_4O_{15}$ crystals, *Science and Technology of Advanced Materials* **7**, 780-784 (2006)

14. Zeng, J.T., Kwok, K.W., Tam, W.K., Tian, H.Y., Kiang, X.P. and Chan, H.L.W., Plate-like $Na_{0.5}Bi_{0.5}TiO_3$ Template Synthesized by Topochemical Method, *Journal of the American Ceramic Society* **89**(12), 3850-3853 (2006)

15. Jiang, C., Zhou, K., Zhou, X., Li, Z. and Zhang, D., Synthesis and characterization of $Na_{0.5}Bi_{0.5}TiO_3$ platelets with preferred orientation using Aurivillius precursors, *Ceramics International* **41**, 6858-6862 (2015)

16. Hussain, A., Rahman, J.U., Ahmed, F., Kim, J., Kim, M., Song, T. and Kim, W., Plate-like $Na_{0.5}Bi_{0.5}TiO_3$ particles synthesized by topochemical microcrystal conversion method, *Journal of the European Ceramic Society* **35**, 919-925 (2015)

17. Jiang, C., Zhang, D., Zhou, K., Yan, H., Zhang, H. and Abrahams, I., Topochemical transformation of two-dimensional single crystalline $Na_{0.5}Bi_{0.5}TiO_3$-$BaTiO_3$ platelets from $Na_{0.5}Bi_{0.5}TiO_{15}$ precursors and their piezoelectricity, *Journal of Materials Chemistry A* **5**, 15780-15788 (2017)

18. Dorcet, B. and Trolliard, G., A transmission electron microscopy study of the A-site disordered perovskite $Na_{0.5}Bi_{0.5}TiO_3$, *Acta Materialia* **56**, 1753-1761 (2008)

19. Beanland, R. and Thomas P.A., Imaging planar tetragonal sheets in rhombohedral $Na_{0.5}Bi_{0.5}TiO_3$ using transmission electron microscopy, *Scripta Materialia* **65**, 440-443 (2011)

20. Beanland, R. and Thomas P.A., Symmetry and defects in rhombohedral single-crystalline $Na_{0.5}Bi_{0.5}TiO_3$, *Physical Review B* **89**, 174102 (2014)

Chapter 8.

General discussion

8.1 Phase formation

In this project, the nominal oxygen content (O_n) of doped NBT was carefully controlled by variable dopants on the A-site or B-site alone or both A and B-sites, where $2.955 \leq O_n \leq 3.02$ The phase formation of perovskite NBT can be accelerated by the presence of oxygen vacancies introduced by acceptor dopants, where single-phase materials can be obtained from calcined powders below 900 °C based on XRD when O_n is < 3, i.e. $Na_{0.5-x}Bi_{0.5+x}TiO_{3+x}$ and $Na_{0.5-z}Bi_{0.5+z}Ti_{1-x}Ga_xO_{3+z-0.5x}$ series as shown in Fig. 4-3 and Fig. 5-21, respectively. However, small amounts of secondary phases, such as $Na_2Ti_3O_6$ and sodium gallium titanate, were still observed by SEM on the sintered pellet surfaces of $Na_{0.52}Bi_{0.48}TiO_{2.98}$ and $Na_{0.5}Bi_{0.5}Ti_{0.97}Ga_{0.03}O_{2.985}$, respectively. It is worth noting that these secondary phases seem to be Bi-free, leading to form relatively Bi-rich bulk NBT compositions. This self-recovery behaviour may be attributed to the compensation of oxygen vacancies introduced by acceptor dopants, which limits the charge carrier concentration for ionic conductivity. In contrast, calcined powders tend to contain $Na_{0.5}Bi_{4.5}Ti_4O_{15}$ (NBiT) as a secondary/intermediate phase when O_n and the Na/Bi ratio are > 3 and < 1, respectively. This is consistent with the phase equilibria in the Na_2O-BiO_3-TiO_2 system at 1000 °C, where NBT tends to transform into NBiT with excess Bi content.[1]

As O_n is fixed at 3 for the solid solution of NBT with end members such as $BiGaO_3$ (BG), $BiFeO_3$ (BF) and $Bi(Ni_{0.5}Ti_{0.5})O_3$ (BNiT), the phase formation of perovskite NBT becomes challenging because the Na/Bi ratio is < 1 and therefore Bi-rich secondary/intermediate phases tend to exist after calcination. The type of Bi-rich secondary/intermediate phases depends on the acceptor dopants on B-site: the trivalent dopants, such as M = Ga^{3+} and Fe^{3+} tend to react with Bi^{3+} atoms to form a mullite-type structure with the general formula $Bi_2M_4O_9$, where sillenite phases with the general formula $Bi_{25}MO_{39}$ may form as the doping level increases for trivalent dopants.[2] Divalent dopants, such as Ni^{2+}, tend to remain as NiO along with NBiT and the sillenite phase $Bi_{12}TiO_{20}$ (BiT). Single-phase NBT samples may be obtained after sintering at high temperature but homogeneity of the bulk composition may strongly depend on the

sintering profile due to the presence of secondary/intermediate phases prior to the sintering process. For example, a core-shell like behaviour was observed based on IS for the BNiT-NBT series when the BNiT content is ≤ 20% although no strong evidence was found based on the backscattering images observed by SEM, possibly due to undetectably small core fractions.

The solubility of BG is similar to $BiAlO_3$ (BA) and much lower than $BiScO_3$ (BS), BF and BNiT, as shown in Table 8-1, where the solid solution limit of the Bi-based perovskite end members tends to increase with increasing ionic size of the acceptor dopant on the B-site. The formation of NBT perovskite may strongly depend on the stability and structure of the secondary/intermediate phases introduced by doping. BF can form a full solid solution with NBT, where it is the only end member in this list that can be synthesised at ambient pressure, while the others are high pressure phases. Both BF and NBT have rhombohedral symmetry and a perovskite structure at room temperature and therefore the Fe atoms can easily accommodate the Ti-site, especially in the Bi-rich environment where Bi atoms are replacing Na atoms with increasing BF content.

For the BNiT-NBT series, single-phase perovskite can be converted from the mixture of the Aurivillius phase NBiT, sillenite phase BiT and NiO at high temperature. It should be noted that the Aurivillius phase $Bi_4Ti_3O_{12}$ (BTO) and sillenite BiT phase are intermediate phases in the phase formation of NBT perovskite.[6] This is possibly because the Aurivillius phases NBiT and BTO have a layered structure, and contain pseudo-perovskite blocks that are structurally similar to NBT. Both NBiT and BTO are common template seeds for fabricating textured NBT via the templated grain growth (TGG) method.[7] No stable phase at ambient pressure is reported in the Bi_2O_3-Sc_2O_3 binary system. Therefore, the formation mechanism for the BS-NBT series may possibly be similar to the one for the BNiT-NBT series. The solubility of BNiT (60%) is almost double that of BS (25 ~ 30%). In fact, the solution limit of Sc^{3+} and Ni^{2+} ions on the B-site is similar ~ 30%.

For the BG-NBT series, the main secondary phase $Bi_2Ga_4O_9$ has a mullite-type structure, where Ga occupies both octahedral and tetrahedral sites.[8] Moreover, it melts incongruently at ~ 1080 °C, which is lower than the sintering temperature commonly used for NBT-type ceramics. The deviation in structural similarity and instability at

high temperature may result in the difficulty for the formation of the perovskite. In addition, $BiGaO_3$ has a pyroxene-like structure, where Ga occupies tetrahedral sites.[9] The preference of Ga occupancy in a Bi-rich environment may also lead to limit the solubility of BG. It is worth noting that the solubility of BA and BG are similar ~ 6%, where they may both contain a mullite-type phase as a secondary/intermediate phase.

End member	SS	Ionic radii (Å)	Reference
$BiGaO_3$ (BG)	~ 6%	0.62	This work
$BiAlO_3$(BA)	~ 6%	0.535	3
$BiScO_3$(BS)	25~30%	0.745	4,5
$BiFeO_3$(BF)	100%	0.645 (high spin)	5
$Bi(Ni_{0.5}Ti_{0.5})O_3$(BNiT)	~60% (30%)	0.69	This work

Table. 8-1. The solid solution limits (SS) of Bi-based perovskite end members and associated ionic radii of the accepter dopants on the B-site in 6-fold coordination. Note that the bracket shown in SS of $Bi(Ni_{0.5}Ti_{0.5})O_3$ indicates the Ni content.

8.2 Electrical properties

The compositional dependence of T_m for the BF-NBT and BNiT-NBT series is summarised in Fig. 8-1. The T_m of NBT occurs between the rhombohedral to tetragonal phase transition. LCR results for the BF-NBT series show clear evidence for the rhombohedral phase stabilisation, where T_m systematically increases as the BF-doping level increases. Coexistence of the rhombohedral and tetragonal phases at room temperature in XRD and ND data for the BNiT-NBT series leads to a decrease in T_m when the BNiT content is > 20%. Similar T_m is observed in both series when the doping level is 0 ~ 20% where the rhombohedral phase is dominant in room temperature XRD data and it increases from 324 ~ 345 ℃. It should be noted that the Bi/Na ratio decrease with increasing doping level, where the same doping level has an equivalent Bi/Na ratio. For the nonstoichiometric NBT as discussed in Chapter 4, T_m tends to increase with decreasing Na/Bi ratio up to 331 ℃ within the solid solution limit. Thus, the increase in T_m for doping level ≤ 20% may be attributed to the decrease in Na/Bi ratio, where the polarisability of NBT is dominated by the A-site, leading to a relatively small deviation. As the doping level increases to > 20%, the structural change in symmetry by the B-site cation can become dominant. For example, the rhombohedral distortion

is much clearer in room temperature XRD data for BF-doping levels > 30% and the tetragonal phase is stabilised for the BNiT-doping levels > 20%. However, the leakage increases as the doping level increases due to the fluctuation of acceptor dopants on the B-site.

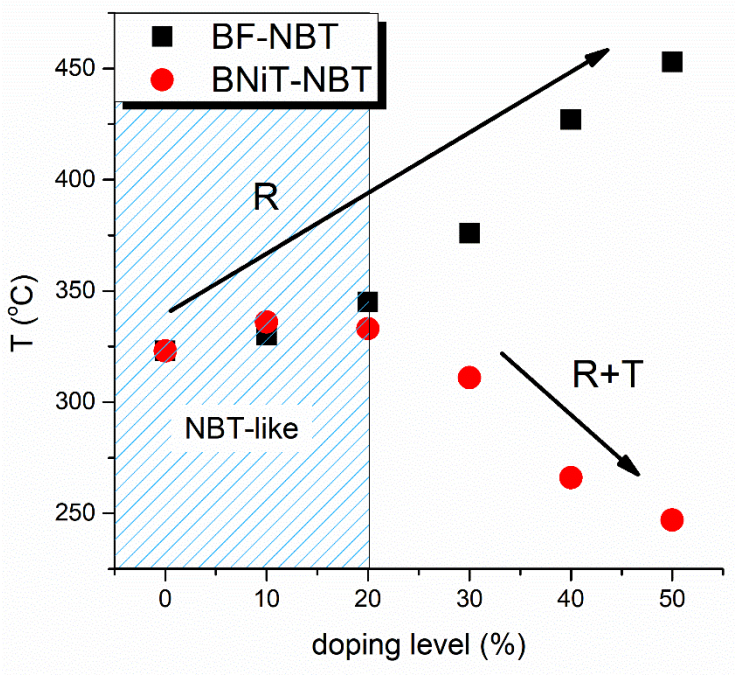

Fig. 8-1. Compositional dependence of T_m for the BF-NBT and BNiT-NBT series

Isothermal plots of bulk conductivity for the solid solution of NBT with end members, such as BG, BF, 1%Nb-BF and BNiT, measured at 600 °C in comparison with the nonstoichiometric NBT are shown in Fig. 8-2. For nonstoichiometric NBT with a small deviation in the Na/Bi ratio from 1.04 ~ 0.96, the bulk conductivity decreases four orders of magnitude from ~ 10^{-2} to 10^{-6} Scm^{-1}, where it switches from an ionic conductor to an insulator, respectively. For the BG-NBT series, it becomes an insulator when it reaches the solid solution limit ~6%. Similar behaviour was reported by Yang *et al*. in the BA-NBT series.[10] They also indicated the suppression of ionic conductivity may be attributed to trapping of oxygen vacancies by acceptor dopants on the B-site. For the BF-NBT series, ionic conduction is still present when the BF-doping level is 50%, where E_a increases systematically with increasing doping level due to trapping of oxygen vacancies by Fe^{3+} ions. The p-type electronic conduction becomes dominant for BF-doping levels ≥ 60%. However, ionic conduction may still be

dominant under lower pO_2 and/or at high temperature. In contrast to the BF-NBT series, the ionic conduction is suppressed more efficiently for the BNiT-NBT series. t_{ion} is only ~ 10% at 600 °C when the BNiT-doping level is 20%, where the acceptor dopant (Ni^{2+}) content is 10 at% of the B-site atoms, which is equivalent to 10% BF-doping. p-type electronic conduction becomes dominant for BNiT-doping level > 20%, where the rhombohedral and tetragonal phases coexist. This suggests the suppression of ionic conduction may possibly be correlated with the stabilisation of the tetragonal phase. Overall, $Na_{0.51}Bi_{0.49}TiO_{2.99}$ shows a comparable conductivity to $Zr_{0.852}Y_{0.148}O_{1.926}$ (8YSZ) as an ionic conductor. With high BF-doping ≥ 60%, it also shows potential as a mixed ionic-electronic conductor, where both ionic and electronic conductivity may be improved by chemical doping.

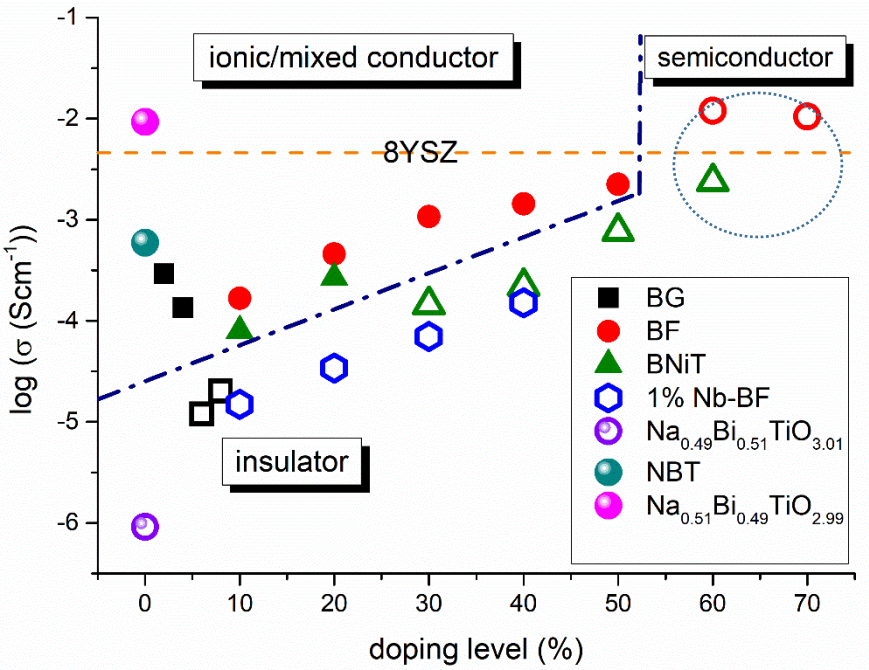

Fig. 8-2. Isothermal plots of bulk conductivity for the solid solution of NBT with end members, such as BG, BF, 1%Nb-BF and BNiT, measured at 600 °C in comparison with nonstoichiometric NBT. The filled symbols indicate an ionic or mixed conductor. The open symbols indicate a semiconductor or insulator. The orange dashed line represents the conductivity of $Zr_{0.852}Y_{0.148}O_{1.926}$ (8YSZ)[9].

8.3 Future work

For the BF-NBT series, a diffusive electrode response was observed in the low frequency range under N_2 gas at 600 ℃ when the BF content is 60%, indicating the presence of ionic conduction. The electronic conductivity is ~ 0.01 Scm^{-1} at this temperature. For Ca-doped $BiFeO_3$ reported by Maso and West, sintering and then cooling in N_2 at 800 ℃ can eliminate p-type electronic conduction introduced by partial reoxidation of Fe^{3+} ions, where ceramics become an oxide ion conductor.[11] Therefore, the conductivity and the associated conduction mechanism(s) can be very sensitive to pO_2 and the sintering conditions. The first thing to do is to confirm the conduction mechanism for the BF-NBT series by EMF measurements. Annealing in N_2 above 600 ℃ may be able to see the tendency for a change in conduction mechanism. Acceptor doping for Bi may potentially increase oxygen vacancies, leading to an increase in ionic conductivity. However, for making an ionic conductor, sintering in N_2 may be required to prevent the reoxidation of Fe^{3+} ions to suppress electronic conduction.

For the BNiT- NBT series, coexistence of rhombohedral and tetragonal phases may start to occur when the BNiT content is between 20 ~ 40%, which needs to be confirmed by ND studies. TEM studies may reveal the presence of a core-shell structure, where the secondary component observed in the IS measurement also have a bulk-type behaviour when the BNiT content is ≤ 20%. Moreover, it should be possible to observe two types of tilting systems: rhombohedral $a^-a^-a^-$ tilting and tetragonal $a^0a^0c^+$ titling for BNiT-doping level > 20%. ε_r ~1000 becomes relatively temperature independent between 150 ~ 600 ℃ when the NBiT content is 60%. However, the leakage increases due to an increase in p-type electronic conductivity. Small amounts of Nb donor doping for Ti (~1 at%) which fills up oxygen vacancies may prevent the reoxidation of Ni^{2+} ions.

8.4 References

1. Uchida, K. and Kikuchi, T., Subsolidus Phase Equilibria in the System Na_2O-Bi_2O_3-TiO_2 at 1000 ℃, *Journal of American Ceramics Society* **61**, 5-8 (1978)

2. Wu, M., Fang, L., Liu, L., Li, G. and Elouadi, B., Dielectric and Ferroelectric Properties of (1-x)$BiFeO_3$-x$Bi_{0.5}Na_{0.5}TiO_3$ Solid Solution, *Ferroelectrics* **478**, 18-25 (2015)

3. Yang, F., Wu, P. and Sinclair, D.C., Suppression of electrical conductivity and switching of conduction mechanism in 'stoichiometric' $(Na_{0.5}Bi_{0.5}TiO_3)_{1-x}(BiAlO_3)x$ ($0 \leq x \leq 0.08$) solid solutions, *Journal of Materials Chemistry C* **5**, 7243-7252 (2017)

4. Nagata H. and Takenaka, T., Lead-free Piezoelectric Ceramics of $(Bi_{1/2}Na_{1/2})TiO_3$-1/2(Bi_2O_3·Sc_2O_3) system, *Japanese Journal of Applied Physics* **36**, 6055-6057 (1997)

5. Marchet, P., Boucher, E., Dorcet, V. and Mercurio, J.P., Dielectric properties of some low-lead or lead-free perovskite-derived materials: $Na_{0.5}Bi_{0.5}TiO_3$-$PbZrO_3$, $Na_{0.5}Bi_{0.5}TiO_3$-$BiScO_3$ and $Na_{0.5}Bi_{0.5}TiO_3$-$BiFeO_3$ ceramics, *Journal of the European Ceramic Society* **26**, 3037-3041 (2006)

6. Aksel, E. and Jones, J.L., Phase Formation of Sodium Bismuth Titanate Perovskite During Solid-State Processing, *Journal of the American Ceramic Society* **93** (10), 3012-3016 (2010)

7. Zhao, W., Liu, N., Gao, K., Wang, Z. and Zhang, S., Synthesis of Anisotropic $Na_{0.5}Bi_{0.5}TiO_3$ crystals using different Topochemical Microcrystal Conversion Methods, *International Journal of Applied Ceramic Technology* **13** (5), 871-875 (2016)

8. Schreuer, J., Burianek, M., Mühlberg, M., Winkler, B., Wilson, D. and Schneider, H., Crystal growth and elastic properties of orthorhombic $Bi_2Ga_4O_9$, *Journal of Physics: Condensed Matter* **18**, 10977-10988 (2006)

9. Arachi, Y., Sakai, H., Yamamoto, O., Takeda, Y. and Imanishai, N., electrical conductivity of the ZrO_2-Ln_2O_3 (Ln = lanthanides) system, *Solid State Ionics* **121**, 133-139 (1999)

10. Yang, F., Wu, P. and Sinclair, D.C., Suppression of electrical conductivity and switching of conduction mechanisms in 'stoichiometric' $(Na_{0.5}Bi_{0.5}TiO_3)_{1-}$

$_x(BiAlO_3)_x$ ($0 \leq x \leq 0.08$) solid solutions, *Journal of Materials Chemistry C* **5**, 7243-7252 (2017)

11 Maso, N. and West, A.R., Electrical Properties of Ca-doped $BiFeO_3$ Ceramics: From p-Type Semiconduction to Oxide-ion Conduction, *Chemistry of Materials* **24**, 2127-2132 (2012)

Chapter 9.

Conclusions

1. The conductivity of NBT is very sensitive to the Na/Bi ratio, which directly influences the oxygen content. It switches from an insulator to an ionic conductor for Na/Bi ≥ 1. Samples prepared by hand grinding show lower conductivity for stoichiometric NBT, suggesting better control of the nominal starting composition. For the $Na_{0.5-x}Bi_{0.5+x}TiO_{3+x}$ series, the solid solution limit is $-0.02 < x < 0.02$. 1 at% Na-acceptor doping for Bi can achieve the maximum ionic conductivity, which suggests the limit of oxygen vacancies in undoped NBT is very low at ~0.33 at%. In contrast, 1 at% Bi-donor doping for Na is enough to eliminate ionic conduction.

2. The phase formation of NBT perovskite depends on the balance of charge configuration between the A (Na/Bi ratio) and B-sites. For example, reducing the Na/Bi ratio can expand the solubility of acceptor dopants (Ga, Fe, Ni) on the B-site because acceptor doping on Ti is compensated by Bi-donor doping for Na on the A-site. Consequently, the Na/Bi ratio may tend to decrease with increasing oxygen vacancies in order to balance the local charge configuration. This self-recovery behaviour limits the oxygen vacancy content and therefore ionic conductivity.

3. f_{max} associated with the large M'' Debye peak associated with the bulk response in electroceramics is a geometry independent parameter and is a useful analysis tool to determine any intrinsic changes in the bulk component associated with a small change in composition.

4. Nominal starting compositions with Na/Bi < 1 prepared by conventional solid state synthesis may easily form Bi-rich secondary/intermediate phases at low temperature, which remain after calcination. These secondary/intermediate phases with high structural similarity to NBT, such as NBiT, may convert into a single-phase perovskite after sintering at an appropriate temperature.

5. For the solid solution of NBT with Bi-based perovskites, such as BG-NBT, BF-NBT and BNiT-NBT, the ionic conduction is suppressed with increasing doping

level, suggesting trapping of oxygen vacancies by acceptor dopants on the B-site.

6. For the BG-NBT series, the solid solution limit is very low ~ 6%, where ionic conductivity is eliminated. At this boundary, the actual composition, especially the Ga content, may be influenced by the formation of secondary phases, leading to a suppression of the bulk conductivity.

7. For the BF-NBT series, the rhombohedral phase is stabilised by BF-doping, leading to an increase in T_m. The bulk conductivity switches from ionic to p-type electronic conduction when the BF content is ≥ 60% for samples processed and measured in air. The ionic conductivity can be eliminated by 1% Nb-doping on the Ti site when the BF content is ≤ 40%.

8. For the BNiT-NBT series, the solid solution limit is ~ 60%. The high temperature tetragonal phase P4bm is stabilised by BNiT-doping at room temperature for BNiT-doping levels ≥ 40%, which is revealed by ND studies. T_m dramatically decreases to a lowest 186 ℃ with permittivity peak broadening when the BNiT content is 60% due to the coexistence of rhombohedral and tetragonal phases. p-type electronic conductivity becomes dominant when the BNiT content is ≥ 30%, which systematically increases with increasing BNiT content.